RESEARCH & REVIEWS IN ENGINEERING

October 2022

Editors

Doç.Dr. Vedat Çavuş
Doç. Dr. Selahattin BARDAK

Research & Reviews in Engineering

OCTOBER 2022

<u>Editors</u>

Doç.Dr. Vedat Çavuş
Doç. Dr. Selahattin BARDAK

CONTENTS

CHAPTER 1

NANOPACKING IN SEAFOOD PRODUCTS

Ayşe Gülin Eser[1], Fatma Burcu Harmantepe [2]

1 Assoc.Prof.Dr., Department of Food Processing, Biga Vocational School, Canakkale Onsekiz Mart University, Türkiye *Corresponding Author: Email: gsezen@comu.edu.tr ORCID ID: https://orcid.org/0000-0001-8799-3073

2 Assoc.Prof.Dr., Department of Food Processing, Biga Vocational School, Canakkale Onsekiz Mart University, Türkiye ORCID ID: https://orcid.org/0000-0002-3277-396X

1. Introduction

Fish and shellfish have a very important place in human nutrition. In addition to being a valuable food source in terms of essential amino acids, they contain substances such as mono and polyunsaturated fatty acids, minerals, vitamins, and antioxidants, which are extremely important for human health. (Prato et al., 2015). They contain docosahexaenoic acid (DHA) and eicosapentaenoic acid (EPA), polyunsaturated fatty acids found in all sea creatures and not found in other foods. (Turan, Kaya & Sönmez ,2006; Bhaskar, Miyashita & Hosakawa, 2006).

Microbiological, enzymatic, chemical, and physical reactions begin after the fishing of fish and other fishery products (Aras Hisar, Hisar & Yanık, 2004). These products, which have high nutritional properties, deteriorate very quickly depending on their postmortem pH being close to neutral, their water activity is high or not, the weak connective tissue that they have, the effect of microorganisms and enzymes in the structure of the food, and the development of spoilage microorganisms. Other factors affecting the rapid deterioration of fish and shellfish products include storage conditions, presence of atmospheric oxygen, reduction-oxidation reactions, non-protein nitrogenous compounds, and containing trimethylamine oxide (TMAO) (Gram & Huss, 1996; Ünlütürk & Turantaş, 1999) Due to these sensitive structures, the cold chain should not be broken in any of the transportation, preservation, storage, and consumer transportation stages of fish and shellfish products, and food safety should be considered in all processes. In addition to cold storage and storage, it is also very important to package these products with protective and durable packaging materials (Kılınç & Çaklı, 2001).

In recent years, consumer preferences and the needs of the food industry have been changing and depending on these changes, studies to increase the functionality of packaging and to ensure food safety gain importance (Dobrucka, 2013a). Modified atmosphere packaging (MAP) (Kuuliala et al., 2018), smart packaging systems (Ge et al., 2020), active packaging systems (Dong et al., 2018), edible film coating (Licciardello et al., 2018) packaging systems are used in food preservation. All these packaging systems and nanotechnological applications are also used in the packaging of fish and shellfish products. Thanks to these applications, hygienic production of fish and shellfish products is ensured, the products' shelf life can be controlled, and the traceability of the products in their shipment and retail sale can be controlled. (Mol, 2014). Nanotechnology, which is a branch of science, covers the examination, control, and acquisition of new properties, production, characterization, and application of materials in the size of a nanometer (Saka, & Terzi ,2015; Joseph & Morrison, 2006). A nanometer is expressed as one billionth of a meter or one millionth of

a millimeter. Structures in the size of 1-100 nanometers are defined as nanomaterials and are generally classified as carbon-based (organic), metal and metal oxide-based (inorganic), or composite (hybrid) materials according to their building blocks (Küçükçobanoğlu & Aktaş, 2018).

Nanotechnological applications have brought innovations to food packaging technology and increased the functionality of packaging (Fig. 1). With the addition of nanoparticles to packaging materials, the barrier and mechanical properties of packaging have been improved, biodegradable packaging and active packaging systems have been developed, nanosensors have been produced, and the development of smart packaging applications has been achieved by using these sensors (Saka & Terzi, 2015) (Fig. 2).
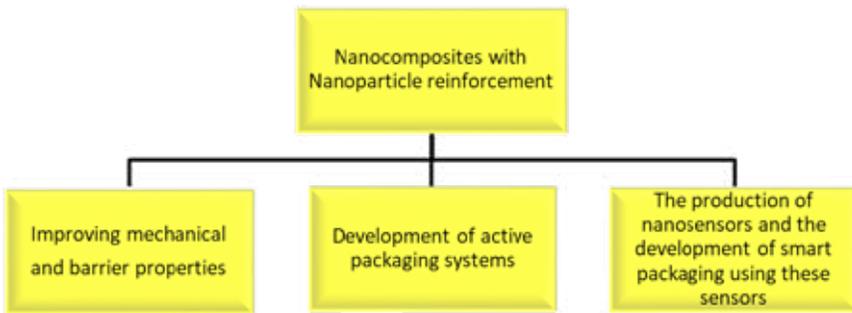
Figure 1. *Nanotechnological Applications in Food Packaging*

Figure 2. *Nanoparticles Used in Food Packaging*

2. Use of Nanoparticles in the Improvement of Barrier and Mechanical Properties of Polymer Films

2.1. Usage in Synthetic Polymer Packaging

The use of polymer-based films in the packaging of foods is quite common. Polymers are high molecular mass compounds formed by the very regular bonding of many molecules with chemical bonds (Dağ, 2018). About 5% of the oil processed in the world is used in the polymer industry. Petroleum is used as a source in the production of many synthetic

polymers. The superior mechanical and thermal properties of polymers have made them the preferred product in many areas of the industry (Hamamcı, Çiftçi & Aktaş, 2018).

Polypropylene (P.P.), polyethylene (HDPE, LDPE, etc.), polyethylene terephthalate (PET), polystyrene (P.S.), and polyvinyl chloride (PVC) are among the most used polymers in food packaging, and these different polymers exhibit different barrier properties. For example, polyethylene terephthalate (PET) provides a better barrier against oxygen than high-density polyethylene (HDPE), while HDPE provides a better barrier against water vapor than PET (Finnigan, 2009). In order to improve the barrier properties of polymer-based packaging materials or to give them different properties, nanoparticles are added to these materials, or composite materials are produced. Composite is a material that consists of two or more components (Hamamcı, Çiftçi & Aktaş, 2018). The use of nanoparticles and nanocomposites in food packaging has also started to gain importance. Nanocomposite packages are polymers containing organic or inorganic-based nanoparticles. The barrier properties of a polymer are affected by many factors such as the degree of branching, hydrogen bonding, polarity, cross-linking, and crystallinity. Nanoparticles added as filler to polymer nanocomposites create an important barrier that will prevent both oxygens, carbon dioxide, and humidity from passing into the food and ensure that the material is light, tearproof, and high temperature resistant. Clay and silicate nanoplatelets silica nanoparticles are most commonly used as filling materials (Zou, Wu & Shen, 2008; Sarfraz, Gulin-Safraz, Nilsen-Nygaard & Pettersen, 2021).

The fact that clay and silicate materials are durable, non-toxic by nature, and available at low prices makes them preferred as fillers. Because of these properties, nanoclay-based polymer nanoclays are used in food packaging works. Nanoclay applications to polymers such as montmorillonite, kaolinite, hectrite, and saponite have been widely studied (Yano & Usuki, 1997). By incorporating the nanoclay particle into the polymer matrix, the moisture stability of the film is increased, and the oxygen permeability is reduced. For example, when the surface of a very small amount of nano-sized clay particles is wrapped with polymer, it shows strong barrier properties against oxygen and moisture and shows high thermal resistance (Çelik & Tümer, 2016). Jung et al. (2019) reported that polypropylene (P.P.) packaging material containing clay and hollow glass microspheres reduces oxygen permeability by 32%.

In addition to clay, in one of the studies conducted with magnesium silicate, one of the silica nanoparticles, Wang et al. (2018) reported that P.P./talc nanocomposite increased the tensile strength and impact strength by 226% and 166%, respectively. Huang et al. (2017) reported in their

study, which they examined the food package film containing laminated clay/polyvinyl alcohol, they developed that the inclusion of MMT-based composite in the film significantly reduces the oxygen permeability, prolongs the retention time of hydrophilic (ascorbic acid) and lipophilic (lycopene) antioxidants, and delays discoloration.

Regarding the packaging of seafood; Khanipour et al. (2020) kept a low-density polyethylene (LDPE) composite film containing 5% clay nanoparticle film was produced to be used in packaging of rainbow trout (*Oncorhynchus mykiss*) fillet and a low-density polyethylene film, produced as a control process, in the refrigerator as samples. As a result of storage, the shelf life of the samples was determined as 13-15 days in the control samples and 18-20 days in the experimental samples.

2.2. Usage in Biopolymer Packaging (Bionanocomposites)

Biopolymers are biodegradable polymers that decompose into their components without causing environmental pollution when they are decomposed by microorganisms in the natural environment and are therefore defined as green materials. Hamamcı, Çiftçi & Aktaş, 2018; Kaya, 2017). The use of biodegradable polymers has become widespread in food packaging instead of using petroleum-based polymers that are not biodegradable and thus cause environmental and ecological problems (Gomez-Guillen et al., 2009). There is an interest in the research of biopolymer materials because they reduce the demand for fossil fuels, do not contain plasticizers such as phthalates and bisphenol A (BPA), and can be obtained from various plant and animal sources that are abundant in nature (Gomez-Guillen et al., 2009; Tharanathan, 2003). Biopolymers are of two types, natural and synthetic, according to the materials from which they are synthesized. Natural material-based polysaccharides (starch, alginate, chitin/chitosan, gums) (Rubilar et al., 2016; Alboofetileh, Rezaei, Hosseini & Abdollahi, 2018), proteins (casein, collagen, gelatin, corn, soy, gluten), and the ones extracted from microorganisms (polyhydroxyalkanoate (PHA), polyhydroxybutyrate (PHB)) are natural biopolymers. Synthetic biopolymers are produced under controlled conditions. Polylactides, polylactic acids (PLA), polyhydroxybutyrate (PHB), polycaprolactone (PCL), polybutylenesuccinate (PBS), starch and their derivatives are synthetic polymers produced with biotechnology (Hamamcı, Çiftçi & Aktaş, 2018).

The structural properties of biopolymers, which have weaker mechanical and permeability properties than petroleum-based polymers, need to be improved in order to make them suitable for use in food packaging. For example, although the proteins and polysaccharides used in the production of biopolymers have good film-forming abilities, their

mechanical and water vapor barrier properties are relatively low (Chiou et al., 2009; Farahnaky, Dadfar & Shahbazi, 2014). Studies on nanotechnological applications continue to improve the weak oxygen, mechanical and barrier properties of biopolymer films. For this purpose, the general properties of nanocomposite films are improved by incorporating nanoscale particles into polymeric matrices (Alboofetileh, Rezaei, Hosseini & Abdollahi, 2018).

Just like in petroleum-based plastics, nano-sized clays are added to biopolymers. For example, by adding layered silicates to the gelatin-based biopolymer, these films' barrier and mechanical properties can be increased (Alboofetileh, Rezaei, Hosseini & Abdollahi, 2018).

Alboofethyleneh et al. (2018) reported that adding clay to the biofilm improved the mechanical properties of the sodium alginate/montmorillonite nanocomposite film they prepared. Farahnaky et al. (2014) included nanoclay particles in the gelatin matrix. They reported that the strength of the nanoclay/gelatin nanocomposite film increased, water vapor permeability and light transmission decreased, and the addition of nanoclay provided positive physical and mechanical properties to the gelatin film. Staroszczyk et al. (2017) investigated the mechanical and water barrier properties of nanocomposites that they prepared from fish gelatin and nanoclays (5-15%) and plasticized with glycerol. Vilarinho et al. (2018) evaluated PLA nanocomposite films obtained by embedding unmodified montmorillonite (MMT) clay in polymer layered silicate (PLS) reinforced polylactic acid (PLA) for its role in delaying lipid oxidation of a packaged fatty food such as sliced salami. They reported that the presence of MMT in nanocomposite films tends to reduce lipid oxidation of packaged fatty foods due to their enhanced water barrier properties and can extend the shelf life of fatty foods. Eddin & Tahergorabi (2017) investigated the effect of surimi-based coating with and without montmorillonite (MMT) nanoclay on shrimp quality. They reported that the clay-containing coating improved the sensory quality of shrimp samples during the cold storage period and delayed lipid oxidation and discoloration.

3. Use of Nanotechnology in Active Packaging Systems

Active packaging is a packaging system in which the packaging environment is changed by adding active ingredients to the packaging material or packaging environment to slow down the rate of food spoilage reactions and extend the shelf life of the food. With the active packaging system, substances such as CO_2, O_2, ethylene, moisture, and bad aroma components that cause food to deteriorate can be removed from the packaging environment or by adding antimicrobial and antioxidant substances, CO_2, ethanol to the packaging environment. It can be ensured

that the food is preserved better (Kızılırmak, Özer & Naserifar, 2020; Majid, Nayik, Dar & Nanda, 2018). Nanotechnological processes applied in active packaging systems include the addition of nano components with antimicrobial and oxygen scavenging properties to the packaging material and the use of metal oxides and nanoclays for the enzyme immobilization system (Singh, Lee, Gaikwad & Lee, 2018; Mizielińska, Kowalsa, Jarosz, & Sumińska 2018b).

In active antimicrobial packaging, the use of metal nanoparticles such as silver, gold, zinc, copper, silver-zeolite, silver-gold and titanium dioxide (TiO_2), zinc oxide (ZnO), silicon dioxide (SiO_2), magnesium oxide, and metal oxide nanoparticles such as (MgO) are preferred due to their small size and surface reactivity properties (Ertekin, 2019). There are studies on the use of different enzymes, bacteriocins, essential oils, anhydrides, and weak organic acids in seafood and other foodstuffs to increase antimicrobial activity with active nanocomponents (Enescu et al., 2019).

The use of antimicrobial nanoparticles in the active packaging of seafood is a broad research topic. Sing et al. (2018) prepared polypropylene (P.P.) films containing 5% and 10% silver silica ($AgSi_2$) and compared the antimicrobial properties of the composite with the control sample. Raw mullet (chub mackerel) packed with the prepared composite was stored at +2 °C for 7 days, the thiobarbituric acid (TBA) value increased in the control sample during storage but remained low in the sample packed with composite. TBA, which is a lipid oxidation index, causes oxidative rancidity and the formation of malodors and taste deteriorations. Trimethylamine TMA increased from 1.6 to 2.5 mg TMA/100 g in the control sample, and there was no change in the nanocomposite sample. Trimethylamine (TMA) is a pungent, volatile amine associated with spoiled seafood's typical "fishy" odor. It was determined that the total number of psychrophilic microorganisms reached 3.06 and 3.11 log CFU/g during storage in the fish packaged with composite, and 4.81 log CFU/g in the control sample, respectively. In this study, it was reported that as a result of antimicrobial packaging, the quality of the product is preserved up to 7 days, and its shelf life is extended in cold storage. Efatian et al. (2021), Nile Tilapia (*Oreochromis niloticus*) fish were packaged with nanocomposite films containing $LDPE/Ag/TiO_2$ and $LDPE/Ag + Cu/TiO_2$ and stored at +4°C and -20°C for 5 and 10 days. It was revealed that the nanocomposites exhibited strong antibacterial activities during storage, and the Ag + Cu-containing film had higher antimicrobial activity in Nile Tilapia samples. Ag and Cu nanoparticles migrated from the film to the Tilapia samples were < 2.0 µg/kg and < 10 µg/kg, respectively. Paidari et al. (2021) investigated the antimicrobial effects of nanoclay and silver nanoparticles added to LDPE polymer on shrimp (*Penaeus semisulcatus*)

samples. After 6 days of storage at 4ºC, they reported that nanoclay and nanosilver showed a synergistic effect against Vibrio parahaemolyticus, Escherichia coli, and Staphylococcus aureus, and putrefaction started from the 7th day. The study also reported that the effectiveness of nanocomposites decreased, and pathogenic bacteria began to reproduce after the shelf-life period. Esmailzadeh et al. (2020) compared the antibacterial activities of CuO/LDPE nanocomposite with ZnO/LDPE nanocomposite and reported that Cu/LDPE nanocomposite provided the antimicrobial effect on two important spoilage bacteria, gram-positive Bacillus subtilis and gram-negative Enterobacter aerogenes, with a slight difference, and both nanoparticles could be effective in active packaging.

There are studies on adding nanomaterial/nanoemulsion combinations to biopolymers to improve their barrier and antimicrobial properties. In one of these studies, Zhang et al. (2017) showed that ZnO and ginger emulsified oil added to fish gelatin significantly reduced lipid oxidation and total volatile nitrogen content during storage, and they reported that psychrotrophs, mesophiles, lactobacillus spp. and in vitro conditions showed strong antibacterial effects against *Escherichia coli* and *Listeria monocytogenes*.

Shahbazi & Shavisi (2018) reported in their study that, in which they examined TVB-N, TBARS, peroxide number, microbial (total viable count, psychrotrophic count *Pseudomonas spp. and Enterobacteriaceae*) and sensory (smell, color, and general acceptability) properties in rainbow trout (*Oncorhynchus mykiss*) flotillas coated with chitosan containing ZnO nanoparticle and peppermint (*Mentha spicata*) essential oil stored for 14 days in refrigerator conditions, that chitosan coating containing ZnO/mint oil extended shelf life by inhibiting microbial growth and formation of lipid oxidation products.

Heydari-Majd et al. (2019) stored Otolithes rubber fish fillets covered with PLA active packaging films containing ZnO/ZEO (*Zataria multiflora*) and MEO (*Menthe piperita*) under refrigerator (4 ± 1 °C) conditions. They followed the changes in microbial, chemical, and antioxidant parameters during storage and reported that the fillets were coated with a combination of PLA/ZnO/ZEO and MEO to preserve their freshness for 16 days. In addition, in the same study, they reported that the migration amount of Zn^{2+} ions from the composite film to the fillet was below the limit value accepted by the National Institute of Health (https://ods.od.nih.gov/factsheets/Zinc-HealthProfessional/) for food contact materials.

Echeverria et al. (2018) evaluated the antimicrobial and antioxidant activity of active nanocomposite films based on soy protein isolate-montmorillonite (MMT)-clove essential oil (CEO) in bluefin tuna (*Thunnus*

thynnus). They determined that lipid autooxidation is reduced. It showed its antimicrobial effect, especially by inhibiting Pseudomonas spp., MMT facilitated the release of some active compounds, and MMT did not diffuse into fish muscle after 17 days of storage at 2 °C. Kakaei & Shahbazi (2016) reported inhibition of Listeria monocytogenes in minced trout, which was covered with chitosan-gelatin film combined with ethanolic red grape seed extract and mountain basil (*Ziziphora clinopodioides*) essential oil, and maintained shelf life for 11 days at 2 °C.

Shruthy et al. (2020) showed that raw shrimp (*Penaeus monodon*) packed with polyvinyl alcohol (PVA) based active packaging film fortified with cellulose nanoparticles (CNP) isolated from potato peel and fennel seed oil were preserved for up to 63 days at -20 °C and reported that shrimps packed and stored at the same temperature in normal polyethylene packages exceeded the control limit during biochemical analysis.

Nazari et al (2019) developed a nanofiber-based structure to maintain the antibacterial effect of herbal essential oils throughout the storage period, and they included cinnamon essential oil in the packaging they prepared as a hybrid with polyvinyl alcohol (PVA), the hybrid active packaging provided a reduction in water vapor permeability and the shelf life of the shrimps they packaged was extended up to 12 days.

Mizielinska et al. (2018) reported that boxes containing cellulose-coated polyethylene (P.E.) films containing ZnO nanoparticles are good packaging materials in maintaining the quality and freshness of cod fillets (*Gadus morhua*) after 144 hours storage at 5 °C.

Ejaz et al. (2018) reported that Bovine gelatin composite films combined with ZnO + clove essential oil showed antimicrobial effect against *L .monocytogenes* and *S. typhim* in shrimps covered with this film, when stored at 4 °C, oxygen and U.V. barrier properties, ZnO and volatile properties of the film increased with the addition of essential oil. Vizzini et al. (2020) designed an active packaging film containing Zn-MgO NPs and Alginate to control L. monocytogenes contamination in smoked salmon (Salmon). Smoked salmon samples inoculated with *d* and packaged with Zn-MgO NPs-alginate nano biocomposites film showed no bacterial growth at 4 °C for 4 days. They reported that L. monocytogenes growth was observed in the contaminated control samples packaged only with alginate film, which did not contain ZnO-MgO under the same conditions.

Seray, Hadj-Hamou & Benhacine (2021) evaluated the shelf life of sea bream, the gas barrier properties of the film, and its antibacterial performances by developing poly (butylene adipate - co-terephthalate) and silver-montmorillonite (PBAT/Ag-MMT) based active packaging film. They proved that adding Ag-MMT to the PBAT matrix was sufficient to

extend the bream storage time up to 15 days.

In a study by Zhang et al. (2021) in which the beef packed with bio-nano composite films containing ginger essential oil, chitosan and montmorillonite were stored at 4 ^{O}C for 15 days, it is reported that lipid oxidation slowed down and growth of surface microorganisms slowed down during storage. These components included in bio-nano composites imparted good mechanical and barrier properties to the packaging, good slow-release properties, and slow migration of active ingredients into food.

In active packaging systems, determining the effectiveness of nanomaterial/nanoemulsion substances included in the packaging during the storage period of the products is an issue that should be considered (Martinez-Abad, Lagaron & Ocio (2014) reported that the effectiveness of nanopackaging decreased during the shelf life, Kuuliala et al. (2015) stated that although TiO_2-Ag nanoparticles reduced the bacterial load in the culture medium, they did not extend the shelf life of nanopackaged meat. In another study, Paidari & Ahari (2021) reported that the effectiveness of nanocomposites decreased, and pathogenic bacteria started to reproduce after the shelf-life period. Contrary to these studies, Tavakoli et al. (2017) reported that the nanocomposite containing Ag nanoparticles for nuts packaging was active even at the end of the 9th. month. These results suggest that nanoparticles show different antimicrobial activity in relation to the samples' different microbial load and physicochemical structures (Paidari & Ahari, 2021.; Kuuliala et al., 2015). Therefore, this indicates that the microbial and physicochemical properties of the product, as well as requested storage time, should be taken into account while formulating the nanocomposites. In addition, it should be taken into account that the number of nanoparticles transferred to the food will increase with the prolongation of the contact time of the packaging with the food.

4. Nanotechnological Applications in Smart Packaging Systems

Smart packaging systems designed to provide a specific indicator of chemical, enzymatic, microbial changes or changes in storage conditions in the packaged food provide the traceability of food quality with the naked eye without harming the packaging integrity. (Alizadeh-Sani et al., 2021; Biji, Ravishankar, Mohan & Srinivasa, 2015). In this system, indicators and nanosensors are applications that provide technological support. Indicators used in packaging are grouped as oxygen indicators, deterioration and contamination indicators, time, temperature, humidity indicators, freshness indicators. Nanosensors are used in pathogen detection, gas detection, aroma detection, freshness detection of processed products, flavor detection, food pollutants, or toxin detection (Ponce et al., 2018). The combined use of nano-active materials and nanocomposites has

found a place in smart packaging systems as well as in active packaging systems and has provided a strengthening effect to smart packaging. It is noteworthy that there are many studies on freshness indicators, which is one of the smart packaging system applications. These indicators have been applied to nano packages. Among these indicators, pH colorimetric indicators have received wide attention. pH change often accompanies the food spoilage process (Ge et al., 2020), and these indicators provide measurability when there is a significant change in the pH of packaged food (Alizadeh-Sani et al., 2021). Total volatile basic nitrogen (TVB-N) is the amount of volatile basic nitrogen that accumulates in the tissues with degradation during the storage of seafood products. These compounds, which accumulate in the headspace of the packaging due to the increase in ammonia, dimethylamine, trimethyl amines (TVB-N), formed as a result of microbial, chemical, and enzymatic deterioration, also increase the pH value of the environment in the package. pH colorimetric sensors have been developed to make the changing pH visible to the naked eye. To enrich the color variety, nanoparticles are included in the sensors. Acid/base indicators such as phenolphthalein (Fleischmann, Cheng, Tabatabai & Ritter, 2012), bromocresol blue, bromocresol purple (Gavrilenko, Saranchina, Sukhanov & Fedan, 2018) n pH indicators, and natural food dyes such as methyl orange (Musso, Salgado & Mauri, 2016) synthetic dyes, anthocyanins, betalains, and natural food dyes such as curcumin, chlorophylls, carotenoids, red pepper extract (*Oleoresin paprika*), saffron (crocetin) are used (Kırca, 2004). Anthocyanins are the leading commercial natural pigments (Kırca, 2004). Since anthocyanins have different characteristic colors under acidic, neutral, and alkaline conditions, they are widely used as sensors over a wide pH range. Most leaves, flowers, and fruits that come in blue, red, and purple colors contain anthocyanins. Purple sweet potato (Choi, Lee, Lacroix, & Han, 2017), mulberry (Ma, Liang, Cao, & Wang, 2018), grape skin (Ma & Wang, 2016), rose (Zhai, 2017), red pitaya peel, black rice bran (Zhang et al., 2019), are some of the anthocyanin-containing plants. Curcumin is also widely used in the food industry. Curcumin is a natural colorant found in the rhizomes of the turmeric plant (Curcuma longa). While curcumin gives a green-lemon yellow color in acidic environments, 11 (pH > 9) color turns orange in alkaline environments (Kırca,2004).

Ge et al. (2020) prepared a pH-sensitive colorimetric film by incorporating chitin nanocrystals to gelatin matrix containing black rice bran anthocyanins to monitor the freshness of shrimp (*Penaeus chinensis*) and hairtail (*Trichiurus haumela*). As a result of the pH change due to the increase in the amount of TVB-N after 1 day of storage at 25°C, the color transformation from purple to gray-blue or brown has been reported

in the films. This study showed that colorimetry films with anthocyanin content of black rice bran are sensitive to volatile amines during storage. Wu et al. (2019) imparted an excellent U.V. barrier, antioxidant and pH sensitivity properties to the smart film, which 1%, 3%, and 5% black rice bran anthocyanins were fixed to the chitin nanocrystals/chitosan matrix. The application results showed that their films containing 3% anthocyanins could monitor the degradation of fish and shrimps with visible color changes, but they reported that their films' mechanical and barrier properties were reduced with the inclusion of anthocyanins. Alizadeh-Sani et al. (2021) reported that the addition of anthocyanin to the pH-sensitive color indicator film they prepared by adding anthocyanin obtained from the rubella plant to the methylcellulose and chitosan nanofiber matrix for monitoring the freshness of lamb meat increased its mechanical and water barrier properties and exhibited antioxidant activity. It has been noted that the indicator film changes from reddish-pink to pale peach and finally yellow when exposed to different pH buffers, and from pink to pale green to yellow in response to ammonia vapor. The color indicator film has shown that it can be used to monitor the freshness of high protein foods such as meat and seafood to inform the quality and safety of the product. Naghdi, Masoud & Mehdi (2021) developed a starch/betocyanin package label for the determination of the freshness status of fish (Caspian sprat (*Clupeonella cultriventris caspia*)) during 4°C storage, and detect the visual change in the color of the label from pink to yellow in parallel with the increase in the amount of TVB-N in fish samples. Liu et al. (2021) developed a carboxymethylcellulose-based gelatin/curcumin/chitosan hybrid film and used curcumin as a pH indicator to monitor the freshness of pork. In the film based on microencapsulation, gelatin/chitosan was used for the capsule wall, and controlled release of curcumin in the microcapsule was ensured, and the color change was observed depending on the deterioration and pH change during storage.

Metal/metal oxide nanoparticles were examined as pH indicators, and it was determined that these particles provided a distinguishable color change with pH change. Lapenna et al. (2020) used biogenic amine-sensitive gold nanoparticles (AuNP) to detect biogenic amines. In their colorimetric test, they reported a change in the color of the solution from burgundy to gray/blue due to the aggregation of AuNP on biogenic amines. Zhai et al. (2019) fabricated a colorimetric hydrogen sulfide (H_2S) sensing sensor based on silver nanoparticles (AgNPs) to detect degradation in silver carp. The sensor quickly detected H_2S, and a visible color change occurred. H_2S is a volatile amine produced during the degradation of fish and is produced during the degradation of sulfur-containing amino acids (Varlet & Fernandez, 2010). Therefore, H_2S is recognized as a characteristic compound for assessing degradation (Chow et al., 2017).

Mustafa, Othman & Andreescu (2021) reported that they developed a nanoenzyme-based biosensor to monitor fish freshness, which measures the release of hypoxanthine (H.X.), a product of nucleotide degradation, in fish (Tilapia fish). The biosensor used cerium nanoparticles as a chromogenic indicator to measure the product of H.X. oxidation. This study has reported that new generation biosensing technologies can be developed to monitor food safety.

In the study of Kim, Swarup & Jon-Whan (2022) color changes in the polymer were observed depending on the changes in pH and TVB-N values during the storage of shrimps packed with pea flower anthocyanin as a pH indicator and gelatin/agar polymer integrated with ZnO as an antimicrobial agent, and it has been reported that it has strong antimicrobial effect against *E.coli.*

Both petroleum-derived polymer and biodegradable polymer films are used in smart packaging, and pH-sensitive dyes are incorporated into these film matrices via hydrogen bonding or ionic reactions. İbrahim, Hager & Shimaa (2021) developed a pH sensor with nanocapsulation technique to monitor the freshness of raw fish (Nile perch) and incorporated this sensor into the polymer composite matrix. The encapsulated methyl red dye, combined with the indicator label, caused a color change in the label due to the changing pH due to the microbial growth developed during the storage in the sea bass fillets stored at 4 ^{O}C for 12 days. This label has been effective in facilitating the monitoring of the shelf life of fresh fish.

Qin et al. (2019) incorporated silver nanoparticles and purple corn extract into the chitosan matrix to develop active-smart hybrid food packaging films. They reported that Ag nanoparticles and anthocyanins provide high barrier properties, mechanical strength, antioxidant and antimicrobial effects in the film. In addition, it has been reported that the presence of anthocyanin in the film can create different colors in pH buffers, and this film with pH-sensitive properties can be used to monitor the freshness of packaged foods (for example, pork, milk, and seafood). Aghaei et al. (2018) used cellulose acetate nanofibers as bio-based polymer packaging as fish spoilage indicator and applied alizarin halochromic sensor to the packaging. Rainbow trout packaged with this smart packaging and stored for 12 days at 4°C, the color of the sensor on the package turned violet on the 12th day due to the increase in total volatile TVB-N and pH value, giving information that the fish could not be consumed. Alizarin is an artificial root dye with a spectral range from yellow (pH 5.8) to purple (pH 7.2). The advantage of this application is important for consumers to evaluate the quality of the product visually.

5. Migration and Food Safety

Nanoparticles (N.P.s) incorporated into polymer matrices to impart flexibility, thermal stability, mechanical and barrier properties to food packaging materials can migrate from packaging to foodstuffs. Migration tests are required to detect the migration of nanoparticles used in packaging. Legislation in terms of health and safety in the European Union and other countries is constantly updated. The ISO 19007:2018 standard published in 2018 is on measuring the cytotoxic effect of nanoparticles. Many studies have been conducted on the migration and health effects of N.P.s. Hafttananya et al. (2021), in their study on the migration of nanoclay and nanosilica from LDPE nanocomposites to food, used distilled water, 3% acetic acid, 95% ethanol as food substitutes, and they reported that they stored these substances at 40 ^{O}C for 10 days and that the migration of aluminum and silicon nanoparticles into 95% ethanol was higher than the others. Nanoparticles are more likely to migrate to foods with high-fat content. Efatyan et al. (2021), studied the migration of Ag, Cu, Ti from the LDPE nanocomposite film, in which they included Ag/TiO$_2$ and LDPE/ Ag + Cu/TiO$_2$ nanoparticles, to Nile Tilapia (*Oreochromis niloticus*) fish. They reported that the migration of these active substances is below the total legal pass limit set by the commission regulation (E.C.) 450/2009 for "unauthorized substances" (0.01 mg/kg food). Störmer, Bott, Kemmer & Franz (2017) reported that nanoparticles fully encapsulated in the polymer matrix do not have the potential to migrate to food so that consumers are not exposed to nanoparticles from food contact polymers when they are fully embedded in the polymer. However, it has been reported that migration may occur due to material fatigue, exposure to ultraviolet, hydrolysis, or degradation of the polymer matrix, and swelling interactions (Noonan, Whelton, Carlander, & Duncan, 2014). Paidari & Ahari (2021) in their study with shrimp (*Penaeus semisulcatus*) samples, examined the migration status of nanoclay and nanosilver particles and reported that there was no migration of Aluminum, Ag, and silicon to the samples after 6 days of storage.

Hosseini et al. (2017) packaged the shrimp samples (Penaeus semisulcatus) with nanocomposites containing Ag nanoparticles at concentrations of 1%, 3%, 5%, 8%, and they suggested that 5% silver nanoparticle coating is suitable for protection, considering the presence of silver nanoparticle release and antibacterial effect, which is below the allowable level in E.U. standards of the coating containing 5% silver nanoparticles. Lin et al. (2014) used 3% acetic acid as a food simulant to determine the Ti transition from the TiO2 nanoparticle and reported that migration occurred. Metak & Nabhani (2015) reported that silver nanoparticles migrated to food simulants (3% acetic acid) after 10 days of

storage. It could possibly be due to the watery nature of the food simulant. Migration status may depend on the oiliness of the food, its microbial, chemical structure, storage conditions, and storage duration.

Exposure to N.P.s raises concerns both in terms of health and environmental impact. (Stueckle et al., 2019). Studies have reported that N.P.s can easily cross cell membranes, interact with intracellular metabolism, and cause toxicity. Some of these disorders that may occur, along with breast, testicular, and prostate cancer, can cause immunosuppression, pituitary, thyroid gland, and functional disorders (Jeevanandam et al., 2018; Kumar, Sharma & Maitra, 2017; Hafttananian et al., 2021). N.P.s are also likely to cross the placental barrier and affect the fetus. Yamashita et al. (2011) exposed pregnant mice to silica N.P.s and reported that N.P.s cross the placenta and are detected in the liver and brain of fetal mice.

Choi et al. (2018) examined the migration of Ag nanoparticles in baby products (pacifier, feeding bottle, breast milk storage bag) and reported that the amount of Ag transported was low, but the migration was dependent on the structure of the food and the polymer. According to in vitro test results, Ag has been reported to be genotoxic, cytotoxic, and possibly carcinogenic (Choi et al., 2018). Ag has also been reported to cause organ damage in rats' liver, spleen, and lymph nodes (Dos Santos et al., 2014). There are studies on the migration of nanoparticles, but more studies are needed.

Conclusion

Nanotechnological studies have made rapid progress in the food industry, mostly in the field of food packaging. Nanotechnology includes innovations in food packaging that will benefit both manufacturers and consumers. Improving the structural properties of packages such as gas barrier permeability, flexibility, and durability by incorporating nanoparticles into polymers and biopolymers, preserving the freshness of perishable foods, and extending the shelf life of products by adding them to active packages, ensuring the traceability of the product by using them in smart packages, and using hybrid use of these packaging systems with nanoparticle supported nanoparticles, and combinations of active- smart packaging have been examined in many scientific studies, and these systems have found a place in the food industry. While nanoparticles included in food packaging systems support food safety, they also raise some concerns. Do consumers have sufficient knowledge of nanotechnological applications? Does it create a sense of trust in the consumer? Are the legal regulations sufficient? What are the effects of nanoparticles on the environment and human health? In order to find answers to such questions, it is necessary to increase the number of scientific studies.

REFERENCES

Aghaei, Z., Emadzadeh, B., Ghorani, B., & Kadkhodaee, R. (2018). Cellulose Acetate Nanofibres Containing Alizarin as a Halochromic Sensor for the Qualitative Assessment of Rainbow Trout Fish Spoilage. *Food and Bioprocess Technology, 11*, 1087–1095. https://doi.org/10.1007/s11947-017-2046-5.

Alboofetileh, M., Rezaei, M., Hosseini, H., & Abdollahi, M. (2018). Morphological, physico-mechanical, and antimicrobial properties of sodium alginate-montmorillonite nanocomposite films incorporated with marjoram essential oil. *Journal of Food Processing and Preservation. 42*:e13596. https://doi.org/10.1111/jfpp.13596

Alizadeh-Sani, M., Tavassoli, M., Hamishehkar, H., & McClements, D.J. (2021). Carbohydrate-based films containing pH-sensitive red barberry anthocyanins: Application as biodegradable smart food packaging materials. *Carbohydrate Polymers*, *255*, 117488, https://doi.org/10.1016/j.carbpol.2020.117488.

Alizadeh-Sani, M., Tavassoli, M., Mohammadian, E., Ehsani, A., Khaniki, G.J., Priyadarshi, R., & Rhim, J-W. (2021). pH-responsive color indicator films based on methylcellulose/chitosan nanofiber and barberry anthocyanins for real-time monitoring of meat freshness. *International Journal of Biological Macromolecules*, *166*, 741-750. https://doi.org/10.1016/j.ijbiomac.2020.10.231.

Aras, A. H., Hisar O., & Yanık, T. (2011). Balıklarda Mikrobiyolojik, Enzimatik ve Kimyasal Bozulmalar. *Atatürk Üniversitesi Ziraat Fakültesi Dergisi*, *35 (3-4)*, 261-265. Retrieved from https://dergipark.org.tr/tr/pub/ataunizfd/issue/2938/40679

Bhaskar, N., Miyashita, K., & Hosakawa, M. (2006) Physiological Effects of Eicosapentaenoic Acid (EPA) and Docosahexaenoic Acid (DHA)—A Review. *Food Reviews International, 22,* 291-307. https://doi.org/10.1080/87559120600694622.

Biji, K. B., Ravishankar, C. N., Mohan, C. O., & Srinivasa Gopal, T. K. (2015). Smart packaging systems for food applications: a review. *Journal of Food Science Technology. 52 (10)*, 6125-35. DOI 10.1007/s13197-015-1766-7.

Choi, I. , Lee, J. Y., Lacroix, M., & Han, J. (2017). Intelligent pH indicator film composed of agar/potato starch and anthocyanin extracts from purple sweet potato. *Food Chemistry*, *218*, 122-128. https://doi.org/10.1016/j.foodchem.2016.09.050.

Choi, J. I., Chae, S. J., Kim, J. M., Choi, J. C., Park, S. J., Choi, H. J., Bae, H., & Park, H. J. (2018). Potential Silver Nanoparticles Migration from Commercially Available Polymeric Baby Products into Food Simulants. *Food Additives & Contaminants: Part A* 35: 996–1005. https://doi.org/10.1080/19440049.2017.1411611.

Chiou, B. S., Avena-Bustillos, R. J., Bechtel, P. J., Imam, S. H., Glenn, G.

M., & Orts, W. J. (2009). Effects of drying temperature on barrier and mechanical properties of cold-water fish gelatin films. *Journal of Food Engineering*, *95 (2)*, 327-331.

Chow, C. F., Ho, P. Y., Sun, D., . Lu, Y. J, Wong, W. L., Tang, Q., & Gong, C. B. (2017). Development of sensitive and selective food sensors using new Re(I)-Pt(II) bimetallic complexes to detect volatile biogenic sulfides formed by meat spoilage. *Food Chemistry*, *216*, 382-389. https://doi.org/10.1016/j. foodchem.2016.08.046.

Çelik, İ., & Tümer, G. (2016). Gıda Ambalajlamada Son Gelişmeler. *Akademik Gıda*, *14 (2)*,180-188. Retrieved from https://dergipark.org.tr/tr/pub/akademik-gida/issue/55784/763590.

Dağ, S. E. (2018). *Polimer/Montmorillonit Kompozitlerin Kimyasal Yöntemle Hazırlanması ve Özelliklerinin Belirlenmesi* [Unpublished doctoral dissertation]. University of Ankara.

Dobrucka, R. (2013). The Future of Active and Intelligent Packaging Industry. *Scientific Journal of Logistics*. *9 (2)*, 103-110.

Dong, Z., Xu, F., Ahmed, I., Li, Z., & Lin, H. (2018). Characterization and preservation performance of active polyethylene films containing rosemary and cinnamon essential oils for Pacific white shrimp packaging. *Food Control*, *92*, 37-46. https://doi.org/10.1016/j.foodcont.2018.04.052.

Dos Santos, C. A., Seckler, M. M., Ingle, A. P., Gupta, I., Galdiero, S., Galdiero, M., Gade, A., & Rai, M. (2014). Silver nanoparticles: therapeutical uses, toxicity, and safety issues. *Journal of Pharmacology Science*, *103,* 1931–1944. https://doi.org/10.1002/jps.24001.

Echeverría, I., López-Caballero, M. E., Gómez-Guillén, M. C., Mauri, A. N., & Montero, M. P. (2018). Active nanocomposite films based on soy proteins-montmorillonite-clove essential oil for the preservation of refrigerated bluefin tuna (*Thunnus thynnus*) fillets**.** *International Journal of Food Microbiology*, *266*, 142-149. https://doi.org/10.1016/j. ijfoodmicro.2017.10.003.

Eddin, A. S., & Tahergorabi, R. (2017). Application of a Surimi-Based Coating to Improve the Quality Attributes of Shrimp during Refrigerated Storage. *Foods*, *6*, 76. https://dx.doi.org/10.3390%2Ffoods6090076

Efatian, H Ahari, H., Shahbazzadeh, D., Nowruzi, B., & Yousefi, S. (2021). Fabrication and characterization of LDPE/silver-copper/titanium dioxide nanocomposite films for application in nile tilapia (*Oreochromis niloticus*) packaging. *Journal of Food Measurement & Characterization, 15(3)*, 2430-2439. http://dx.doi.org/10.1007/s11694-021-00836-7.

Ejaz, M., Arfat, Y. A, Mulla, M., & Ahmed, J. (2018). Zinc oxide nanorods/clove essential oil incorporated Type B gelatin composite films and its applicability for shrimp packaging *Food Packaging and Shelf Life*, *15*, 113-121. https://doi.org/10.1016/j.fpsl.2017.12.004.

Enescu, D., Cerqueira, M. A., Fucinos P., & Pastrana, L.M. (2019). Recent advances and challenges on applications of nanotechnology in food packaging. A literature review. *Food Chem Toxicol. 134,*110814. https://doi.org/10.1016/j.fct.2019.110814

Ertekin, B. (2019, November). Gıda Ambalajlarında Nanoteknolojinin Sağladığı Yenilikler. Oral presentation of *ASD Packaging Congress International Packaging Industry Congress*, İstanbul, Türkiye.

Esmailzadeh, H., Sangpour, P., Shahraz, F., Eskandari, A., Hvizinii, J., & Khaksar, R. (2020). CuO/LDPE nanocomposite for active food packaging application: a comparative study of its antibacterial activities with ZnO/LDPE nanocomposite. *Polym. Bull.,* 1–12. https://doi.org/10.1007/s00289-020-03175-7.

Farahnaky, A, Dadfar, S. M. M., & Shahbazi, M. (2014). Physical and mechanical properties of gelatin-clay nanocomposite. *J Food Eng., 122*, 78–83. http://dx.doi.org/10.1016/j.jfoodeng.2013.06.016.

Finnigan, B. (2009). Barrier polymers. Yam, K. L. (Ed.), The Wiley Encyclopedia of Packaging Technology, (3th. Edition), John Wiley and Sons, Inc., New York, 103-109.

Fleischmann, C., Cheng, J., Tabatabai, M., & Ritter, H. (2012). Macromolecules, *45*, 5343 -5346. https://doi.org/10.1021%2Fma300670x.

Gavrilenko, N. A., Saranchina, N. V., Sukhanov, A., & Fedan, D. A. (2018). Reversible pH-sensitive element based on bromocresol purple immobilized into the polymethacrylate matrix. *Mendeleev Communication, 28*, 450–452. https://doi.org/10.1016/j.mencom.2018.07.038.

Ge, Y., Li, Y., Bai, Y., Yuan, C., Wu, C., & Hu, Y. (2020). Intelligent gelatin/oxidized chitin nanocrystals nanocomposite films containing black rice bran anthocyanins for fish freshness monitorings *International Journal of Biological Macromolecules, 155*, 1296-1306. https://doi.org/10.1016/j.ijbiomac.2019.11.101.

Gómez-Guillén, M. C., Pérez-Mateos, M., Gómez-Estaca, J., López-Caballero, E., Giménez, B., & Montero, P. (2009). Fish gelatin: a renewable material for developing active biodegradable films. *Trends in Food Science & Technology, 20*, 3-16. https://doi.org/10.1016/j.tifs.2008.10.002

Gram, L., & Huss, H. H. (1996). Microbiological spoilage of fish and fish products. *Int. J. Food Microbiol. 33*, 121–137. https://doi.org/10.1016/0168-1605(96)01134-8.

Hafttananian, N., Zabihzadeh Khajavi, M., Farhoodi, M., Jahanbin, K., & Pure, A. E. (2021). Migration of nano-clay and nano-silica from low-density polyethylene nanocomposites into different food simulants. *Food Measure, 15*, 3893–3900. https://doi.org/10.1007/s11694-021-00972-0.

Hamamcı, B., Çiftçi, M., & Aktaş, T. (2018). Yeşil Kompozitlerde Biyopolimerlerin Kullanımının Önemi. *Karadeniz Fen Bilimleri Dergisi, 8*, 12-24. https://doi.

org/10.31466/kfbd.395192.

Hazar Yoruç, A. B., & Uğraşkan, V. (2017). Yeşil Polimerler ve Uygulamaları. *Afyon Kocatepe Üniversitesi Fen Ve Mühendislik Bilimleri Dergisi*, *17*, 318-337. https://dergipark.org.tr/tr/pub/akufemubid/issue/43198/516985.

Heydari-Majd, M., Ghanbarzadeh, B., Shahidi-Noghabi, M., Najafi, M. A., & Hosseini, M. (2019). A new active nanocomposite film based on PLA/ZnO nanoparticle/essential oils for the preservation of refrigerated Otolithes ruber fillets. *Food Packaging and Shelf Life, 19*, 94–103. https://doi.org/10.1016/j.fpsl.2018.12.002

Hosseini, R., Ahari, H., Mahasti, P., & Paidari, S. (2017). Measuring the migration of silver from silver nanocomposite polyethylene packaging based on (TiO$_2$) into Penaeus semisulcatus using titration comparison with migration methods. *Fisheries Science, 83,* 649–659 https://doi.org/10.1007/s12562-017-1090-4.

Huang, J.Y., Limqueco, J., Chieng, Y. Y., Li, X., & Zhou, W. (2017). Performance evaluation of a novel food packaging material based on clay/polyvinyl alcohol nanocomposite. *Innovative Food Science & Emerging Technologies, 43*, 216-222. https://doi.org/10.1016/j.ifset.2017.08.012.

Ibrahim, S., Hager, F., & Shimaa, S. (2021). Application of Interactive and Intelligent Packaging for Fresh Fish Shelf-Life Monitoring. *Frontiers in Nutrition 8*, 677884. https://dx.doi.org/10.3389%2Ffnut.2021.677884.

Jeevanandam, J., Barhoum, A., Chan, Y. S., Dufresne, A., & Danquah, M. K. (2018). Review on nanoparticles and nanostructured materials: history, sources, toxicity and regulations. *Beilstein J. Nanotechnol. 9,* 1050-1074. https://doi.org/10.3762/bjnano.9.98.

Joseph, T., & Morrison, M. (2006). Nanotechnology in agriculture and food. Retrieved from: http://www.nanowerk.com/nanotechnology/reports/reportpdf/report61.pdf/. Accessed February 27, 2015.

Jung, B. N., Kang, D., Cheon, S., Shim, J. K., & Hwang, S. W. (2019). The addition effect of hollow glass microsphere on the dispersion behavior and physical properties of polypropylene/clay nanocomposites, *J. Appl. Polym. Sci., 136*, 47476. https://doi.org/10.1002/app.47476.

Kakaei, S., & Shahbazi, Y. (2016). Effect of chitosan-gelatin film incorporated with ethanolic red grape seed extract and Ziziphora clinopodioides essential oil on survival of Listeria monocytogenes and chemical, microbial and sensory properties of minced trout fillet. *Lebensmittel-Wissenschaft und -Technologie- Food Science and Technology, 72*, 432 438. 10.1016/j.lwt.2016.05.021.

Kaya A. İ. (2017). Kompozit Malzemeler ve Özellikleri. *Putech & Composite Poliüretan ve Kompozit Sanayi Dergisi*, *29*, 38-45.

Khanipour A. A., Bahmani, Z. A., Oromiehie, A. R., & Motalebi, A. A. (2020). Effect of Packaging with Nano-composite clay/LDPE Film on the Quality of Rainbow Trout (*Oncorhynchus mykiss*) Fillet at Refrigerated Storage. *Iran J*

Fish Sci., 19, 698–714. DOI:10.22092/ijfs.2018.116825.

Kılınç, B., & Çaklı, Ş. (2001). Paketleme Tekniklerinin Balık ve Kabuklu Su Ürünleri Mikrobiyal Florası Üzerine Etkileri. *Journal of Fisheries & Aquatic Sciences, 18*, 279-291.

Kırca, A. (2004). Siyah Havuç Antosiyoninlerinin Bazı Meyve Ürünlerinde Isıl Stabilitesi [Unpublished doctoral dissertation]. University of Ankara.

Kızılırmak Esmer, Ö. & Özer, Ö., & Naserifar, F. (2020). Taze tavuk etlerinde aktif ambalajlama uygulamaları. *Etlik Veteriner Mikrobiyoloji Dergisi*, *31*, 87-92. DOI: 10.35864/evmd.623386.

Kim, H.-J., Roy, S., & Rhim, J.-W. (2021). Gelatin/agar-based color-indicator film integrated with *Clitoria ternatea* flower anthocyanin and zinc oxide nanoparticles for monitoring freshness of shrimp. *Food Hydrocolloids*, *124*, 107294. https://doi.org/10.1016/j.foodhyd.2021.107294.

Kumar, V., Sharma, N., & Maitra, S. S. (2017). In vitro and in vivo toxicity assessment of nanoparticles. *Int Nano Lett 7,* 243–256. https://doi.org/10.1007/s40089-017-0221-3.

Kuuliala L., Al Hage, Y., Ioannidis, A.-G., Sader, M., Kerckhof, F.-M., Vanderroost, M., Boon, N., De Baets, B., De Meulenaer, B., Ragaert, P., & Devlieghere, F. (2018). Microbiological, chemical and sensory spoilage analysis of raw Atlantic cod (*Gadus morhua*) stored under modified atmospheres. *Food Microbiology*, *70*, 232-244. https://doi.org/10.1016/j.fm.2017.10.011.

Kuuliala, L., Pippuri, T., Hultman, J., Auvinen, S.-M, Kolppo, K., Nieminen, T., Karp, M., Björkroth, J., Kuusipalo, J., & Jaaskelainen, E. (2015). Preparation and antimicrobial characterization of silver-containing packaging materials for meat. *Food Packaging and Shelf Life, 6*, 53-60. https://doi.org/10.1016/j.fpsl.2015.09.004

Küçükçobanoğlu, Y., & Yıldız Aktaş, L. (2018). Nanokompozit Kaynağı ve Uygulama Alanı Olarak Bitkiler. *Marmara Fen Bilimleri Dergisi*, *4*, 429-436. https://doi.org/10.7240/marufbd.357278.

Lapenna, A., Dell'Aglio, M., Palazzo, G., & Mallardi, A. (2020). "Naked" gold nanoparticles as colorimetric reporters for biogenic amine detection. *Colloids Surfaces A Physicochem. Eng. Asp.,* 124903. https://doi.org/10.1016/j.colsurfa.2020.124903.

Licciardello F., Kharchoufi, S., Muratore, G., & Restuccia, C. (2018). Effect of edible coating combined with pomegranate peel extract on the quality maintenance of white shrimps (*Parapenaeus longirostris*) during refrigerated storage. *Food Packaging and Shelf Life, 17*, 114-119. https://doi.org/10.1016/j.fpsl.2018.06.009.

Lin Q.-B, Li, H., Zhong, H. N., Zhao, Q., Xiao, D. H., & Wang, Z. W. (2014). Migration of Ti from nano-TiO(2)-polyethylene composite packaging into food simulants. *Food Addit Contam Part A Chem Anal Control Expo Risk Assess.*, *31*, 1284–1290. https://doi.org/10.1080/19440049.2014.907505.

Liu, Y., Ma, Y., Liu, Y., Zhang, J., Hossen, Md A.,Sameen, D. E., Dai, J., Li, S., & Qin, W. (2021).Fabrication and characterization of pH-responsive intelligent films based on carboxymethyl cellulose and gelatin/curcumin/chitosan hybrid microcapsules for pork quality monitoring. *Food Hydrocolloids*, *124*, 107224. https://doi.org/10.1016/j.foodhyd.2021.107224.

Ma, Q., & Wang, L. (2016). Preparation of a visual pH-sensing film based on tara gum incorporating cellulose and extracts from grape skins. *Sensors and Actuators B -Chemical, 235*, 401-407. https://doi.org/10.1016/j.snb.2016.05.107.

Ma, Q., Liang, T., Cao, L., & Wang, L. (2018). Intelligent poly (vinyl alcohol)-chitosan nanoparticles-mulberry extracts films capable of monitoring pH variations. *International Journal of Biological Macromolecules*, *108*, 576-584. https://doi.org/10.1016/j.ijbiomac.2017.12.049.

Majid I, Nayik G. A , Dar, S. M., & Nanda, V. (2018). Novel food packaging technologies: Innovations and future prospective. *Journal of the Saudi Society of Agricultural Sciences. 17,* 454– 462. http://dx.doi.org/10.1016/j.jssas.2016.11.003.

Martínez-Abad A., Lagaron, J. M., & Ocio, M. J. (2014). Characterization of transparent silver loaded poly(l-lactide) films produced by melt-compounding for the sustained release of antimicrobial silver ions in food applications. *Food Control, 43,* 238-244. https://doi.org/10.1016/j.foodcont.2014.03.011.

Metak, A. M., Nabhani, F., & Connolly, S. N. (2015). Migration of engineered nanoparticles from packaging into food products. *LWT-Food Sci Technol, 64,* 781-787. https://doi.org/10.1016/j.lwt.2015.06.001.

Mizielińska, M., Kowalska, U., Jarosz, M., & Sumińska, P. (2018). A comparison of the effects of packaging containing nano ZnO or polylysine on the microbial purity and texture of Cod (*Gadus morhua*) fillets. *Nanomaterials, 8*, 158. https://doi.org/10.3390/nano8030158.

Mol, S. (2014). Gıda Güvenliği Yönünden Su Ürünleri Sektörünün Değerlendirilmesi. Dünya Gıda, 8, 32-37.

Musso, Y. S., Salgado, P. R., & Mauri, A. N. (2016). Gelatin based films capable of modifying its color against environmental pH changes. *Food Hydrocolloids, 61,* 523-530. https://doi.org/10.1016/j.foodhyd.2016.06.013.

Mustafa, F., Othman, A., & Andreescu, S. (2021). Cerium oxide-based hypoxanthine biosensor for Fish spoilage monitoring. *Sensors and Actuators B: Chemical, 332*, 129435. https://doi.org/10.1016/j.snb.2021.129435.

Naghdi, S., Masoud, R., & Mehdi, A. (2021). A starch-based PH-sensing and ammonia detector film containing betacyanin of paperflower for application in intelligent packaging of fish. *Int J Biol Macromol*., *191*, 161–170. https://doi.org/10.1016/j.ijbiomac.2021.09.045.

Nazari, M., Majdi, H., Milani, M., Abbaspour-Ravasjani, S., Hamishehkar, H., & Lim, L.-T. (2019). Cinnamon nanophytosomes embedded electrospun nanofiber: Its effects on microbial quality and shelf-life of shrimp as a

novel packaging. *Food Packaging and Shelf Life, 21*, 100349. https://doi.org/10.1016/j.fpsl.2019.100349

Noonan, G. O., Whelton, A. J. , Carlander, D., & Duncan, T.V. (2014). Duncan Measurement methods to evaluate engineered nanomaterial release from food contact materials**.** *Comprehensive Reviews in Food Science and Food Safety*, *13*, 679-692. https://doi.org/10.1111/1541-4337.12079.

Paidari, S., & Ahari, H. (2021). The effects of nanosilver and nanoclay nanocomposites on shrimp (Penaeus semisulcatus) samples inoculated to food pathogens*. Food Measure 15*, 3195–3206. https://doi.org/10.1007/s11694-021-00905-x.

Ponce, A. G., AyalaZavala, J. F , Marcovich, N. E., Vazquez, F. J., & Ansorena, M. R. (2018)**.** Nanotechnology trends in the food industry: recent developments, risks, and regulation. A. M. Grumezescu, & A. M. Holban (Eds.), *Impact of Nanoscience in the Food Industry: Handbook of Food*, (*12*, 113-141). *Academic Press*.

Prato, E., & Biandolino, F. (2015). Chapter 16 - The Contribution of Fish to the Mediterranean Diet. V. R. Preedy, & R. R. Watson (Eds), *The Mediterranean Diet, Academic Press,* (pp 165-174). https://doi.org/10.1016/B978-0-12-407849-9.00016-6.

Qin Y., Liu, Y., Yuan, L., Yong, H., & Liu, J. (2019). Preparation and characterization of antioxidant, antimicrobial and pH-sensitive films based on chitosan, silver nanoparticles and purple corn extract. *Food Hydrocolloids*, *96*, 102-111. https://doi.org/10.1016/j.foodhyd.2019.05.017.

Rubilar J. F., Candia, D., Cobos, A., Diaz, O., & Pedreschi, F. (2016). Effect of nanoclay and ethyl-Nα-dodecanoyl-l-arginate hydrochloride (LAE) on physico-mechanical properties of chitosan films. *LWT-Food Sci. Technol., 72*, 206-214. 10.1016/j.lwt.2016.04.057.

Saka, E., & Terzi Gülel, G. (2015). Gıda Endüstrisinde Nanoteknoloji Uygulamaları. *Etlik Veteriner Mikrobiyoloji Dergisi*, *26*, 52-57 . https://doi.org/10.35864/evmd.513387.

Sarfraz, J., Gulin-Sarfraz, T., Nilsen-Nygaard, J., & Pettersen, M. K. (2021). Nanocomposites for Food Packaging Applications: An Overview. *Nanomaterials*, *11*, 10. https://doi.org/10.3390/nano11010010.

Seray, M., Hadj-Hamou, A. S., Uzunlu, S., & Benhacine, F. (2021). Development of active packaging films based on poly (butylene adipate-*co*-terephthalate) and silver–montmorillonite for shelf life extension of sea bream. *Polymer Bulletin*. https://doi.org/10.1007/s00289-021-03671-4

Shahbazi, Y., & Shavisi, N. (2018). Chitosan coatings containing Mentha spicata essential oil and zinc oxide nanoparticle for shelf life extension of Rainbow trout fillets. *Journal of Aquatic Food Product Technology, 27*, 986–997. **https://doi.org/10.1080/10498850.2018.1518945.**

Shruthy, R., Jancy, S., & Preetha, R. (2020). Cellulose nanoparticles synthesised

from potato peel for the development of active packaging film for enhancement of shelf life of raw prawns (*Penaeus monodon*) during frozen storage. *International Journal of Food Science & Technology, 56,* 3991– 3999. https://doi.org/10.1111/ijfs.14551.

Singh, S., Lee, M., Gaikwad, K. K., & Lee, Y. S. (2018). Antibacterial and amine scavenging properties of silver-silica composite for post-harvest storage of fresh fish. *Food Bioprod Process*, *107*, 61–69. https://doi.org/10.1016/j. fbp.2017.10.009.

Staroszczyk, H., Malinowska-Panczyk, E., Gottfried, K., & Kołodziejska, I. (2017). Fish gelatin-nanoclay films. Part I: effect of a kind of nanoclays and glycerol concentration on mechanical and water barrier properties of nanocomposites. *J. Food Process. Preserv*., *41,* 13211. https://doi.org/10.1111/jfpp.13211.

Störmer, A., Bott, J., Kemmer, D., & Franz, R. (2017). Critical review of the migration potential of nanoparticles in food contact plastics. *Trends in Food Science & Technology, 63*, 39-50. https://doi.org/10.1016/j.tifs.2017.01.011.

Stueckle, T. A, White, A., Wagner, A., Gupta, R. K, Rojanasakul, Y., & Dinu, C. Z. (2019). Impacts of Organomodified Nanoclays and Their Incinerated Byproducts on Bronchial Cell Monolayer Integrity. *Chemical Research in Toxicology*, *32*, 2445-2458. https://doi.org/10.1021/acs.chemrestox.9b00277.

Tavakoli, H., Rastegar, H., Taherian, M., Samadi, M., & Rostami, H. (2017). The effect of nano-silver packaging in increasing the shelf life of nuts: An in vitro model. *Italian Journal of Food Safety, 6,* 6874. https://dx.doi. org/10.4081%2Fijfs.2017.6874.

Tharanathan, R. N. (2003). Biodegradable films and composite coatings: Past, present and future. *Trends in Food Science & Technology, 14,* 71-78. https:// doi.org/10.1016/S0924-2244(02)00280-7.

Turan, H., Kaya, Y., & Sönmez, G. (2006). Balık etinin besin değeri ve insan sağlığındaki yeri. *E. Ü. Su Ürünleri Dergisi*, *2*3, 505-508.

Ünlütürk, A., & Turantaş, F. (1999). Gıda Mikrobiyolojisi. s.53. Mengi Tan Basımevi, Çınarlı, İzmir.

Varlet, V., & Fernandez, X. (2010). Review. Sulfur-containing volatile compounds in seafood: Occurrence, odorant properties and mechanisms of formation. *Food Science and Technology International*, *16*, 463-503. https:// doi.org/10.1177/1082013210379688

Vilarinho, F., Andrade, M. A, Buonocore, G., Stanzione, M., Vaz, M., & Silva, A. S. (2018). Monitoring lipid oxidation in a processed meat product packaged with nanocomposite poly (lactic acid) film. *European Polymer Journal*, *98*, 362–367. https://doi.org/10.1016/J.EURPOLYMJ.2017.11.034.

Vizzini, P., Beltrame, E., Zanet, V., Vidic, J., & Manzano, M. (2020). Development and Evaluation of qPCR Detection Method and Zn-MgO/Alginate Active Packaging for Controlling Listeria monocytogenes Contamination in Cold-Smoked Salmon. *Foods, 9*, 1353. https://doi.org/10.3390/foods9101353.

Wang, G., Zhao, G., Dong, G., Mu, Y., & Park, C. B. (2018).Lightweight and strong microcellular injection molded PP/talc nanocomposite. *Composites Science and Technology, 168*, 38–46. https://doi.org/10.1016/j.compscitech.2018.09.009.

Wu, C., Sun, J., Zheng, P., Kang, X., Chen, M., Li, Y., Ge, Y., Hu, Y., & Pang, J. (2019). Preparation of an intelligent film based on chitosan/oxidized chitin nanocrystals incorporating black rice bran anthocyanins for seafood spoilage monitoring. *Carbohydrate Polymers, 222*, 115006. https://doi.org/10.1016/j.carbpol.2019.115006.

Yamashita, K,, Yoshioka, Y., Higashisaka, K., Mimura, K., Morishita, Y., Nozaki, M., Yoshida, T., Ogura, T., Nabeshi, H., Nagano, K., Abe, Y., Kamada, H., Monobe, Y., Imazawa, T., Aoshima, H., Shishido, K., Kawai, Y., Mayumi, T., Tsunoda, S., …Tsutsumi, Y. (2011). Silica and titanium dioxide nanoparticles cause pregnancy complications in mice. *Nature Nanotechnology*, *6*, 321-328. https://doi.org/10.1038/nnano.2011.41.

Yano, K., Usuki, A., & Okada, A. (1997). Synthesis and properties of polyimide-clay hybrid films. J. Polym. Sci. Part A Polym. Chem., *35*, 2289-2294. https://onlinelibrary.wiley.com/doi/10.1002/(SICI)1099-0518(199708)35:11%3C2289::AID-POLA20%3E3.0.CO;2-9.

Zhai, J., Shi, J., Zou, X., Wang, S., Jiang, C., Zhang, J., Huang, X., Zhang, W., & Holmes, M. (2017). Novel colorimetric films based on starch/polyvinyl alcohol incorporated with roselle anthocyanins for fish freshness monitoring. *Food Hydrocolloids*, *69*, 308-317. https://doi.org/10.1016/j.foodhyd.2017.02.014

Zhai, X., Li, Z., Shi, J., Huang, X., Sun, Z., Zhang, D., Zou, X., Sun, Y., Zhang, J., Holmes, M., Gong, Y., Povey, M., & Wang, S. (2019). A colorimetric hydrogen sulfide sensor based on gellan gum-silver nanoparticles bionanocomposite for monitoring of meat spoilage in intelligent packaging. *Food Chemistry*, *290*, 135-143. https://doi.org/10.1016/j.foodchem.2019.03.138.

Zhang, L., Liu, A., Wang, W., Ye, R., Liu, Y., Xiao, J., & Wang, K. (2017). Characterisation of microemulsion nanofilms based on Tilapia fish skin gelatine and ZnO nanoparticles incorporated with ginger essential oil: Meat packaging application. *International Journal of Food Science and Technology, 52*, 1670–1679. https://doi.org/10.1111/ijfs.13441.

Zhang, X., Liu, Y., Yong, H., Qin, Y., Liu, J., & Liu, J. (2019). Development of multifunctional food packaging films based on chitosan, TiO2 nanoparticles and anthocyanin-rich black plum peel extract. *Food Hydrocolloids*, *94*, 80-92. https://doi.org/10.1016/j.foodhyd.2019.03.009.

Zhang, Y. P., Wang, X., Shen, Y., Thakir, K., Zhang, J. G., Hu, F., & Wei Z. J. (2021). Preparation and Characterization of Bio-Nanocomposites Film of Chitosan and Montmorillonite Incorporated with Ginger Essential Oil and Its Application in Chilled Beef Preservation. *Antibiotics*, *10*, 796. https://doi.org/10.3390/antibiotics10070796.

Zou, H. Wu, S., & Shen, J. (2008). Polymer/silica nanocomposites: preparation, characterization, properties, and applications. *Chemical Reviews*, *108*, 3893–3957. https://doi.org/10.1021/cr068035q.

International Organization for Standardization. (2018). Nanotechnologies — In vitro MTS assay for measuring the cytotoxic effect of nanoparticles (ISO Standart No. 19007:2018). https://www.iso.org/standard/63698. html#:~:text=ISO%2019007%3A2018%20specifies%20a,variability%20 in%20the%20assay%20results.

Commission Regulation (EC) No 450/2009 of 29 May 2009 on active and intelligent materials and articles intended to come into contact with food (Text with EEA relevance). https://eur-lex.europa.eu/legal- content/EN/ ALL/?uri=CELEX%3A32009R0450
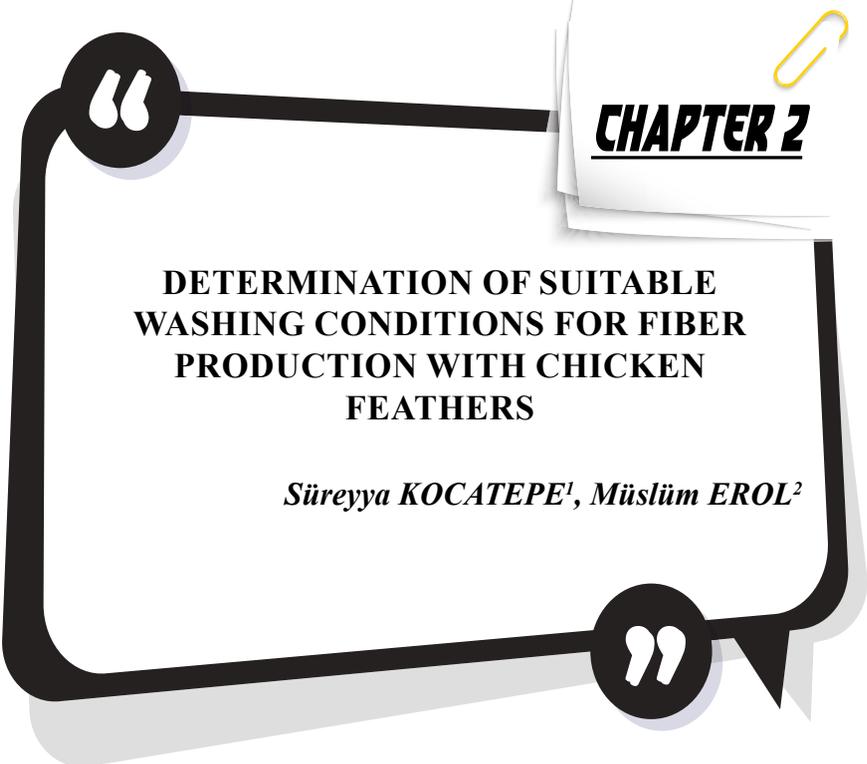
DETERMINATION OF SUITABLE WASHING CONDITIONS FOR FIBER PRODUCTION WITH CHICKEN FEATHERS

Süreyya KOCATEPE[1], Müslüm EROL[2]

1 Dr., Fırat University, Organized Industrial Zone Vocational School, Department of Textile, Clothing, Shoes and Leather, ORCİD: 0000-0002-0646-1380
2 Assist. Prof. Dr., Bingöl University, Technical Sciences Vocational School, Department of Textile, Clothing, Shoes and Leather, ORCİD: 0000-0002-6905-7481

1. INTRODUCTION

Chicken feathers obtained as a byproduct in the production of white meat and important part of the separated waste are natural protein materials. The content of 90% these fibers approximately consist of protein (Arunkumar et al. 2013). Chicken feathers are not suitable for using with its current form. We can not use this feathers as filling materials like waterfowl's feathers. Because, this situation is about the features of chicken feathers have low elasticity, high fragility and the lack of pile feathers. Nevertheless, it is known that chicken feathers have important features and the research about chicken feathers is expanding day by day. In recent years, the perspective of production of natural protein fibers from chicken feathers has attracted scientist more.These fibers, which is named as chicken feather fibers, are obtained by mechanically cutting of fibrils from rachis part which constitute the body of the feathers. Investigations about chicken feather fibers reveal important properties of these fibers (Jones et al. 1998; Reddy et al. 2007; Martínez-Hernández et al. 2012; Chinta et al. 2013). However, there is no industrial technology of fiber production on today. Such a technology is being developed in the Department of Textile Engineering at Erciyes University. Fiber production from chicken feathers have two stages. First stage is preparation feathers for the production of fibers, second stage is production of fibers. During the preparation of feathers for the production fibers, cleaning the feathers from dust and other mechanical mixture, washing, drying and disinfected should be considered. These operations are also available in the manufacture of bird feathers. Washing processes take place in front between these processes. During washing, it is requested that feathers are cleaned from oil as well as purified from the dirts. Because the presence of oils leads to a special smell in the feathers and this smell makes them attractive for pests.

In literature, it is observed that the chicken feathers were washed with different methods. Different researches have applied different methods for this purpose. In a US patent, it is recommended that chicken feathers should be agitated wash (preferably 95% ethanol) in an organic solvent. The method of claim is recommended 1…1,5 gallons of solvent for each feather weight, 60…120ºC in air drying furnace is recommended for drying process (Patent US5705030, 1998).

Ye et al washed the chicken feathers in canvas bags in household washing machines at their study of chicken feathers to produce nonwovens from the chicken feather rag. Drying process was conducted in domestic dryers with warm temperature (Ye et al., 1999). In study, it was not investigated that how the washing process effected the properties of fibers. Martinez-Hernandez et al who investigated the chicken feather features as a precious material in order to produce ecological composite

structures, washed the feathers with ethanol and dried for sterility and odorless fibers (Martinez-Hernandez et al., 2005). Sayed et al aimed that remove some contaminating ions from industrial water by using chicken feathers have implemented the chicken feathers for 20 minutes' treatment with petroleum ether at 40…60ºC temperature to fibers, then had washed with water several times, at the end of washed with ethanol and after dried feathers for a night (Sayed et al., 2005). Kock aimed using the materials which was obtained from chicken fathers with simple cutting method, had washed the chicken feathers with antimicrobial soap solution which had about 7 L/m³ concentration in the washing machine, then had dried in a rotary dryer (Kock, 2006). Coward-Kelly et al had washed the chicken feathers with a water several times to get rich liquid product which can be used as an additive in animal feed, then had dried at ambient temperature and finally have heat treatment at 105ºC (Coward-Kelly et al., 2006). Wrnesniewsk-Tosik and Adamiec who were aimed to get different keratin forms from chicken feathers, had washed the chicken feathers with hot water and detergent, dried up, had filter and dried with operation by using ethlyne alcohol (Wrześniewska-Tosik and Adamiec, 2007). Xiling Fan had used the rate of 5% solution of soap to wash the chicken feathers at studies for production of fibers. After rinsing, feathers were dried at household laundry drier. Four different methods were used to sterilize the feathers. a) Mixture of acetone and water, b) rate of 10% peroxide solution, c) rate of 95% ethanol solution, d) rate of 5% chlorine bleach rate. The pH of the solution was adjusted to 8. The best results were obtained with bleach. The use of this substance has eliminated all bacteria and bacteria has storageted for 3 months, after 3 months they were no bacteria (Fan, 2008). Cervantes-Gonzales et al who were aimed to production sorbents for biodegration petroleum hydrocarbons from chicken feathers kepted feathers in neutral detergent solution for a night in their studies, then washed and rinsed them to purify detergent with tap water and dried under the sun (Cervantes-Gonzalez et al, 2008). De la Rosa et al who aimed to benefit from chicken feathers as biosorbent in cleaning the Pb ions from aqueous solutions, washed the chicken feathers with deionized water and detergent in several times, then implemented to feathers for 12 hours with 5:1 percent deionized water and ethanol solution (Rosa et al., 2008).

Lam et al kept the chicken feathers in alcohol for 24 hours, washed them in organic solvents and dried them for 24 hours at 60ºC to sterilize them in order to produce biocomposite from chicken feather mixture with polylactic acid (Lam et al., 2009). Cesur who was aimed that removing heavy metal ions from aqueous solution by the aid of chemically modified feathers, washed the chicken feathers with deionized water and detergent in several times and dried in an oven at 40ºC (Cesur, 2010). Menandro and

Acda who was aimed to produce the composite structures with blended cement, washed the chicken feathers with salt mixture and detergent in water in several times in for removing the impurities from chicken feathers. Clean feathers were spreaded on the galvanized iron sheet and then dried under the sun for 3 days (Menandro and Acda, 2010). Tseng and Verbeek who were aimed to obtain fibers from chicken fibers, washed chicken feathers into 25 liters of water, with 0,15% sodium hypochlorite solution at Ph 10,0 at two stages in 30 minutes, then washed the feathers into 25 liters of water, with 0,15% sodium hypochlorite solution at three stages in 30 minutes, clean feathers were dried at 700ºC temperature. Morphological studies have shown that surface of fibers did not disruption after the cleaning process (Tseng and Verbeek, 2011). Uzun et al who were investigated the mechanical properties of chicken feathers and composite structures produced from these feathers, washed the chicken feathers in polar solvent (ethanol) by using laboratory washing machine. After washing, feathers were rinsed with water and dried for 24 hours at normal room temperature (Uzun et al., 2011).

Wrzesnieeska-Tosik et al who aimed to obtain the hydrophobic nonwoven composite from chicken feathers and synthetic fibers (polyester, polpropylene), washed the chicken feathers with water contains detergent for 1 hour at 40ºC , then soaked the feathers for 10 minutes at centrifugation, they soaked the feathers at 15% rate of hydrogen peroxide solution after squeezing. Then water was soaked, then feathers were dried (Wrześniewska-Tosik et. al, 2012). Saravan who was examined the chemical structure of chicken feathers, washed raw feathers with soap 5% solution and dried warm temperature after rinsing. Chicken feathers washed in order to sterilization at room temperature (21ºC) were dipped into polar solvent (Ph 8) and water for 30 minutes, then applied the soaping process, at last rinsed and dried with air (Saravanan, 2012). Moore et al who were aimed to examine the amino acids which forms the chicken feathers, washed the freshly-cut wet feahers in water and dried in ventilated oven at 40ºC for 72 hours. Feathers were treated with petroleum ether to eliminate fat for 12 hours at Soxhlet device (Moore et al., 2012). Tiwary and Gupta who were aimed to obtain protein content of feed ingredients, washed the chicken feathers with detergent and rinsed feathes with tap water in several times. Feathers were dried at 80ºC for 6 hours (Tiwary and Gupta, 2012).

Alonso et al investigated the mechanical and physical properties of fibers obtained from chicken feathers. They washed feathers 3 times by using 5% sodium chloride and detergent to remove the adhesive material and waste feathers, then sterilized (Alonso et al., 2013). Canpolat has used Soxlet system in order to remove lipids and waste products found in chicken feathers by using solvents as a dichloromethane and toluene in

his study. Chicken feathers were purified from other contaminants for 6 hours. After extraction, chicken feathers were dried in a vacuum drying oven (Canpolat, 2013).

Kiew et al who investigated the dielectric properties of composite structures which are made from chicken fibers and kenaf fibers, washed the chicken fibers with water-soluble ethanol and dried under the sun for 7…8 hours. Then, feathers were dried in oven at 800ºC for 24 hours to ensure complete drying of feathers (Kiew et al., 2013). Ghani et al who researched that about the properties of composite structures made from low density polyethylene and differently treated chicken feathers, washed the chicken feathers with water and dried in vacuum drying cabinet at 80ºC for 2 hours (Ghani et al, 2014). Jagadeeshgouda et al who studied about producing the composite structures from chicken feather fibers, washed chicken feathers with hot water and detergent for cleaning the feathers, then dried feathers. At a later stage, the rate of 6% NaOH solution was prepared, the fibers were processed in the solution, then washed in running water and dried for 10 hours in the daylight (Jagadeeshgouda et al., 2014). Amieva et al researched about producing composite structures from chicken feathers and polypropylene. They washed the chicken feathers with water and ethanol to make them odor-free and clean, then dried them at room temperature (Amieva et al., 2014). When look at the literature which is connected washing feathers, it has just shown that the dirt is removed from fibers, sometimes it is being for sterilization. There has been no researching about if structure of fibers had changed or not about physical or mechanical changes.

As shown, although there are various studies related to washing operation about chicken feathers, washing process have not been a detailed researching subject. At the end of the literature researching, there is no literature about if different washing conditions had change structural and mechanical properties of fibers obtained from chicken feathers. Most of the researchers in the literature have used detergent, soap solution and organic polar solvents in many cases. Sodium hypochlorite has preferred for disinfection. However, in these researches, it has not been investigated how the properties of chicken feathers are changed after washing process with different materials, washing conditions, and the effects of these conditions on the materials. This study will help to overcome these deficiencies.

2. EXPERİMENT

2.1. Approach

When viewed the chicken feather fibers, which were obtained from chicken feathers, it is seen that they are looking like a small model of bird feathers under a microscope. There is a relatively thick ″stalk″ in the middle of the fibers and fibrils which are branched from rachis are present (Figure). Such a structure imparts some advantages and disadvantages to the chicken feather fibers. Thanks to this structure, the fibers can not be tightly bondend to each other and therefıre they do not have a matting property. On the other hand, the fibers can not hold together due to this property and consequently problems arise in yarn or production of nonwoven surface.

The other most important properties of the fibers, which are obtained from the chicken feathers, is that these fibers have microporous internal structure. There pores are in the form of micro chambers and they provide important insulation properties to the fibers. In Figure 2, the fiber image, which was washed several times without using any chemicals and dried, is seen under scannig electron microscope. As can be seen on figure, the fibers are not yet clean as a result of washing with water, they have still dirt and oil particles on them. However, when look at the fiber section, the internal structure of the fiber is seen as natural.
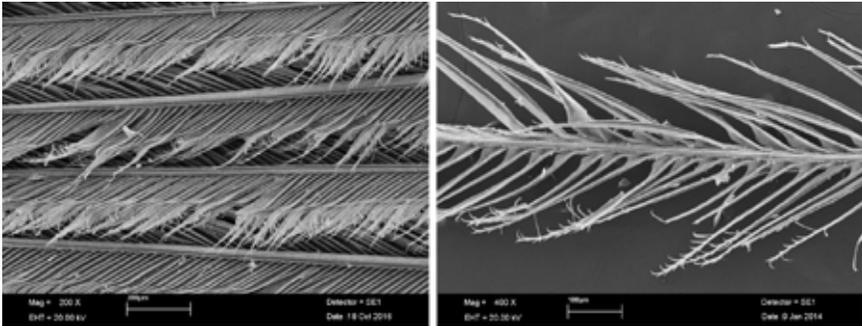
Figure 1. SEM images of the fibers which was obtained from chicken feather

Preliminary investigations about washing of feathers have shown that deterioration of the cellular structure of feathers during washing and drying process, shrinking and constrict of cells are possible. Experimental studies have been carried out, which is aiming to determine the best washing conditions and washing materials, in order to protect this valuable property of the fibers during washing process.
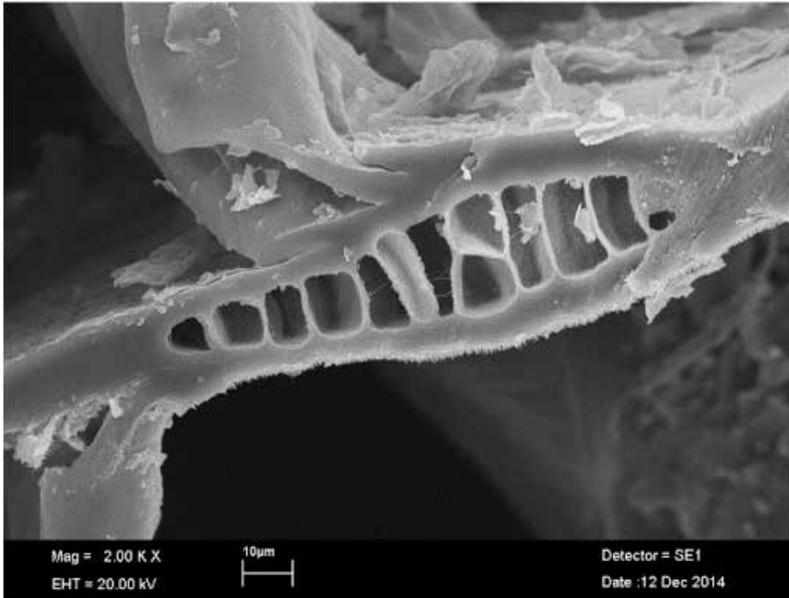
Figure 2. SEM image of washed chicken feather fibers

Even though the material is chicken feather fibers that concern us, the washing and disinfecting operations are carried out before disassembling the fiber that is when the materials are feather condition. Accordingly, in this study, washing was applied to the feathers, tests and analyzes were carried out on the fibers, which were obtained from the washed feathers. One of the most important issues is washing process temperature. Not to deteriorate the microporous microstructure of the fibers, the most suitable washing temperature should be selected. Another important issue is the selection of the washing materials and washing regime in terms of the protection surface of the fibers and internal structure. Accordingly, SEM analysis of the surface structure and internal structure of the fibers was carried out after washing process.

2.2. Material

Chicken Feather

The chicken feathers, which were used in this study, were obtained from ''Tad Piliç''which is located in Gaziantep in Turkey.

Washing Materials

As it is known, chicken feather is a protein based material which has an unpleasant odor, hangs on the fat and oil on them due to the living conditions and natural structures of the chickens. The amount of this pollution can vary depending on the type of animal, the climate of the enviroment, living conditions. The fibers, which were obtained from

the feathers, must be clean and not dangerous in terms of bacteria. For this reason, it is important that the selected washing and disinfecting substances are effective in the washing phase. Selecting the chemicals that have a pH range of 6-8, dirt and oil-repellent and conforms to the washing conditions in terms of not damaging the fibers, are important. The suitable washing material for the washing of chicken feathers was selected from between four different chemicals with cationic and nonionic structure, only soil remover and both soil and oil remover properties. These materials are manufactured by Setaş Colour Center. The trade names of the materials are Setalan IK30, Setawash PY Conz. The trade names of materials of Rudolf Group are Rucogen Yes and SSA. Rucogen Yes has also oil-repellent feature. As a disinfectant material, sodium hypochlorite (NaCIO) based washing substance with a commercial name ACE, which is a degreasing additive, was used. The selection of this material, which is based sodium hypochlorite, has been based on the recommendations in the literature on the washing of chicken feathers. Some properties of the washing substances are given in Table 1.

Table 1. Properties of washing materials

Washing material	Setawash PY Conz	Setalan IK 30	Rucogen Yes	Verolan SSA
Ionic structure	Cationic	Nonionic	Nonionic	Nonionic
Appearence of material	Colorless clear liquid	Colorless clear liquid	Colorless clear liquid	Brown liquid
pH range	6,0-8,0 (%2'lik çözelti)	5,0-7,0 (2% solution)	6,0-7,0 (2% solution)	6,0-7,0 (2% solution)
Solubility	Mixed easily with water	Mixed easily with water	Mixed easily with water	Mixed easily with water

2.3. Method

Washing

Washing operations were carried out in household washing machine at laboratory. For each washing operations, 0,5kg of feathers were taken, one of the washing materials listed in Table 1 and sodium hypochlorite were used. Washing temperature was 40°C, the amount of washing substance was determined as 2% of water volume and the amount of sodium hypochlorite was determined as 2% of water volume. The amount of water takes for washing is 10L.Washing operation with two different programs was carried out with each washing material.

Program 1:

a. Pre-washing for 20 minutes with sodium hypochlorite

b. Rinsing for 17 minutes and squeezing

c. Main washing for 1 hour with washing material

d. Rinsing for 17 minutes and squeezing

Program 2:

a. Pre washing for 20 minutes with sodium hypochlorite

b. Rinsing and squeezing for 17 minutes

c. Final washing with sodium hypochlorite for 20 minutes

d. Rinsing and squeezing for 17 minutes

After washing, the feathers were dried for 3 days in the drawer. The test samples were taken from the dried feathers and placed in the locked bags.

Evaluation of washing results

In experiments, the criteria for selection of the washing material were accepted as the visually evaluated cleaning of feathers (no dirt and oil particles on feathers), fiber surface and microporous internal structure of fibers which were not damaged and the breaking strength from mechanical properties. For his purpose, SEM analysis as well as tensile tests were applied to examine the structural properties of fibers produced from washed and dried feathers.

Among the fibers produced from the feathers washed with different washing substances and washing programs, average size is 20 ± 1 mm long fibers were taken and tensile test was applied to these fibers. Variance analysis of the tensile strength values was carried out in order to reveal whether if the washing substances and washing program has an effect on the results of the tensile tests. The aim is to find out whether if the average values of the tensile strenght values of fibers produced from feathers washed with different washing substance and different washing program are different or not from the average values of the tensile strenght values of fibers produced from unwashed feathers. Fort this purpose, the Dunnett test was applied and Minitab 17 program was used.

Test results of fibers produced from unwashed feathers was accepted as control data. Test results of feather fibers washed with different washing substance and washing program are coded with the initials of the washing substance and numbers 1 and 2 indicating the washing program. As each washing process was carried out according to two programs, 8 groups of data were obtained from the control group.

Firstly, the normality of the data according to all data groups and the homogeneity of the variances accordind to groups were tested. Then, one-way variance analysis involving Dunnett test which allows multiple comparisons to data groups, was performed. According to this analysis, the significance of the data groups averages containing indivual washing results was tested according to the control group. An experiment was conducted to determine the optimal values of washing substance concentration in washing solutions. This experiment was carried out as a full factorial experiment which is planned as 3^2 by managing the amount of NACIO in the preliminary and final washings and the amount of washing substances in the main washing. Experimental design and statistical analysis of the test results were carried out by Design Exper 11 program. The parameters of change of the manageable factors are given in Table 2. In the experiments, visually cleaning degree of the washed feathers, whether damage to the microporous microstructure, which is visually evaluated from the SEM appearance of the fibers, and the tensile test results of the fibers were examined. The Experimental plan is given in Table 4. In the experiments, visually cleaning degree of the washed feathers, whether damage to the microporous microstructure, which is visually evaluated from the SEM appearance of the fibers, and the tensile test results of the fibers were examined. The Experimental plan is given in Table 4.

Table 2. Chang parameters of Experimental factors

Experiment Factors	Sign	Range Levels of Factors	Factor levels		
			-1	0	+1
The amount of NaCIO, %	X_1	2…6	2	4	6
The amount of washing material, %	X_2	2…6	2	4	6

SEM analysis

Leo440 Scanning Electron Microscope (SEM), which is located at Erciyes University Technology Research and Application Center, was used to visualize the surface and cross-section structure of the non-washed chicken feather samples and washed with different programs in the studies.

Tensile Test

Chicken feather fiber samples were subjected to pull-out tests at Erciyes University Technology Research and Application Center. For this purpose, strength tester (SHIMADZU mark) was used in laboratories at Erciyes University Technology Research and Application Center. Chicken feather fibers were prepared precisely for the strength test. These fibers, which are very thin, are placed in the sample bag after conditions in test

cabinet for 24 hours under normal conditions. Because of these fibers are very sensitive and short, it was not possible to apply a certain standart in the tests and therefore pulling was performed by applying the lowest force. The test results were transferred to the TRAPEZUIMW program in computer. In this program, the minimum and maximum force values for sample and the measured diameter value of the fiber after SEM analysis are written. The graph of the results is drawn automatically. In order to obtain a good result, at least five measurements were made from each sample and the average value of these measurements was written and the strengt and other properties of the sample were interpreted.

3. RESULTS AND DISCUSSION

3.1. Investigations of the effects of washing process on the internal structure of the fibers

In Figure 3, the unwashed chicken feather and the fiber sample, which was obtained from this feather, are shown. In figure, surface view of feather, the sections of the root part of the fiber and the middle part of the body are given. These images reveal the dirt and oil particles on fibers, which were obtained from this feathers. It can be also appears that the walls of the porous have a smooth and unconstrained shape.

Figure 3. SEM images of unwashed chicken feather and chicken feather fibers

In Figure 4, SEM images of the surfaces and section of the fibers, which were obtained from chicken feathers (washed for 1 hour in water at a temperature of 40°C without using washing material and disinfectant), are shown. As can be seen in Figure 5, the microporous microstructure of the fibers consists of very smooth, undamaged and undeformed cells-pores. This means that washing process at 40°C didn't damage the internal structure of the fibers. This washing process with only water did not give a good results in terms of cleaning the washing fibers. In addition, the intense smell of chicken feathers is stil available after washing. However, these problems will be solved by the use of washing substances.

A washing operation at a temperature of 80°C has been carried out to know how washing temperatures is important in terms of the protection of

the internal structure of the fibers. SEM images of the fibers, which were obtained from cutten fibers after washing, are given in Figure 5. As can be seen in Figure, the fibers, which were washed at 80°C, are cleaner and the microporous core of the fibers was also damaged. As a result, the walls of the micro-pores are distored and the cells become smaller. These pictures are a proof that the washing temperature parameter is correct.

In Figure 6, SEM images of the surfaces and sections of fibers, which were obtained from feathers washed with washing substance (Rucoges Yes) and sodium hypochlorite is given. The images in Figure 6a are belongs the fibers which were washed at washing Program 1(washing first with NaCIO, then with washing substance). The images in Figure 6b are belongs the fibers which were washed at washing program 2 (washinng first with washing substance, then with sodium hypochlorite).


Lflerin kök kısmından alınan görüntüler
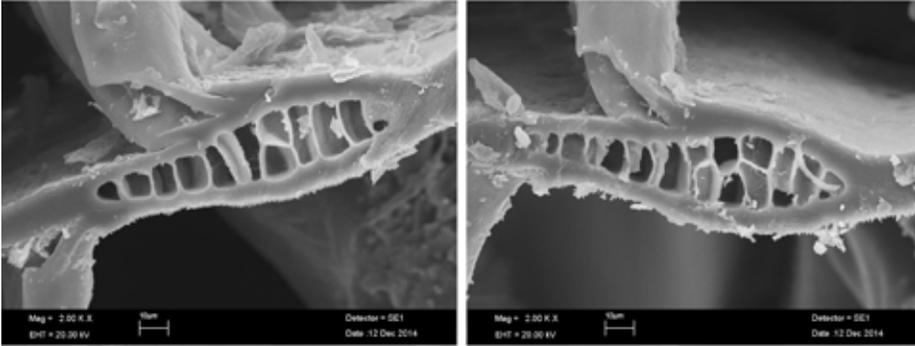
Lflerin orta kısmından alınan görüntüler
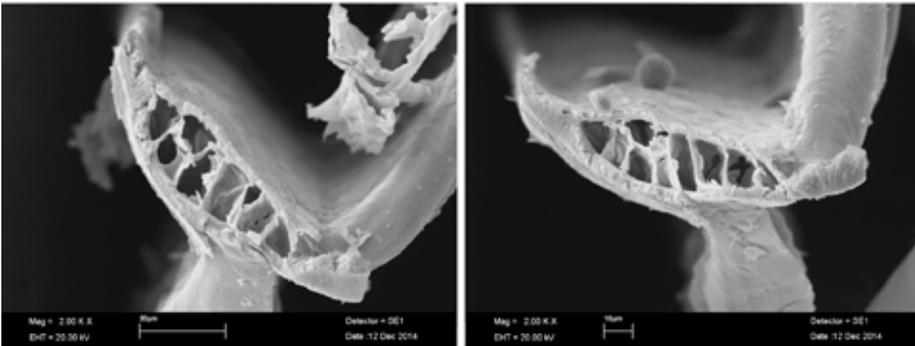
Figure 4. SEM images of surfaces and sections of fibers, which were produced from water-washed feathers at 40 °C
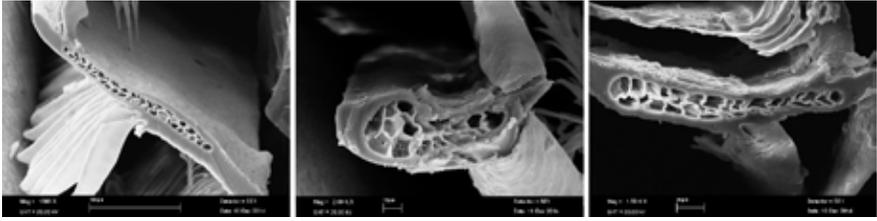
Figure 5. Images of the internal structure of the fibers, which were washed at high temperature

In Figure 6, when look at the surface and cross-sectional images of fibers, which were obtained from feathers(washed with Rucogen Yes and NaCIO), using the sodium hypochlorite before washing gives beter results in terms of cleaning. The use of other washing products gives the same result. According to our opinion, the operation of the sodium hypochlorite solution of the feathers before washing causes the removal of the surface contaminants and oils significiantly, this situation facilitates the work of surfactants in the subsequent washing process, as a result there is a cleaner washing process.

SEM images of the surfaces and sections of the fibers, which were obtained from feathers (washed with washing substance (Verolan SSA) and sodium hypochlorite solution), are shown in Figure 7. The images in Figure 7a belong to the Program 1, the images in Figure 7b belong to the program 2. Washing with this material is worse in terms of cleaning and both surface and internal structure of fibers when compare to the previous substance.

a)
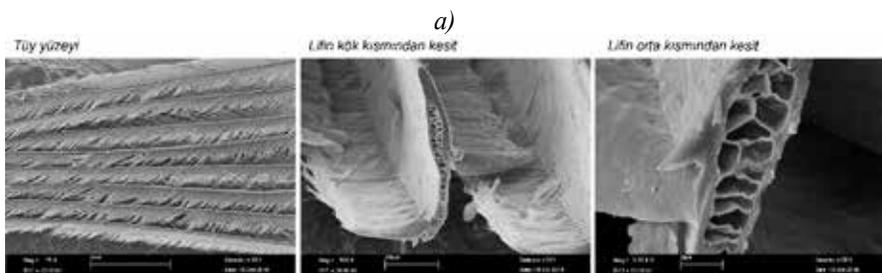
Figure 6. Surface and cross-section images of fibers, which were taken from washed feathers (washed with Rucogen Yes and NaCIO)

b)

a)

b)
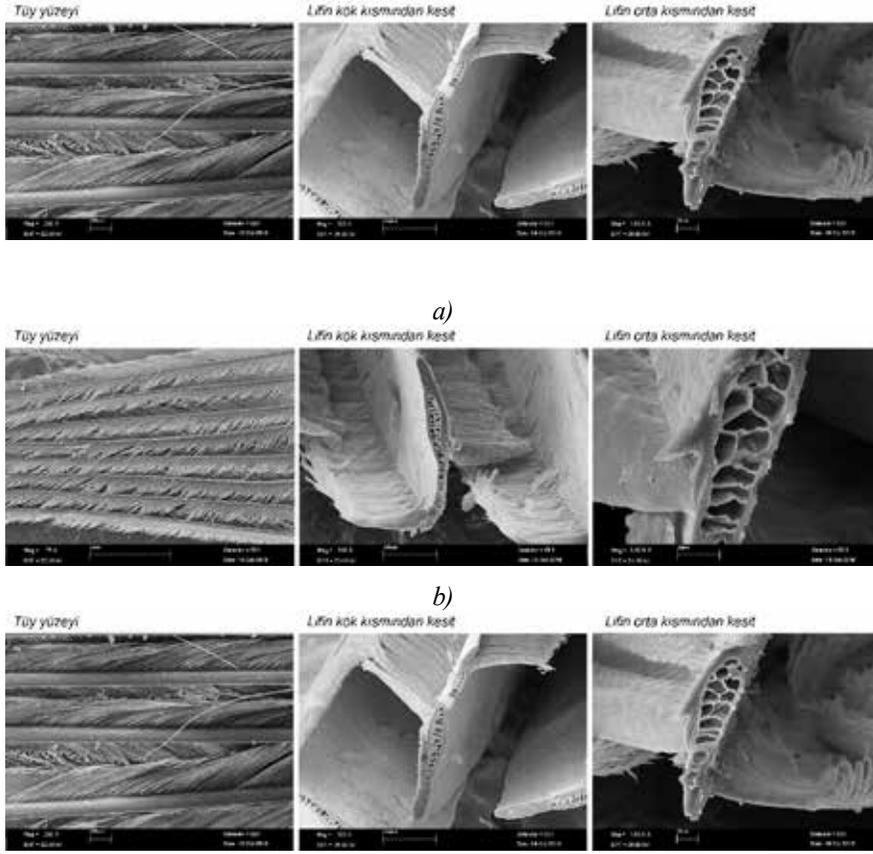
Figure 7. Surface and cross-sectional images of the fibers, which were produced from feathers (washed with Verolan SSA and NaCIO)

In Figure 8, there is a surface and cross-section images of fibers, which were obtained from feathers washed with Setalan IK 30, and in Figure 9, there is a surface and cross-section images of fibers, which were obtained from feathers washed with Setawash PY Conz are shown. The fibers in Figure 8a and Figure 9a were produced from feathers, which were washed with Program1 and the fibers in Figure 8b and Figure 9b were produced from feathers, which were washed with Program 2. When compare the Figure 6, 7, 8 and 11 with each others, it is seen that the best result is obtained with Rucoges Yes in terms of cleaning and protection of the surface structure of the fibers. It has seen that the fibers produced from washed feathers were cleaned from the dirt and oil particles and it has proven that there was no demostration in surface and cross-sectional appearence of fibers.
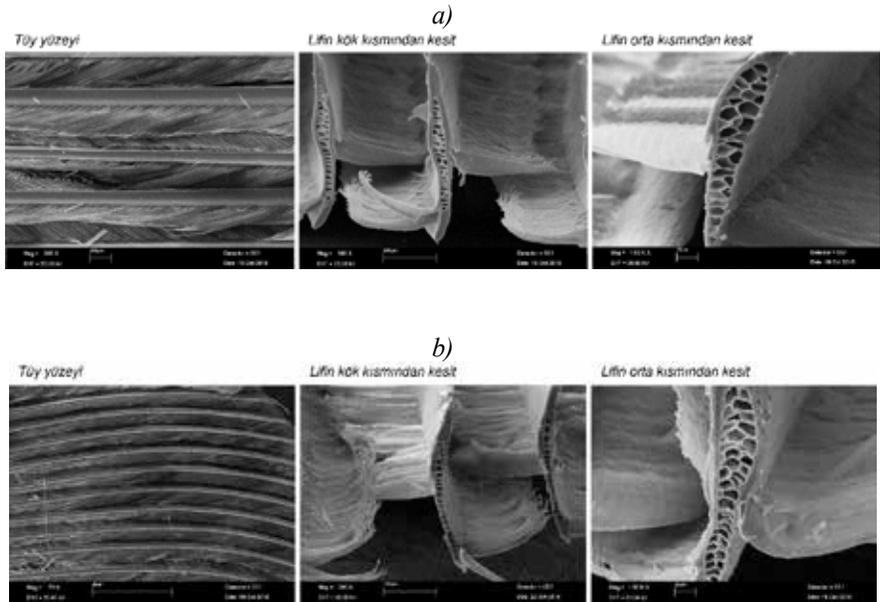
Figure 8. Surface and cross-section images of fibers, which were produced from feathers   (washed with Setalan IK 30 and NaCIO)
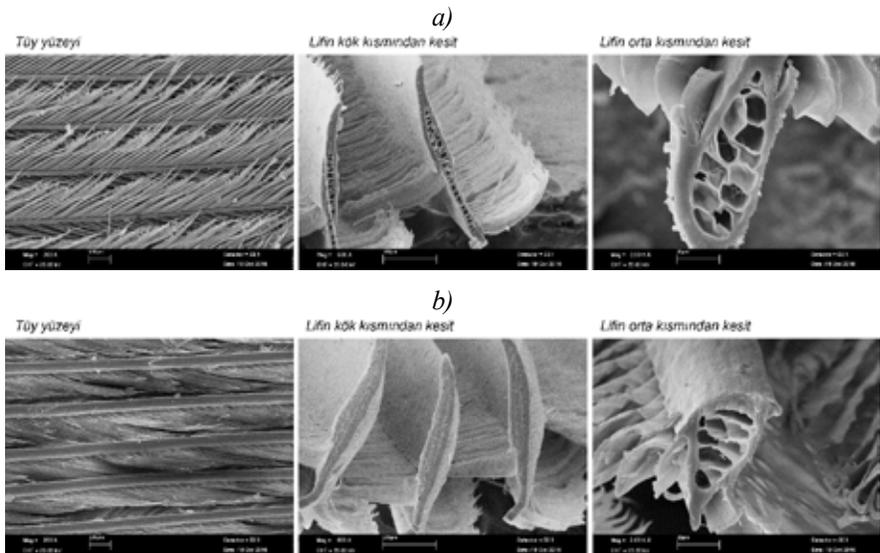

Figure 9. Surface and cross-section images of fibers, which were produced from feathers (washed with Setawash PY Conz and NaCIO)

The properties in the SEM images are shown in Table 3 in order to detter illustrate how the washing substance and washing program effect the internal structure of feathers. Taking in to consideration the images in

Figure 3-9 and the evaluations in Table 3, it is suggested that the Rucogen Yes washing substance and 1st washing program be preferred in order to maintain the surface and internal structure of the fibers during washing.

Table 3. Analysis of SEM images of fiber sections before and after washing

Washing substance	Washing program	The state of the surface and internal structure of fibers obtained from washed feathers					
		Dirt particles	Oil particles	Surface deterioration	Internal structure deterioration at the fiber root part	Internal structure deterioration at the fiber middle part	Pore narrowing
Unwashed		Much	Much	Not	Not	Not	Not
Washed with water		Much	Much	Not	Not	Not	Not
Rucogen Yes	1	Very little	Very little	Not	Not	Not	Not
	2	Little	Little	Not	Not	Not	Not
Verolan SSA	1	Very little	Very little	Not	Medium	Not	Little
	2	Little	Little	Not	Medium	Medium	Medium
Setalan IK 30	1	Very little	Little	Little	Little	Not	Very little
	2	Very little	Medium	Medium	Medium	Little	Little
Setawash PY Conz	1	Little	Little	Medium	Medium	Not	Medium
	2	Very little	Very little	Medium	Much	Little	Medium

3.2. Investigation of the effects of washing process on the mechanical properties of the produced fibers

Tensile test were performed on different fibers, which washed with different washing materials at different washing program and cutten from feathers, to determine how the washing materials and washing programs affect the mechanical properties of the fibers and results of tests are given in Table 4.

Table 4. Pull-out test results of fibers, which were obtained from chicken feathers (washed with different washing substance and cutten)

Washing substance	Washing substance	Breaking strength, N	Max. Stress, N/mm²	Break length, mm
Unwashed feathers		0,30549	0,38897	0,53833
		0,15259	0,19428	0,34954
		0,29580	0,37662	0,62038
		0,37193	0,47356	0,63673
		0,34285	0,43653	0,87929
Rucogen Yes	Washing process with Program 1	0,68426	0,87123	0,57727
		0,56076	0,71398	0,72694
		0,41962	0,53427	0,67550
		0,32711	0,41649	0,37904
		0,55313	0,70427	0,55783
	Washing process with Program 2	0,60383	0,76883	0,86356
		0,51053	0,65003	0,74296
		0,40436	0,51484	0,79813
		0,54169	0,68970	0,88490
		0,52452	0,66784	0,72917
Verolan SSA	Washing process with Program 1	0,60081	0,76498	0,83717
		0,46825	0,59620	0,51733
		0,50306	0,64052	0,92119
		0,50036	0,63708	0,48900
		0,69793	0,88863	0,97023
	Washing process with Program 2	0,62227	0,79230	0,68188
		0,45697	0,58183	0,74265
		0,41914	0,53367	0,79963
		0,59779	0,76114	0,88760
		0,48701	0,62008	0,68238
Setalan IK 30	Washing process with Program 1	0,30613	0,38978	0,42821
		0,35922	0,45737	0,58640
		0,50116	0,63809	0,58033
		0,36208	0,46101	0,60733
		0,27482	0,34991	0,60960
	Washing process with Program 2	0,34142	0,43470	0,45869
		0,23158	0,29486	0,46063
		0,27561	0,35092	0,67233
		0,33490	0,42641	0,71294
		0,28292	0,36023	0,68494
Setawash PY Conz	Washing process with Program 1	0,28054	0,35719	0,57504
		0,40150	0,51120	0,61948
		0,37543	0,47801	0,70690
		0,30295	0,38573	0,85652
		0,20631	0,26268	0,54877
	Washing process with Program 2	0,22157	0,28211	0,72583
		0,16149	0,20561	0,57202
		0,20901	0,26612	0,62781
		0,15529	0,19772	0,56835
		0,18819	0,23961	0,58977

In order to able to perform a multiple comparison test on the tensile strength values of the fibers from the data in Table 4, the data distribution in the data groups should be normal, the variances on groups should be homogeneous. The normality of data distributions in the data groups which contains tensile strength values of the fibers produced from feathers washed with different washing substance and washing program was evaluated according to the Ryan-Joiner test and it was seen that the data were distributed normally (Table 5).

Table 5. Test results of normality of distribution according to data groups

Groups	Ryan-Joiner test	Result
Unwashed feathers	$N = 5$, $RJ = 0,962$, $P > 0,100$	Normal distribution
Washed feather according to RY-1	$N = 5$, $RJ = 0,960$, $P > 0,100$	Normal distribution
Washed feather according to RY-2	$N = 5$, $RJ = 0,957$, $P > 0,100$	Normal distribution
Washed feather according to VSSA-1	$N = 5$, $RJ = 0,955$, $P > 0,100$	Normal distribution
Washed feather according to VSSA-2	$N = 5$, $RJ = 0,961$, $P > 0,100$	Normal distribution
Washed feather according to SIK-1	$N = 5$, $RJ = 0,971$, $P > 0,100$	Normal distribution
Washed feather according to SIK-2	$N = 5$, $RJ = 0,966$, $P > 0,100$	Normal distribution
Washed feather according to SPY-1	$N = 5$, $RJ = 0,984$, $P > 0,100$	Normal distribution
Washed feather according to SPY-2	$N = 5$, $RJ = 0,961$, $P > 0,100$	Normal distribution

The homogeneity of the variances was tested according to the Levene criterion and the variances were found to be of the same type (Table 6).

Table 6. Test results of homogeneity of variances

```
Method
Null hypothesis        All variances are equal
Alternative hypothesis At least one variance is different
Significance level     α = 0,05

95% Bonferroni Confidence Intervals for Standard Deviations

C11  N    StDev           CI
 1   5  0,0548086  (0,0092209; 0,73140)
 2   5  0,0687021  (0,0111788; 0,94793)
 3   5  0,0723450  (0,0114326; 1,02779)
 4   5  0,0592306  (0,0190893; 0,41261)
 5   5  0,0890052  (0,0291898; 0,60930)
 6   5  0,0746218  (0,0151418; 0,82563)
 7   5  0,0454866  (0,0117397; 0,39568)
 8   5  0,0778886  (0,0189616; 0,71831)
 9   5  0,0534969  (0,0086243; 0,74502)

Individual confidence level = 99,4444%

Tests
                         Test
Method              Statistic  P-Value
Multiple comparisons     —      0,795
Levene                  0,32    0,951
```

The results of the TYANOVA administered after all the conditions for the analysis of variance of group data are given in Table 7

Table 7. Dunnett test and TYANOVA results

```
One-way ANOVA: Kontrol; RY-1; RY-2; VSSA-1; VSSA-2; SIK-1; SIK-2; SPY-1; SPY-2

Method
Null hypothesis        All means are equal
Alternative hypothesis  At least one mean is different
Significance level     α = 0,05

Equal variances were assumed for the analysis.

Factor Information
Factor  Levels  Values
Factor       9  Kontrol; RY-1; RY-2; VSSA-1; VSSA-2; SIK-1; SIK-2; SPY-1; SPY-2

Analysis of Variance
Source  DF  Adj SS  Adj MS  F-Value  P-Value
Factor   8  0,6921  0,086519   19,01    0,000
Error   36  0,1638  0,004550
Total   44  0,8560

Model Summary
      S   R-sq  R-sq(adj)  R-sq(pred)
0,0674570  80,86%    76,61%      70,10%

Means
Factor   N   Mean   StDev      95% CI
Kontrol  5  0,3117  0,0548  (0,2505; 0,3729)
RY-1     5  0,5770  0,0687  (0,5158; 0,6382)
RY-2     5  0,5170  0,0723  (0,4558; 0,5782)
VSSA-1   5  0,5381  0,0592  (0,4770; 0,5993)
VSSA-2   5  0,5166  0,0890  (0,4555; 0,5778)
SIK-1    5  0,3905  0,0746  (0,3293; 0,4517)
SIK-2    5  0,2933  0,0455  (0,2321; 0,3545)
SPY-1    5  0,3133  0,0779  (0,2522; 0,3745)
SPY-2    5  0,2142  0,0535  (0,1530; 0,2754)

Pooled StDev = 0,0674570

Dunnett Multiple Comparisons with a Control

Grouping Information Using the Dunnett Method and 95% Confidence
Factor              N   Mean  Grouping
Kontrol (control)   5  0,3117  A
RY-1                5  0,5770
VSSA-1              5  0,5381
RY-2                5  0,5170
VSSA-2              5  0,5166
SIK-1               5  0,3905  A
SPY-1               5  0,3133  A
SIK-2               5  0,2933  A
SPY-2               5  0,2142  A

Means not labeled with the letter A are significantly different from the control level mean.
```

As can be seen from Table 7, some washing substances significantly affect the tensile testing results of the fibers. According to the results of the multiple comparison test, the values of the tensile strength of the fibers produced from the feathers washed according to the two washing program with using Setalan IK30 and Setavash PY Conz washing substances are not statistically different from the values of the tensile strength of the fibers produced from unwashed feathers. This means that washing process conducted with this washing substances has not significantly affected the breaking strength of the feather fibers.
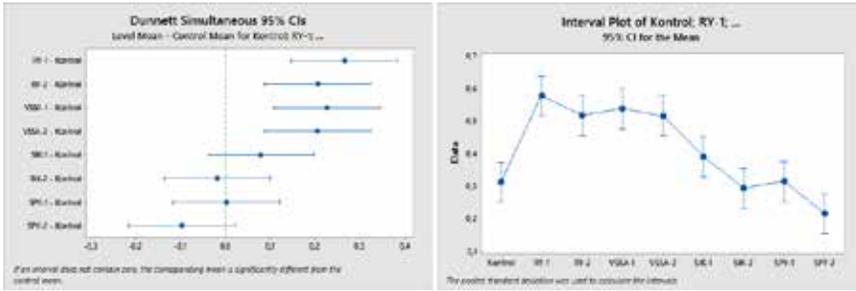
Figure 10. Multiple comparison test results

It is seen that washing process conducted with using the Rucegen Yes and Verolan SSA washing substance have significantly affected the breaking strength of the fibers. Washing conducted with using of Rucogen Yes according to the Program 1 was more effective and the tensile strength of these fibers were increased at the end of the this washing process. This is probably its result that some bonds between the molecules forming the fibers are broken off by the actionf of sodium hypochlorite before washing and reconstituted during washing. According to the results in Table 7, washing with Program 1 was better than washing with Program 2 in all cases. The same results can be seen from the pictures in Figure 6-9. In our opinion, this is the results of fibers that were much cleaned with washing being more affected by sodium hypochlorite.

3.3. Research results on the determination of the amount of washing substances

Washing were performed according to the 3-Level Factorial experiment plan designed using the Design Exper 11 program to determine the optimal values of the washing substance concentration in the washing solutions. SEM analysis of fiber surface and fiber sections produced from washed feathers and tensile test were performed to fibers. The average values of test results is given in test plan is Table 8.

Table 8. Mucti-factorial experimental design and results

	Std	Run	Factor 1 A:The amount of NaClO % (v/v)	Factor 2 B:The amount of washing agent % (v/v)	Response 1 Breaking strength 0,001N	Response 2 Max. Stress kPa	Response 3 Break length 0,001m
	4	1	0,20	0,40	474,49	604,132	0,58
	9	2	0,60	0,60	168,128	239,324	0,198
	12	3	0,40	0,40	574,59	731,59	0,79
	2	4	0,40	0,20	606,154	771,782	0,69
	10	5	0,40	0,40	527,86	672,09	0,62
	11	6	0,40	0,40	560,28	713,33	0,66
	1	7	0,20	0,20	509,368	648,543	0,648
	5	8	0,40	0,40	546,424	695,729	0,566
	7	9	0,20	0,60	414,748	528,07	0,496
	6	10	0,60	0,40	465,966	593,285	0,58
	3	11	0,60	0,20	627,042	798,372	0,788
	13	12	0,40	0,40	596,21	759,11	0,71
	8	13	0,40	0,60	364,746	464,412	0,596

As a results of statistical analyses of the test results, a second-order regression model was obtained for each dependent variable. The model was tested with Fisher criteria and found significant. The resuts of variance analysis for models are given in Table 8.

Table 9. ANOVA table of test results

As can be seen from Table 9, each three dependent parameters are significantly affected by the test factors. However, some terms of models that express the dependence of the these parameters from factors are meaningless in the chosen field of experimentatiton (the terms with "Prob>F" value above 0,05 are meaningless). In this respect, term of A is meaningless, term of B is meaningfull in all three models. We can see which terms is more effective by looking at the S2 values of the indivual model terms. Based on the experimental results, the solution of the optimizatiın problem, which is performed as maximization of the dependent parameter, is given in Table 10. The reaction surfaces and the optimum point of output parameters can be seen in Figure 11.

Table 10. Solution of optimization problem

Constraints

Name	Goal	Lower Limit	Upper Limit	Lower Weight	Upper Weight	Importance
A:The amount of NaClO	is in range	0,2	0,6	1	1	3
B:The amount of washing agent	is in range	0,2	0,6	1	1	3
Breaking strength	maximize	188,128	627,042	1	1	3
Max. Stress	maximize	239,534	798,372	1	1	3
Break length	maximize	0,198	0,79	1	1	3

Solutions
84 Solutions found

Number	The amount of NaClO	The amount of washing agent	Breaking strength	Max. Stress	Break length	Desirability	
1	0,462	0,215	638,655	813,162	0,791	1,000	
2	0,485	0,215	639,518	814,261	0,790	1,000	
3	0,470	0,200	642,998	818,692	0,798	1,000	
4	0,484	0,202	643,367	819,161	0,797	1,000	
5	0,455	0,211	638,873	813,440	0,792	1,000	
6	0,433	0,207	636,371	810,255	0,790	1,000	
7	0,480	0,200	643,644	819,515	0,798	1,000	Selected
8	0,509	0,203	642,422	817,944	0,793	1,000	

It can be seen that the best washing results are obtained in washing solutions conducted with 0,2% washing substance according to water volume and 0,48% of sodium hypochloriteWashing in this solution should give good results in terms of the mechanical parameters of the fibers. The tensile strength of the fibers washed in solution of 0,2% Rucogen Yes and 0,48% HCIO solution at Program 1 should be thereoretically 0,644N, maximum tension should be 819,515KPa and breaking extension should be 0,798mm. The surface and cross-sectional SEM images obtained fibers at the end of these washing are given in Figure 12.
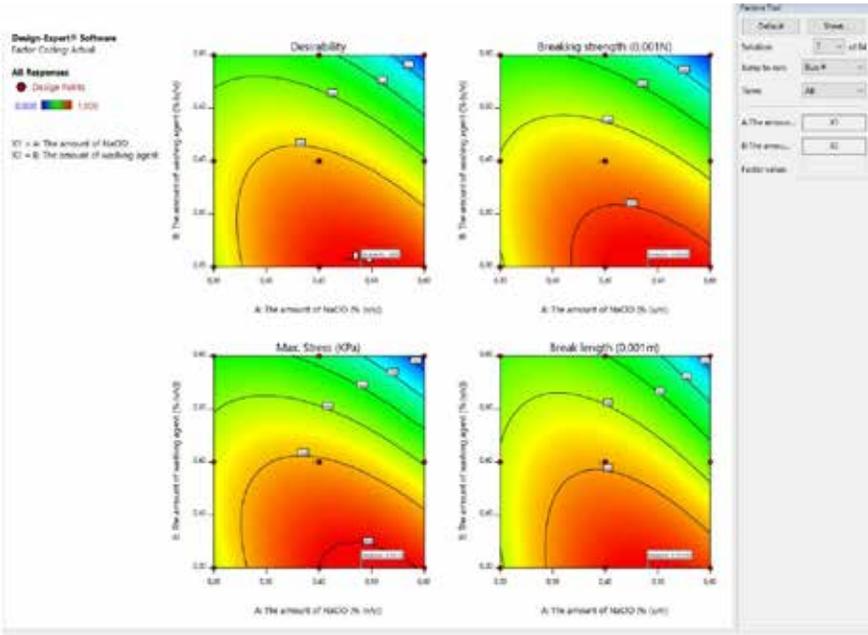

*Figure 11. Response surfaces of dependent variables according to the factors*
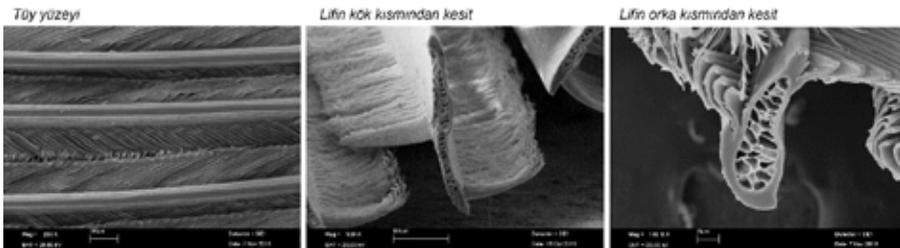
Figure 12. Surface and cross-section images of fibers obtained from feathers washed in optimal conditions

When compare the images in Figure 12 with images in Figure 6…9, it is seen that washing process in solutions having concentrations determined from both the cleaning of the fibers and protection of surfaces and the internal structures gives better results. The effects of individual factors to the output parameters can be seen from the graphs in Figure 13.
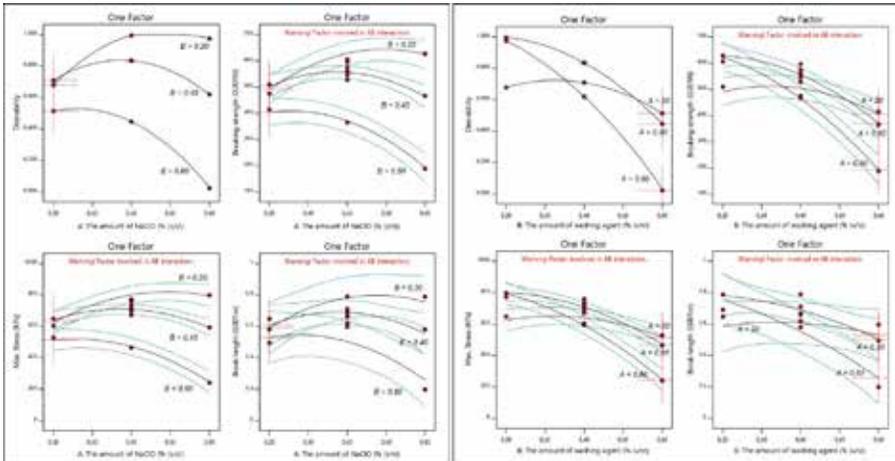

Figure 13. The effects of individual factors to the output parameters

As can be seen in Figure 13, values of the mechanical properties of the fibers produced from the washed feathers rise up at first, then fall off as a result of increase the NaCIO in the prewashing solution at factor B (the ratio of the washing substance in washing solution) of low, medium and high value. The values of the mechanical properties of the fibers fall off at the end of increasing the rate of washing substance in main washing solutions at factor A (the ration of NaCIO in pre-washing solution) of low, medium and high value.

4. CONCLUSIONS

This study was carried out in order to protect as much as possible the surface and internal structure and properties of chicken feather fibers which are obtained from feathers during the washing process of chicken feathers. During the investigations, it was found that the washing temperature of feathers affected the surface structure and the internal structure of the fibers obtained from these feathers. Thus, although there is cleaner washed material is obtained at high temperatures, the surface structure and the internal structure of the fibers may deteriorate and this danger increases with increasing temperature. Studies have shown that that the bath temperature for chicken feathers should be below 50ºC as

in other protein-based fiber. In our next studies, this temperature was accepted as 40ºC. It has found that the materials used for washing and disinfecting can affect the cleaning properties and mechanical properties of the fibers. Nonionic and cationic washing substances were used as a washing material and the best washing results were obtained with nonionic washing substance which as a Ph value of 6.0-7.0 and contain property of oil solubility.

Based on previous studies, sodium hypochlorite has been chosen which is cheap and effective. With the use of disinfectant material, the washing process was carried out in two programs which have a two phases. According to the results of analysis of the washing results, it was determined that the washing program, which has contain 20 minutes pre-washing, rinsing and squeezing in 0,48% of sodium hypochlorite solution, gave much better results than the washing program which has contain 1 hour main-washing, rinsing and squeezing in 0,2% water substance solution. Washing of feathers under these conditions allows to maintain the protective of surface and microporous microstructure of fibers. At the same time, it allows that the properties of tensile strength and elongation can be improved according to unwashed feathers.

REFERENCES

1. Alonso, R.S., R. Sanches and J.P. Marcicano. (2013). Chicken feather - Study of physical properties of textile fibers for commercial use. *International Journal of Textile and Fashion Technology*, 3(2), 29-38.

2. Amieva, E.J.C, C. Velasco-Santos, A.L. Martinez-Hernandez, J.L. Rivera-Armenta, A.M. Mendoza-Martinez and V.M. Castano. (2014). Composites from chicken feathers quill and recycled polypropylene. *Journal of Composite Materials*, 49(3), 275-283.

3. Arunkumar, C., Megwal, H.S., Borkar S.P., Bhongade, A.L. (2013). Recycling of Chicken Feather and Wool Fibre Waste into Reinforced Multilayer Composite - A Review, *Technical Textile*, *Jornal of the Textile Association*, 2, 371-378.

4. Canpolat, I. (2013). *Graft Copolymerization into Chicken Feather Keratin*. Thesis for the Degree Doctor of Philosophy. İTÜ, İstanbul.

5. Cervantes-Gonzalez, E., L.I. Rojas-Avelizapa, R. Cruz-Camarillo, J. Garcia-Mena and N.G. Rojas-Avelizapa. (2008). Use of chicken feathers and shrimp waste as sorbents on biodegradion of petroleum hydrocarbons. *Haz Waste Management,*3

6. Cesur, N. (2010). *Removal of Heavy Metal İons from Aqueous Solutions by Chemically Modified Chicken Feather*. Thesis for the Degree Doctor of Philosophy. EÜ, İzmir.

7. Chinta S.K., Landage S.M., Yadav Krati. (2013).Application of Chicken Feathers inTechnical Textiles. *International Journal of Innovative Research in Science, Engineering and Technology*, 2(4), 1158-1165

8. Coward-Kelly, G., V.S. Chang, F.K. Agbogbo and M.T. Holtzapple. (2006). Lime treatment of keratinous materials for the generation of highly digestible animal feed: 1. Chicken feathers. *Bioresource Technology* 97(11), 1337-1343

9. Fan, X. (2008). *Value-added Products From Chicken Feather Fibers and Protein*. Thesis for the Degree Doctor of Philosophy. Auburn University, Alabama.

10. Ghani, S.A., M.H. Jahari and Tan Soo-jin. (2014). Effects of sodium hydroxide treatment on the properties of low-density polyethylene composites filled with chicken feather fiber. *Journal of Viny & Additive Technology* 20(1), 36-41.

11. Jagadeeshgouda, K.B., P.R. Reddy and K. Ishwaraprasad. (2014). Experimental study of behaviour of poultry feather fiber - a reinforcing material for composites. *International Journal of Research in Engineering and Technology* 3(2), 362-371

12. Jones L. N., Riven D. E., Tucker DJ. (1998). *Handbook of Fiber Chemistry*, Marcel Dekker, Inc., New York, 147-149

13. Kiew, K.S., S. Hamdan and Md.R. Rahman. (2013). Comparative study of dielectric properties of chicken feather/kenaf fiber reinforced unsaturated polyester composites. *BioResources* 8(2), 1591-1603.

14. Kock, J.W. (2006). *Physical And Mechanical Properties Of Chicken Feather Materials.* Thesis for the Degree Master of Science. Georgia Institute of Technology, Atlanta.

15. Lam, P.M., K.T. Lau, Y.Q. Zhao, S. Cheng and T. Liu. (2009). Development of an eco-friendly CFF/PLA biocomposite. *ICCM 17th International Conference on Composite Materials,* Edinburgh, UK

16. Martinez-Hernandez, A.L., C. Velasco-Santos, M. De Icaza and V.M. Castano. (2005). Microstructural characterisation of keratin fibres from chicken feathers. *International Journal of Environment and Pollution* 23(2), 162-178.

17. Martínez-Hernández A.L., Velasco-Santos C. (2012).Keratın Fıbers From Chıcken Feathers: Structure And Advances In Polymer Composıte. *Keratin: Structure, Properties and Applications*. Editors: Dullaart R. et al. Nova Science Publishers, Inc. N.Y., 149-211.

18. Menandro, N. Acda. (2010). Waste Chicken Feather as Reinfocement in Cement-Bonded Composites. *Philippine Journal of Science* 139 (2), 161-166.

19. Moore, G.R.P., S.M. Martelli, C.A. Gandolfo, A.T.N. Pires and J.B. Laurindo. (2012). Queratina de Penas de Frango: Extração, Caracterização e Obtenção de Filmes. *Ciência e Tecnologia de Alimentos* 26(2), 421- 427.

20. Patent US5705030. (1998). Fiber and fiber products produced from feathers.

21. Reddy N., Yang Y. (2007). Structure and Properties of Chicken Feather Barbs as Natural Protein Fibers. *Journal of Polymers and the Environment*. 15, 81–87

22. Rosa, G., H.E. Reynel-Avila, A. Bonilla-Petriciolet, I. Cano-Rodríguez, C. Velasco-Santos and A.L. Martínez-Hernández. (2008). Recycling poultry feathers for Pb removal from wastewater: Kinetic and equilibrium studies. *World Academy of Science, Engineering and Technology* 2(11), 323-331.

23. Saravanan, K. (2012). Exploration on amino acid content and morphological structure in chicken feather fiber. *Journal of Textile and Apparel Technology and Management* 7(3), 1-6.

24. Sayed, S.A., S.M. Saleh and E.E. Hasan. (2005). Removal of some polluting metals from industrial water using chicken feathers. *Desalination* 181(1–3), 243-255.

25. Tiwary, E. and R. Gupta. (2012). Rapid conversion of chicken feather to feather meal using dimeric keratinase from bacillus licheniformis ER-15. *Bioprocessing & Biotechniques* 2(4), 2-6.

26. Tseng, F-C.J. and C.J.R. Verbeek (2011). Biofibre production from chicken

feather. *Paper presented at SCENZ-IChemE annual conference in New Zealand, University of Waikato, New Zealand;* 1-2 December

27. Uzun, M., E. Sancak, I,P. Usta, M Akalın and M. Yuksek. (2011). Mechanical behaviour of chicken quills and chicken feather fibres reinforced polymeric composites. *Archives of Materials Science and Engineering* 52(2), 82-86.

28. Wrześniewska-Tosik, K. and J. Adamiec. (2007). Biocomposites with a content of keratin from chicken feathers. *Fibres & Textiles in Eastern Europe* 15(1), 106-112.

29. Wrześniewska-Tosik, K., M. Szadkowski, M. Marcinkowska and M. Pałczyńska. (2012). Chicken feather-containing composite non-wovens with barrier properties. *Fibres & Textile in Eastern Europe* 20(6B), 96-100.

30. Ye, W., R.M. Jr. Broughton and J.B. Hess. (1999). Chicken feather as a fiber source for nonwoven insulation. *International Nonwovens Journal* 8(1), 112-120.
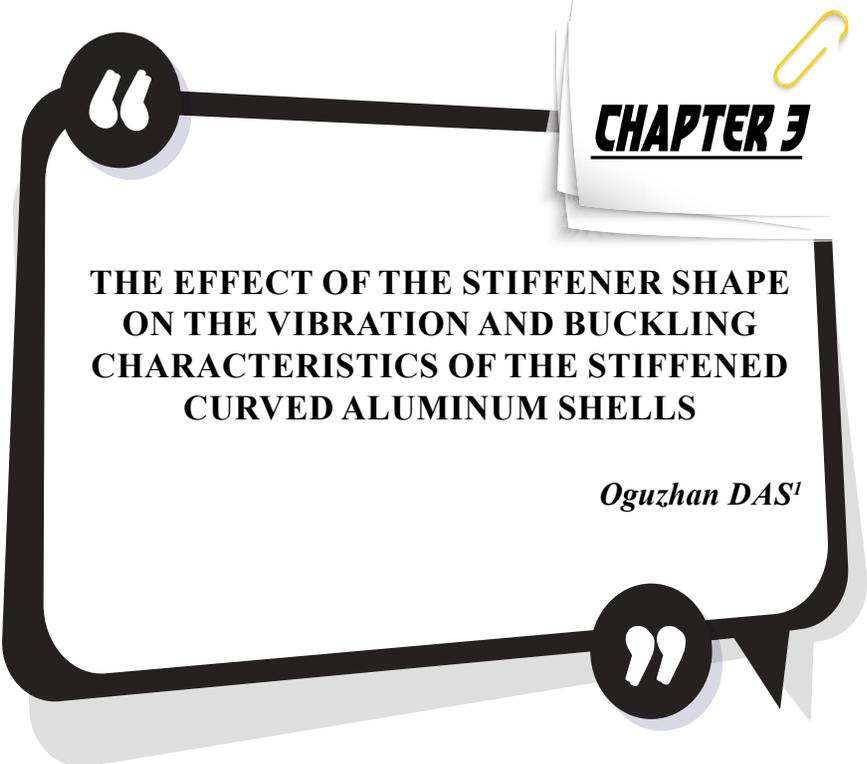
THE EFFECT OF THE STIFFENER SHAPE ON THE VIBRATION AND BUCKLING CHARACTERISTICS OF THE STIFFENED CURVED ALUMINUM SHELLS

Oguzhan DAS[1]

1 Assist. Prof. Dr., National Defence University, Air Force NCO Higher Vocational School, Gaziemir, Izmir, Türkiye, ORCID: 0000-0001-7623-9278

1. Introduction

Thin-walled structures are widely utilized in various fields of engineering due to satisfy to obtain low structural weight. However, in some cases, they are prone to be affected adversely by dynamic loads or buckling, which may lead them to ultimate failure. Stiffened shells enabled researchers and engineers to both eliminate such a negative aspect and keep the structural weight at a low level. A stiffened shell is mainly composed of beams that are connected to a shell. The shape of the cut section, the number, and the orientation of those beams vary depending on the purpose of usage. To obtain the best design for a specific task, various studies were conducted comprising the vibration or buckling behavior of stiffened structures under different circumstances.

Sahoo & Barik (2020) conducted free vibration analyses of stiffened plates to understand the vibration behavior of those structures considering different sizes, shapes, orientations, boundary conditions, and disposition. Jafarpour & Khedmati (2020) utilized conventional and super finite element methods to perform free vibration analysis of stiffened plates with initial geometric imperfections. Ton-That (2021) presented a new C0 third-order shear deformation theory to understand the non-linear free vibration characteristics of functionally graded stiffened plates. Damnjanović et al. (2017a) investigated the vibrational behavior of stiffened cracked laminated composite plate structures by employing higher-order shear deformation theory and first-order shear deformation theory. They examined the transverse shear deformation, side-to-thickness ratios, boundary conditions, reinforcement amount, and crack length on the vibration characteristics of such structures. Damnjanović et al. (2017b) proposed an alternative method, namely the dynamic stiffness method (DSM) to conduct free vibration analysis of stiffened composite plates. They utilized DSM-based higher-order shear deformation theory to understand the vibrational characteristics of those structures. The validity of the proposed approach was performed by comparing the results with existing analytical studies and the Finite Element Method-based results. Cho et al. (2016) analyzed the vibrational behavior of stiffened panels with multiple lumped attachments. For this purpose, they employed the assumed mode method. They found that the proposed method is accurate and applicable when comparing the results with those of existing studies and the results of the Finite Element Analysis. Sadamoto et al. (2017) conducted buckling analysis of stiffened plate structures regarding an improved mesh-free flat shell formulation. They approximated the membrane deformations and plate bending by using reproducing kernel particle method. The numerical results indicated that the proposed technique is effective for buckling of perforated and stiffened plates. Huang & Qiao (2020) presented a novel semi-analytical

method to perform buckling analysis of stiffened laminated composite plate structures. They uniquely employed Heaviside to satisfy the variable stiffness of the stiffened structure in two orthogonal directions. They validated their proposed approach by comparing the results with those of the Finite Element Method. Ton-That et al. (2020) employed quadrilateral elements to conduct static and buckling analysis of stiffened plate and curved shell structures. They found that the considered finite element is robust in analyzing the buckling and static behavior of stiffened plates and curved shells. Wang & Qiao (2021) employed the spline finite strip method to conduct buckling analysis of stiffened laminated composite plates subjected to axial compressive loads. For this purpose, they considered the first-order shear deformation theory and thin-walled composite beam theory. They validated of the developed technique by comparing the results with those of existing studies and the numerical results obtained by the Finite Element Method. Zhou et al. (2019) proposed an analytical solution to perform elastic buckling analysis of stiffened panels under pure bending. They replaced the skin's effect on the buckling of the structure with an elastically built-in boundary condition. They measured the effectiveness of the proposed technique regarding the geometry of the panel. Kumar et al. (2018) conducted a comparative analysis to examine the impact of the type, height, width, number, and position of the stiffener on the buckling characteristics of the laminated stiffened composite plate and the effect of the fiber orientation, length-to-thickness ratio, cut-out shape, and layup configuration on an un-stiffened structure. Zhao et al. (2019) investigated the thermal buckling and optimization of the curvilinearly stiffened plates having variable angle tow laminates. They developed a technique in which plate and stiffeners are modeled separately without placing any finite element nodes along the interface between the stiffeners and the plate to join them together. The optimization phase included the maximization of the critical temperature that causes buckling for the stiffened structure.

This study presents the impact of the stiffener shape on the vibration and buckling characteristics of stiffened curved aluminum shells, as shown in Figure 1. For this purpose, the stiffened shells have been designed and analyzed via SolidWorks and ANSYS Workbench. Three different stiffener shapes, namely flat-profile, angle-profile, and T-profile, have been considered. In addition, the impact of the pair-wise combinations of those stiffener profiles has been investigated. To provide an effective meshing, the SHELL181 finite element has been considered since it satisfies the requirements for the thin-walled structures. The impact of the stiffener shape on the vibration of the stiffened structure has been measured considering the first three natural frequencies. As for the boundary conditions, for the free vibration analysis, the stiffened structures have been considered to be

fixed from two straight edges (SE) where the stiffener does not intersect with the structure. For the buckling analysis, the curved structure has been fixed from one of the same ends.
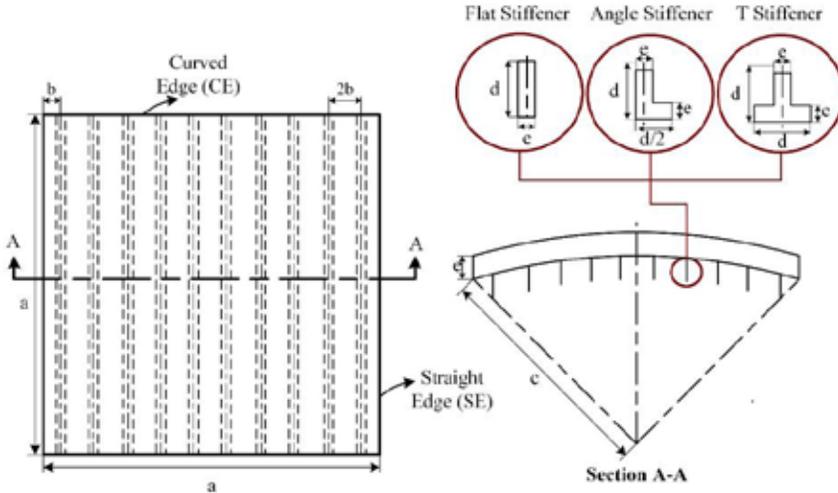
Figure 1: *Stiffened Curved Shell Structures*

2. Structural Design and Analysis

The structural design and numerical analyses have been conducted as follows. First, stiffener shells having three different stiffener profiles have been designed in SolidWorks as shown in Figure 2. Afterward, the models have been imported to ANSYS Workbench for meshing, vibration analyses, and buckling analyses. Aluminum alloy has been considered as the material of the structure. The properties of the aluminum alloy are as follows. $E=71$ GPa, $G=27$ GPa, $v=0.33$, and $\rho=2770$ kg/m^3. As for the mesh parameter, the mesh size has been considered as 1.0 mm. Therefore, resulted in a high mesh quality with a value of 0.9383 where 1.0 is the perfect quality. An illustration of the meshed structure considering the structure with a T-shaped stiffener has been shown in Figure 3.
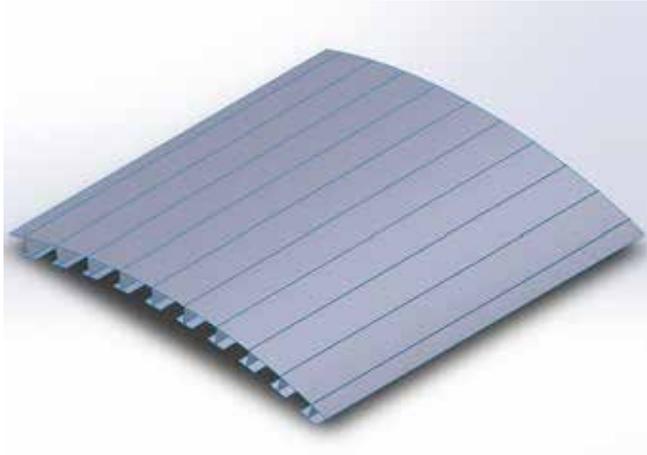
Figure 2: *The SolidWorks Model of the Stiffened Structure with T-Shaped Stiffener*
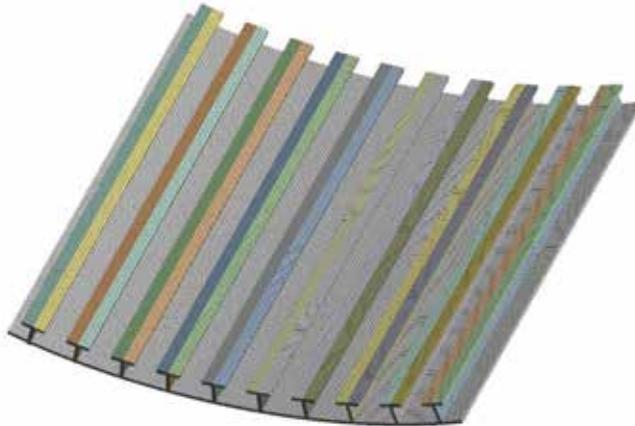
Figure 3: *Meshed Structure*

Following the meshing procedure, for the free vibration analyses, the boundary conditions of the structures have been defined as fixed from two straight edges (SE) where no intersections between the plate and the stiffeners take place. For the eigenvalue buckling analysis, the structure has been fixed from one of the same ends.

Mathematically, the natural frequencies, mode shapes, and the critical buckling load of a structure have been acquired considering the eigenvalue problem given in Eq (1).

$$\left(K + FK_{geo} - \omega^2 M\right)Q = 0 \tag{1}$$

where $\boldsymbol{K}$ is the global stiffness matrix, $\boldsymbol{K}_{geo}$ represents the global geometric matrix, and $\boldsymbol{M}$ is the global mass matrix. F is the compressive load subjecting to the straight edge of the structure, ω is the natural frequencies and $\boldsymbol{Q}$ is the eigenvector that represents the nodal displacement regarding the corresponding vibration mode of the structure. $\boldsymbol{K}$, $\boldsymbol{K}_{geo}$, and $\boldsymbol{M}$ matrices are evaluated by assembling their corresponding local matrices, $\boldsymbol{k}$, $\boldsymbol{k}_{geo}$, and $\boldsymbol{m}$, which can be calculated by using strain energy (U), work done by the load (W), and kinetic energy (T) expressions as follows.

$$U = \frac{1}{2} \int_A \boldsymbol{\varepsilon}^T \boldsymbol{D} \boldsymbol{\varepsilon} dA$$

$$U = \boldsymbol{q}^T \boldsymbol{k} \boldsymbol{q} \tag{2}$$

$$W = \frac{1}{2} \int_A F \left(\frac{\delta w}{\delta x} \right)^2 dA$$

$$W = \boldsymbol{q}^T \boldsymbol{k}_g \boldsymbol{q} \tag{3}$$

$$T = \frac{1}{2} \rho t \int_A (\dot{u}^2 + \dot{v}^2 + \dot{w}^2) dA$$

$$T = \boldsymbol{q}^T \boldsymbol{m} \boldsymbol{q} \tag{4}$$

where ε represents the strain components, $\boldsymbol{D}$ is the matrix of the stiffness of the material, ρ is the density of the material, t denotes the thickness of the structure, u, v, and w represent the displacements in x-, y-, and z- axes respectively, and $\boldsymbol{q}$ is the total degrees of freedom vector of the finite element. The details of those mathematical expressions can be found in various studies and textbooks (Dey & Singha, 2006, Petyt, 2015)

3. Numerical Results

The free vibration analyses have been performed regarding the first three natural frequencies and corresponding mode shapes. Figures 4-6 show the first three mode shapes of the stiffened structures having flat-profile, angle-profile, and T-profile stiffeners. The displacement magnitudes given in the figures are calculated for discussion purposes. They are the multipliers of the eigenvalues not represent the real displacement values during the vibration.
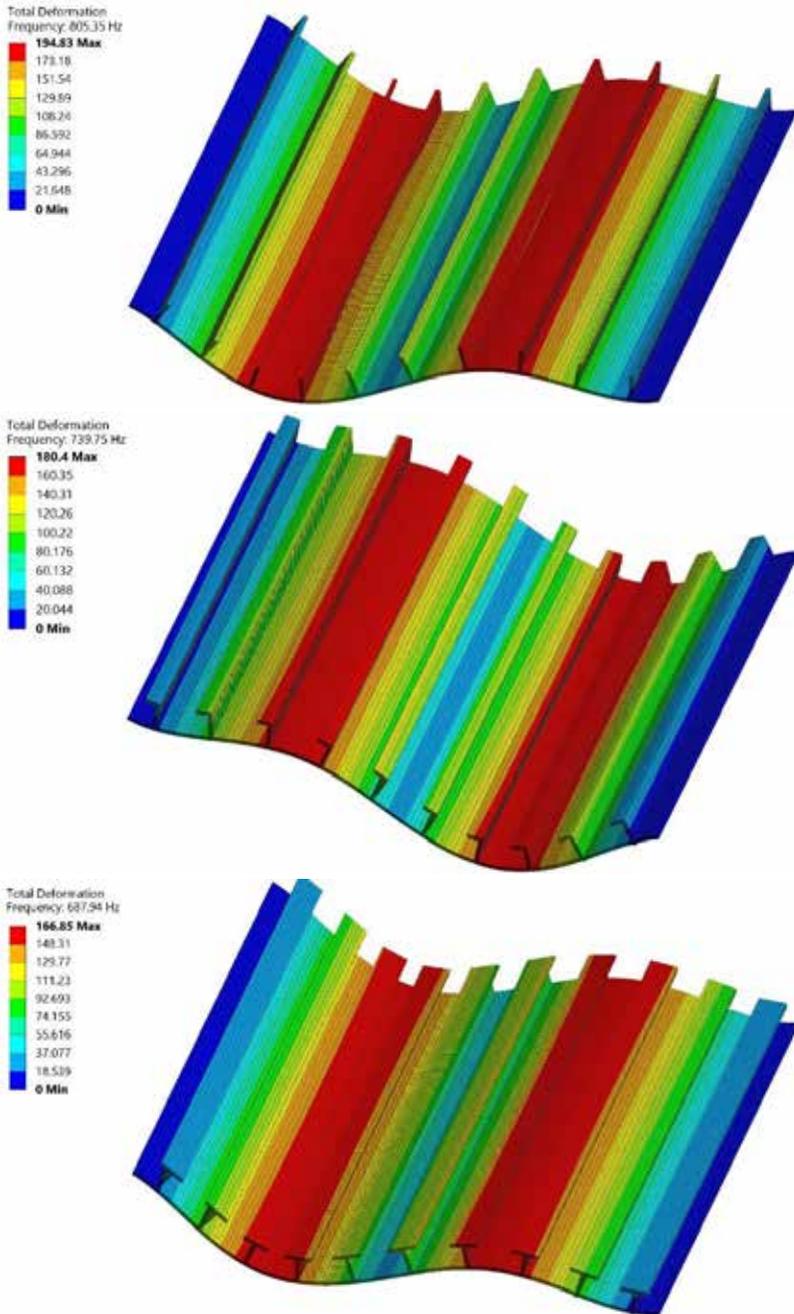
**Figure 4:** *The First Mode Shape of the Stiffened Shells with (a) Flat-Shaped, (b) Angle-Shaped, and (c) T-Shaped Stiffener*
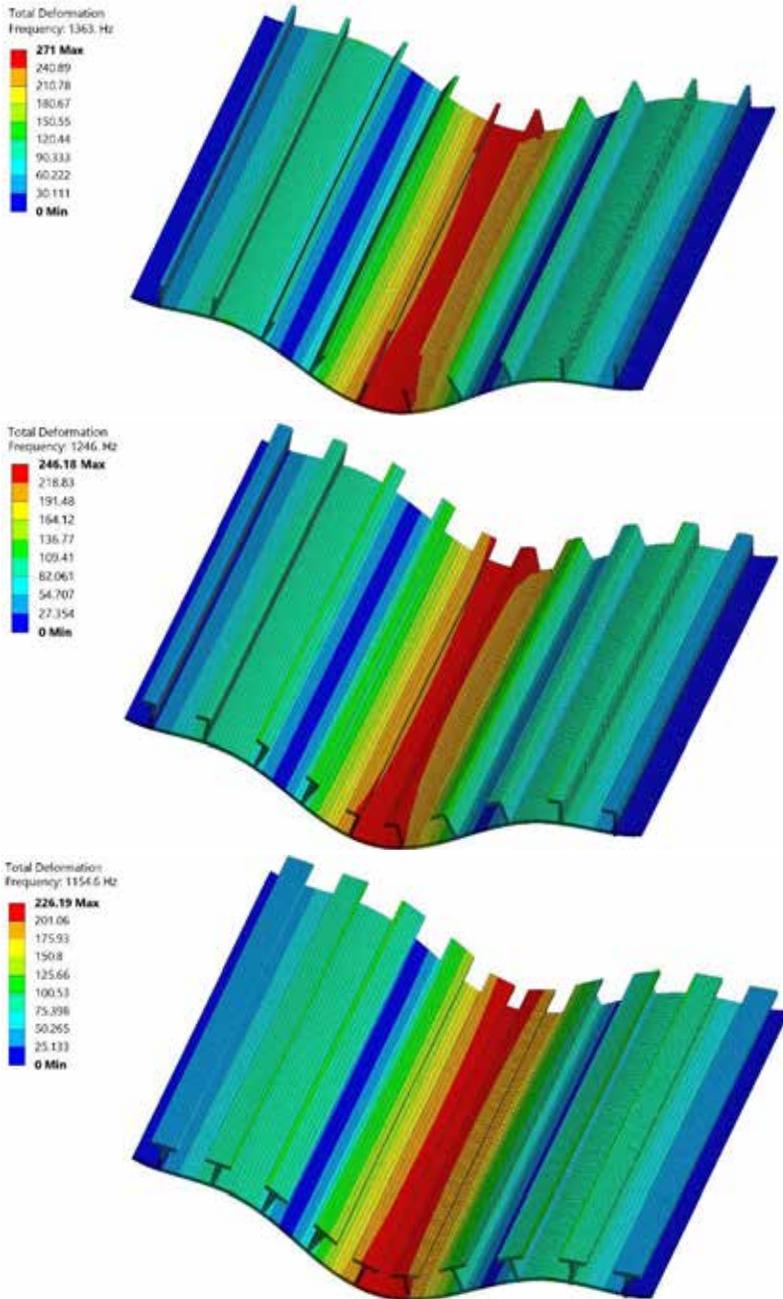
Figure 5: *The Second Mode Shape of the Stiffened Shells with (a) Flat-Shaped, (b) Angle-Shaped, and (c) T-Shaped Stiffener*
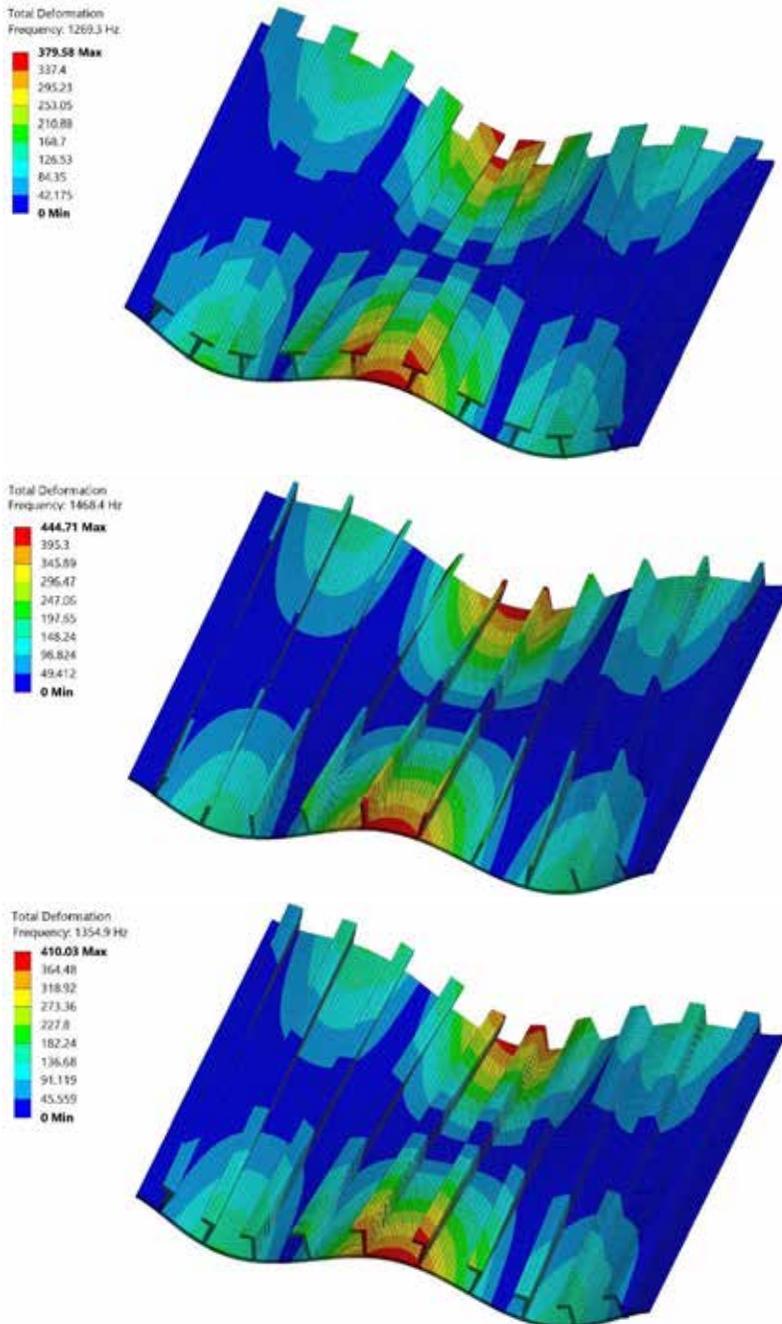
Figure 6: *The Third Mode Shape of the Stiffened Shells with (a) Flat-Shaped, (b) Angle-Shaped, and (c) T-Shaped Stiffener*

As seen in Figures 4-6, the vibrational behaviors of the structures are the same regardless of the stiffener profile. However, the illustrative displacement magnitudes show that the structure with the flat-profile stiffener is the most deformed, while that with the T-profile stiffener is the least. The reason for obtaining such an outcome is the difference between the stiffness characteristics of the structures due to the stiffener shape. Therefore, it can be concluded that using a T-profile stiffener has increased the the structure's stiffness in such a manner that it has not affected the first three modal behavior of the structure, but decreased the displacement for those corresponding modes. Table 1 presents the natural frequencies of the stiffened aluminum shell structures having different stiffener profiles.

Table 1: *The First Three Natural Frequencies of the Stiffened Curved Aluminum Shell Structures Under Fixed From Two Straight Edges Boundary Conditions and Having Different Stiffener Profiles*

Natural Frequency	Stiffener Profile		
	Flat-Shaped	**Angle-Shaped**	**T-Shaped**
1	805.35 Hz	739.75 Hz	687.94 Hz
2	1363.00 Hz	1246.00 Hz	1154.60 Hz
3	1468.40 Hz	1354.90 Hz	1269.30 Hz

It is seen from Table 1 that the highest frequency values have been observed for the structure with a flat-shaped stiffener, while the lowest frequency values have been obtained for that of the T-shaped stiffener. Although the mode shapes indicated that the structure with the T-shaped stiffener is stiffer than others due to the low displacement ratio, the natural frequencies have been obtained lower than the others, while the natural frequencies should have been increased with respect to the increment in the stiffness of the structure. Such an unexpected phenomenon has occurred due to the difference in the mass of the structures. The natural frequency decreases with respect to the increment in mass while it increases when the stiffness of the structure increases. Therefore, it can be interpreted that the difference in the stiffness values of the structures with the flat-shaped stiffener and T-shaped stiffener is lower than the difference in the mass values of those structures.

Figure 7 shows the critical buckling load of the stiffened shell structures with three different stiffener profiles. As seen in Figure 7, all structures have the same displacement distribution (buckling mode) and the same maximum displacement values no matter which stiffener profile they have.
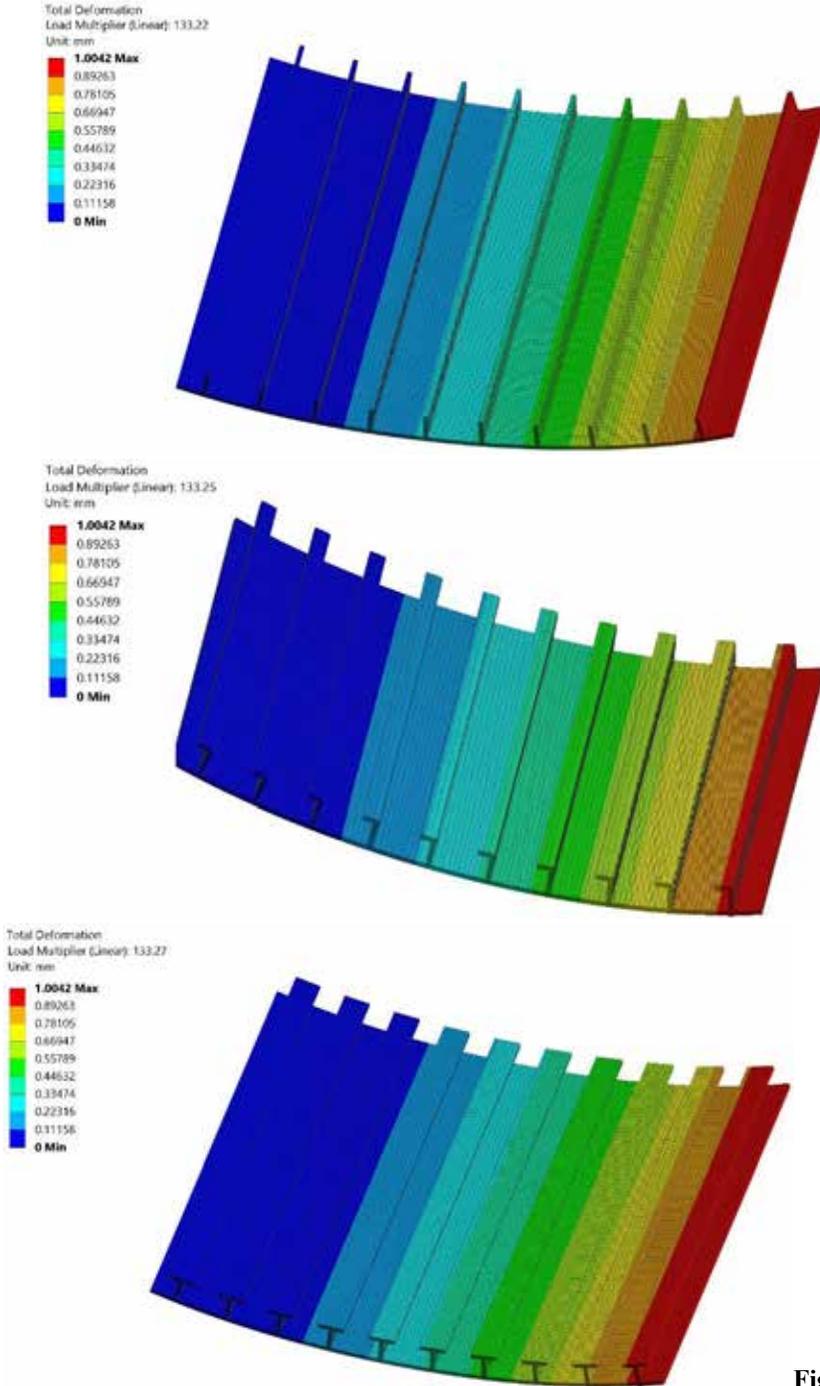
Figure 7: *The Buckling Modes of the Stiffened Shells with (a) Flat-Shaped, (b) Angle-Shaped, and (c) T-Shaped Stiffener*

Table 2 shows the critical buckling load values of the stiffener structures with three different stiffener shapes.

Table 2: *The Critical Buckling Load Values of the Stiffened Curved Aluminum Shell Structures Having Different Stiffener Profiles*

	Stiffener Profile		
	Flat-Shaped	**Angle-Shaped**	**T-Shaped**
Critical Buckling Load (N)	133.22	133.25	133.27

As seen in Table 2, the change in the stiffener profile has a very slight impact on the critical buckling load. Therefore, the structure with the T-shaped stiffener has the highest critical buckling load, while the structure with the flat-shaped stiffener has the lowest one. However, as indicated, the difference is so small (0.05) that it can be neglected. Hence, it can be concluded that the difference in the stiffness of the stiffened curved structure is small when using the angle-shaped or T-shaped stiffener instead of the flat-shaped stiffener. This situation also supports the reason for the decrement in the natural frequencies that have occurred when considering the T-shaped stiffener instead of the flat-shaped stiffener.

In addition to the stiffener orientations considering only flat, angle, and T-shaped stiffener profiles, the orientation regarding symmetrical pair-wise combinations of those stiffener shapes has been also analyzed. Therefore, half of the stiffeners have been modeled considering one type of stiffener profile, while the other half has been designed considering another one. Hence, three different combinations have been obtained. These are represented as flat-angle-shaped, flat-T-shaped, and angle-T-shaped stiffeners. Table 3 presents the first three natural frequencies of the stiffened structures regarding those combinations under fixed from two straight edges boundary conditions. The first three mode shapes of those structures have been shown in Figures 8-10.

Table 3: *The First Three Natural Frequencies of the Stiffened Curved Aluminum Shell Structures Under Fixed From Two Straight Edges Boundary Conditions and Having Different Stiffener Profile Combinations*

Natural Frequency	Stiffener Profile		
	Flat-Angle Shaped	**Flat-Angle Shaped**	**Angle-T Shaped**
1	770.06 Hz	738.64 Hz	711.68 Hz
2	1293.40 Hz	1238.80 Hz	1196.00 Hz
3	1397.10 Hz	1339.90 Hz	1304.30 Hz
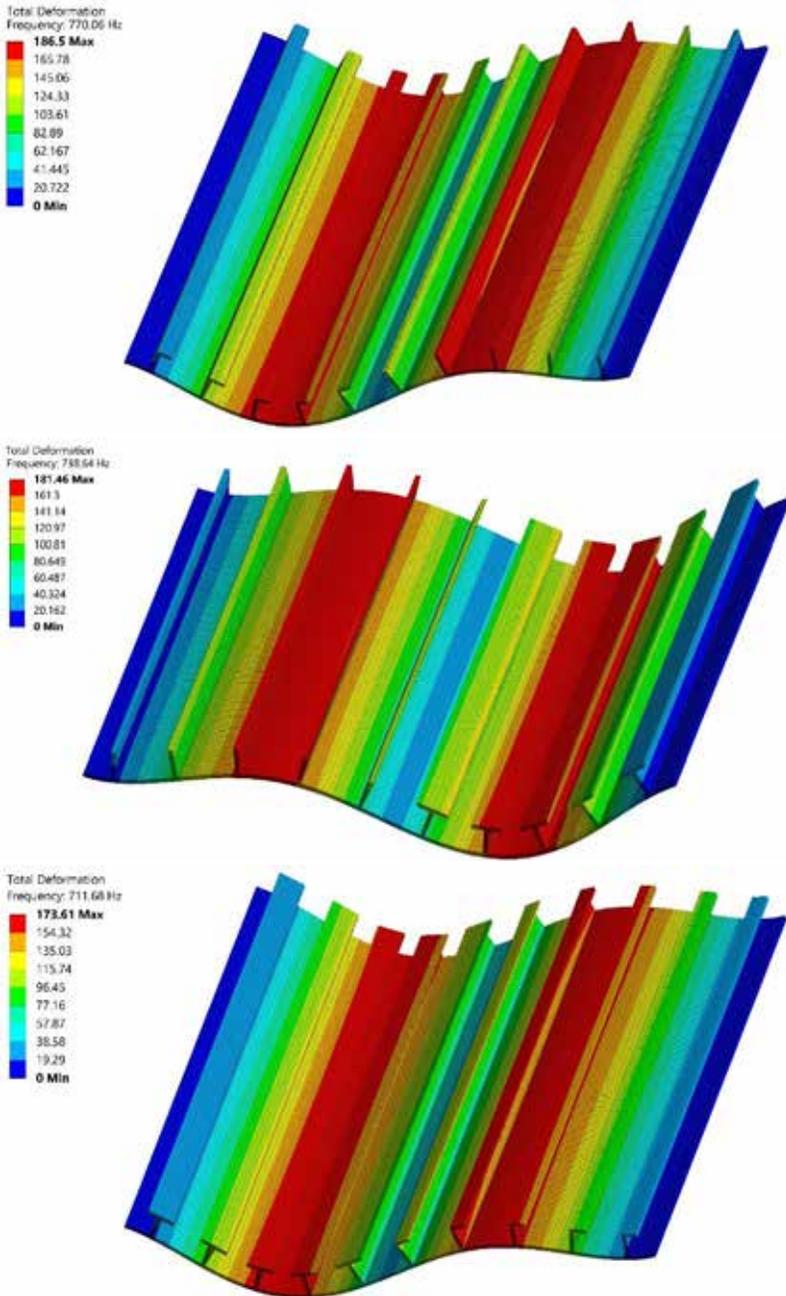
Figure 8: *The First Mode Shape of the Stiffened Shells with (a) Flat-Angle-Shaped, (b) Flat-T-Shaped, and (c) Angle-T-Shaped Stiffener*
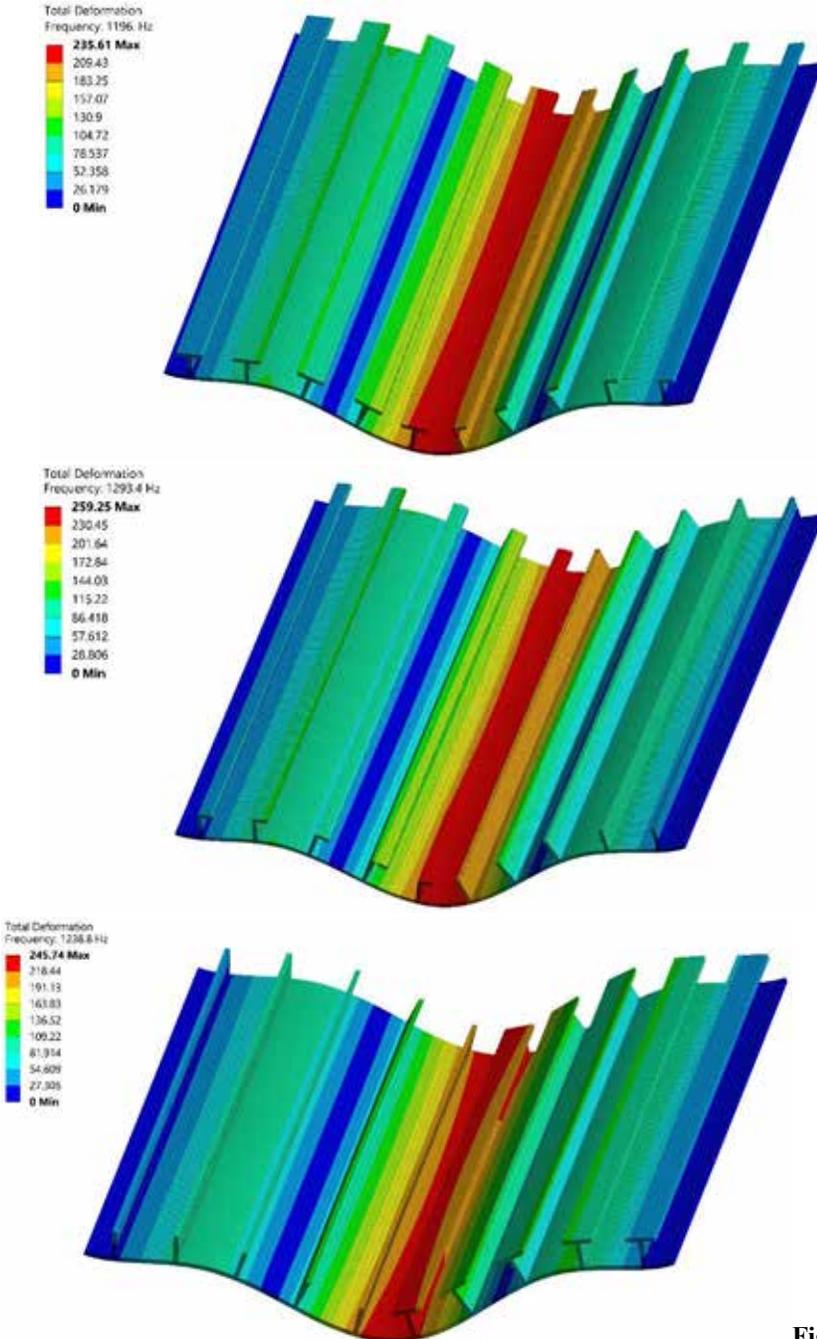
Figure 9: *The Second Mode Shape of the Stiffened Shells with (a) Flat-Angle-Shaped, (b) Flat-T-Shaped, and (c) Angle-T-Shaped Stiffener*
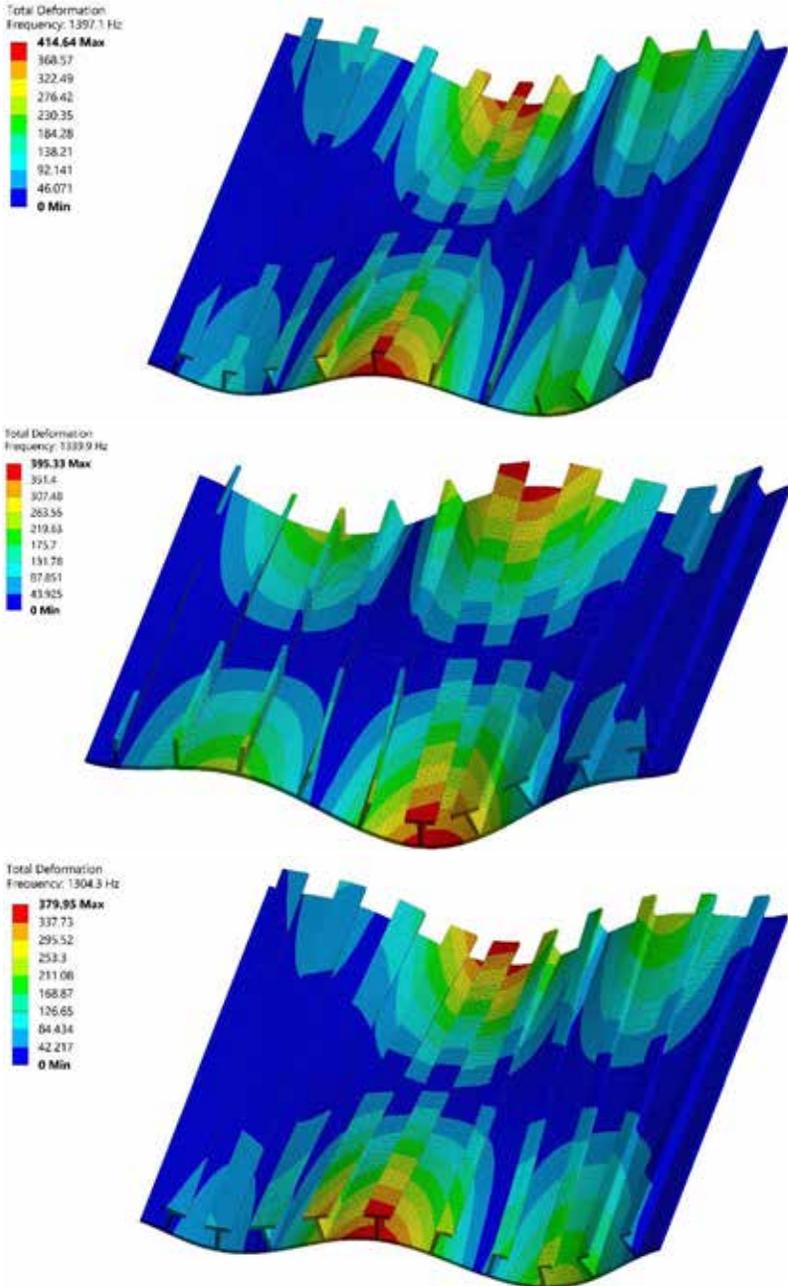
Figure 10: *The Third Mode Shape of the Stiffened Shells with (a) Flat-Angle-Shaped, (b) Flat-T-Shaped, and (c) Angle-T-Shaped Stiffener*
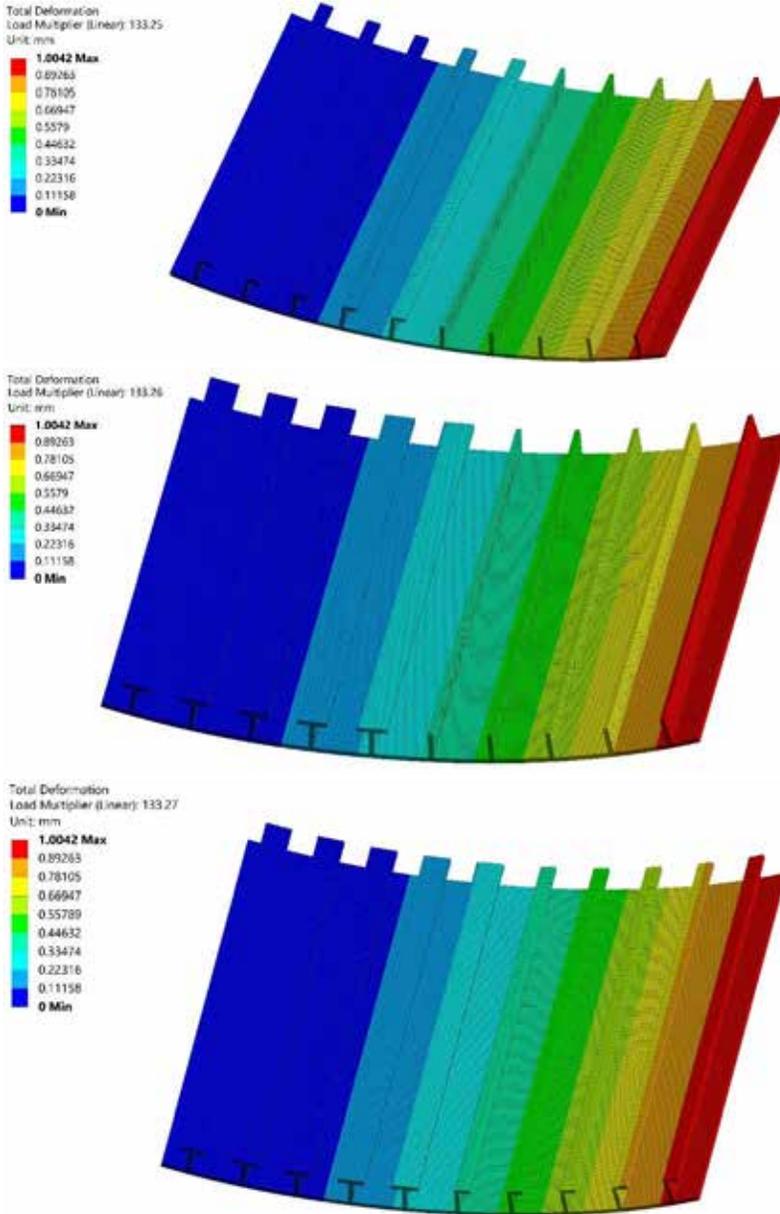
Figure 11: *The Buckling Modes of the Stiffened Shells with (a) Flat-Shaped, (b) Angle-Shaped, and (c) T-Shaped Stiffeners*

As seen in Table 3, the highest natural frequency values have been obtained for the structure, which has the flat-angle-shaped stiffener combination. The lowest natural frequency values, on the other hand, have been evaluated for the structure having the angle-T-shaped stiffener combination. Compared with the stiffened structures that have only one type of stiffener, it has been observed the natural frequencies of the structures having a pair-wise stiffener profile combination are lower than those which have only one type of stiffener profile. Figures 8-10 indicated that the displacement distributions of the structures having a pair-wise stiffener profile combination are the same for those which have a single type of stiffener profile regarding the first two mode shapes. On the other hand, the displacement distributions of those structures have some differences. For the stiffened structures having a pair-wise stiffener profile combination that includes the T-shaped profile, the regions, which are close to the fixed edge where T-shaped stiffeners exist, have lower displacements when compared with the regions, which are also close to the fixed edge but contain flat or angle shaped stiffeners. The same situation has been observed for the flat-angle-shaped stiffener. The displacements are low for those regions where angle-shaped stiffeners exist while they are higher for those regions where flat-shaped stiffeners exist. Figure 11 shows the critical buckling load of the stiffened shell structures with different stiffener profile combinations.

As seen in Figure 11, the critical buckling load values are almost the same no matter which combination has been considered. In addition, the structures having different stiffener profile combinations have almost the same critical buckling load as those which have only a single stiffener profile.

4. Conclusions

This study covered the impact of the stiffener shape on the free vibration and buckling characteristics of the stiffened curved aluminum shells. The results of the numerical analyses indicated that the difference in the stiffener shape regarding flat-shaped, angle-shaped, and T-shaped stiffener, has a small impact on the stiffness of the stiffened curved aluminum shell. The difference in the stiffener shape has not changed the first three mode shape of the structure in terms of the displacement pattern that occurred during vibration in the corresponding frequency. However, the displacement ratio (eigenvectors) has been affected by the stiffener shape. Therefore, the highest displacement ratios have been observed for the flat-shaped stiffener, while the lowest ones have been observed for the T-shaped stiffener. Such a change has been occurred due to the increment in the stiffness of the structure mentioned above. However, that increment in the stiffeness of the structure that has taken in place due to the change in the stiffener shape is lower than the change in the mass properties of the

structure since the first three natural frequency values has been decreased. Such a conclusion is also supported by the buckling analysis results. The difference in the critical buckling load has been negligible as the stiffener shape has varied.

The combination of different stiffener profiles decreased the first three natural frequency values of the stiffened structures (combined profile structures) when compared with the structures, which have only a single type of stiffener profile (single profile structures). The displacement distribution of the first two mode shapes of the combined and single profile structures are the same while the displacement regions of the third mode vary with respect to the stiffener profile. Therefore, since the T-shaped stiffener profile increases the stiffness of the structure, the magnitude of the displacements in the regions that contain T-shaped stiffeners are lower than the other stiffeners. A similar interpretation can be made when considering angle and flat-shaped stiffeners.

Considering the structure as a shell structure having a slight curvature, the impact of the stiffener shape may vary for different structures. In addition, the dimensions and orientation of the stiffeners have been considered as constant parameters to only measure the impact of the stiffener shape. Hence, future studies may cover the effect of the stiffener shape by also regarding the structural dimensions and the orientation of the stiffeners.

REFERENCES

Cho, D. S., Kim, B. H., Kim, J., Choi, T. M., & Vladimir, N. (2016). Free vibration analysis of stiffened panels with lumped mass and stiffness attachments. Ocean Engineering, 124, 84-93. doi:10.1016/j.oceaneng.2016.07.055

Damnjanović, E., Marjanović, M., & Nefovska-Danilović, M. (2017). Free vibration analysis of stiffened and cracked laminated composite plate assemblies using shear-deformable dynamic stiffness elements. Composite Structures, 180, 723-740. doi:10.1016/j.compstruct.2017.08.038

Damnjanović, E., Nefovska-Danilović, M., Petronijević, M., & Marjanović, M. (2017). Application of the dynamic stiffness method in the vibration analysis of stiffened composite plates. Procedia Engineering, 199, 224-229. doi:10.1016/j.proeng.2017.09.005

Dey, P., & Singha, M. (2006). Dynamic stability analysis of composite skew plates subjected to periodic in-plane load. Thin-Walled Structures, 44(9), 937-942. doi:10.1016/j.tws.2006.08.023

Huang, S., & Qiao, P. (2020). A novel semi-analytical method for buckling analysis of stiffened laminated composite plates. Thin-Walled Structures, 148, 106575. doi:10.1016/j.tws.2019.106575

Jafarpour, S., & Khedmati, M. R. (2020). Vibration analysis of stiffened plates with initial geometric imperfections. Proceedings of the Institution of Mechanical Engineers, Part M: Journal of Engineering for the Maritime Environment, 235(2), 521-531. doi:10.1177/1475090220967520

Kahya, V. (2016). Buckling analysis of laminated composite and sandwich beams by the finite element method. Composites Part B: Engineering, 91, 126-134. doi:10.1016/j.compositesb.2016.01.031

Petyt, M. (2015). Introduction to finite element vibration analysis. Cambridge: Cambridge Univ. Press.

Ravi Kumar, P., Gupta, G., Shamili, G., & Anitha, D. (2018). Linear buckling analysis and comparative study of un-stiffened and stiffened composite plate. Materials Today: Proceedings, 5(2), 6059-6071. doi:10.1016/j.matpr.2017.12.211

Sadamoto, S., Tanaka, S., Taniguchi, K., Ozdemir, M., Bui, T., Murakami, C., & Yanagihara, D. (2017). Buckling analysis of stiffened plate structures by an improved meshfree flat shell formulation. Thin-Walled Structures, 117, 303-313. doi:10.1016/j.tws.2017.04.012

Sahoo, P. R., & Barik, M. (2020). Free vibration analysis of stiffened plates. Journal of Vibration Engineering & Technologies, 8(6), 869-882. doi:10.1007/s42417-020-00196-4

Ton-That, H. L. (2021). A new C0 third-order shear deformation theory for the nonlinear free vibration analysis of stiffened functionally graded plates. Facta Universitatis, Series: Mechanical Engineering, 19(2), 285. doi:10.22190/

fume200629040t

Ton-That, H. L., Nguyen-Van, H., & Chau-Dinh, T. (2020). Static and buckling analyses of stiffened plate/shell structures using the quadrilateral element SQ4C. Comptes Rendus. Mécanique, 348(4), 285-305. doi:10.5802/crmeca.7

Wang, Y., & Qiao, P. (2021). Improved buckling analysis of stiffened laminated composite plates by spline finite strip method. Composite Structures, 255, 112936. doi:10.1016/j.compstruct.2020.112936

Zhao, W., Singh, K., & Kapania, R. K. (2019). Thermal buckling analysis and optimization of curvilinearly stiffened plates with variable angle tow laminates. Journal of Spacecraft and Rockets, 56(4), 1189-1204. doi:10.2514/1.a34378

Zhou, W., Li, Y., Shi, Z., & Lin, J. (2019). An analytical solution for elastic buckling analysis of stiffened panel subjected to pure bending. International Journal of Mechanical Sciences, 161-162, 105024. doi:10.1016/j.ijmecsci.2019.105024
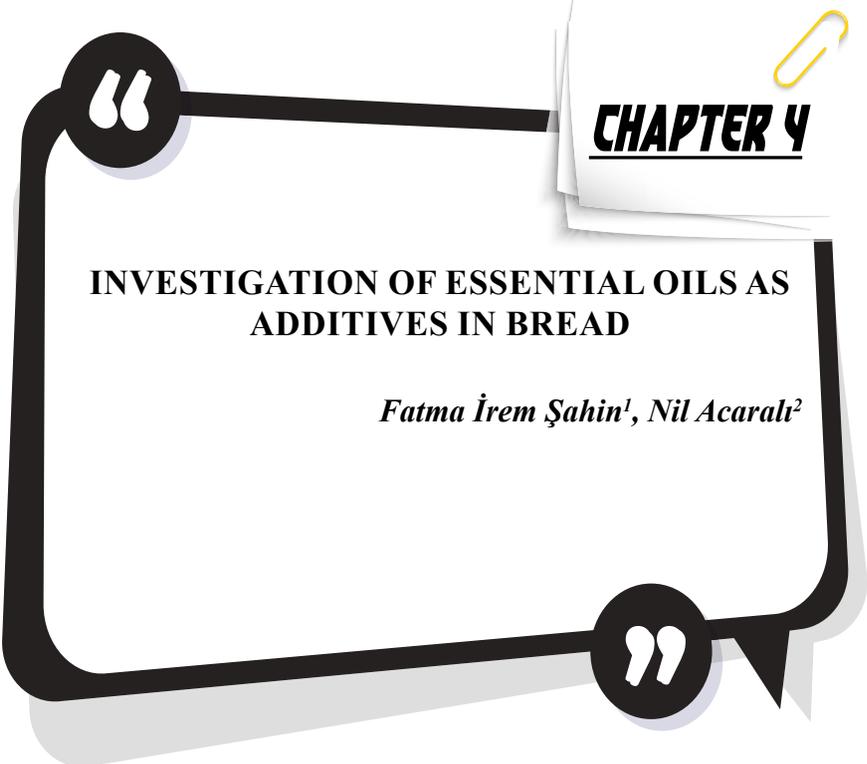
INVESTIGATION OF ESSENTIAL OILS AS ADDITIVES IN BREAD

Fatma İrem Şahin[1], Nil Acaralı[2]

1 Yildiz Technical University, Department of Chemical Engineering, Davutpasa Campus, 34220, Esenler-Istanbul, Turkey.
2 Yildiz Technical University, Department of Chemical Engineering, Davutpasa Campus, 34220, Esenler-Istanbul, Turkey. nilbaran@gmail.com

1. INTRODUCTION

Nutrition was one of the most significant issues to sustain vital activities in our world has increasing population in recent years. Necessity of storage has emerged from the period when food is abundant to the period when it is scarce since foods were always not available in the same abundance in the world. From another point of view, it was not possible to consume every food immediately. In particularly, a certain period was required for packaged foods to leave the production line and reach the consumer. Foods needed to be stored without losing their rheological, nutritional, or qualitative characteristics (Özdemir et al., 2021). It became unavoidable to use additives in food stuffs, to preserve the first-day quality attributes and to reduce potential financial loss. The use of food additives determined by many international organizations. At the same time, countries could also impose limits on the use of additives within their own borders and followed them. In recent years, consumers have started to prefer products with natural additives (Omedi et al., 2021). This situation increased the interest in the use of organic and economical essential oils, which could be an alternative to synthetic additives (El-Saber Batiha et al., 2020; Moraczewski et al., 2020).

2. FOOD ADDITIVES

Any kind of substance necessary for the existence of mankind, raw, semi-processed or fully processed, in which it was the source of nutrients such as protein, fat, carbohydrates, vitamins, mineral substances, was called food. Each food item had a period during which it could be stored and preserved without spoiling under appropriate conditions from the date of manufacture, this period was called shelf life. The main preservation methods used in the industry were heating, freezing, drying and irradiation, but in cases where these were not applicable or insufficient, preservatives added to foods (Arslan, 2011). According to the definition made by the Food Preservation Commission of the US National Research Council, the substances that could be added during the processing of food, during the production, storage, packaging, and inclusion of the food in the final product were called food additives (Arslan, 2011; Çalışır & Çalışkan, 2003). Food additives used to improve the structure, texture, appearance, and taste of foods, to preserve or improve their nutritional and biological value, and to prevent undesirable changes that might occur in food. Another reason for the use of food additives was the increasing demand for ready-to-eat foods and offering a wider variety of foods to consumers, as the working population increases day by day (Alan & Öksüztepe, 2020).Considering the beneficial aspects of food additives, it provided a positive effect on taste, aroma, odour, colour, shape, and appearance, increases durability and shelf life, and prevents the development of microorganisms. On the other hand, if did not

use in the right amounts, it caused loss of natural taste, loss of nutrients and increased the risks of various diseases such as food poisoning and cancer (Arkan, 2020). Additives did not be harmful to human health. If there was technological requirement, it could be added in appropriate conditions. In addition, it was vital to use it only in designated foods and in quantities permitted by authorized institutions. Food additives used to maintain quality, did not be used to shade poor quality (Yurttagül & Ayaz, 2008). It was not possible to make a harmless and consumable substance from a substance that deteriorates with the use of preservatives in foods (Arslan, 2011). According to the information in the literature, there were 2800 food additives approved by the FDA. However, most of these substances were not used because they had other alternatives. There were 297 food additives approved for use in the European Union (Boğa & Binokay, 2010).

2.1 History

Since the history of humanity, the needed to preserve and protect food has arisen. First, natural additives salt and some spices were used. It was known that in the 50th century BC, the ancient Romans used some spices as flavourings. In 400 BC, the Roman Empire established a police organization to conduct health checks to ensure food safety. In the BC 220s, the Huns found that the meat could be preserved by making sausage, pastrami and roasting to make it last for a long time. The Indians preserved the meat by freezing it. There were also additives such as saffron dye and sulphur dioxide, the use of which dates to ancient times. Food colouring was first used by the Egyptians. According to the information in the Dede Korkut epics, the Turks roasted the meat, and dried the milk and kept it in 772 AD (Boğa & Binokay, 2010). It was around 1580 that official controls on the slaughter and marketing of meat became widespread in Europe. In 1856, aniline purple was used as an artificial dye. For the first time, a mixture of salt and calcium phosphate was produced in 1886 as a food additive and commercially traded as a flavoring agent (Arslan, 2011, Çalışır & Çalışkan, 2003). It was known that the use of food additives became widespread uncontrollably in the 19th century. The main reason for this was the lack of legal regulation and the inadequacy of the analysis method. This negative development brought under control by developments in modern food legislation and control method (Arslan, 2011). The WHO organization published lists of 114 artificial colorants covering 40 countries in 1956, allowing their use and putting them into practice. According to official documents, approximately 300 000 tons of food additives were used in the USA in 1965 (Çalışır & Çalışkan, 2003).

2.2 E Code

E codes showed the codes that were the expression of the safety given to the food additives that passed the necessary safety tests of the relevant

health/food authorities of the European Union and all specifications determined. The additives allowed to be used were not the same in every country, and countries such as America, Austria and Europe have restrictions within their own country borders. The number of additives other than flavouring substances allowed in the Turkish Food Codex regulation was around 300. According to the Regulation that entered into force in 1997, the products in the ingredients section of the labels, the function, name, E code of the additive added to the product. (Arslan, 2011). E-codes were shown in Table 1 (Karatepe, 2018).

Table 1. E-code food additives (Karatepe, 2018)

Food Additives	E Codes
Colorants	E100-180
Protectors	E200-297
Antioxidants	E300-321
Emulsifiers and Stabilizers	E322-500
Acid-base providers	E500-578
Sweeteners, Flavorings	E620-637
Wide-purpose Food Additives	E900-927

2.3 Practices in Turkey on Food Additives

All services related to food in Turkey were provided by the state. The authority of the institutions responsible for food control in Turkey was not gathered in one hand and there were 26 laws, 6 statutes, 10 regulations, 6 circulars, various communiqués, and standards within the institutions (Çalışır & Çalışkan, 2003). Every producer company in Turkey was inspected twice a year by the Ministry of Agriculture. In addition, inspections could be made in case of any complaint or doubt. Control at the market stage was provided by the Ministry of Health in some regions jointly by the local government and the ministry (Arslan, 2011).

2.4 Effects of Food Additives on Health

In many studies, it determined that food additives had serious side effects on our body when not used correctly. Some of these side effects were nausea, vomiting, diarrhea, eczema, urticaria, irritable bowel disease, brain damage (Karatepe, 2018). In another study, it was reported that some additives and similar chemicals in foods cause hyperactivity and some neuropsychological disorders in some children. Artificial sweeteners aspartame (E951) and monosodium glutamate (E621) were also included in the list of foods that were said to trigger migraine attacks in children and adults. It stated that sodium benzoate might cause DNA damage, and that sodium benzoate (E211) and potassium benzoate (E212) might had

genotoxic effects. It determined that nitrites in foods could transform into carcinogenic N-nitroso compounds (Karatepe, 2018). It was known that phenolic matter found spontaneously in the roots of some plants were anti-carcinogenic, but unnatural phenols had effects such as co-carcinogens that cause precancerous lesions and cancer. The use of substances considered toxic and carcinogenic in terms of food health prohibited (Çalışır & Çalışkan, 2003). On the other hand, in a study conducted in England, although it was claimed that 7% of the population is sensitive to additives, studies in this population showed that only 0.01 - 0.23% of them are affected by additives (Yurttagül, & Ayaz, 2008). In summary, the increase in the use of food additives to increase sales brings with it many dangers and in the absence of necessary control, allergic, carcinogenic, mutagenic, and teratogenic effects on human health could be ignored. Consumers should be made aware of food additives; the state should establish an effective control mechanism and the health risks of food additives be minimized and thus contribute to the development of the food industry (Boğa & Binokay, 2010; Yurttagül, & Ayaz, 2008).

3. ESSENTIAL OILS

Oily mixtures that had a strong odour and were liquid at room temperature called essential oils. While they were known as volatile because they knew evaporation at low temperatures such as room temperature, they got the etheric name because they fly similarly to their ether properties, while they called essences because they were used in the cosmetic industry in perfumery due to their pleasant smell (Çalıkoğlu et al., 2006). Essential oils were very worthwhile natural products that were used as raw materials in many areas such as the food, health, cosmetics, and perfume industries. In addition to environmental factors such as climate, soil composition, geographic region, soil moisture content during the growing season, essential oils. The order might vary in character, amount, and component according to the age of the plant, the plant organ, the development periods of the plant and even the harvest time (Çon et al., 2021). Essential oils differ from fixed oils in some of their properties. For example, essential oils had the property of being entrained in water vapour, while fixed oils were not entrained in water vapour. The most significant feature that distinguishes essential oils was that they were soluble in aqueous ethanol (Demirok, 2019). About 300 of the 3000 known essential oils were used commercially in the fields of health, food, especially perfume and cosmetics, due to their biological, antibacterial, antifungal and antioxidant properties. Due to the antimicrobial and antioxidant properties of essential oils, their use as an alternative to antibiotics has recently gained currency and their alternative uses in animal nutrition as feed additives are increasing day by day (Çon et al., 2021). In recent years, with the increasing in the importance given

to environmentally friendly products, the interest in the organic features of essential oils due to their antimicrobial and antioxidant effects increased as well as their aromatic and sweetening commercial properties (de Araúj et al., 2020).

3.1 Fabrication of Essential Oil

Obtaining essential oils from various organs of medicinal and aromatic plants with appropriate methods was significant in terms of quality and efficiency. Essential oils from plants were obtained with extraction of various methods (Selçuk, 2020). Essential oil extraction methods could be basically classified into four groups. In the first group, there were distillation types such as water distillation, steam distillation, vacuum distillation, fractional distillation, and microwave assisted distillation. In the second group, maceration, infusion, percolation, anflorage, and decoction were listed as extraction types. As the third essential oil extraction method, the squeezing method and the drawing method come under the heading of mechanical processes. In the fourth group, which was the last group, advanced extraction methods were used (Yaman & Kuleaşan, 2016).

3.2 Use of Essential Oils as Conservatives in Food Industry

To expand the shelf life in the food industry, the use of plant extracts begun to increase. Plants rich in essential oils or their essential oils used as antimicrobials in the production and marketing of organic food because they were natural. Studies showed that plants with antimicrobial effects, which used in the food industry, are safer than many other antimicrobials. The extracts obtained by appropriate methods, besides being primarily aroma and flavouring, also show antimicrobial effect against harmful microorganisms in food preservation. Essential oils, which had antimicrobial effects against bacteria and molds, were found in high amounts in marjoram, thyme, sage, rosemary, clove, black cumin, garlic, and onion. This antimicrobial effect was due to components such as phenol, aldehyde, and alcohols in the composition of essential oils (Sayın, 2019). It was possible to use certain essential oils in cakes and pastries, and sometimes in desserts, especially beverages. Essential oils obtained from plants could be an alternative to unnatural preservatives used in the food industry due to their antimicrobial activity. When these compounds were used in foods, they had an important role in preventing the development of pathogens that cause food poisoning or delaying food spoilage. It was volatile against microorganisms that spoil food and cause food poisoning. It was known that there were a lot of studies on the impact of oils (Bülbül, 2016).

3.3 Antimicrobial Impact of Essential Oils

In the past, the investigation of the antimicrobial effect of essential oils gained momentum. Nowadays, with the decrease or loss of effect of antibiotics, it led to the search for alternatives. Studies showed that plant extracts and essential oils could be effective in antimicrobial use as an alternative to chemical use, especially in foods (Sayın, 2019).

3.4 Clove Oil (Syzygium aromaticum Oleum)

Clove essential oil, which was distilled from the Syzygium aromaticum plant, the other name of the plant is Eugenia caryophyllata the plant belongs to the Myrtaceae family, was obtained from dried flower buds, its active ingredient was eugenol. The clove plant was obtained from a plant that grows on trees that could reach 20 meters in height, with leaves that remain green all seasons, and pink flowers in bunches. The plant originated in Indonesia in tropical Asia. The image of the clove plant was given in Figure 1 (Oktay, 2021; Koptaget, 2019).

Figure 1. Clove (syzgium aromaticum) plant (Koptaget, 2019)

Clove oil used in the cosmetic industry for its aromatic scent in world trade from past to present, as well as widely used in medicine and food in different sectors. Clove essential oil used commonly in the medical field for the cure of burns and wounds, as a suffering reliever in dental treatment, and as a nerve stimulant in liver and stomach ailments. (El-Saber Batiha et al., 2020). It had antipyretic, antinociceptive and anti-inflammatory effects, and in one study it reduced oxidative stress and reported a positive effect on memory (Cambaz & Çankaya, 2021). In the field of food, it was accepted that it could be used as an alternative food preservative to chemicals, thanks to various studies and reports that determined its antimicrobial, antifungal and antioxidant properties (El-Saber Batiha et al., 2020). It contained rich phenolic composite such as 75-85% eugenol, 5-15% eugenol acetate and gallic acid. Eugenol, which was the active ingredient in its structure, makes it a powerful antioxidant with an activity index of 6.94. The molecular

structure of eugenol and eugenol acetate was shown in Figure 2 (Çon et al., 2021).
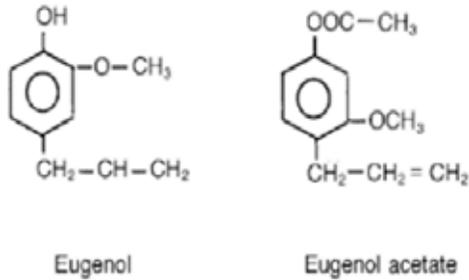
Figure 2. Eugenol and eugenol acetate molecular structure (Çon et al., 2021)

In studies with various essential oils, it found that the antioxidant level in meat fat depends on the concentration, and clove was the most effective among sage, thyme, and ginger. In another study, the effects of garlic, onion, clove, and cinnamon extracts on natural microflora were investigated in meatballs and kebab dishes in Egypt. It was determined that garlic and clove extracts showed the highest antimicrobial effect against bacteria that cause food poisoning and spoilage (Emir Çoban et al., 2012).

3.5 Orange Oil (Citrus aurantium var dulcis Oleum)

Orange oil was acquired Citrus aurantium var dulcis plant, belonging to the Rutaceae family, from the peel of the fruit and waste-products formed during industrialized orange juice manufacturing (de Araúj et al., 2020). The active ingredient of the orange essential oil obtained from the orange peel is limonene with 93.4%, which was the highest ratio compared to other citrus species. The plant specimen of Citrus aurantium var dulcis Oleum was shown in Figure 3 (Aydın et al., 2018).

Figure 3. Citrus aurantium var dulcis oleum plant example (Aydın et al., 2018)

The citrus group, which consists of bergamot, grapefruit, lemon, lime, orange, and tangerine, was among the most cultivated fruit group in the world, with a total world production of 115,650,545 tons. Oranges account for 55.26% of the production of fruits in this group. (Aydın et al., 2018). Orange trees were widely grown in places suitable for tropical and subtropical climates, including the Mediterranean region of Turkey (Baba, 2018). The content of orange essential oil obtained from the orange peel consists of 85% to 99% monoterpene, also known as limonene, sesquiterpene, hydrocarbons, and 1-15% of non-volatile components. Limonene molecule found in Citrus aurantium var dulcis was shown in Figure 4 (Çon et al., 2021).
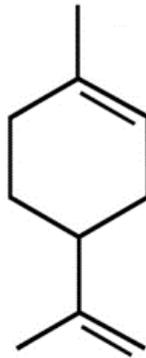
*Figure 4. Limonene molecule found in citrus aurantium var dulcis (Çon et al., 2021)*

Studies showed that orange oil, which was one of the citrus varieties, was very effective in preventing mold formation and could be used for antimicrobial purposes in foods (Özpolat, 2019). Orange oil used in

apricot, peach, mango, and pineapple flavors, while creating the desired orange flavor along with the cooling effect in the product it was used in (Jiang et al., 2011).

4. BREAD

Cereals and cereal products were consumed in many countries of the world to meet the daily calorie needs of people as basic nutrients. Wheat was the most popular and most consumed grain. At the same time, with more than 200 million agricultural areas, it was the most produced grain in parallel with consumption needs. Although there were over 3000 known wheat species, the most widely grown wheat was Triticum Aestivum, also called bread wheat (Arkan, 2020). Since it was one of the basic nutrients and occupies significant place in daily consumption habits, it also had direct effects on human health. Since the fiber content was high and the fat rate was low, it also influences protection from heart diseases, stroke, cancer, and some chronic diseases. In addition, studies showed that bran and legumes were a good source of fiber for the body, so consuming whole wheat bread was significant for intestinal health in diets (Yılmazaslan, 2008). Bread was also culturally unifying and showed as the only food item consumed by people of all races, cultures, and religions. It concluded that bread was a common element of cultures, as well as having positive effects on the psychology of societies. In a study conducted with students and workers, it was concluded that people who consume crusty bread keep their blood sugar at an ideal level for a longer period and positively affect physical and mental performance (Aydın & Yıldız, 2011). Bread example was given in Figure 5.

Figure 5. Bread example (Şahin, 2022)

Bread was one of the most preferred foodstuffs for reasons such as being nutritious, satisfying, high energy values, easy access, and cheap price. Bread did not belong to a certain taste class when compared to other nutrients and considered neutral. For this reason, it consumed with

many foodstuffs such as aromatic foodstuffs (Çon et al., 2021). Bread, which counted as a good source of energy, also contains various minerals, especially B vitamins and protein. Although bread had different nutritional values according to the material it was made from, the amount of moisture, protein, carbohydrate, and energy values it contains were close (Arkan, 2020). Studies showed that bread consumption depends on many parameters. The gender, age, education level, income level, occupation and geography of the individuals were among the factors affecting it (Aydın & Yıldız, 2011).

4.1 History of bread

Bread, which was as old as human history, is thought to date back to 10,000 years ago, since the Neolithic age. Although grains such as wheat were consumed by roasting directly over the fire in the early ages, it was used in bread making by turning it into flour in 7000 BC. Traces of the first furnace were found in 4000 BC. From this, it was concluded that the Babylonians consumed the bread and were engaged in bakery. The ancient Egyptians saw grain and bread as a great blessing and took part in ceremonies at every stage of life. It was known that baker's yeast was discovered by a woman in the 1800s BC. It was known that bread making became widespread in the Mediterranean region, Egypt, and Israel with the spread of commercial bakeries (Kalkışım et al., 2012). Turks, who had been dealing with grain agriculture since the Neolithic age, a bread culture was formed with the transition to the settled order. The Turkish tribes coming from Central Asia carried this culture to Anatolia and the bread culture continued until the Seljuk state, the Ottoman State, and the Republic of Turkey (Kaya, 2021). Beginning from the 19th century, mechanization in bread production started and the transition to modern production techniques began. Breads diversified and their quality features begun to come to the fore. Standardization started in the features such as taste, smell, and additives to be used in breads offered to the consumer (Kalkışım et al., 2012). Today, in parallel with meeting the consumption needs of the increasing population, production increased on an industrial scale and time saved.

4.2 Food Additives Used in Bread

It mainly consisted of flour, salt, water, and yeast, although different additives used in bread making. Sometimes additives were used to eliminate defects arising from raw materials and processes, sometimes to improve bread quality and delay staling. Although additives were prohibited in breads to be sold unpackaged, additives were used for reasons such as protection, baking, acidity regulation, thickening, emulsifier, etc. in breads produced for special purposes (Aydın & Yıldız, 2011; Gültekin et al.,

2019). In addition to all these, natural source substances such as ascorbic acid, roasted malt flour and amylase were added, which did not belong to the food additive class and were added with the aim of increasing the quality characteristics. Wheat bran, rye, oat, soy flour, potato flour, malt flour listed as natural additives used (Aydın & Yıldız, 2011; Gültekin et al., 2019).

4.3 Mold in Bread

One of the main causes of spoilage in bread was mold. It was known that there were mold spores in the flour, which was the raw material of bread, and when a suitable environment was created, these spores could multiply and caused the bread to become moldy starting from the surface. On the other hand, the high mold load of the air, the use of mold-contaminated tools while slicing, the entry of too much air into the sliced bread during storage, the long-term storage in a hot and humid environment were among the reasons that affected and accelerated the formation of mold (Sevim, 2019). Mold in bread example was shown in Figure 6.

Figure 6. Mold in the bread (Şahin, 2022)

4.4 Waste of Bread

It determined that 123 million breads were produced every day and 6.14 million breads were wasted in Turkey. This wasted bread was even more than the population of many countries. According to the United Nations data, while 6 million children lose their lives due to hunger and malnutrition every year, the number of daily wastages for bread alone was strikingly revealed (Kaya, 2021). When the distribution of 6.14 million wasted bread within itself was analysed, the highest rate of waste was houses with 41%. This rate was followed by bakeries with a rate of 38 percent. In the studies conducted, when asked about the reason for wasting

bread, the thought of buying more bread than needed came first with a rate of 68.2%, according to the households. In the second place, there were opinions with 18.5% that the bread cannot be stored under suitable conditions and that stale bread cannot be re-evaluated. In the study, another opinion was that the bread was not long-lasting with a rate of 13.8%, which causes bread wastage (Taşçı et al., 2017).

4.5 Bread Consumption in the World

Bread production consumption on an annual basis was not constant in countries. It tends to increased depending on the increasing population. When compared according to the level of development, it was observed that bakery products, especially bread, were consumed less in developed countries. Annual bread consumption of some European countries in 2013 was shown in Table 2 (Eglite & Kunkulberga, 2017).

Table 2. Annual bread consumption of some European countries in 2013 (Eglite & Kunkulberga, 2017)

Country	Consumption, kg	Trend with the previous year
Belgium	55.0	stable
Bulgaria	95.0	stable
Denmark	45.0	stable
Finland	42.0	stable
France	57.0	stable
Germany	56.0	stable
Greece	68.0	stable
Italy	52.0	stable
Netherlands	62.0	-1.0%
Russia	55.0	+2.0%
Slovenia	42.0	stable
Spain	37.0	+4.2%
Turkey	104.0	-10.0%
Ukraine	89.0	-7.5%
Great Britain	32.0	-1.0%
Average	59.4	

4.6 Bread Production

Today, bread making ceased to be an art branch and has started to become a science where production was made with technological methods. The most practical and economical method adopted in all countries of the world was to produce with the direct dough method. In bread making, first,

all the raw materials were brought together and mixed. After the dough elements come together, kneading was done. The kneading process ended when the dough reaches 25-27°C. In the second stage, the fermentation process was carried out under suitable conditions and for a sufficient time in order to obtain a well-risen bread. The dough left to rest becomes soft after the final fermentation process and becomes suitable for shaping. Finally, the cooking process began. Commercially produced breads were generally baked at 230°C and 25 minutes for 400 grams of bread. To produce standard quality breads, the temperature constantly controlled, and for this, thermostat systems expanded (Elgün, 2010). In bread production, there were three main processes: kneading, which turned the flour into dough, leavening, which turns the dough sour and rises, and baking, which turned it into a final product. The traditional process of bread making, reconstructed from Thielecke et al., 2020, was shown in Figure 7 (Thielecke et al., 2020).
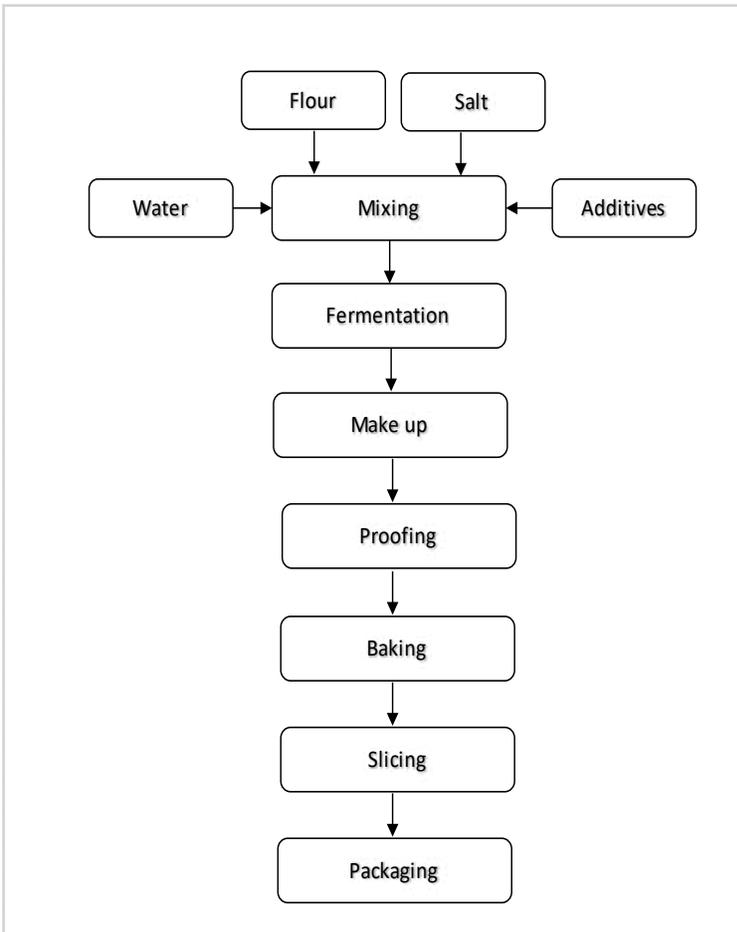

Figure 7. Traditional process for bread making (Thielecke et al., 2020)

5. LITERATURE REVIEW

Bhavaniramya et al. (2019) focused a study on essential oils. In the study, it was revealed aromatic volatile components could be used safely in foods without a decrease in quality. Especially in future studies, it showed that it used in cereals by increasing the shelf life along with quality. Gavahian et al. (2018) revealed that essential oils could be used instead of chemical alternatives by checking the appropriate packaging and sensory properties before commercial use in their review. Essential oils could be used as protective packaging in the future, especially in bakery products known for their short shelf life. Matan et al. (2005) in their study, observed the dual effects of cinnamon and cloves under different pressures, including shelf life and antimicrobial properties in foods. It was concluded that as the amount of essential oil increased, it was recorded a higher antimicrobial effect. Mishra et al. (2014) focused to impact of essential oils against fungi formed in bakery were investigated. Penicillium Oxalicum and Aspergillus Flavus bacteria were identified from the wheat flour sample. It determined that only clove oil had an antifungal effect against the fungal species defined among the essential oils used. Ibrahium et al. (2013) considered effect of clove oil, one of the essential oils, on the shelf life of cakes and whether it replaced synthetic antimicrobial and antioxidant substances. As a result of this study, it was concluded that the use of clove oil can replace synthetic preservatives in cakes and there was no significant decrease in quality. In addition, it observed that the antioxidant effect becomes stronger as the ppm of the added amount was increased from 400 to 800. Only the sensory test results were negative in the highest amount of oil used. Sharma et al. (2021) conducted a review on active packaging to protect food safely. In recent years, with the increasing interest in essential oils, it brought forward those essential oils be used for active packaging. While synthetic preservatives affected the composition and quality of the food negatively by staying on top of the food, it helped to extend the shelf life by controlling the humidity, temperature, microbial activity by using naturally obtained essential oil. Sunil and Desai (2018) investigated the antimicrobial activity of orange peel oil on bread. In their study, it was concluded that it had an inhibitory effect against Aspergillus Niger and Penicillium Chrysogenum fungi found in bread. It concluded that soon, essential oils be used in systems to prolong the shelf life of foodstuffs. Ahmed et al. (2009) studied the effects of different levels of orange products on the shelf life of the cake. Among the orange peel, orange oil and orange juice, it was discovered that the highest antifungal activity against mold fungi in bread was in orange oil. It was also noted that the amounts used in the study did not have a negative effect on the sensory properties of the cake. Sharma et al. (2022) carried out various

tests for characterization on bread with thyme from essential oils. Thanks to the active ingredient in the thyme added with casting, it was concluded that it had an antimicrobial effect against molds. Oliveira et al. (2020) studied the ability to store bread for a long time by adding it with different additives and lemongrass essential oil. Using lemongrass in the packaging process encouraged its preservation. García-Gómez et al. (2022) conducted a study on which sensory characteristics consumers pay attention to when buying bread. It was determined that the most important feature in the consumption of the researched bread is the moisture level in the bread. Accordingly, the homogeneity on the bread surface was sensorial effective on the consumers. It was believed that this study will shed light on the bakery industry in order to increase the purchase intention of consumers. Özdemir et al. (2021) examined the purchase value of consumers by adding additives to bread. It was concluded that the quality and sensory properties of bread could be increased by using naturally obtained medicinal plants as additives. Zorba et al. (2005) revealed the necessity of investigating food spoilage with more objective methods. In the study, quality criteria were determined, and models were created by applying chemical kinetic principles. Mohamad Asri et al. (2020) obtained organic preservatives from palm kernels. Consequently, it was seen that it delayed the bread deterioration.

REFERENCES

Ahmed, H. F., Abu-Zaid, A.A. & Sayed, H.S. (2009). Antimicrobial effect of orange juice, peel and its essential oil on the shelf life of cake. Mansoura University Journal of Agricultural Sciences. 34(2), 1019-1028.

Alan S. & Öksüztepe G. (2020). Food additives and antimicrobials used in the dairy industry. Bozok Veterinary Sciences. 1(1-2), 44-50.

Arkan, Z. M. (2020). The analysis of food additives and inorganic anions in bread by ion chromatographic method with conductivity detector. M.Sc. Thesis. İstanbul Technical University. Graduate School of Natural and Applied Sciences, İstanbul.

Arslan, G. (2011). Addition agents of foods and the investigation about usability of the dioximes produced recently as addition agents. M.Sc. Thesis. Selçuk University. Graduate School of Natural and Applied Sciences, Konya.

Aydın, A., Korkunç, M., Şentürk Demirel, D. & Gül, S. (2018). The importance of essential oil isolated from orange peel (Citrus sinensis L.). International Journal of Eastern Mediterranean Agricultural Research, 1(2), 13-19.

Aydın, F. & Yıldız, Ş. (2011). Determination of bread consumption habits and consumer dynamics in Sivas city. Atatürk University. Journal of the Faculty of Agriculture, 42(2), 165-180.

Baba, E. (2018). In vitro antibacterial effect of orange (Citrus sinensis) peel essential oil against bacterial fish pathogens. Süleyman Demirel University. Eğirdir Faculty of Fisheries Journal, 14(3), 208–214. https://doi.org/10.22392/egirdir.391075

Bhavaniramya, S., Vishnupriya, S., Al-Aboody, M. S., Vijayakumar, R. & Baskaran, D. (2019). Role of essential oils in food safety: Antimicrobial and antioxidant applications. Grain & Oil Science and Technology, 2(2), 49–55. https://doi.org/10.1016/j.gaost.2019.03.001

Boğa, A. & Binokay, S. (2010). Food additives and their effects on our health. Archive Resource Review Journal, 19(3), 141-154.

Bülbül, L. E. (2016). Components, antimicrobial, and antioxidant activities of essential oils of some plant species grown in Erzurum. PhD Thesis. Atatürk University. Graduate School of Natural and Applied Sciences, Erzurum.

Çalıkoğlu, E., Kıralan, M. & Bayrak, A. (2006). What is essential oil, how it is produced and an overview of its situation in Turkey. Turkey 9th Food Congress Proceedings Book, 569- 570, Bolu.

Çalışır, Z. E. & Çalışkan, D. (2003). Food additives and effects on the human health. Ankara Faculty of Pharmacy Journal, 32, 193-206.

Cambaz Kurt, N. & Çankaya, İ. İ. (2021). Aromatherapy applications and essential oils. Mersin University. Medical School. Lokman Hekim Journal of Medical History and Folkloric Medicine, 11(2), 230-241. https://doi.org/10.31020/

mutftd.882997

Çon, A. H., Tekeli, A., Küçükgülmez, A., Öztürk, E., Ocak, E., Giray, E. S., Seyis, F., Kırkpınar, F., Pazır, F., Yıldız, G., Kutlu, H., R., Baykal Çelik, L., Çelik, M., Tunçtürk, M., Tunçtürk, R., Yurtseven, S., Kırıcı, S., Demir, S. & Açıkgöz, Z. (2021). Essential Oils: Production, uses in food and animal nutrition. 1st Edition, Institution of Economic Development and Social Researches, Iksad Publications, Ankara.

de Araújo, J. S. F., de Souza, E. L., Oliveira, J. R., Gomes, A. C. A., Kotzebue, L. R. V., da Silva Agostini, D. L. & Cavalcanti, M. T. (2020). Microencapsulation of sweet orange essential oil (Citrus aurantium var. dulcis) by lyophilization using maltodextrin and maltodextrin/gelatine mixtures: Preparation, characterization, antimicrobial, and antioxidant activities. International Journal of Biological Macromolecules, 143, 991-999.

Demirok, H. (2019). The effect of ultrasound assisted enzyme pretreatment before distillation on process time, yield and essential oil composition in bay essential oil production. M.Sc. Thesis. Burdur Mehmet Akif Ersoy University. Graduate School of Natural and Applied Sciences, Burdur.

Eglite, A. & Kunkulberga, D. (2017). Bread choice and consumption trends. Foodbalt 2017, 178-182. https://doi.org/10.22616/foodbalt.2017.005

Elgün, A. (2010). Bread making technology and our bread making. Journal of Atatürk University Faculty of Agriculture, 13(1-2), 153-164.

El-Saber Batiha, G., Alkazmi, L. M., Wasef, L. G., Beshbishy, A. M., Nadwa, E. H. & Rashwan, E. K. (2020). Syzygium aromaticum L. (Myrtaceae): Traditional Uses, Bioactive Chemical Constituents, Pharmacological and Toxicological Activities. Biomolecules, 10(2), 202. https://doi.org/10.3390/biom10020202

Emir Çoban, Z., Patir, B. & Yilmaz, K. (2012). Protective effect of essential oils on the shelf life of smoked and vacuum-packed rainbow trout (Oncorhynchus mykiss W.1792) fillets. Journal of Food Science and Technology, 51(10), 2741–2747. https://doi.org/10.1007/s13197-012-0795-8

García-Gómez, B., Fernández-Canto, N., Vázquez-Odériz, M. L., Quiroga-García, M., Muñoz-Ferreiro, N. & Romero-Rodríguez, M. N. (2022). Sensory descriptive analysis and hedonic consumer test for Galician type breads. Food Control, 134, 108765. https://doi.org/10.1016/j.foodcont.2021.108765

Gavahian, M., Chu, Y.H., Lorenzo, J. M., Mousavi Khaneghah, A. & Barba, F. (2018). Essential oils as natural preservatives for bakery products: Understanding the mechanisms of action, recent findings, and applications. Critical Reviews in Food Science and Nutrition. 60 (2), 310-321.

Gültekin, F., Akın, S. & Elgün, A. (2019). Up to Date Review about Bread: Health Effects, Food Additives and Halal Issues. Academic Platform Journal of Halal Lifestyle, 1(1), 1-17.

González, M., Vernon-Carter, E., Alvarez-Ramirez, J. & Carrera-Tarela, Y. (2021). Effects of dry heat treatment temperature on the structure of wheat

flour and starch in vitro digestibility of bread. International Journal of Biological Macromolecules, 166, 1439–1447. https://doi.org/10.1016/j.ijbiomac.2020.11.023

Ibrahium, M. I., El-Ghany M.A. & Ammar, M. (2013). Effect of clove essential oil as antioxidant and antimicrobial agent on cake shelf life. World Journal of Dairy & Food Sciences. 8(2), 140–146.

Jiang, M.-H., Yang, L., Zhu, L., Piao, J. H. & Jiang, J.-G. (2011). Comparative GC/MS analysis of essential oils extracted by 3 methods from the bud of citrus aurantium L. var. amara engl. Journal of Food Science, 76(9), C1219–C1225. https://doi.org/10.1111/j.1750-3841.2011.02421.x

Kalkışım, Ö., Özdemir, M. & Bayram, O. (2012). Bread Making Technology. SAGE Publishing, Ankara.

Karatepe, T. U. & Ekerbiçer, H. Ç. (2018). Food Additives. Sakarya Medical Journal, 7(4), 164-167. https://doi.org/10.31832/smj.368978

Kaya, M. (2021). A study on the determination of bread consumption status and waste of university students. M.Sc. Thesis. Department of gastronomy and culinary arts. Ankara Hacı Bayram Veli University. Graduate School of Natural and Applied Sciences, Ankara.

Koptaget, E. (2019). Investigation of Antimicrobial Activity of Cinnamon Oil and Clove Oil by Microbiological Assay. M.Sc. Thesis. Sakarya University. Institute of Health Sciences, Sakarya.

Matan, N., Rimkeeree, H., Mawson, A.J., Chompreeda, P., Haruthaithanasan, V. & Parker, M. (2006). Antimicrobial activity of cinnamon and clove oils under modified atmosphere conditions. International Journal of Food Microbiology, 107, 180–185.

Mishra, V. K., Gupta, S. & Pundir, K. (2014). Synergistic antimicrobial activity of essential oil and chemical food preservatives against bakery spoilage fungi. CIBTech Journal of Microbiology. 4(1), 6–12.

Mohamad Asri, N., Muhialdin, B. J., Zarei, M. & Saari, N. (2020). Low molecular weight peptides generated from palm kernel cake via solid state lacto-fermentation extend the shelf life of bread. LWT, 134, 110206. https://doi.org/10.1016/j.lwt.2020.110206

Moraczewski, K., Pawłowska, A., Stepczyńska, M., Malinowski, R., Kaczor, D., Budner, B., Gocman K. & Rytlewski, P. (2020). Plant extracts as natural additives for environmentally friendly polylactide films. Food Packaging and Shelf Life, 26, 100593. https://doi.org/10.1016/j.fpsl.2020.100593

Oktay E., (2021). Effect of chlorpropham (cipc), mint oil and clove oil treatment on sprout physiology of storaged potato. PhD Thesis. Ankara University. Graduate School of Natural and Applied Sciences, Ankara.

Oliveira, M. A., Gonzaga, M. L., Bastos, M. S., Magalhães, H. C., Benevides, S. D., Furtado, R. F., Zambelli, R. A. & Garruti, D. S. (2020). Packaging with

cashew gum/gelatin/essential oil for bread: Release potential of the citral. Food Packaging and Shelf Life, 23, 100431. https://doi.org/10.1016/j.fpsl.2019.100431

Omedi, J. O., Huang, J., Huang, W., Zheng, J., Zeng, Y., Zhang, B., Zhou, L., Zhao, F., Li, N. & Gao, T. (2021). Suitability of pitaya fruit fermented by sourdough LAB strains for bread making: its impact on dough physicochemical, rheo-fermentation properties and antioxidant, antifungal and quality performance of bread. Heliyon, 7(11), e08290. https://doi.org/10.1016/j.heliyon.2021.e08290

Özdemir, G., Dülger Altıner, D. & Şahan, Y. (2021). The sensory properties of bread enriched with some medicinal plants and its effect on purchase intention. The Journal of Food, 767–784. https://doi.org/10.15237/gida.gd21044

Özpolat, E. (2019). Effects of Lemon (Citrus limon) and Bitter Orange (Citrus aurantium) Essential Oils on Microbiological Quality of Stored at 4±1°C Rainbow Trout (Oncorhynchus mykiss) F, 44(2), 185-190. https://doi.org/10.15237/gida.GD18128

Sayın, Ü. A. (2019). Investigation of antibacterial effects of some plant essential oils. Nevsehir Hacı Bektaş Veli University. Graduate School of Natural and Applied Sciences, Nevşehir.

Selçuk, B. (2020). Determining the clinical aromatherapy perspective of the patients applying to the pharmacy and the role of the clinical pharmacist in aromatherapy practices. M.Sc. Thesis, Istanbul Medipol University. Health Sciences Institute, İstanbul.

Sevim, M. G. (2019). Food safety risks in bakeries and hygiene and sanitation practices for safe bread production. M.Sc. Thesis, Bursa Uludağ University. Graduate School of Natural and Applied Sciences, Bursa.

Sharma, P., Ahuja, A., Dilsad Izrayeel, A. M., Samyn, P. & Rastogi, V. K. (2022). Physicochemical and thermal characterization of poly (3-hydroxybutyrate-co-4-hydroxybutyrate) films incorporating thyme essential oil for active packaging of white bread. Food Control, 133, 108688. https://doi.org/10.1016/j.foodcont.2021.108688

Sharma, S., Barkauskaite, S., Jaiswal, A. K. & Jaiswal, S. (2021). Essential oils as additives in active food packaging. Food Chemistry, 343, 128403. https://doi.org/10.1016/j.foodchem.2020.128403

Sunil, R. E. & Desai K. (2018). Vapour phase antifungal activity of C. Aurantium essential oil and its effectiveness in controlling common bread spoilage molds. World Journal of Pharmacy and Pharmaceutical Sciences. 7(4), 1603–1616.

Şahin, F. İ. (2022). Extending shelf life and optimizing effective parameters by using organic additives in food products. Graduation Thesis, Yildiz Technical University. Department of Chemical Engineering, İstanbul.

Taşçı, R., Karabak, S., Bolat, M., Pehlivan, A., Şanal, T., Acar, O., Külen, S., Güneş,

E. & Albayrak, M. (2017). The Production Structure of Bakery and Bread Wastage in Ankara Province. Journal of Agricultural Economics Research, 3(1), 1-16.

Thielecke, F., Lecerf, J. M. & Nugent, A. P. (2020). Processing in the food chain: do cereals have to be processed to add value to the human diet? Nutrition Research Reviews, 1–43. https://doi.org /10.1017/s0954422420000207

Yaman, T. & Kuleaşan, Ş. (2016). Advanced extraction methods for obtaining essential oil. Mehmet Akif Ersoy University. Journal of the Graduate School of Natural and Applied Sciences, Special Issue, 1, 78-83.

Yılmazaslan, B., (2008). The effect of natural food additives on bread making quality. M.Sc. Thesis. Afyon Kocatepe University. Graduate School of Natural and Applied Sciences, Afyonkarahisar.

Yurttagül, M. & Ayaz, A. (2008). Additives: wrong and right. Hacettepe University. Faculty of Health Sciences. Department of Nutrition and Dietetics. 1st Edition. Klasmat Printing. Ministry of Health Publication. Ankara.

Zorba, M., Demirağ, K. & Ova, G. (2005). Degradation kinetics of foods life prediction models. Akademik Gıda, 3(4), 17-22.
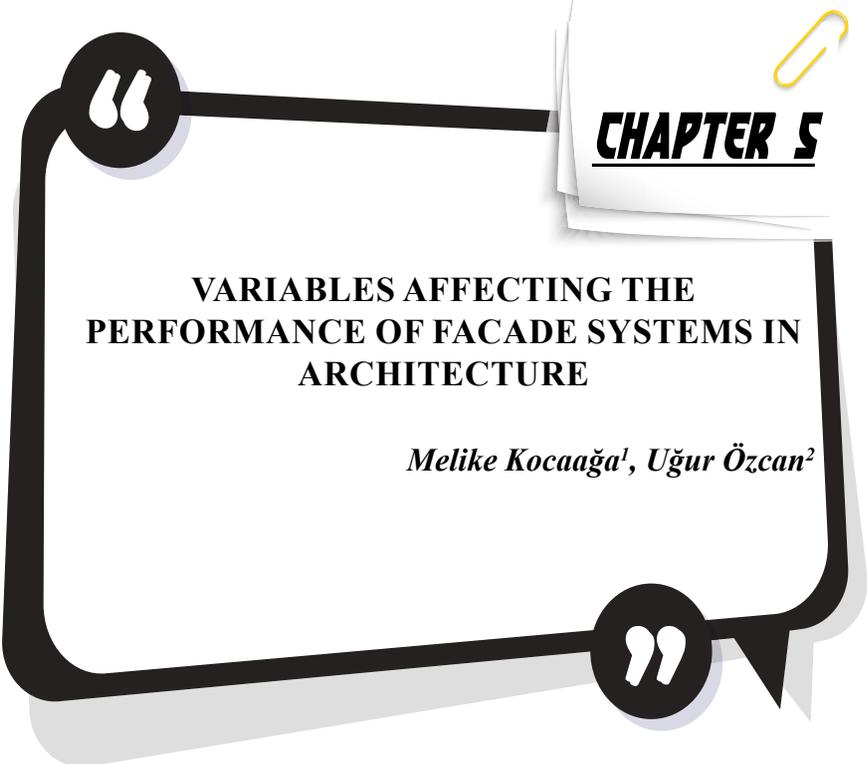
CHAPTER 5

VARIABLES AFFECTING THE PERFORMANCE OF FACADE SYSTEMS IN ARCHITECTURE

Melike Kocaağa¹, Uğur Özcan²

1 Master Architect, Fatih Sultan Mehmet Vakıf University, Graduate School, Department of Architecture, Architecture Graduate Program, İstanbul, Türkiye, e-mail: archmelikekocaaga@gmail.com (ORCID: 0000-0003-2295-6671)
2 Assistant Professor Dr., Fatih Sultan Mehmet Vakıf University, Faculty of Architecture and Design, Department of Architecture, İstanbul, Türkiye, e-mail: uozcan@fsm.edu.tr (ORCID: 0000-0003-0002-4478)

INTRODUCTION

Building systems should be considered as integrated packages, not as a stand-alone product. All systems of the structure, which can affect all organizational activities in the living spaces of the users, should be examined one by one and designed with a focus on user comfort. One of the challenges faced in the building industry today is the efficient use of energy. In recent years, we see that the priority of architects in sustainable architectural studies is to optimize the energy performance of buildings.
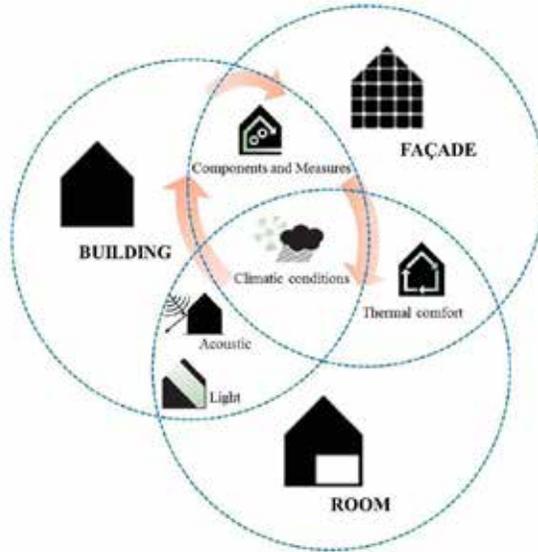
Figure 1. *Relationship Between Building-Facade-Interior (Jahed, 2018)*

The building, which is considered as a whole, interacts with the building directly and indirectly through the façade, which is the first contact surface it encounters with the outdoor conditions. The performance of the building is determined by the features of the facades in the face of the energy flow. The reactions that adaptive façades can realize in these various environments and conditions within the predetermined indicators, commands, targets and standards constitute the characterization of the building. With the correct planning of the specified performance indicators, energy resources can be managed in a controllable way depending on the surrounding physical areas. There are some factors that affect the performance of facade systems. These will be examined under the headings of various applications made with direct or indirect exposure to light, heat, noise, pollution, wind effect or security concerns. As seen in Figure 1., common components that are effective on the building, interior and facade are seen. When the building itself is considered as a whole, its scale, function, location; The factors

affecting the interior and the façade and each parameter should be planned accurately and effectively.

1. LIGHT EFFECT ON FACADE SYSTEMS

The use of daylight, which plays a strategic role in sustainable architecture, reduces energy use in buildings and provides energy savings. It reduces its formation and consequently global warming (Guzowski, 2000).

"The goals of daylight design can be defined from a variety of perspectives. These; ecological concerns (energy, consumption of natural resources and environmental impacts), services and activities (qualitative and quantitative lighting requirements), system integration (lighting, heating and cooling loads), human experience (visual comfort, health, well-being, orientation and orientation, environmental connections, etc.), aesthetic concerns (space, form, structure and articulation of materials, hierarchy and order) and other factors" (Guzowski, 2000). In the building design processes, these applications should be evaluated as a whole and it should be aimed to make the use of light effective. Sustainable use of light penetrating the surface or interior of the building should be taken into account, anticipating situations that may have a negative impact on the building (overheating, glare, etc.). Analysis of bioregional data is very important for a sustainable and renewable facade application. Bioregional factors affecting daylight, which is one of the environmental factors affecting buildings, are examined in Table 1.

The opacity-transparency ratios are redefined with the effective use of light in adaptive architecture. With the light models created, a sustainable design model is created by responding to the needs of the users, while the textures on the surface can be emphasized. A more dynamic version of the architectural composition can be created. Shading systems that can be applied in adaptive controlled facade systems are very important for more effective use of light indoors. Although temperature control is the first goal, shading elements provide efficient use of light. Adaptive shading systems can change shape, width, location or properties simultaneously or in a time sequence, as well as changing properties or behaviors on a macro or micro scale (Hraska, 2019). Here, the shading of the facade of the building with macro-scale moving elements; On the other hand, microscale is the optical and thermophysical changes in the materials of these elements against excessive temperature or excessive light intensity.

Observed Movement of the Sun		
Hours of the day	**Seasons**	**Geographic and spatial location**
The quality of the light, the degree of brightness and the mood it creates in people depend on different times of the day. is changing. This situation affects the users in the place, the activities and programs organized during the day. Rooms, window organization, form, texture and detailing in space at different times of daylight shaped by its effect.	Space design and organization of activities can be handled simultaneously with the effect of the seasons on daylight. Architecture that responds to the seasonal changes of daylight has to be dynamic in order to respond to the rhythm of the sun. Organization, position and detailing of windows; summer, winter, spring or it should respond to the needs of brightness and warmth in autumn.	The position of the sun not only gives us information about the latitude in the northern – southern hemisphere, but also gives us information about the spatial organization using the main directions.
Weather Forecast		
Universal Sequence	**Place**	**Colors and Form**
Agricultural, ceremonial, etc. many events not only depend on the movement of the sun but also on the weather. adjusted accordingly. Architecture that cares about the changing conditions and characters of the weather over time; It helps us to better observe and experience local, regional, global, and ancient universal formations.	Daylight design in architecture It should be location specific. The color, angle and quality of light depends on the latitude, weather and varies according to the climate prevailing in the region.	Weather affects the color and quality of daylight reflected in the architectural space. The relationship between weather and light also helps us to understand the form of the building. On a clear day the colors are saturated and bright, light and shadow increase depth and three-dimensional quality. Different weather conditions also provide different degrees of illumination and daylight distribution.
Climate and Area		
Relationship with the Environment	**Access to the Sun**	**Comfort**
Sunlight, environment and people critical in defining the quality of the link between has place. This situation primarily depends on the organization of windows in architectural design. This situation is the connection between the external environment and the internal environment and degree of discrimination, physical and visual relationship with the environment; and in terms of defining the entrance of the sun, wind, sound, smell is important.	The most important thing to consider in accessing the sun. The factor is land structure. The topography, slope, plant type and climate of the land are in this regard. are the subheadings to consider. In addition, for the spaces to be constructed in the architectural design process; direct sunlight? or? indirect light from the sky? should be preferred.	Regarding climate and terrain experiences are also related to our comfort regarding light and warmth. Different temperature in different climates The strategies for acquiring daylight are similar, although the effects of light and light are captured. Comfort in architectural design is generally; with shelter, warmth and light are associated.

Table 1. *Bioregional Factors Affecting Daylight Use (Tatar, 2013)*

Every application to be made should be specific to the place and the project itself. The size of the opening in the building, the material used in the facade, the type of glass used, the effectiveness of the solar control elements, etc. in the use of light on the facades. Improvements can be made with parameters such as Since each surface of the buildings receives light in different ways and degrees, for example, as in the example in Figure 2., the transparency of the surfaces and the panel shape to be added to the facade surface were determined and the goal of using daylight efficiently was established.
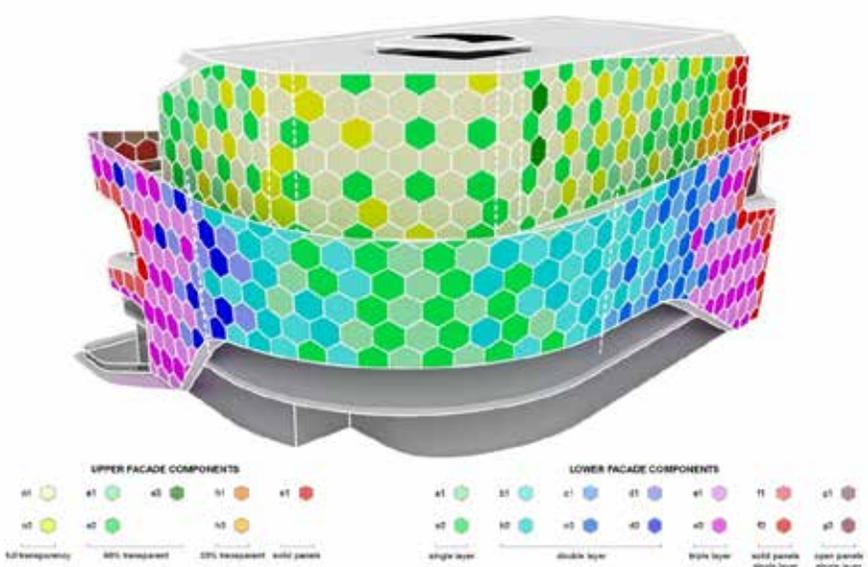
Figure 2. *Lane 189, UNStudio, Shanghai (url 1)*

Figure 3. *Lane 189, UNStudio, Shanghai (url 1)*

Shading elements can be considered under three headings as interior, exterior and alternative glazing. Overhangs and canopies, shutters and awnings, light shelves, exterior roller blinds are some of the exterior shading elements. Curtains and blinds are some of the interior shading elements. Electrochromic and liquid crystal glazing, photochromic glass and thermochromic glass are alternative glazing types (Phillips, 2004).

Shading elements to control light on adaptive facades can be applied depending on manual or motor-mechanical movement. When these elements are controlled manually, they will not meet the energy savings

and standardized parameters of the interior. An example of adaptive shading systems is the Arab World Institute (Institut du Monde Arabe) in Paris. The elements in the façade are controlled by motors connected to a central computer control and there are 30,000 photosensitive mechanical control diaphragms (Hraska, 2019). The radiation permeability values of the materials used to protect the building from the radiation coming from the sun's rays are also an important parameter.
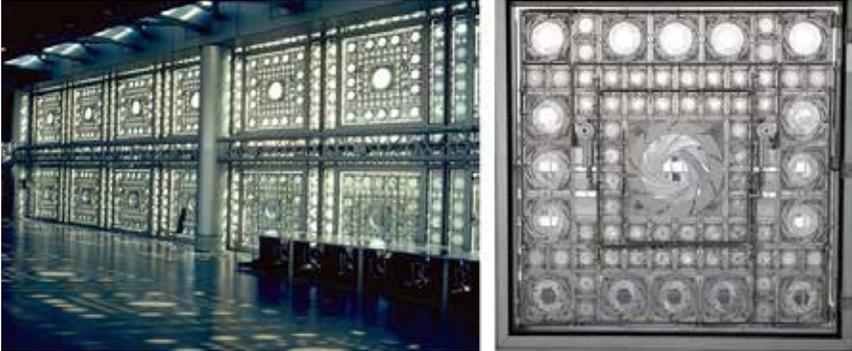
Figure 4. *Paris Arab World Institute's Adaptive Shading System (Hraska, 2019)*

Light-Material Effect on Facades

Material selection is one of the most effective components of facades, which is an important element in the formation of architectural design in buildings and the interaction between indoor and outdoor environment. While evaluating the physical environmental conditions, the most influential factor on the building in establishing a relationship with the light, which is one of the most effective data of the design, is the material. Adaptive facades are formed with smart materials that make qualified changes. Smart materials are materials that can change and adapt their properties (chemical structure, conductivity, fluidity, hardness, color, etc.) reversibly under the influence of environmental stimuli (wind, magnetic-electric field, heat, light, pressure, etc.). The quality changes made are very important in terms of the continuous or long-term response of the facade to the external environment, the sustainability of natural resources against global warming and the strengthening of building physics. We can consider the use of smart materials on the facade as Smart Materials Modifying Properties and Smart Materials for Energy Exchange.

On the facade of the building, this relationship can be interpreted in two ways;

1. To prevent the negative effects of solar radiation on the facade with elements that can be used on the facade.

2. To provide some or all of the energy required for the building from solar energy through the parts designed on the facade.

In both ways, the efficiency level of the facades can change according to the materials and types of use used in the relationship between the building and the sun. When determining the materials to be used in the building, based on environmental data, it can be preferred as interior-exterior or materials to be integrated later in the building itself. Adaptive shading systems can be systematized with physical/optical processes that protect a building from excessive solar radiation, as well as a combination of reflecting, absorbing, directing or filtering its light (Hraska, 2019).

For smart materials used for shading systems;

• Temperature reactive materials (shape memory alloys, shape memory polymers, shape memory hybrids, thermochromic polymers, thermotropic materials, phase change materials (PCM)),

• Materials that react to solar radiation (photosensitive polymers, photochromic materials, photovoltaic cells),

• Chromogenic materials (electrochromic glazing, gasochromic materials, liquid crystals, suspended particle devices),

• Other materials (electroactive polymers, piezoelectric materials, materials that change their magnetic properties) can be classified as. (Hraska, 2019).

The use of photochromic glass, which is one of the passive glass systems, in glasses, which is one of the most important factors affecting the performance of the facade, provides a change in quality with the effect of light. Photochromic glasses, which are widely used, reduce glare and the negative effects of ultraviolet rays. With different processes applied on the glass, its properties can be changed and its permeability can be adjusted according to different wavelengths. In cases where we can prefer this aesthetically, there are examples such as dichroic coated glasses, cold mirror coated glasses, reflective glasses, ceramic-enamel coated glasses, liquid crystal coated electrochromic glasses. In this case, a reflectivity level can be determined at the desired rate.

A passive shading system can be created on the facades with some textile materials with photochromic properties. This system; It can be applied as a result of the material to be added to the outside of the façade and the phase change of the sun rays depending on the direction and intensity conditions, as a result of receiving the light passing into the

interior at various intensities or ensuring that it is completely reflected.

The behavior patterns of the materials used on the exterior surfaces of the facades also change according to their durability, maintenance needs, shape and reflection properties. For example, blinds that can be applied vertically or horizontally are less durable materials. Various treated materials can also be used for less and longer durability (galvanized steel, anodized aluminum, etc.). In order to provide sunlight control on the façade, lower cost building elements and technologies such as sun shading, blinds, roller blinds have been developed recently. These systems, which are used as fixed or static shading elements, have a limited effect in terms of their potential to respond to environmental effects within a certain period of time.

Rigid facades, which increase the transparency of the facades and allow more daylight to enter the interior, reduce the long-term expected interior comfort and energy saving of the users in the building with glare or overheating problems after a while (Grynning, Lolli, Wågø, Risholt, 2017). For this reason, while a traditional window may be sufficient to allow sunlight to enter the spaces on the facades, advanced solution alternatives are being researched to provide more natural light to the space as the space depth increases.

2. HEAT EFFECT ON FACADE SYSTEMS

Throughout history, people have created various living spaces for their shelter by controlling natural conditions. It met these comfort conditions with natural and local materials, while the construction technologies were not that advanced yet; Suitable insulation applications have been made to the ground. However, the depletion of our energy resources has made it necessary to develop insulation technologies, make energy use more effective and produce new solutions in this regard. The reactions of the facades according to their potentials in the face of the sun effect; reflecting, absorbing, directing, filtering, transforming energy with the effect of stratification, etc. facade performance can be regulated as methods.

The façades mentioned in the first three items are the outer surface technologies that are in direct contact with solar effects. Double-skinned façades, green façades and roofs absorb sunlight so that they can reach the comfort targets set in summer and winter. Fixed systems are generally designed to direct sunlight and radiation; Systems that can be operated can be used to provide effects such as realization of thermal gain, reduction of glare or directing the energy in sunlight. While these can be manual or automatic, their intended use is to respond to outdoor conditions and provide compatibility. Thus, flexibility is gained to the structure.
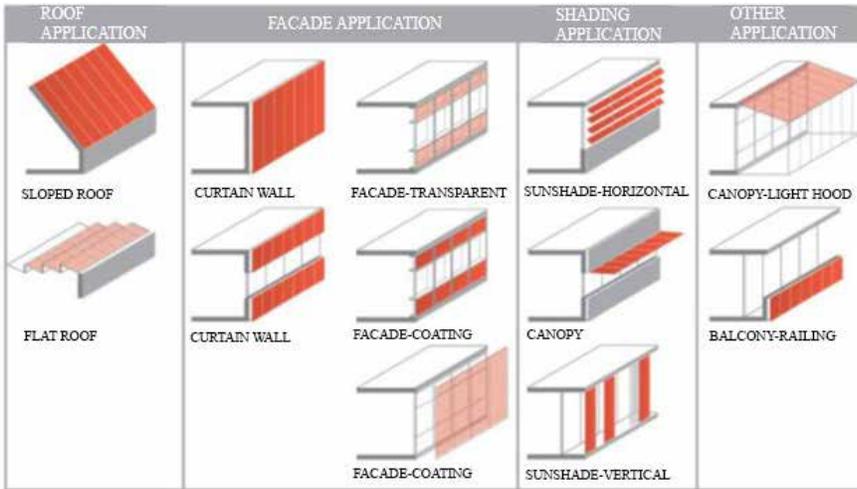
Figure 5. *Facade Integrations of Photovoltaic Systems (Aydoğan, 2018)*

The RMIT Design Center, located in Melbourne, structure is double-skinned and has an experimental façade that uses 17,000 solar-sensitive opaque glass panels on top. While the panels protect the building surface from the harmful rays of the sun, it is predicted that even though it does not contain photovoltaic panels, it can generate enough electricity for the entire building with glass panels. Inspired by Jean Nouvel's World Arab Institute in Paris, the structure provides thermal gain and structural resonance, while passive ventilation is also possible. Despite the World Arab Institute, the way it performs is more stable in the long run due to the presence of a building management system here.

Figure 6. *RMIT Design Center, Melbourne. (url 2)*

It is very important to store thermal energy in buildings to benefit from the radiation from the sun. In contemporary architectural designs, the building envelope is expected to maintain thermal comfort and lighting quality in the indoor environment under different conditions caused by climate changes (Schumacher, M., Schaeffer, O., & Vogt, M. 2010). Today, one of the first and first applied parameters to come to mind when it comes to ensuring energy efficiency in buildings is to determine the insulation properties of the elements that make up the outer shell of the building and to increase their thermal resistance. Various measures can be taken to prevent thermal bridges that may occur in buildings that cannot provide adequate thermal insulation, to balance indoor conditions, and to reduce the energy to be used for heating and cooling the building. For the building to be energy efficient and in appropriate thermal insulation applications; climatic conditions (sun radiation, wind, humidity, temperature, etc.), geographical features of the region where the building is located (location, altitude, etc.) factors should be considered. The solutions created to store the thermal energy integrated into the building are basically to reduce the time mismatch between the available energy and the demand for this energy and to store the energy for later use in the building. With the use of smart materials and systems, this need can be met and the attitudes of the facades towards heat can be adapted. But the important point is not only to generate power, but to create a smart skin with the effect of a mechanism that can learn this production and process data.

Heat Conduction and Thermal Expansion

The heat capacity of the elements used in the building is an important parameter to reduce the temperature fluctuations during the day and to balance the indoor temperature. Since industrial countries began to live in a Figure dependent on electricity and other fossil fuel energy sources, various ways have been developed to store thermal energy. In this section, the thermal conductivity of the materials used in the facades, the gains and losses as a result of this situation; The storage of thermal energy and the reuse of the stored energy by converting it into energy for the performance of the building when necessary will be mentioned.

The materials used can change their forms or directions, for example, with the reactions of the organisms in their components according to different environmental conditions. One of the examples of sensitive architecture without a mechanism, the Bloom Statue, designed by DO|SU Architecture, is designed as a sun tracking device with its computational form and the performance of the material against time against heat. Bloom Statue, one of the visible examples of smart material usage, was created with thermo-bimetal (TBM) material. Bimetallic elements consisting of thin strips react by combining two metals with different coefficients of

thermal expansion (CTE) by orienting in the heated direction when the temperature changes. The sensitive and hollow surface of the form shade and ventilate certain areas of the shell with the heating of the sun. By using materials with different levels of thermal expansion together, different performances can be achieved against other environmental stimuli.

Figure 7. *Bloom Statue by DO|SU Studio Architecture (url 3)*

Figure 8. *Homeo Static Facade System Example, New York (url 4)*

Innovative technologies are encountered when the movements of the smart elements used on the facades are examined within the scope of the energy conservation law. For example, insulating strips coated with silver electrodes can be seen between the glasses in the Homeo Static Facade seen in Figure 8. These strips provide solar control in the space by opening the strips with the increase in the temperature of the environment, while providing energy savings by balancing the heat loss and gain of the building (Edupuganti, 2013).

The type of behavior explained with the concepts of homeostasis or balancing is a phenomenological movement in which the cell regulates its internal structure in the face of adverse conditions developing in their

environment. This reaction to temperature occurs when the solar energy coming on the façade strips generates an electrical charge and moves by changing the structure of the elastomer. As a result of this movement, a balanced ambient temperature is formed within the structure. With thermal energy storage systems, direct cooling-heating can be done without the need for chlorofluorocarbons (CFCs), which damage the ozone layer (Konuklu, Paksoy, 2011). Thermal (heat) energy storage methods are divided into two as thermal method and chemical method. While the thermal method consists of sensible heat and latent heat; chemical method consists of reaction heat, chemical heat pump and thermochemical heat pump (Konuklu, Paksoy, 2011). This situation varies according to the thermal conductivity coefficient of the material used, that is, how fast it transmits heat and its thermal capacity or how much heat it can store. For example, phase change materials, which are one of the heat reactive materials, generally have low thermal conductivity. Summer and winter thermal comfort levels can be regulated by using materials with different melting and freezing temperatures together. The use of phase change materials at the point of providing thermal insulation in buildings increases energy storage efficiency and helps to balance the indoor temperature. Phase change materials are attractive because they have high latent heat storage density. Thus, they can be used as a solution to the energy mismatch in the production of renewable energy and 'Net Zero Energy', where the energy needs of the buildings are out of phase (Cellura, Guarino, Longo, Mistretta, 2014).

In a study commissioned by Rubitherm, FDMs (Phase Change Material) were placed on the ground to provide building insulation. When the system used is compared with conventional heating systems, it has been determined that it provides 35% reduction in energy consumption. It has the features of ease of application of phase change materials to building materials and increasing the heat gains of the building in the short term.

Applications such as façade systems with PCM material or microencapsulated paraffin wax-based PCM additive as a polymer added to the mortar and filling material enables the building to consume less energy by using the heat storage properties of phase change materials.

Glass is one of the smart materials that can change its properties according to temperature and light intensity by changing its structural properties or supporting it with different mechanisms in adaptive facades that generally provide passive movement. If we examine smart facades as single-layer or double-layer (skinned) facades, the type and thickness of the glass used, the number of layers, the distance between the layers, the filler gas, the coating material applied to the glass surface, especially in order to provide the desired level of sun and heat control in single-

layer smart facades. and the type and location of the solar control element (Okumus, 2020).

The effectiveness of smart glass systems used in facades on the facade is quite diversified today. The choice of glass type, which has a passive effect, is one of the important factors that determine the performance of the facade, because these points are one of the points in the building that are directly exposed to climatic factors and where the building exchanges the most energy. Low-e glass, known as low-emission and climate-controlled glasses, minimizes glass-related heat losses on facades in adverse climatic conditions. Unlike other solar control glasses used, the task of Low-e glasses is not to absorb sunlight, but to reduce the heat gain of the building by reflecting the light outside.

Thermochromic materials can also be used in various structures by adding them to some smart paints. For example; Thermochromic paint, which changes color between yellow and red all day long by interacting with the ambient temperature, is used in the stainless steel sculpture named "Earth", designed by Kiyoyuki Kikutake, standing in front of the Tokyo Museum of Modern Art (Orhon, 2012).

Figure 9. *Kiyoyuki Kikutake's "Earth" Sculpture (Orhon, 2012)*

In open weather conditions, cooling the building in the face of heating problems due to solar effect on the facades increases the cost of the building considerably. For this reason, alternative solutions are produced with the use of heat sensitive glass on the facades. Smart glasses; It is divided into two parts as passive systems activated by environmental effects such as light and heat, and active systems activated by electrical stimulation (Erkol, Sayın, 2021). Glass gains its character by changing its structural properties while it is being produced. With a normal fritting application, the glasses become fine-pored and gain the ability to pass liquid or gas molecules. In other words, it becomes a filter. This technology helps to

reduce the heat gain inside the building and can be used on facades to modulate daylight. Solar control is realized with a graphical solution in itself without the need for an additional element. While controlling this system with a motor provides a dynamic modulation, at the same time, with the movement that takes place, a traditionally fixed pattern is exceeded and an adaptively controlled permeability can be achieved. Figure 10. shows an example of the façade designed by Hoberman with the Adaptive Fritting System.
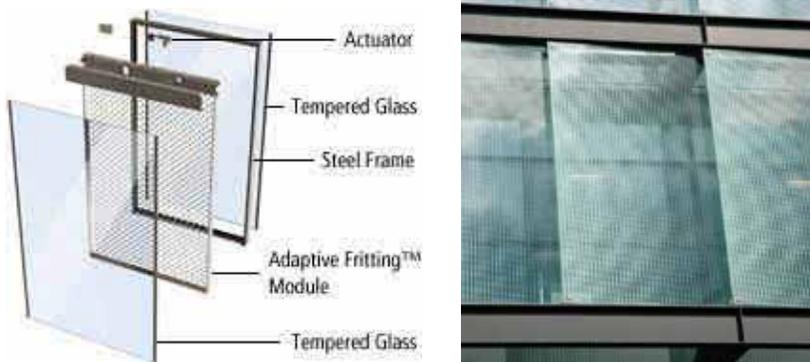
Figure 10. *Adaptive Fritting Front, Harvard Graduate School of Design, Hoberman (url 7)*

Living, responsive and energy-transforming facades can be created with systems working with the greenhouse effect applied to the facade. These applications can be applied between two layers in curtain wall or double-skinned facade, as well as in Figure integrated into the structure with photobioreactors. Experimental studies can be carried out on the conservation of CO_2 level on bio-fronts created by the use of aquatic or photosynthetic microorganisms that contain chlorophyll-a, such as algae. The main systems used to create a growth environment for algae are either open or closed culture systems, and closed systems in which algae are grown are called "photobioreactor" (Kükdamar, 2018). Algae cells activated by artificial or natural light energy; It is an effective application in the long term to use it for a sustainable, energy efficient and adaptive facade design by increasing the evaluation areas in the urban environment. For a thermally effective façade application, the algae layer applied to the façade surface as a different layer in the SymBIO2 project specified in Figure 11 passively manages climate change and the use of natural resources between environmental effects and the façade. A kind of aquarium layer created for the growth or activation of micro-algae is integrated into the façade surface. Compared to photovoltaic panels, it is a more active system in terms of cost, maintenance, installation and reaction process. Another example that establishes an interactive communication

on facades with solar energy is as an example to the building; It is the ICT (Information and Communication Technologies) Media Building, which helps to improve indoor conditions by working with the diaphragm movement against outdoor heat. It can be said that it is one of the lightest interactive structures with the use of a coating material called ethylene tetrafluoroethylene (ETFE), which is an eco-efficient material.

Figure 11. *Project SymBIO Facade View (url 8)*

Elements, which can be called a kind of air cushion applied with pneumatic systems on the facade of the building, begin to inflate by increasing their volume after a certain temperature level in the face of solar energy. The area inside the inflated part forms an air chamber and a thermal regulation is provided in this Figure. A flexible design was created by the ETFE elements acting as a cushion in the structure constructed with metal elements, creating a series of tensile forces in the structure. There is no central control system in the building, it detects environmental effects with the microcontrollers and pneumatic system on the hollow material used on the façade. With the movement realized by the deformation of this material, the structure adapts to the environmental elements.

Figure 12. *Media-TIC Building, Barcelona (url 9)*

One of the smart material technologies that respond to Solar Energy is the use of Figure memory alloys as facade material. The use of renewable energy with this innovative technology, which is becoming increasingly important especially in hot climate conditions, provides performance to the facade by minimizing the need for power sources. These materials, which can change their shape or size according to various stimuli, have the ability to have a reversible effect compared to other systems. They can work with detection, machine control or activator methods. They are interesting because of their low activation energies.

SHA (Figure Memory Alloys), which can be named in different Figures according to the environmental stimulus type; Working classes due to thermal changes are called Thermostrictive. With the 'Glass Panel Shutter' facade system, which is similar to the shutter system applied between two glass layers on the facade, and the thermo-bimetal (TBM) material, one of the Figure memory materials, when the panels are heated according to the temperature of the external environment, the surface performs a fractal change with an approach similar to the Hoberman design in the figures.

Figure 13, designed as a prototype by Yuliya Sinke. It is an application that affects the transparency rate of the structure during the day by changing the geometry and solid-liquid state transition by reacting against the temperature distribution of the Phase Change Materials (FDM) on the facade, with the transparent foil and the sensing components on it.

Figure 13. *The Broader Joint, Yuliya Sinke, 2018 (url 10)*

3. WIND EFFECT ON FACADE SYSTEMS

It is possible to reduce the amount of energy consumed in the building sector, especially for air conditioning systems, by targeting the use of renewable energy resources in the life cycles of buildings and the right

material selection, and the use of these resources on the building surface or incorporating them into the building. Heating of different parts of the earth at different values causes the air temperature, humidity and pressure to be different, and these pressure differences cause the air masses to move. This air flow is called wind (Aronin, 1953). When wind energy is considered as a transformed form of solar energy, active wind energy has great importance for the building. It is an environmental factor that is natural, does not produce waste, has a minimum negative impact on the environment since it does not have any harmful effects in its content, and is quite open to technological development.

Air movement, flow rate, directional movement, distribution of pressure zones created around and inside the building, etc., in the natural way of providing ventilation at an acceptable level for the building. factors should be examined. In this case, the location of the building is important in terms of air movement and benefiting from the heating effect of the sun (Balanlı and Darçın, 2012). The situation that occurs in positive or negative pressure differences affecting the surface determines the character of the wind. The performance of wind movement in passive ventilation systems varies according to the way the building meets the wind. As a result of this effect, the panels in the direction parallel to the wind movement show a push response towards the outside, while the panels placed in the perpendicular direction show a push response towards the inside. For this reason, facade systems should be planned in a figure that will balance the pressure exerted by the wind on the indoor and outdoor environments.
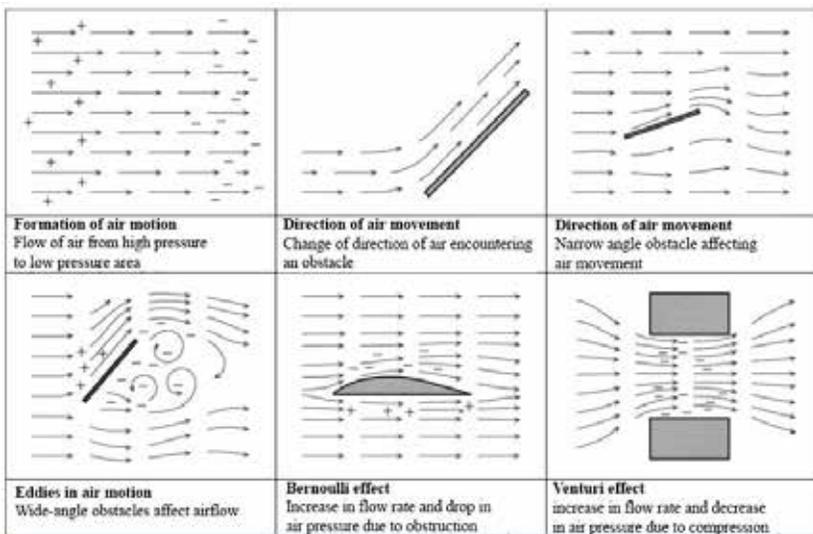
Figure 14. *Behavior Figures of Wind Movement (Balanlı, Darçın, 2012)*

As one of the passive ventilation examples in sustainable façade applications, it is aimed to provide energy efficiency with natural ventilation realized with ventilation shafts placed on the facade of the building seen in Figure 14. With the wind chimneys placed on the south façade, the efficiency of the air movement inside the chimney increases when the weather conditions are windy; In hot seasons, while the air is evacuated with the rise of the heated air, the air inside the building is also sucked due to the pressure difference. It is a very efficient application in catching the wind.

Positioning and pressure distribution at right angles to the direction of motion

Positioning and pressure distribution at an angle of 45 degrees with the direction of motion
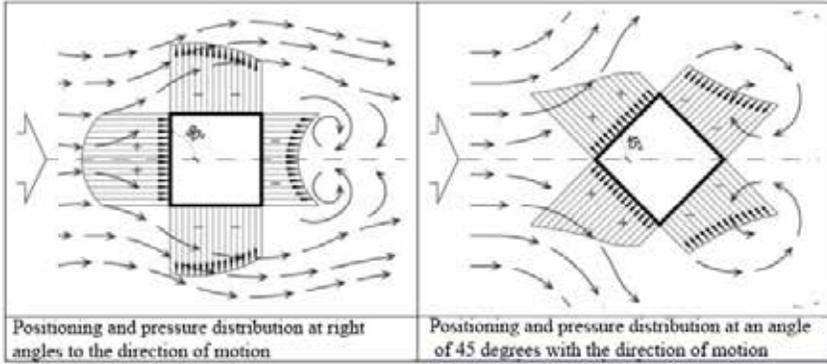
Figure 15. *Location of the Structure - Air Circulation and Pressure Relationship (Balanlı, Darçın, 2012)*

Figure 16. *BRE Office Building, Feilden Clegg Architects, England (url 11)*
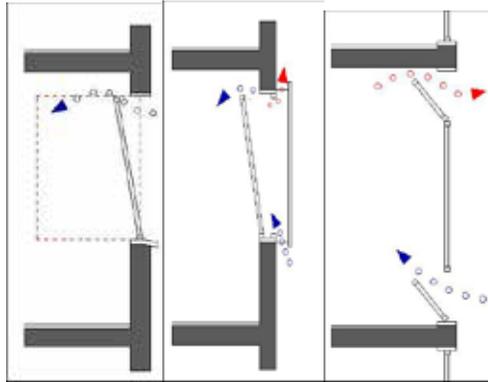
Figure 17. *Types of Ventilation Openings a) Window Ventilation b) Ventilation Through Double Shell Facade c) Ventilation Covers (Hausladen, Saldanha, Liedl, 2006, s.54)*
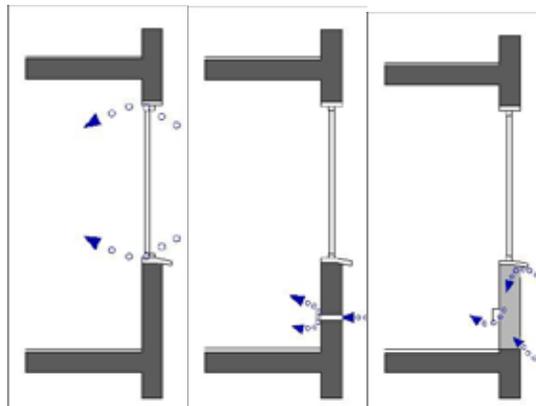
Figure 18. *Types of Ventilation Openings d) Infiltration e) Controlled Ventilation Elements f) Sound Insulated Ventilation Elements (Hausladen, Saldanha, Liedl, 2006, p.54)*

Figure 17 mentioned above and window ventilation applications are shown in Figure 18. In these cases, ventilation is performed on the facade by means of leakage. Window ventilation, in principle, can be provided if there are ventilation elements of different qualities on the facade (Hausladen, Saldanha, Liedl, 2006).

The amount of energy used for air conditioning in buildings is quite high. In particular, the energy consumed for cooling the building is higher than the energy spent for heating. Passive systems are insufficient when the outdoor temperature is very high or low. Double-layer facades, which can be used to enable natural ventilation for surfaces with high wind effect, especially in high-rise buildings, have been created to control the climatic effects throughout the building life cycle and to provide energy efficiency. Noise pollution is also reduced in the structure where a kind of buffer zone

is created. It can be examined in two groups according to the circulation method of the air between the double layer or the zoning method of this space created. In double-skinned facade systems, which can be applied naturally, mechanically and hybridly, the circulation can operate passively, with the pressure differences resulting from the wind force applied to the structure, or as the rising of the heated air. Figure 19. According to the application figures shown in , their performance changes according to the circulation intervals in the building.
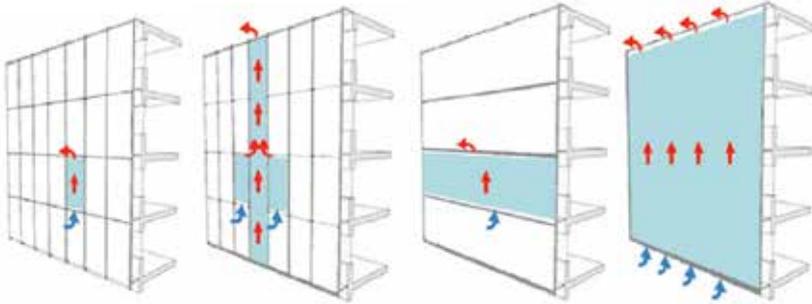
Figure 19. *Ventilation Options on Double Skin Facades (Saroglou, Theodosiou, Givoni, Meir 2020)*

In double-walled structures that provide air protection against solar shielding, the space through which the air can pass affects the amount of energy change it undergoes during the air movement. As seen in the third figure, more efficient results can be obtained from the double-layered facade applications, in which a corridor type is created at floor height, in order to have air exchange with the indoor environment on a floor basis and to intervene in a possible problem on the facade. Especially in high-rise buildings, it is not possible to open elements such as windows if the users want to interfere with the physical conditions of the interior.

Figure 20. *Wind Responsive Facade Design, Ned Kahn (url 12)*

If the air created by the fan systems used in the interior is given to the outside through the layers on the facade, it helps to reduce the heat loss from the facade. Fresh air is taken back into the building from this intermediate area and this space on the façade is included in the HVAC system. By placing the shading devices in the space, the cooling load is reduced in the summer months (Erturan, 2010). Today, wind energy is used as a primary use in buildings to generate energy. Wind turbines, which can be integrated into the building or installed, are one of the most used active systems against wind energy. Turbines used with photovoltaic cells produce the energy that the building needs daily and increase the facade performance. A long-term adaptation efficiency to the changes of climatic conditions cannot be achieved with conventional movements or the elements used alone.

In active ventilation systems, an action takes place when the elements on the facade surface or between the layers sense the air movement and as a result provide energy conversion. This conversion can usually be realized with smart sensors such as turbines, phase change materials (FDM) or mechanical actuators. For example; The Air Flower application, which helps to regulate indoor air quality by managing indoor and outdoor air flow on the façade without the need for a central computer system and a power supply, can be seen in Figure 21. Adapted from the movement of the yellow crocus flower in its natural environment, this mechanism offers active ventilation on the facades. By sensing the impact on it with the activator points on its corners, it opens and closes as a result of the movement of the wires inside with the effect of increasing or decreasing temperature or pressure.
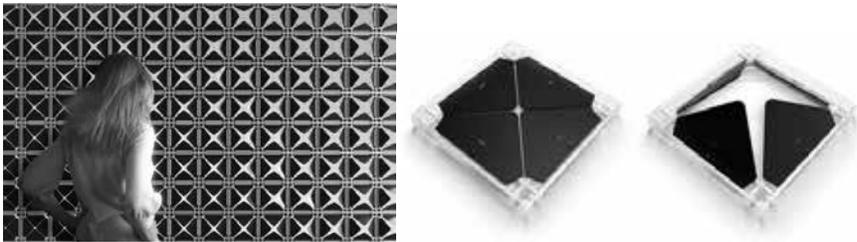
Figure 21. *The Air Flower, Lift Architects (url 13)*

OLED system, which is one of the materials that detect and react to environmental stimuli, basically responds quickly to the electricity applied to it and emits light. It is similar to conventional diode or LED systems but provides this movement with organic molecules. Figure 22 of the OLED system. It is a design that provides rotation with the wind

movement by applying it in the form of a turbine on the façade, as seen in Fig. Although they are designed to emit light, as can be seen in the Figures below, the turbine blades rotate according to the wind speed in the implemented project, creating different angle movements and different views are obtained on the facade. With the sensors on the panels, it gives the structure a characteristic appearance with its variability even in the absence of wind.
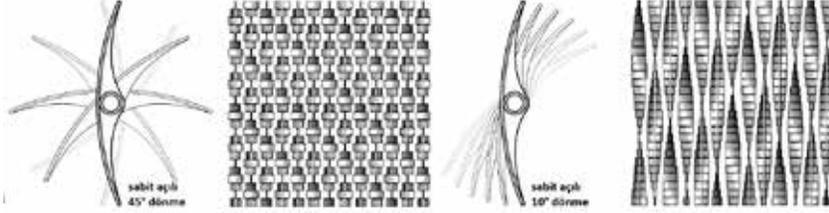
Figure 22. *Aliasing OLED Turbine Working Principle (url 14)*

In the Living Glass application created by S. Yang and D. Benjamin in 2005 in order to control the CO_2 concentration of Figure memory alloys (ŞHA) in spaces, it is aimed to create a gill effect on the facades with the inspiration taken from nature. When the CO_2 level increases, the electrical stimulus shortens the CHA wires and opens the slits to allow fresh air to flow in (Figure 23); the system becomes normal when the CO_2 level is equalized to the external environment (Ergin, Girgin, 2020). Innovative designs applied with the aim of efficient use of environmental resources such as natural ventilation are seen on double or more layered facades, which have started to be used in buildings in recent years. A more advanced version of double-skinned façades and a highly advanced system called closed-cavity façade or CCF (Closed Cavity Facade) is applied between two glass layers. It provides high amount of heat and sound insulation. The intervention for the air conditioning control, which is normally provided in addition to the double-walled system, is reconfigured in this system in a closed Figure and implemented in this Figure.
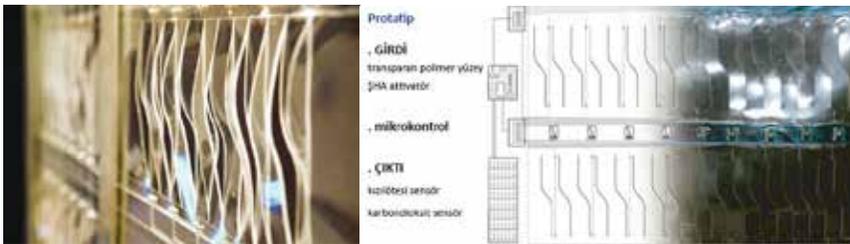
Figure 23. *Living Glass, S. Yang ve D. Benjamin (url 15)*

Figure 24. *K11 Musea, Kowloon, Hong Kong (url 17)*

Since it is a closed system, it is not affected by many environmental effects such as wind and rain, so it should be more careful in the selection of materials according to the performance it will determine against solar energy. By analyzing the environmental conditions well in the first steps of the design, for example, it is possible to adapt the louver, one of the shading control elements, to the environment with a central control software. With the active or passive system to be placed in this space, the facade performance can be increased to much higher levels. Since it does not have features such as reflection, diffusion, and filter, it is very efficient in terms of energy conservation in the interior. It can be ensured that the façade can communicate with the air conditioning systems, and the conditions of the system can be reprogrammed according to the changes in the external environment. In order to prevent condensation between layers, some dry air is fed.

While the purpose of the actively ventilated CCF is to control the air flow in the space, the purpose of the auto-operated windows is to control the air entering the building (Attia, Lioure, & Declaude, 2020).

4. EFFECT OF WATER AND MOISTURE ON FACADE SYSTEMS

The increase in water consumption with the effect of global warming and population growth on the earth causes a rapid decrease in natural water resources. Even if you are in a region with abundant water resources, the amount of water per person may be low. As a result of the water problem, it is not enough to try to protect natural resources; We need to minimize the amount of energy we use in our buildings and create an environment that is compatible with environmental elements.

Humidity effect is one of the biggest problems for buildings. There are many parameters that need to be examined, such as humidity in the air, the effect of rain, groundwater, the amount of moisture in the air flow, the liquid materials operating in the building, the effect of the wet volumes in the interior, the moisture holding capacity of the materials. Water (H_2O) increases its volume when it freezes, and when it is pure, it can react and damage the structure by forming mold and fungus. When a material receives an undesirable amount of moisture, the water holding capacity of the indoor or outdoor air affects its performances such as heating and lighting.

Smart buildings consist of many subsystems. Smart buildings, which meet their energy needs through these subsystems, need to protect themselves or adapt to these conditions from the effects of wind, humidity, precipitation, etc. These structures contain certain systems to prevent or incorporate weather conditions such as humidity and rain to which they are exposed. This water conversion in the air adapts to the humidity of the facades; It can be operated as absorption, collection and evaporation. Rainwater affecting the exterior surfaces of the building such as the roof and façade is collected and accumulated by various drainage methods or passed through carbon filters and used in areas such as toilet flushes and water needs of landscaping areas in daily need situations within the building and has an environmentalist approach in this figure.

Another method of evacuating rain water on building facades with waterproofing applied on the facade is the capillary suction method. The surface tension of water molecules is realized by being drawn into the pores in the materials of the structure. The longer the time the water comes into contact with the building, increases the amount of being taken in or trapped by the building. For this reason, it is very important to drain the water or to use the water efficiently. It also occurs when moisture enters the building in the form of steam with the air flow. Due to the moisture resistance of the material used on the facade or the pressure difference in the environment, it will exert a repulsive force between the spaces to the gaseous water vapor by diffusion of moisture or water vapor. The required application is to balance the humidity on the facade of the building or between other spaces. This balancing application is carried out with passive or active systems.

The volume of moisture entering a building through airflow through through holes can be 100 times greater than by diffusion. Diffusion through a 4 by 8 painted gypsum board can deliver about a third of a liter of water per day in a cold climate, but airflow through a one inch hole can be up to 30 liters (Hamilton, 2019). For this reason, various barrier applications are made in buildings against moisture and precipitation. While evaluating the "wetting potential" of the building, the "drying potential" should not be

forgotten. When it comes to waterproofing on the facade, it comes to mind that the surface is completely impermeable from water. There is no such expectation, on the other hand; Some kind of water-resistant barrier or moisture stabilizing elements should be placed after the coatings in place changes.

With the use of 'breathing' textile materials, which are increasingly used in architectural design, it is possible to create a passive working mechanism to control the flow of humid air inside and outside the building, to help air-conditioning the indoor environment and to create a buffer zone for some kind of humidity. This moisture-reactive material type, which helps the structure to adapt to humidity by providing the relative humidity balance in the environment and adapting to the changes in the humidity level in the environment, is called *hygroscopic*. Hygroscopic materials are materials that have the ability to absorb or absorb moisture. In particular, placement is made by taking advantage of the natural effects of cellulose-based hollow materials.

The amount of moisture also varies depending on the geographical effects in the regions on the earth. It is used in the air conditioning of the environment by ensuring the movement of the air in a mechanism consisting of several overlapping wet and dry layers with the *Evaporative Ventilation System*, which is applied in order to establish the humidity and temperature balance in regions where the humidity in the air is low.

As can be seen in Figure 25, Warka Towers, which are inspired by the basket knitting technique made in Ethiopia and formed with bamboo structure, harvest water. It was created to collect and store the potable water in the atmosphere. The outer bamboo structure supports a polyester material on the inside. The water drops caught from the air in the tower, which takes its working principle from various creatures in nature (Namib beetle carrying water vapor with the help of its wings, respiration method of cacti, dew grains caught in spider web, Lotus flower, etc.), accumulates in the tank formed in the center at the bottom, and in this region where it is very difficult to reach water. Harvested water is used with the application.

High relative humidity can cause high temperatures to be felt even higher, as the body is able to lose less heat to the surrounding air by evaporative cooling (through perspiration). Ventilated rain screen coatings created on facades are ventilated facade systems, especially in high or multi-layered structures. Rain screen coverings, which are generally made of natural materials, provide a structural protection by creating a ventilation gap between the facade and the facade.
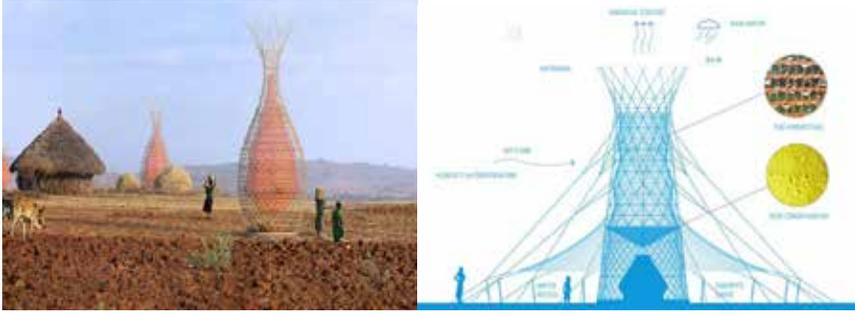
Figure 25. *Warka Tower Schematic Represantation (url 18)*
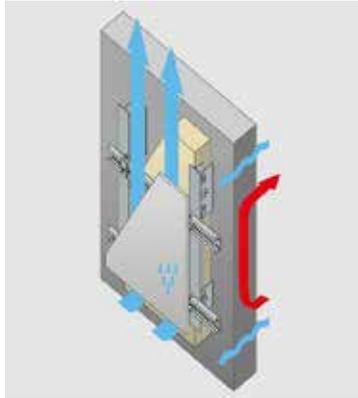
Figure 26. *Rainscreen Facade (url 19)*

The impregnation method, which is generally known to prevent the oxidation of wooden materials, that is, the nano-particle SiO_2 coating to prevent water leakage of the material, causes the pores to become water-repellent as a result of becoming a thin layer. For this reason, they can be used in buildings to prevent water from passing into the structure of the facade materials.

5. SOUND EFFECT ON FACADE SYSTEMS

The waves formed by the vibration of the particles in the environment create pressure changes in the air. These pressure changes are converted into electrical signals by the ear and perceived as "sound" by the brain (Özgüven, 1986). The sound frequency range that humans can perceive and be sensitive to is 16-20,000 Hz. An annoying level of sound can be described as noise. However, the characterization of a sound as disturbing may vary from person to person, depending on the type of sound, frequency level, duration and content and pressure. The sound pressure level (SPL) created by the noise reflections must be controlled while the sound

propagating in waves is dissipating. Two methods can be mentioned to control sound pressure. The first is to control the noise reflections with the façade setup and to ensure that the reflections are separated from the street canyon; the second is to use materials with high absorption coefficient, which cause effective loss in acoustic energy, on building facades (Sanchez, Van Renterghem, Thomas, Botteldooren, 2016).

Noise has various negative effects on human health. These include physical, physiological, psychological and performance effects. Depending on the noise intensity and duration of exposure, temporary or permanent hearing loss, acceleration in blood pressure and respiration, sleepiness and behavioral disorders can be seen in humans. In addition, decrease in work efficiency and concentration disorders may occur (Anonymous, 1998).

An increase of 10 dBA in the sound pressure level affecting the building increases the sound intensity, that is, the sound perceived by the user, by 2 times. Therefore, sound pressure control is very important. In order to ensure the auditory comfort that comes at the beginning of the comfort conditions of the users in the building, the factors that create the noise should be determined before the effect of the noise on the building. These factors should start with the planning that should be done on an urban scale, for example, residential buildings should not be placed near structures such as main traffic arteries, industrial or airport zones. Noise from the external environment; It passes into the interior space from areas such as the facade of the building, cavities, transparent openings or due to the low sound insulation properties of the materials. The selection of materials to be applied at these points should be determined by considering the optimum sound range. Although it is a less costly and environmentally friendly approach to reduce the level of noise from its main source, control of sound transmission is essential in any environment.

While designing the facade, the noise regulation for the environment and interior should be checked and the noise limit values and exposure times should be calculated for the environments. The determined average Leq (Equivalent Noise Level) values should be based on. Depending on the characteristics of the environment in which the buildings are located, there may be different levels and characteristics of noise from each other. These noises, which reach the building by spreading in the air or solids, affect the building users by passing through various openings or the building envelope (Yüksel, Akdağ, & Aknesil, 2016).

Noise situations that are not caused by the external environment affecting the building are mostly seen in curtain wall. In this case, the sound is generated by rippling through the spaces created in the façade volume or indoors due to the absence of sound insulation or noise-preventing elements

between the floors or the separating elements. There are situations that cause direct and indirect noise effects on the structure. Various barriers are used to reduce the noise effect in buildings or in areas where there is dense outdoor space. As an example of passively preventing noise barriers;

• Noise barrier application with polycarbonate or sound absorbing materials applied to roadsides and highways

Figure 27. *Noise Barrier Application (url 20)*

• Providing sound insulation with geo-textile-based green wall application created with landscape elements on the facade

Figure 28. *Green Wall Application (url 21)*

• Use of multiple layers on facades

Figure 29. *Cambridge Library Double Skin Facade Example (url 22)*

- The use of materials that absorb sound or reduce sound pressure on the façade reduces sound transmission.

Figure 30. *Rue des Suisses Apartments, Herzog de Meuron, Paris (url 23)*

In case of exposure to low-frequency sound (<1000 Hz) on façades, the use of passive methods cannot be healthy solutions for the façade as it may cause changes in the structural load and volume of the building. Adaptive façade targets can be realized by improving the properties of façade elements from active systems. The façade should be active, have an effective, light and environmentally friendly structure in terms of noise effect or acoustic performance.

Among the traditional passive methods used to prevent noise and provide sound insulation, the use of multi-layered glass or sound insulation materials is one of the most used methods with the effect of technological developments today. There are various noise barriers applied to slow down the sound transmission, reduce its frequency or stop it completely. The first of these is the use of soundproof glass.

Figure 31. *Sonomorph, NatasaZednik (url 24)*

In the smart system called Sonomorph, designed by Natasa Zednik, inspired by the biophilic design, it absorbs sound energy and transforms the stored energy into kinetic and lighting energy with a smart mechanism. It reacts to stimuli by making opening and closing movements. The LED lighting response is realized by the touch of the users.

6. POLLUTION EFFECT ON FACADES

Today, the deteriorating climatic balances, the destruction of our natural resources and the deterioration of the balance of energy transformations in the ecosystem are warnings that we should take into account in order to use our resources with great care in sustainable building design. It is thought that the expenditures for the cleaning of the facades of the buildings have a significant share among the cleaning services, which are estimated to spend 150 billion dollars a year worldwide (Pauli, 2010). When it comes to the cleaning of facades, especially high-rise buildings, loss of life and injuries are among the most stated causes of death in the cleaning sector. For example: In the UK, 20 people die annually in accidents during window cleaning, while 1500 people are injured (BRE, 2016).

In the Self-Cleaning (KT) façade category created in this direction, the aim is to reduce and eliminate the environmental pollution and the building's own use on the façade without any intervention. This application, which is created 'actively' with smart materials, is realized with three types of surface mechanisms. These; (Orhon, 2014)

- Superhydrophobic Surfaces

- Photocatalytic/Superhydrophilic Surfaces

- Non-Stick Surfaces

Barthlott, who received a patent as the 'Lotus Effect' in 1988, examines the self-cleaning, nano/micro dimension with the 'superhydrophobic surface' application and produces various paints, etc., by giving a reaction similar to the reaction of the lotus flower in nature. It has led to the start of studies for its use in materials. The paint creates a lotus effect by creating a wavy micro-structure on the surface; It creates a 140° contact angle between the surface and the water droplet falling on it, making the surface it covers superhydrophobic. Matte-colored paint, which can be applied to masonry surfaces (concrete, masonry, etc.) with a brush, roller or airless spray, cannot be applied to wood and metal surfaces (STO, 2005).

Figure 32. *Self-Cleaning Surface Mechanism with Lotus Effect (Zhang, Feng, Wang, Zheng, 2016)*

With the use of Titanium Dioxide (TiO₂) on the facade, the surfaces that have the effect of breaking down substances that have a polluting effect or potential on the surface under the influence of light, water (H_2O) and carbon dioxide (CO_2) molecules are called Photocatalytic / Superhydrophilic Surfaces. have also earned. Even though the process is a little slow, even when the weather is not sunny, the system can work thanks to a thin film applied on the glass and it removes the polluting elements on the surface and prevents water from remaining on the surface.
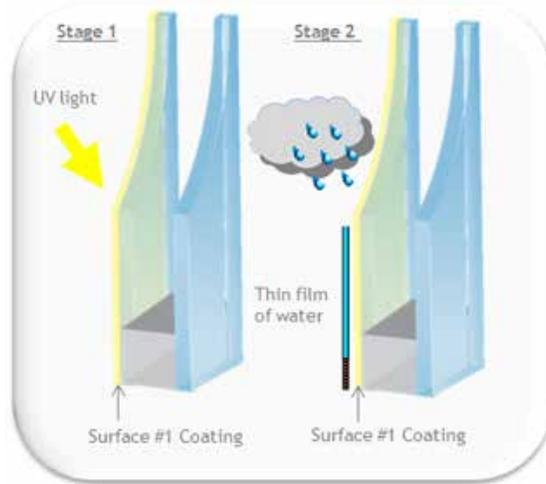
Figure 33. *Working Mechanism of Self Cleaning Glasses (url 26)*

Figure 34. *Pollution Eating Concrete Application Adams-Sangamon Park, Chicago (Orhon, 2014)*

As can be seen in Figure 34, the feature of the material, such as taking the pollutant elements under its influence and removing them or not keeping them on the surface, was implemented in a playground in the USA. In a study conducted in the Netherlands within the scope of a similar application (PCA, 2012), it was found that the photocatalytic concrete

pavement reduced the amount of nitrogen oxide in the region by 25-45% when the effectiveness of the coating of photocatalytic concrete material used on the pavement in a heavily trafficked area was compared with the effectiveness of a normal concrete pavement pavement. The facade with photocatalytic material, seen in Figure 35, is another example showing self and air cleaning performance.

Figure 35. *Photocatalytic Facade Example, Manuel Gea Gonzalez Hospital, Mexico City (url 27)*

CONCLUSION

Facades are non-load bearing structural elements that contribute to buildings, both structurally and architecturally. From an architectural viewpoint, facades are the soul of the building as they establish the tone for the rest of the building and they play a significant part in its aesthetics. Technically, facades are barriers that inhibit the aggressive exterior environmental conditions and forces from entering the "artificial" interior environment (Moghtadernejad, Mirza, 2014).

The performance of a structure is realized by reducing the risks that may pose a threat to structural security. Influencing its performance with technical interventions on the structure; It can be realized by the functional effectiveness of materials, building components and various elements inside and outside the building units and the building's ability to maintain this effectiveness. The performance of the structure is directly related to the service ability and service life of the structure. Service life of building surfaces; The resistance of the facade to external environmental conditions and its ability to adapt itself to ambient conditions affect it. The performance of an adaptive façade, apart from the static phenomena affecting the façade; light, heat, wind, precipitation, humidity, noise, pollution, protection against chemicals, safety, fire, cost, etc. can be

achieved by properly addressing the effects.

Loonen et al. (2015) on 130 projects, environmental stimuli were examined according to the adaptation needs of the facades. As seen in Figure 4.1.1., the factors triggering the adaptation process of the façade are approximately 73% solar variable effect, 72% temperature-temperature variable effect, 25% wind variable effect, 19% based on residential structures. precipitation effect, humidity variable effect with 9% and noise effect with 9%.
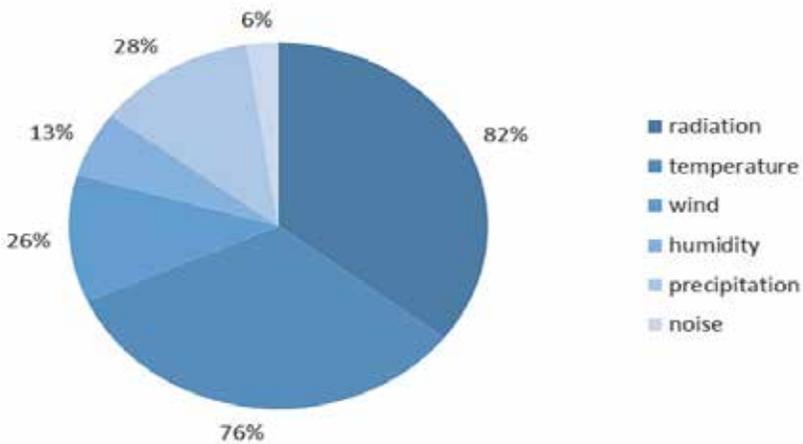
Fig. 4. Global distribution of external factors.

Figure 36. *Distribution of External Factors Most Influencing the Front (Loonen ve oth. 2015)*

Adaptable building skins based on performance, which can change according to environmental factors, increase the living comfort of users, ensure sustainability, reduce operating costs and extend the life of the building thanks to the integration of other disciplines with architecture (Karakoç, 2015). Performative fronts can change their behavior recursively and reversibly in the face of environmental variables over time, and thus they can adapt to boundary conditions. With the systems used in the building, efficiency can be achieved by adapting to environmental boundary conditions and dynamic variables such as climatic or user needs.

REFERENCES

Akdağ N., Aknesil A. ve Yüksel Z., (2016). Yalıtım, Gürültü Denetimi, TMMOB Makine Mühendisleri Odası, Yayın No: MMO/664, ISBN: 978-605-01-0899-6, İstanbul.

Anonim, (1998). Türkiye'nin Çevre Sorunları, Türkiye Çevre Vakfı Yayın No: 131, Ankara.

Attia, S., Lioure, R., & Declaude, Q., (2020). Future Trends And Main Concepts Of Adaptive Facade Systems. *Energy Science & Engineering*, *8*(9), p: 3255-3272.

Aydoğan, Ö. Ç. D., (2018). Ses Verileri Etkileşimli Dinamik Adaptif Bir Cephe Önerisi Sound Shield, İstanbul Teknik Üniversitesi, Fen Bilimleri Enstitüsü, Yüksek Lisans Tezi. İstanbul.

Balanlı, A. ve Darçın, P., (2012). "Yapılarda Doğal Havalandırmanın Sağlanmasına Yönelik İlkeler", Tesisat Mühendisliği Dergisi, sayı:128, p: 33-42.

BRE, (2006). "The quantification and evaluation of the benefits of self-cleaning glass", Building Research Establishment (BRE), Research Report.

Cellura, M., Guarino, F., Longo, S., & Mistretta, M., (2014). Energy life-cycle approach in Net zero energy buildings balance: Operation and embodied energy of an Italian case study. *Energy and Buildings*, *72*, p: 371-381.

Edupuganti, S. R., (2013). Dynamic Shading: An Analysis, Master's thesis, University of Washington.

Ergin, Ö., & Girgin, Z. C., (2020). Uyarlanabilir Cephe Sistemlerinde Figure Hafızalı Alaşımlar ve Uygulamaları. *AURUM Journal of Engineering Systems and Architecture*, *3*(2), p: 169-181.

Erkol, E., & Sayın, S., (2021). Akıllı Cam Cephe Sistemleri ve Teknolojileri. *Online Journal of Art and Design*, *9*(1), p: 2.

Grynning, S., Lolli, N., Wågø, S. I., & Risholt, B. D., (2017). Solar shading in low energy office buildings-design strategy and user perception.

Guzowski, M., (2000). *Daylighting for sustainable design*. Mc Graw Hill.

Hamilton, L., (2019). Moisture Management and Façade Design, Building Enclosure.

Hraska, J., (2018). Adaptive solar shading of building. International Review of Applied Sciences and Engineering. s, 9(2), p: 107–113. doi: 10.1556/1848.2018.9.2.5

Jahed, N., (2018). *Performance based façades: retrofit strategies for energy efficiency and comfort in existing office buildings* /Master's thesis, Middle East Technical University/.

Karakoç, E. (2015). *Performansa Dayalı Adaptif Bina Kabuğu Tasarımı*, İstanbul Teknik Üniversitesi, Fen Bilimleri Enstitüsü, Doktora Tezi. İstanbul.

Konuklu, Y., & Paksoy, Ö. H., (2011). Faz değiştiren maddeler ile binalarda enerji verimliliği. Ulusal Tesisat Mühendisliği Kongresi, İzmir.

Kükdamar, İ., (2018). Cephelerde Fotobiyoreaktör Kullanımının Binaların Sürdürülebilirliğine Etkisi. *Tesisat Mühendisliği*, *2018*(166), s: 34-48.

Loonen, R. C. G. M., Rico-Martinez, J. M., Favoino, F., Brzezicki, M., Ménézo, C., La Ferla, G., & Aelenei, L., (2015). Design for façade adaptability– Towards a unified and systematic characterization. In *Proc. 10th Energy Forum-Advanced Building Skins, Bern, Switzerland* (p.p. 1274-84).

Moghtadernejad, S., & Mirza, S. (2014). Performance of building facades. *4th Structural Specialty, Canadian Society for Civil Engineers (CSCE), Halifax*.

Okumuş, E. M., & Eren, Ö. (2015). Sustainable Approaches In Sun Controlled design On Facades. Presented at the The 2nd International Conference with Exhibition S.ARCH "Environment and Architecture", Montenegro

Okumuş, E., (2020). Sürdürülebilir Mimarlık Kapsamında Akıllı Cephe Sistemlerinin İncelenmesi. Academic Perspective Procedia, 3(1), p: 267-281. DOI: 10.33793/acperpro.03.01.54

Orhon, A.V., (2012). 'Akıllı Malzemelerin Mimarlıkta Kullanımı', Ege Mimarlık, Aralık, 82, p: 18-21.

Özgüven, N., (1986). Endüstriyel Gürültü Kontrolü, TMMOB Makine Mühendisleri Odası Yayın No: 118, Ankara.

PCA, (2012). "Self-Cleaning Concrete: Building a Better (Cleaner) World in the 21st Century", PCA – Portland Cement Association.

Saroglou, T., Theodosiou, T., Givoni, B., & Meir, I. A. (2020). Studies on the optimum double-skin curtain wall design for high-rise buildings in the Mediterranean climate. *Energy and Buildings*, p: *208*.

Schumacher, M., Schaeffer, O., & Vogt, M. M. (2012). *Move: architecture in motion-dynamic components and elements*. Walter de Gruyter.

STO, (2005). "StoLotusan Color", STO AG., Technical Data Sheet: 3206/INT. EN.

Tatar, E., (2013). Sürdürülebilir mimarlık kapsamında çalışma mekanlarında gün ışığı kullanımı için bir öneri. *Süleyman Demirel Üniversitesi Fen Bilimleri Enstitüsü Dergisi*, *17*(1), p: 147-162.

Zhang, M., Feng, S., Wang, L., & Zheng, Y. (2016). Lotus effect in wetting and self-cleaning. *Biotribology*, *5*, p: 31-43.

INTERNET REFERENCES

Url-1:<https://www.unstudio.com/en/page/11768/> (Erişim Tarihi 08.02.2022).

Url-2: <https://www.ribaj.com/intelligence/rapid-response-unit> (Erişim Tarihi 14.03.2022).

Url-3:<https://www.archdaily.com/215280/bloom-dosu-studio-architecture?ad_medium=gallery> (Erişim Tarihi 14.03.2022)

Url-4:<https://www.archdaily.com/101578/moving-homeostatic-facade-preventing-solar-heat-gain> (Erişim Tarihi 14.03.2022).

Url-5:<http://www.rubitherm.com> (Erişim Tarihi 07.04.2022).

Url6:https://www.cloudchem.com.cn/?gclid=EAIaIQobChMI_Ofc78Tb6QIVy5RCh2LiQTuEAAYASAAEg%20JHFvD_BwE (Erişim Tarihi 08.04.2022).

Url-7:<https://wyss.harvard.edu/news/ingber-ecological-urbanism/> (Erişim tarihi 24.03.2022).

Url-8:<https://www.archilovers.com/projects/160853/symbio2.html> (Erişim Tarihi, 13.04.2022).

Url-9:<https://www.archdaily.com/49150/media-tic-enric-ruiz-geli> (Erişim Tarihi 07.04.2022).

Url-10:<https://fcbstudios.com/work/view/new-environmental-office-bre> (Erişim Tarihi 08.04.2022).

Url-11:<https://fcbstudios.com/work/view/new-environmental-office-bre> (Erişim Tarihi 08.04.2022).

Url-12:<https://nedkahn.com/portfolio/wind-veil> (Erişim Tarihi 7.04.2022).

Url-13:<http://www.liftarchitects.com/air-flower> (Erişim Tarihi, 12.04.2022).

Url-14: <https://aoarchitect.us/2015/08/oled/> (Erişim Tarihi, 13.04.2022).

Url-15:<https://www.architectmagazine.com/technology/products/six-responsive-products-that-have-a-mind-of-their-ownalmost_o> (Erişim Tarihi, 13.04.2022).

Url-16: <https://gbdmagazine.com/closed-cavity-facades/> (Erişim Tarihi, 15.04.2022).

Url-17:<https://www.archdaily.com/49150/media-tic-enric-ruiz-geli> (Erişim Tarihi 07.04.2022).

Url-18:<https://www.warkawater.org/design-is-not-how-things-looks-but-how-things-work/> (Erişim Tarihi, 16.04.2022).

Url-19: <https://keil-fixing.de/en/system/ventilated-rainscreen> (Erişim Tarihi, 18.04.2022).

Url-20:<https://www.palram.com/solution/acoustic-barriers-construction-architecture/> (Erişim Tarihi, 20.04.2022).

Url-21: <https://jakob.co.uk/gallery/solution/green-walls/> (Erişim Tarihi, 20.04.2022).

Url-22:<https://www.archiexpo.com/prod/josef-gartner/product-58213-992751. html> (Erişim Tarihi, 21.04.2022).

Url-23:<https://arquitecturaviva.com/works/viviendas-en-la-rue-des-suisses-paris-4> (Erişim Tarihi, 21.04.2022).

Url-24: <https://materialdistrict.com/> (Erişim Tarihi, 22.04.2022).

Url-26:<https://www.pilkington.com/en/global/products/product-categories/self-cleaning#> (Erişim Tarihi, 23.04.2022).

Url-27:<https://inhabitat.com/mexico-citys-manuel-gea-gonzalez-hospital-has-an-ornate-double-skin-that-filters-air-pollution/> (Erişim Tarihi, 23.04.2022).S
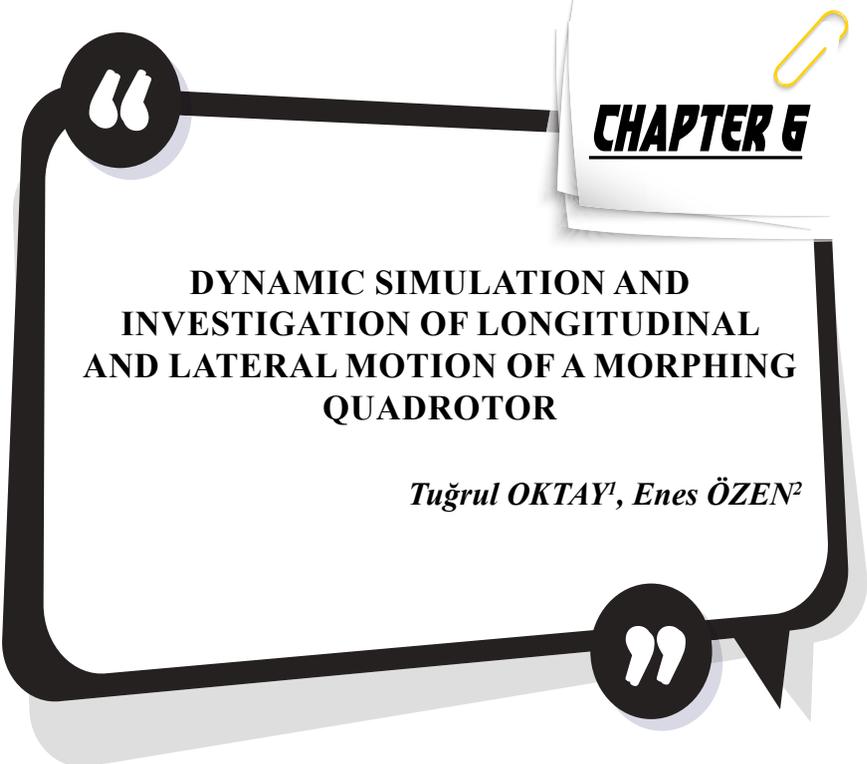
DYNAMIC SIMULATION AND INVESTIGATION OF LONGITUDINAL AND LATERAL MOTION OF A MORPHING QUADROTOR

Tuğrul OKTAY[1], Enes ÖZEN[2]

1 Prof. Dr., Erciyes Üniversitesi Havacılık Ve Uzay Bilimleri Fakültesi, Uçak Mühendisliği, oktay@erciyes.edu.tr
2 Öğr. Gör. Hasan Kalyoncu Üniversitesi, Meslek Yüksekokulu, İHA Tek. Ve Op. Pr., enes.ozen@hku.edu.tr

1. Introduction

Unmanned aerial vehicles are vehicles controlled from the ground by radio waves. It is widely used for civil and military purposes [1]. Different aircraft types are used for indoor and outdoor missions [2]. Thanks to the sensors on the aircraft, they are autonomous [3]. For indoor applications, rotary wing aircraft are preferred due to their hovering ability [4]. The shape change feature is necessary for aircraft to be able to avoid obstacles and pass through narrow places for indoor missions [5]. Aircraft can change shape during or before flight [6]. Just as birds bring their wings close to their body during short flight [7]. Rotary-wing aircraft can change shape by shortening and lengthening its arms [17]. In this study, the effects of the shape change of a quadrotor aircraft on forward and side flight were prepared by evaluating similar studies [8]. The dynamics of the quadrotor aircraft were derived using Newton Euler management [9]. The effects of shape change were examined [10]. Simulation was carried out in the matlab program using the obtained mathematical modeling [18].

The main components of the quadrotor are the following in figure 1. The frame, which gives physical support and binds the other components together. The frame consists of a central part and four arms. At the center of the frame electronics and the battery are hosted. On each arm there is a motor connected to a propeller. So we can say that the quadrotor has five main components the frame, the electronics, the battery, the motors, and the propellers [19]. This is a block diagram of the quadrotor system.
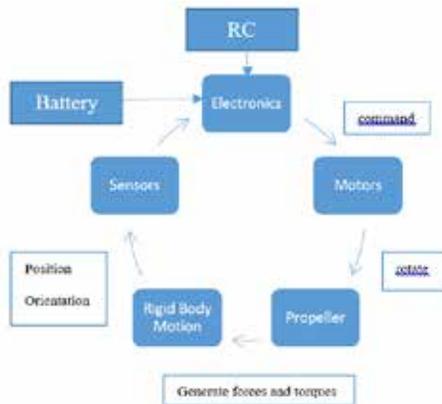
Fig. 1. Block Diagram

Here is the overview, the battery powers the electronics. The electronics contain flight code and communicate with the Remote Control or a Supervisory Control Center. The electronics output command signals for each of the motors. The motors are connected to the propellers which will spin and generate forces and torques on the quadrotor frame (Fig. 2). From

forces and torques, by the laws of physics, the quadrotor changes position and orientation. We will look in more detail at three elements the physical laws of motion that is the rigid body motion block. At the flight code on the electronics namely PID controllers for flights stabilization and the position control.

Fig. 2. Sahinbey-Quad Izometrik View

2. MATERIAL AND METHOD

2.1. Principles of Flight

A spinning propeller creates thrust a force that is perpendicular on the propellers rotation plane. For example if the propeller is rotating in the horizontal plane the thrust force will be vertical either up or down depending on the rotation of the propeller and its type. Besides the thrust force a spinning propeller also produces torque or a turning effect on the quadrotor frame [20]. It is important to mention that by clockwise and counterclockwise we mean the directions of rotation as seen from above looking down at the quadrotor. And finally, a quadrotor has two type 1 and two type 2 propellers. And now let's see some propeller in figure 3 we are now looking at a type 1 or counterclockwise propeller. This means that when the propeller is rotating counterclockwise like on the left hand side figure, the produced thrust is up. The black dashed line shows the rotation of the propeller. The thrust force is shown in blue. The turning effect of the propeller on the quadrotor frame is shown in green. The turning effect is always opposite the propellers own rotation irrespective of the propellers type. In Figure 3, we see that for an opposite clockwise rotation the thrust forces is down.

Fig. 3. About Propellers- Type 1 a) CCW and b) CW [23]

In figure 4, this is a type 2 or clockwise propeller. To produce upward thrust the propeller must turn clockwise like on the left hand side.
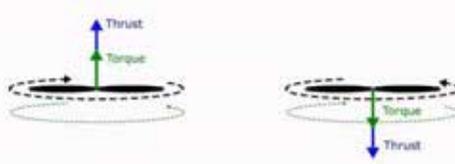
Fig. 4. About Propellers- Type 2 a)CW and b)CCW [23]

An interesting fact about quadrotors is that that they are an underactuated system. There are six degrees of freedom or maneuvers or motions that can be performed in the 3D space. Three of them are translational and three of them are rotational [18]. The translational degrees of freedom are moving up and down forwards and backwards left and right. The three rotational degrees of freedom are changing heading pitch and roll. But we have only four commands that we send to the motors. We will see that because of this, some of the degrees of freedom are coupled. This means that we cannot perform some maneuvers mentioned before independently without implicitly performing another.

There are two possible quadrotor configurations. The plus configuration shown in fig.5.a and the cross configuration shown in fig.5.b. In the plus configuration the forward and left directions are taken along the arms of the frame. When flying the quadrotor sees forward as being a along arm one, and left along arm two. In the cross configuration the forward and left directions are in between the arms of the frame. When flying the quadrotor sees forward as being in the air in between arms one and two and left as being in between the arms two and three. In figure 5 show a top view of the quadrotors. The dashed circles with the arrow heads show the propellers clockwise and counterclockwise direction of rotation [13].
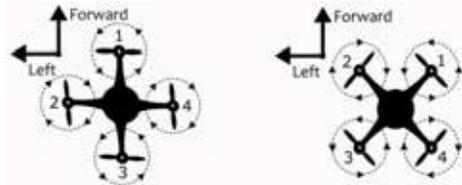
Fig. 5(a). Plus Configuration **(b)** Cross Configuration [23]

Moving up and down is the most basic maneuver. When the quadrotor is level with the ground moving up and down can be performed by giving the same command to all four motors. This is shown on the side view figure 6 of the quadrotor. The total trust is the sum of the individual four trust forces from the four propellers. If the total thrust is bigger than the force of gravity the quadrotor will move up. If the total trust is less than gravity the quadrotor will fall down[14].
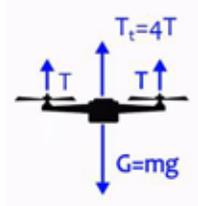
Fig. 6. Moving Up and Down [23]

Pitching is rotation around the left-right axis. Pitching is performed by creating an unbalanced between the quadrotor's front-side and back-side forces. Let's see what this means for a plus configuration in the figure 7, the propeller rotation is shown with a dashed circle. The bigger the circle, the faster the propeller rotation. The direction of rotation is shown with arrows on the dashed circles. In figure 6.a shows a pitch forward maneuver performed by decreasing the command to the front motor one and increasing the command to the back motor three. This maneuver will create a nose-down rotation. The figure 7 on the right shows the opposite nose-up rotation performed by increasing the command on motor one and decreasing the command on motor three.
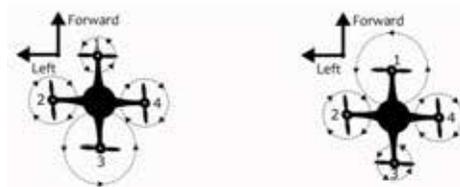
Fig. 7. a) Plus config. Pitch Forward. b) Plus config: Pitch backward [23]

We are now looking at a cross configuration in the figure 8. We perform actions that create an imbalance between the front side and the back side forces on the quadrotor frame. The same nose up and nose down maneuvers are now performed by increasing the command to two motors.
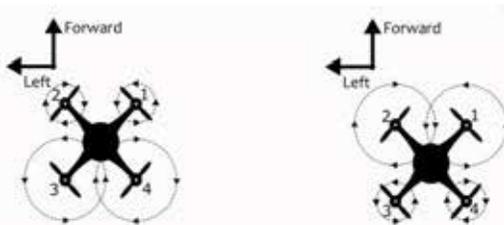
Fig. 8. a) Cross config: Pitch Forward. b) Cross config: Pitch Backward [23]

When it is pitching backward it will also move backward. In figure 9a is a side view of the quadrotor. We first see the force imbalance between the front and the back side. The front side propeller thrust is less than the back

side propeller thrust. As the frame is pitching forward, the trust force remains perpendicular on the quadrotor's frame. The thrust is now pointing not only up but also forward. This produces forward acceleration and thus forward motion. The same is shown on the right hand side figure for a backward pitch maneuver. The quadrotor will move in the backward direction.
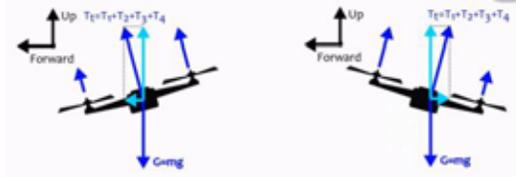
Fig. 9. a) Forward Pitch and Acceleration. b) Backward Pitch and Acceleration[23]

Rolling is rather similar to pitching. It is rotation around the forward backward axis. Rolling is performed by creating an imbalance between the quadrotor's left side and right side forces. Let's see what this means for a plus configuration. In the figure 9a shows the right side rotation performed by decreasing the command to motor four and increasing the command to motor two. This will create a rotation to the right side. In the figure 10 b shows a left side rotation performed by increasing the command to the motor four and decreasing the command to motor two.
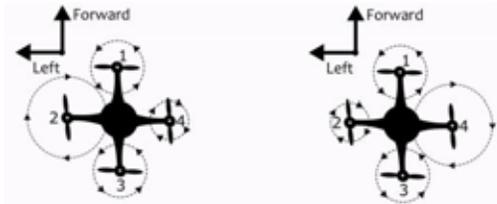
Fig. 10. a) Plus Config: Roll Right b) Plus Config: Roll Left [23]

We are now looking at a cross configuration in the figure 11. Again we are performing actions that create an imbalance between the left side and the right side forces on the quadrotor frame.
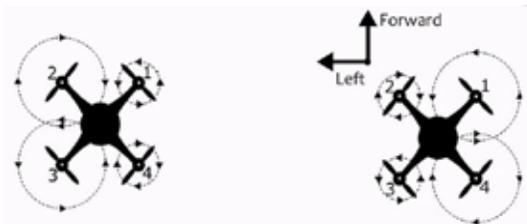
Fig. 11. a) Cross Config: Roll Right. b) Cross Config: Roll Left [23]

We can see why in the figure 12 we first see the forced imbalance between

the left and right side when the frame of the quadrotor rolls, the thrust remains perpendicular onto the frame. It is now pointing not only upward but also in the left direction. This produces acceleration and thus movement on the left side. The same is shown in the figure 12 for a right pitch maneuver. The quadrotor will move to the right side.
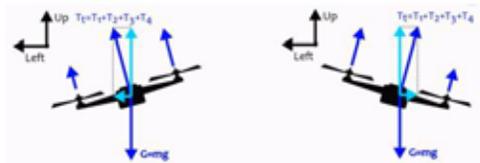
Fig. 12. a) Left Roll and Acceleration b) Right Roll and Acceleration [23]

The final of the six maneuvers is yawing or change of heading. Yawing is rotation around the up-down direction. We are going to first discuss during or heading stability. Remember the rotating propellers are causing a turning effect onto the frame. If all the propellers are of the same type, and thus turning in the same direction, there will be an overall net turning effect onto the frame. This is undesirable and this is why the quadrotor has two type of propellers rotating in different directions. The turning effect will cancel. We can see this in the figure 13. On the left side all propellers are of type counterclockwise and are creating a total clockwise turning effect onto the frame. In the figure 13 b there are two clockwise and counterclockwise propellers and the turning effect cancel each other. The turning effect is opposite the propellers rotation direction.

Fig. 13. a) All CCW propellers. b) Two CW and two CCW propellers [23]

Figure 14 a, the clockwise propellers receive a bigger command and create the opposite counterclockwise turning effect onto the frame. In the figure 14 b the counterclockwise propellers receive a bigger command and create the opposite clockwise turning effect onto the frame.
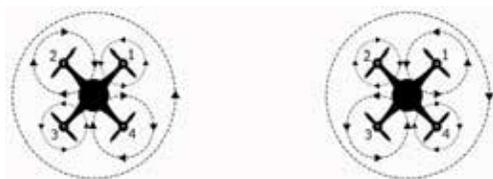
Figure 14. a) Yawing/Heading to the left. b) Yawing/Heading to the right [23]

2.2. Kinematics

To create a simulation that will help prototype and test control algorithms, we need to model rigid body motion given forces and torques. To be able to simulate rigid body motion we will look first at the kinematics, then the dynamics and finally add a numerical integration of the dynamic and kinematic equations. This part is on kinematics, that is the motion of object without a reference to the forces and torques which cause the motion. We look at position vectors, velocities and accelerations from different reference frames.
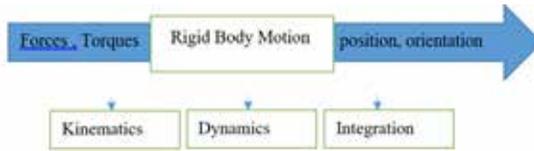
Fig. 15. Rigid Body Motion

We will first review the notions of 3D vectors and coordinate systems then look at translational motion followed by a rotational motion and at their combination. What are 3D vectors ? Most quantities of interest related to motion in 3D space, such as forces, torques velocities, accelerations have not only a size, a magnitude, but also a direction [21]. For example the wind speed is seven meters per second and has a north south direction, or the gravity force has a magnitude of mass times G and acts in the direction pointing down to the center of Earth. 3D vectors are mathematical objects that have both a magnitude and a direction.

Imagine a line segment in 3D space determined by an initial point A and a terminal point B. This can be thought of as a 3D vector. The length of the segment is its magnitude, the direction of the vector is given by two things: the dashed line and the arrow orientation, or by any other line parallel to it and with the same orientation. Therefore in the figure 16 the two arrow segments represent the same vector.
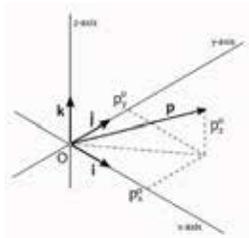
Fig. 16. Cartesian Coordinate System [23]

Next, a 3D Cartesian Coordinate System consists of three oriented lines we'll call them axes X, Y, and Z. They are perpendicular to each other and intersect at the same point called the origin. i,j and k are so-called basis

vectors. They each point along the x, y and z axis respectively and have a length of unit one. Given a Cartesian Coordinate System vector P can be represented in two ways: a geometrical form which is shown in equation one and which is a representation in terms of the bases vectors. i,k,k and the signed projection lengths of the vector onto the three axes. These are: p_x^0, p_y^0 and p_z^0. These lengths are called the vector components. Another representation is in the algebraic form as shown in equation 2.

$$p = p_x^0 i + p_y^0 j + p_z^0 k \qquad (1)$$

$$p^0 = \begin{bmatrix} p_x^0 \\ p_y^0 \\ p_z^0 \end{bmatrix}, \qquad i^0 = \begin{bmatrix} 1 \\ 0 \\ 0 \end{bmatrix}, j^0 = \begin{bmatrix} 0 \\ 1 \\ 0 \end{bmatrix}, k^0 = \begin{bmatrix} 0 \\ 0 \\ 1 \end{bmatrix} \qquad (2)$$

The 3 vector components are organized in a column array projecting the 3D vector onto another Cartesian coordinate system will give a different set of coordinates therefore the coordinate system in which the components are resolved is denoted in this study by a superscript notation. In this case we call the coordinate system 0. When writing a vector algebraic form. It is very important to use the superscript notation to precisely identify the coordinate system in which the components are resolved. When a vector equation is expressed in geometric form it holds true also in an algebraic form provided that all vectors are resolved in the same coordinate system. This means that we attach the same superscript to all vector quantities in the relation.

We will now look at the Translational motion. Let's take a fixed coordinate system. We'll also call a coordinated system a reference frame or simply a frame. So let's take a fixed frame one that is not moving with respect to the earth's surface. We will use superscript letter e to denote this frame. Let's also consider a controller object that is in motion through space. The position vector of the quadrotor at time t its vector p, p for position. Vector P is defined by points. O and C, where O is the origin of our fixed frame and C is the center of mass of the quadrotor. Try to identify vector r in the figure 17 . Next, Let A be a point in the quadrotor volume and let vector r be defined by the points O and A. In the figure 15 vector r is pointing at the propeller center. We have also vector s defined by point C and A. Vector S represents the relative position of the propeller center. with respect to the center of mass. Equation 3 shows that the position vector r can be seen as the sum of vectors P and vector S. If the quadrotor motion is a translation , vector r and p will change in time, but the vector s will be constant.
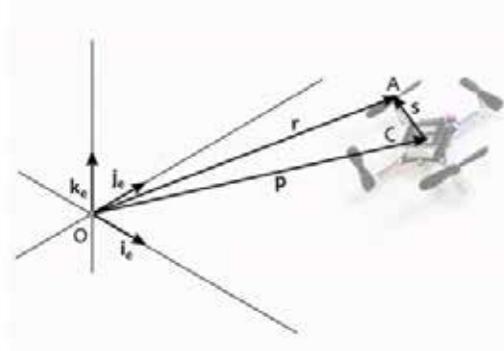
Fig. 17. Vectors of Position [23]

- p, position vector of C relative to O
- r, position vector of A relative to O
- s, position vector of A relative to C

$$r = p + s \tag{3}$$

Vectors r, p and s are shown at time t and time t plus delta t. The motion is a translation. The orientation of the quadrotor is the same. It has not rotated. We can see that vectors R and P have changed while S remained the same magnitude and direction.
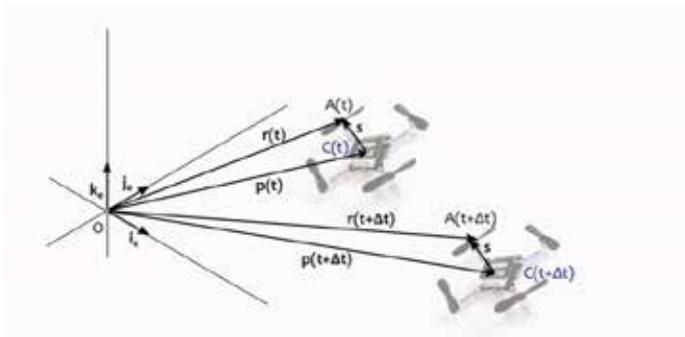
Fig. 18. Translation Motion [23]

The velocity and acceleration of the quadrotor are defined as the time derivatives of the position vector P.

$$V_p(t) \triangleq \dot{p}(t) = \frac{dp(t)}{dt} = \lim_{\Delta t \to 0} \frac{p(t + \Delta t) - p(t)}{\Delta t}, \left[\frac{m}{s}\right] \tag{4}$$

$$a_p(t) \triangleq \dot{v}(t) = \ddot{p}(t) = \frac{dv(t)}{dt} = \frac{d^2 p(t)}{dt^2}, \left[\frac{m^2}{s}\right] \tag{5}$$

That is the velocity of a point in a rotating frame is the cross product

between the angular velocity and the position vector.

$$V^e = [\omega^e]_x r^e \qquad (6)$$

Similar to linear acceleration we introduced the angular acceleration as the time derivative of the angular velocity vector. The unit of the angular velocity is radians per second while the unit of the angular acceleration is radian per square second.

The angular acceleration is defined as

$$\alpha(t) = \dot{\omega}(t) = \frac{d\omega(t)}{dt} \qquad (7)$$

Unit of angular velocity ω is [rad/s], unit of angular acceleration α is [rad/s^2]

2.3. Dynamics

In the previous two parts on kinematics we studied the translation and rotational motion of objects in 3D space from one geometrical point of view. Looking at points without the physical properties this part is on the dynamics of motion and complements the kinetics. We will relate linear and angular accelerations to forces and talks and give objects a mass distribution on the agenda for this part. We have Newton's laws of motion which are suitable for point mass objects and all those laws of motion which are adequate for rigid bodies. Yes laws can be derived from Newton's laws and we will catch this in this part. The objective is to be able to understand and operate with the final two occasions. The translation application of motion and the rotation application of motion the translation application of motion relates the external forces with the linear acceleration and the total loss of a rigid body the rotation of location of motion relate to the talk with the angular acceleration the angular velocity and the inertial matrix the inertia matrix characterizes the distribution of mass of an object. Newton's second law of motion states that in any nations reference frame the sum of forces acting on a point mass object is equal to its mass times its acceleration [22]. We will also call a point mass a particle an inertial reference frame can be said to be a frame which is not having any transitory acceleration and which does not rotate for the purpose of studying quadrotor their flight. We considered the earth fixed frame to be inertial. In other words we mainly neglect the impact of Earth's rotation on the other flight Newton's second law is stated in the duration one the sum of all forces f$_k$ (eqn. 8) acting on a particle equals the mass m times inertial acceleration of the particle all vectors are expressed in the fixed Earth frame Newton's Law of Action and reaction also known as Newton's third law states that when the first particle acts with a force on a second particle following either a contact interaction or a form of the distance interaction [15].

$$\sum_k f_k^e = ma^e = m\ddot{p}^e \Leftrightarrow \sum_k \begin{bmatrix} f_{k,x}^e \\ f_{k,y}^e \\ f_{k,z}^e \end{bmatrix} = m \begin{bmatrix} a_x^e \\ a_y^e \\ a_z^e \end{bmatrix} = \begin{bmatrix} \ddot{p}_x^e \\ \ddot{p}_y^e \\ \ddot{p}_z^e \end{bmatrix}$$

3. Flight Stabilization

3.1. Feedback Controllers

Feedback happens when the outputs of our system are processed and then used as inputs. This is done via an intermediary block called the controller feedback changes the dynamic properties of the original system and causes new behaviors. The controller makes the new behavior good or desirable behavior.
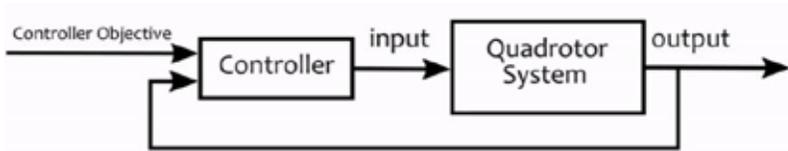
Fig. 19. Control Block Diagram

Let's look first at the dynamical system block dynamical system has the states X inputs you outputs white X you and white are here. Continuous time signals but derivatives of the state X are given by a function f dependent on the time t the state takes and the input signal u the outputs are given by the function g.
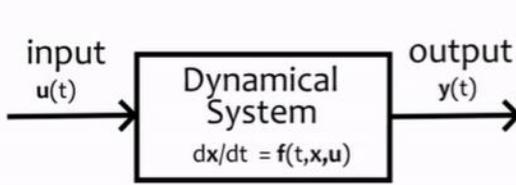
Fig. 20. A General Dynamical System

A general dynamical system is defined as follows: Where x are states, u are inputs, y are the output.

3.2. State Space Model

The representation of the differential equations describing the motions of the systems in the form of matrix vector product depending on the initial conditions within the input-output relationship is called the State Space representation. Stability, performance and durability features expected from a control system can be added to the controller design with quadratic performance constraints in the time domain. Another advantage of the State-Space equations and time domain analysis technique is that, thanks

to advanced linear algebra techniques, it works in harmony with digital computer technology and allows the analysis of systems with multiple inputs and multiple outputs [11].

Differential equations describing the motions of dynamical systems can be expressed with State-Space equations in the form of vector matrix multiplication. With State-Space representation, n. A first-order differential equation is converted into a set of equations consisting of n first-order differential equations [12].

$$\dot{x} = Ax(t) + Bu(t)$$
$$y = Cx(t) + Du(t) \tag{9}$$

$$x = [x\ \dot{x}\ y\ \dot{y}\ z\ \dot{z}\ \emptyset\ \dot{\emptyset}\ \theta\ \dot{\theta}\ \varphi\ \dot{\varphi}] \tag{10}$$

$$u = [U_1 U_2 U_3 U_4]^T \tag{11}$$

$$\begin{bmatrix} U_1 \\ U_2 \\ U_3 \\ U_4 \end{bmatrix} = \begin{bmatrix} b & b & b & b \\ \frac{-lb}{\sqrt{2}} & \frac{lb}{\sqrt{2}} & \frac{lb}{\sqrt{2}} & \frac{-lb}{\sqrt{2}} \\ \frac{lb}{\sqrt{2}} & \frac{-lb}{\sqrt{2}} & \frac{lb}{\sqrt{2}} & \frac{-lb}{\sqrt{2}} \\ d & d & -d & -d \end{bmatrix} \begin{bmatrix} \omega_1^2 \\ \omega_2^2 \\ \omega_3^2 \\ \omega_4^2 \end{bmatrix} \tag{12}$$

In the longitudinal state space model output matrix, the outputs followed in this study are given as outputs since z and θ are followed (eqn 13) [25].

$$\begin{bmatrix} \dot{x} \\ \dot{z} \\ \dot{u} \\ \dot{w} \\ \dot{q} \\ \dot{\theta} \end{bmatrix} = \begin{bmatrix} 0 & 0 & 1 & 0 & 0 & 0 \\ 0 & 0 & 0 & 1 & 0 & 0 \\ 0 & 0 & 0 & 0 & 0 & -g \\ 0 & 0 & 0 & 0 & 0 & 0 \\ 0 & 0 & 0 & 0 & 0 & 0 \\ 0 & 0 & 0 & 0 & 1 & 0 \end{bmatrix} \begin{bmatrix} x \\ z \\ u \\ w \\ q \\ \theta \end{bmatrix} + \begin{bmatrix} 0 & 0 \\ 0 & 0 \\ 0 & 0 \\ 1/m & 0 \\ 0 & 1/I_y \\ 0 & 0 \end{bmatrix} \begin{bmatrix} U_1 \\ U_3 \end{bmatrix}$$

$$y = \begin{bmatrix} 0 & 0 & 0 & 0 & 0 & 0 \\ 0 & 1 & 0 & 0 & 0 & 0 \\ 0 & 0 & 0 & 0 & 0 & 0 \\ 0 & 0 & 0 & 0 & 0 & 0 \\ 0 & 0 & 0 & 0 & 0 & 0 \\ 0 & 0 & 0 & 0 & 0 & 1 \end{bmatrix} \begin{bmatrix} x \\ z \\ u \\ w \\ q \\ \theta \end{bmatrix} \tag{13}$$

The lateral flight state space model is given as output because $\emptyset$ and φ are followed in the output matrix (eqn 14) [26].

$$
\begin{bmatrix} \dot{y} \\ \dot{v} \\ \dot{p} \\ \dot{r} \\ \dot{\emptyset} \\ \dot{\varphi} \end{bmatrix} = \begin{bmatrix} 0 & 1 & 0 & 0 & 0 & 0 \\ 0 & 0 & 0 & 0 & g & 0 \\ 0 & 0 & 0 & 0 & 0 & 0 \\ 0 & 0 & 0 & 0 & 0 & 0 \\ 0 & 0 & 1 & 0 & 0 & 0 \\ 0 & 0 & 0 & 1 & 0 & 0 \end{bmatrix} \begin{bmatrix} y \\ v \\ p \\ r \\ \emptyset \\ \varphi \end{bmatrix} + \begin{bmatrix} 0 & 0 \\ 0 & 0 \\ 1/I_x & 0 \\ 0 & 1/I_z \\ 0 & 0 \\ 0 & 0 \end{bmatrix} \begin{bmatrix} U_2 \\ U_4 \end{bmatrix}
$$

$$
y = \begin{bmatrix} 0 & 0 & 0 & 0 & 0 & 0 \\ 0 & 0 & 0 & 0 & 0 & 0 \\ 0 & 0 & 0 & 0 & 0 & 0 \\ 0 & 0 & 0 & 0 & 0 & 0 \\ 0 & 0 & 0 & 0 & 1 & 0 \\ 0 & 0 & 0 & 0 & 0 & 0 \end{bmatrix} \begin{bmatrix} y \\ v \\ p \\ r \\ \emptyset \\ \varphi \end{bmatrix}
\tag{14}
$$

3.3. PID Controllers

PID, one of the oldest but most versatile type of controllers in our very widespread in the industry in the previous part we talked about controller objectives before looking at ideas.

We'll take a look at a specific controller objective the set point. Instead point control the objective of the controller is to stabilize one or more of the output of the system. The value given by the external set point the set point controls the particular case of the more general reference striking objective in the general case.

The reference can be any type of signal for example or a ramp signal side or another freeform a signal in the set point case the reference is peace quiet constant this is the set point controller structure the output is fed back with a negative sign and the reference is broadly the positive sign to construct the error signal U of T your signal is the main input to the controller and the controller objective is to drive the error signal to zero (Fig. 21). It might take some time from the moment that the new set point is received and until the output value has reached an equilibrium position or a steady state at the desired set point depending on the dynamic characteristics of the dynamical system and on the performance of the controller for the general meaning of this structure is simple the controller makes sure that the system output we are staying put set point [24].
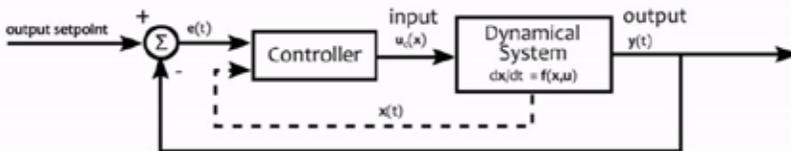
Fig. 21. Type Of Set Point Controllers For Single Input Single Output Systems Or Subsystems.

The control signal usage of T generated by PID is built out of three components and uses the set point there are signal u of t the three components are dear or proportional to characterized by coefficient KP The are integral term characterized by coefficient Ki and error derivative term characterized by coefficient KD when only the proportional term is present we talk about controllers and it means that a key ally and KD coefficients are equal to zero. Similarly PID controller its KD equal to zero and a PID controller has Ki equal to zero. There is no PID view without the proportional part (eqn. 8).

$$u(t) = K_p e(t) + K_i \int_0^t e(\tau)d\tau + K_d \frac{de(t)}{dt}; e(t) = y_r(t) - y(t) \quad (8)$$

4. Results and Discussion

The angle between the arms of the aircraft is 90 degrees. The arms were mounted parallel to the body. As seen in Figure 2, the angle between the arms is 90 degrees and the arm elevation angle is 0 degrees. This state where there is no shape change is configuration 1. Configuration 2, where the angle between the arms is 60 degrees, is shown in Figure 22.

Fig. 22. Configuration 2 (Hub angle 60)

Figure configuration 3, which occurs when the arms rise 30 degrees, can be seen in figure 23.

Fig. 23. Configuration 3 (Hub angle 60, arm tilt angle 30)

The deformation of the aircraft affects the moments of inertia. The
change is given in Table 1.

Table 1. General Characteristics Of The Aircraft In Different
Configurations

Quadrotor Configuration	Width/Length	Ix (kgm2)	Iy (kgm2)	Iz(kgm2)
Config. 1	375/375	0,01233	0,01233	0,02434
Config. 2	265/459	0,00643	0,01824	0,02434
Config. 3	246/427	0,00651	0,01681	0,02132

The aircraft was simulated longitudinally and laterally in MATLAB
program for 3 different configurations. For each case, the pitch and roll
angles were simulated for 40 seconds by entering 2 degrees reference
values. Rise time, overshoot and settling times were compared.

4.1. Longitudinal and Lateral Motion Simulation of Config. 1

Configuration 1 (figure 1) was designated when the aircraft did not change
shape. In Table 1, the moment of inertia values of the aircraft are shared.
The results of the longitudinal motion simulation graph (Figure 24)
performed using these values are shared in Table 2.

Table 2. Longitudinal Motion Simulation Results

Config. 1	Rise Time	O.S.	Settling Time
	0,121	13,3%	1,4
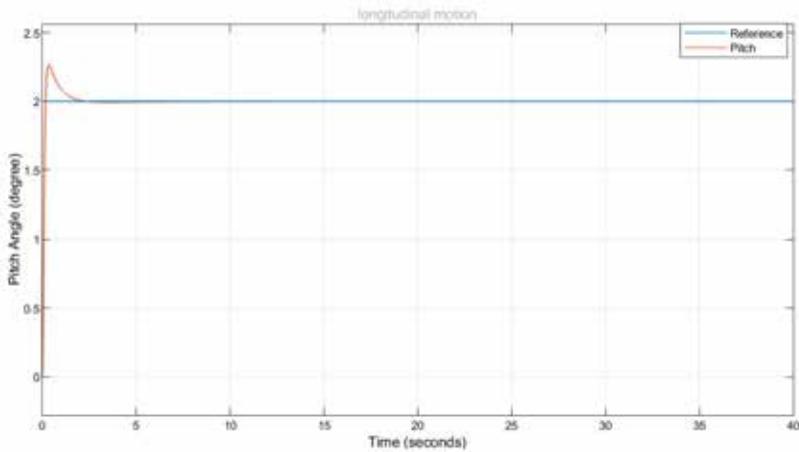
Fig. 24 Longitudinal Motion Simulation Results

The results of the lateral motion simulation graph (Figure 25) performed for Configuration 1 are shared in Table 3.

Table 3. Lateral Motion Simulation Results

Config. 1	Rise Time	O.S.	Settling Time
	0,164 s	14%	1,75
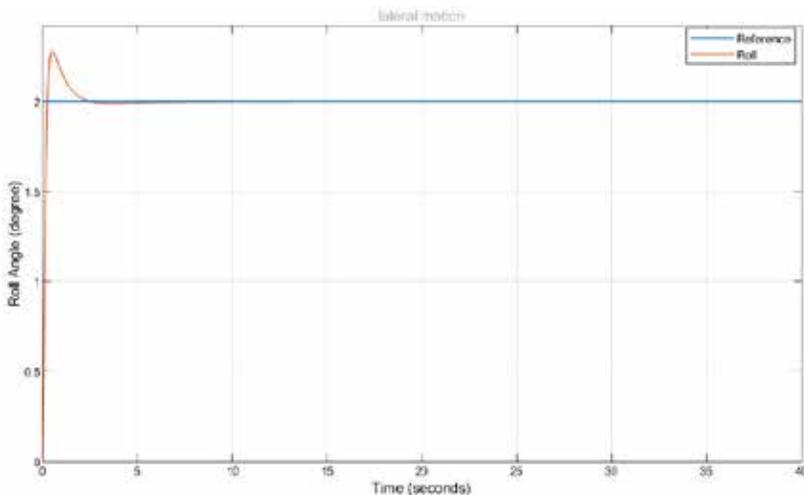
Fig.25 Lateral Motion Simulation Results

4.2. Longitudinal and Lateral Motion Simulation of Config. 2

When the aircraft hub angle is 60 degrees, it is referred to as configuration 2 (Figure 22). In Table 1, the moment of inertia values of the aircraft are shared. The results of the longitudinal motion simulation graph (Figure 26) performed using these values are shared in Table 4.

Table 4. Longitudinal Motion Simulation Results

Config. 2	Rise Time	O.S.	Settling Time
	0,172	16,9%	1,59
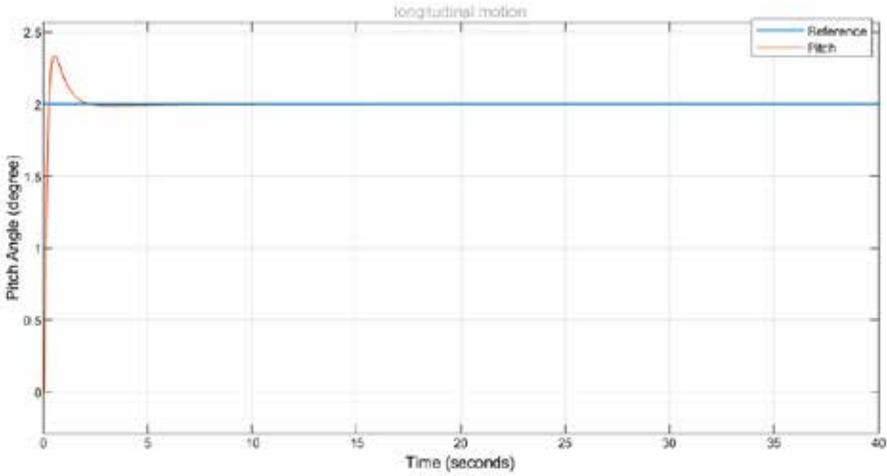
Fig. 26. Longitudinal Motion Simulation Results

The results of the lateral motion simulation graph (Figure 27) performed for Configuration 2 are shared in Table 5.

Table 5. Lateral Motion Simulation Results

Config. 1	Rise Time	O.S.	Settling Time
	0,0887 s	9.85%	1,33 s
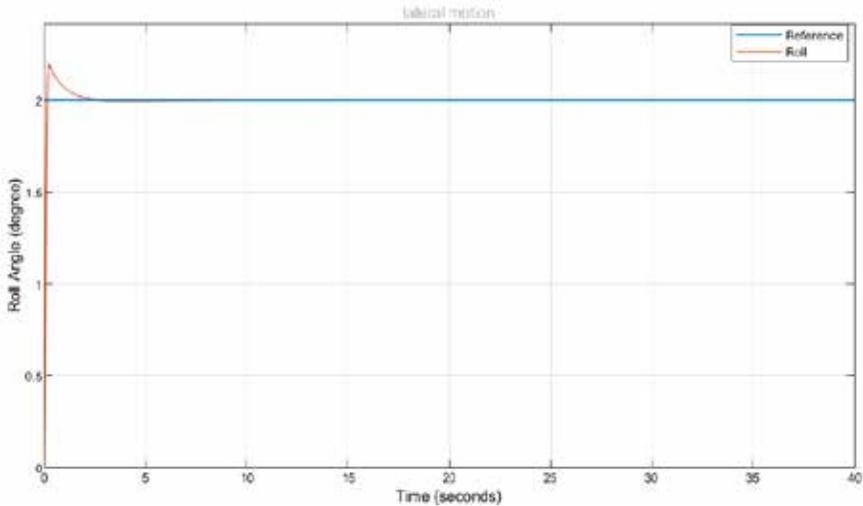
Fig. 27. Lateral Motion Simulation Results

4.3. Longitudinal and Lateral Motion Simulation of Config. 3

When the aircraft arm height is 30 degrees, it is referred to as configuration 3 (Figure 23). In Table 1, the moment of inertia values of the aircraft are shared. The results of the simulation graph (Figure 28) performed using these values are shared in table 6 for longitudinal motion.

Table 6. Longitudinal Motion Simulation Results

Config. 3	Rise Time	O.S.	Settling Time
	0,16	16%	1,55
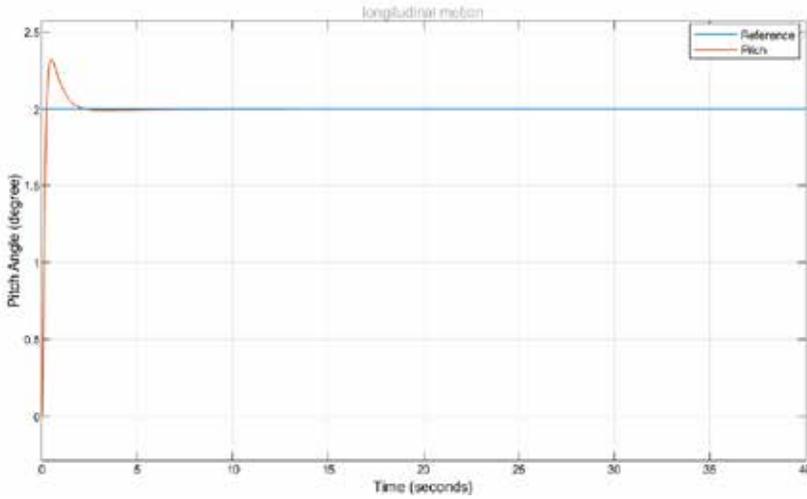
Fig.28. Longitudinal Motion Simulation Results

The results of the lateral motion simulation graph (Figure 29) performed for Configuration 3 are shared in Table 7.

Table 7. Lateral Motion Simulation Results

Config. 1	Rise Time	O.S.	Settling Time
	0,0898	9,86%	1,34s
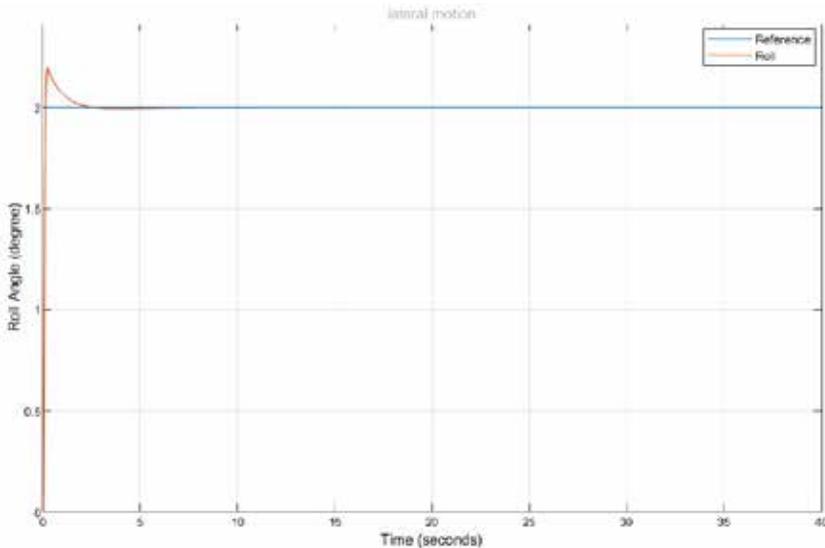
Fig.29. Lateral Motion Simulation Results

5. Conclusion

Three different states of the quadrotor were studied. Changing dynamics and geometric measurements are shared in Tables 1,2 and 3. Quadrotor simulation was done in MATLAB program for 3 different situations. Results for Forward Movement; The rise time for the quadrotor forward movement without hub angle change and elevation angle change (hub angle 90° and elevation angle 0°) is 0.0138 s, O.S. 21.8% and the sitting time was calculated as 0.0726. When the hub angle is 60°, the rise time is 0.0166 s, O.S. 17% and settling time 0.0601 s. When the hub angle is 60° and the arm elevation angle is 150°, the rise time is 0.0162 s, O.S. 17.7% and settling time 0.0588s were calculated. Three different configurations were performed with the same PID coefficients. The change in Iy was obtained from the CATIA program of 0.01632 kgm2 in configuration 1, 0.02087 kgm2 in configuration 2 and 0.02021 kgm2 in configuration 3. The rise time of changes in the moment of inertia, O.S. and the change in settling time, with reference to configuration 1, the rise time respectively increased and remained unchanged in the final state compared to configuration 2. O.S. It was calculated that the value decreased and did not change in configuration 3 compared to configuration 2. It was calculated that the sitting time in Configuration 3 decreased and did not change compared to Configuration 2.

Results obtained for Lateral Movement; The rise time of the quadrotor is 0.164 s, O.S. without hub angle change and elevation angle change (hub angle 90° and elevation angle 0°). 14% and the settling time was calculated as 1.75 s. When the hub angle is 60°, the rise time is 0.172 s, O.S. 16.9% and sitting time 1.59 s. calculated. When the hub angle is 60° and the arm elevation angle is 150°, the rise time is 0.0898 s., O.S. 9.86% and settling time 1.34 s. calculated. Three different configurations were performed with the same PID coefficients. The change in Ix was obtained from the CATIA program of 0.01233 kgm2 in configuration 1, 0.00643 kgm2 in configuration 2 and 0.00651 kgm2 in configuration 3. The rise time of changes in the moment of inertia, O.S. and the change in settling time, with reference to configuration 1, the rise time respectively decreased and remained unchanged in the final state compared to configuration 2. O.S. It was calculated that the value did not change in configuration 3 compared to configuration 2. It was calculated that the sitting time in Configuration 3 did not change compared to Configuration 2.

As a result, the reduction of the hub angle increases the stability during the forward scrimmage, while prolonging the response time. During lateral movement, the stability decreases, while the response time is shortened. As the arms rise, the rotors become closer to the center of gravity than the initial state, there are no significant changes since the wind speed is assumed to be zero.

References

[1]   Desbines, A., Expert, F., Boyron, M., Diperi, J., Viollet,S., Ruffier, F. (2017). X-Morf: A   crash-separable quadrotor that morfs its X-geometry in flight. 2017 Workshop on Research, Education and Development of Unmanned Aerial Systems (RED UAS)

[2]   2.   Falanga, D., Kleber, K., Mintchev, S., Floreano, D., Scaramuzza, D. (2018) The Foldable Drone: A Morphing Quadrotor that can Squeeze and Fly. IEEE Robotics And Automation Letters. Preprint Version. Accepted November, 2018

[3]   Bai, Y., Gururajan, S. (2019). Evaluation of a Baseline Controller for Autonomous "Figure-8" Flights of a Morphing Geometry Quadcopter: Flight Performance. Drones 2019, 3, 70

[4]   Wallace, D. (2016). Dynamics and Control of a Quadrotor with Active Geometric Morphing. Computer Science Published 2016E. H. Miller, "A note on reflector arrays," IEEE Trans. Antennas Propagat., to be published.

[5]   E. E. Reber, R. L. Michell, and C. J. Carter, "Oxygen absorption in the earth's atmosphere," Aerospace Corp., Los Angeles, CA, USA, Tech. Rep. TR-0200 (4230-46)-3, Nov. 1988.

[6]   Prisacariu, V., Sandru, V., & Rău, C. (2011). Introduction morphing technology in unmanned aircraft vehicles (UAV). Paper presented at the International Conference of Scientific Paper, AFASES.

[7]   Di Luca M, Mintchev S, Heitz G, Noca F, Floreano D. (2017). Bioinspired morphing wings for extended flight envelope and roll control of small drones. Interface Focus 7: 20160092.

[8]   T.Oktay and K. Oğuz, "Non Simultaneous Morphing System Design for Yaw Motion in Quadrotors," Journal of Aviation, vol. 3, no. 2, pp. 81-88, 2019.

[9]   O. Kose and T. Oktay, "Dynamic Modeling and Simulation of Quadrotor for Different Flight Conditions," European Journal of Science and Technology, no. 15, pp. 132-142, 2019

[10]   O. Köse and T. Oktay, "Non Simultaneous Morphing System Desing for Quadrotors," Avrupa Bilim ve Teknoloji Dergisi, no. 16, pp. 577-588,2019.

[11]   S. Bay, Fundamentals of Linear State-Space Systems, Mc-Graw Hill, 1999.

[12]   M.Ö. Efe, Otomatik Kontrol Sistemleri, Seçkin Yayıncılık, 2012.

[13]   Oktay, T., Özen, E. (2021). Döner Kanatlı İnsansız Hava Aracının Sistem Tasarımı Ve Kontrolü. Avrupa Bilim ve Teknoloji Dergisi, (27), 318-324.

[14]   Tuğrul Oktay , Metin Uzun , Harun Çelik , Mehmet Konar. (2017). Pıd Based Hıerarchıcal Autonomous System Performance Maxımızatıon Of A Hybrıd Unmanned Aerıal Vehıcle (Huav). Anadolu University Journal Of Science And Technology A- Applied Sciences And Engineering

[15]   Dustin A. Wallace. (2016). Dynamics and Control of a Quadrotor with Active Geometric Morphing. Master of Science in Aeronautics & Astronautics University of Washington

[16]   Enes YALÇIN, Ertuğrul ÇAM, Tevfik VARDAR,Murat LÜY. (2013).

PID Kontrolör ile İki Bölgeli Güç Sistemlerinde Yük Frekans Kontrolünün İncelenmesi. International Journal of Engineering Research and Development, Vol.5, No.2, June 2013

[17]   Oguz Kose, Tugrul Oktay.(2022). Hexarotor Yaw Flight Control with SPSA, PID Algorithm and Morphing. International Journal of Intelligent Systems and Applications in Engineering. IJISAE, 2022, 10(2), 216–221

[18]   Oguz Kose, Tugrul Oktay.(2021). Quadrotor Flight System Design using Collective and Differential Morphing with SPSA and ANN. International Journal of Intelligent Systems and Applications in Engineering. IJISAE, 2021, 9(4), 159–164

[19]   Hüseyin Sahin, Oguz Kose, Tugrul Oktay. (2021). Simultaneous autonomous system and powerplant design for morphing quadrotors. Aircraft Engineering and Aerospace Technology. DOI 10.1108/AEAT-06-2021-0180

[20]   Y.Eraslan, T. Oktay, E. Özen. The Effect Of Change In Angle Between Rotor Arms On Trajectory Trackıng Qualıty Of A Pıd Controlled Quadcopter. Ejons 10th Internatıonal Conference On Mathematıcs, Engıneerıng, Natural & Medıcal Scıences. Batumi/Georgia between May 15-17, 2020

[21]   Oktay, T., Özen, E. (2021). Döner Kanatlı İnsansız Hava Aracının Sistem Tasarımı Ve Kontrolü. Avrupa Bilim ve Teknoloji Dergisi, (27), 318-324.

[22]   Semat, Henry and Katz, Robert, "Physics, Chapter 11: Rotational Motion (The Dynamics of a Rigid Body)" (1958). Robert Katz Publications. 141.

[23]   Paolo Ceppi. (2020). Model-based Design of a Line-tracking Algorithm for a Low-cost Mini Drone through Vision-based Control. Master of Science in Electrical and Computer engineering in the Graduate College of the University of Illinois at Chicago, 2020

[24]   Çoban S., Bilgiç H.H., Oktay T. (2019). Designing, dynamic modeling and simulation of ISTECOPTER . Journal of Aviation, 3 (1), 38-44. DOI: 10.30518/jav.564376

[25]   O. Kose and T. Oktay, "Hexarotor Yaw Flight Control with SPSA, PID Algorithm and Morphing", Int J Intell Syst Appl Eng, vol. 10, no. 2, pp. 216–221, May 2022.

[26]   Kose, O., Oktay, T. (2021). Hexarotor Longitudinal Flight Control with Deep Neural Network, PID Algorithm and Morphing. European Journal of Science and Technology, (27), 115-124.

CHAPTER 7

PROPELLER DESIGN FOR DRONE EFFICIENCY UNDER HOVER CONDITIONS

Alihan Atilla Çınar[1], Özge Özdemir[2]

1 Research Asst., Department of Aeronautical Engineering, Istanbul Technical University, Türkiye, cinarali17@itu.edu.tr, ORCID: 0000-0002-0034-9646
2 Asst.Prof.Dr., Department of Aeronautical Engineering, Istanbul Technical University, Türkiye, ozdemirozg@itu.edu.tr, ORCID: 0000-0002-4755-2094

Nomenclature

C_T	Thrust coefficient	$C_{l\alpha}$	Lift coefficient slope
λ	Inflow ratio	θ	Pitch angle
r	Nondimensional radial distance	ϕ	Inflow angle
y	Radial distance	α_0	Zero lift angle
R	Rotor radius	v_i	Induced velocity
σ	Solidity	F	Prandtl tip loss correction factor
C_l	Lift coefficient	α_{eff}	Effective angle of attack
V_R	Radial velocity	U	Resultant velocity
V_{tip}	Tip velocity	Ω	Rotational frequency of rotor
L	Lift force	D	Drag force
ρ	Air density	c	Chord length
T	Thrust	Q	Rotor Torque
N_b	Blade Number	W	Drone Weight
c_p	Power coefficient	λ_{tip}	Inflow ratio at blade tip
c_{pi}	Induced power coefficient	α_1	Angle of attack at maximum efficiency
c_{tip}	Chord length at blade tip	C_s	Slope of the taper
θ_{tip}	Pitch angle at blade tip	θ_s	Slope of the twist
y	Height of the first mesh layer	δ	Boundary layer thickness
Re	Reynolds number	μ	Dynamic viscosity
U_τ	Friction velocity	τ_w	Wall shear stress
C_f	Skin friction coefficient	U_∞	Freestream Velocity
GR	Growth rate	NL	Number of inflation layers

A. Introduction

Drones have become one of the most important air vehicles recently. They can be classified into three groups as fixed wing, multirotor and hybrid. In addition to these, there are also rare types of drones such as ornithopter that are neither multirotor nor fixed wing. The drone type discussed in this study is multirotor. Ease of use, having many different areas of operation and being cheaper than alternatives are some of the reasons for the increase in multirotor drone use. The widespread use of drones has led to an increase in research in this area. A lot of research has been done to increase the performance and efficiency of these vehicles. Although the areas of application are almost unlimited, military, police force, cinematography, meteorology, archeology, recreational fields are the areas where drones are used the most (Andria et. Al, 2018). Also there are types of drones used for spraying, fertilizing, plant growth analysis and water quality analysis. In the field of meteorology, there are drones that collect pressure, radiation, temperature and humidity data with special sensors. Another area of utilization of multirotor drones is archeology. Another crucial reason why drone research has been so abundant in recent years is the capacity of drones to be used in life-saving activities. Because

multirotor drones can hover in the air and are small in size, they can reach critical places that humans cannot reach under normal conditions. So, they can deliver supplements like food, water and medicine to a mountain climber who stuck in the mountain. Similarly, they can be used in search and rescue operations. They can provide early access to the casualties by scanning the areas where access is limited. It can also fix collapsed communication network by flying around with Wi-Fi after disasters. On the other hand, it can save many lives by allowing a terrorist organization to be caught before it takes action when used by police forces. In short, there are life-saving activities where multirotor drones are used today, and thanks to the researches, these activities are expected to increase in the near future (Vergouw et al., 2016)

In summary, drones have been the subject of many studies due to their wide usage area, cheapness and life-saving features. In parallel with the efforts to increase performance and efficiency, the dimensions and weights of the drones have decreased over time. Increasing the flight time of multirotor drones depends on the flight efficiency and the light weight of the drone. Efficiency can be expressed as the thrust generated per power consumed.

This study will focus more on drone blade design to increase the aerodynamic efficiency. Before moving on to propeller design, it was focused on modeling the blade close to the reality. In some of the researches on propeller flow modeling, firstly the propeller is designed, or on shelf propellers with known properties were used. Afterwards, flow is modeled by using the Blade Element Momentum Theory (BEMT) and thrust, power and efficiency calculations are made from the obtained model. Then air tunnel tests were used to compare the results of this theory with the actual results. Test data and model results were compared and comments were made about the accuracy of the model. In some studies, blade element theory and CFD simulations were compared to determine the accuracy of the model built with BEMT was to be determined. In these studies, different assumptions were made in BEMT formulation and different loss calculations were taken into account.

B. Development of the Blade Element Momentum Theory Model for A Rotor System

BEMT is used to calculate aerodynamic forces acting on the blades. BEMT is a hybrid method developed by Gustafson and Gessow between 1946-1948. The method was basically formed by combining the Blade

Element Theory and the Momentum Theory. Differential momentum theory developed by Froude is used in the momentum theory part. In the differential momentum theory, the actuator disk area modeled by the conventional momentum theory is divided into infinitely small annuluses as shown in Fig. 1. The area of these rings is calculated as $2\pi y \, dy$. Therefore, in this theory, the problem is considered to be 2D and the rings do not affect each other.

(a)   (b)
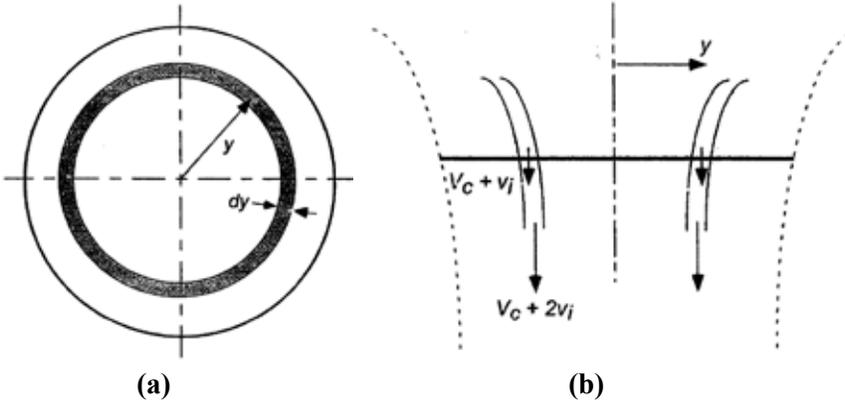
Figure 1 (a) Top view of the annulus on the actuator disk **(b)** Side view of the flow field through the annulus (Leishman, 2006)

Here, V_c is the climbing velocity in the vertical flight condition and is taken to be zero under hover conditions and v_i is the induced velocity given to the flow field through the actuator disk.

The thrust coefficient defined in the differential Momentum Theory for the thrust generated over the annulus is given as follows

$$dC_T = 4\lambda^2 r \, dr \tag{1}$$

Here λ is the dimensionless parameter and r is the dimensionless spanwise coordinate, $r = y/R$ while the dC_T expression obtained in the Blade Element Theory is obtained by the following equation.

$$dC_T = \frac{1}{2}\sigma C_l r^2 dr \tag{2}$$

Here, σ is the dimensionless parameter calling solidity and C_l is the airfoil lift coefficient.

$$C_l = C_{l\alpha}(\theta - \phi - \alpha_0)$$

There are four parameters that can be used while defining the lift coefficient as in Eqn. (3). $C_{l\alpha}$ is the airfoil lifting line slope, θ is the total angle of attack (AOA), ϕ is the induced angle due to the induced velocity

v_i and α_0 is the zero lift angle. In Fig.2, the angles and the aerodynamic forces are demonstrated.
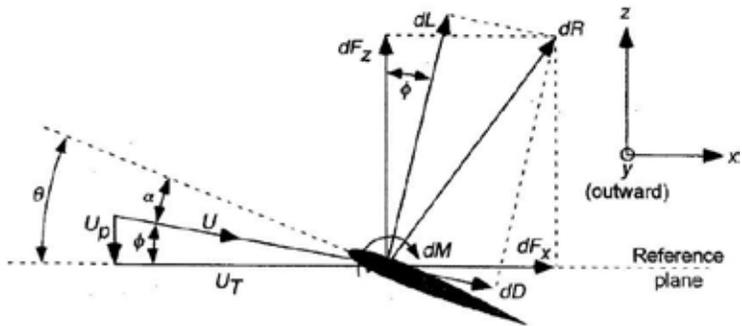
Figure 2 Aerodynamic forces and flow field on an airfoil, BEMT representation (Leishman, 2006)

If the dC_T equations from blade element theory and differential momentum theory are equalized, the two theories are combined and the λ value is obtained as a function of other blade related parameters as follows (Leishman, 2006)

$$\lambda = \frac{\sigma C_{l\alpha}}{16}\left(\sqrt{1 + \frac{32}{\sigma C_{l\alpha}}\theta r} - 1\right) \qquad (4)$$

While λ value is assumed to be uniform (constant) in the Momentum Theory and the Blade Element Theory, it is a function of twist angle distribution, chord length distribution, pitch angle distribution and airfoil selection in BEMT. In this paper, the above inflow ratio obtained from BEMT was used by being modified with tip loss effect. This modified equation is obtained using Prandtl's tip loss model and added to the BEMT code.

$$\lambda(r) = \frac{\sigma C_{l\alpha}}{16F}\left(\sqrt{1 + \frac{32F}{\sigma C_{l\alpha}}\theta r} - 1\right) \qquad (5)$$

In Eqn.(5), an iterative procedure is followed to get a converged value of λ for hover conditions. Inflow ratio plays a key role in BEMT theory. When the inflow ratio is obtained, the inflow angle can also be calculated as follows

$$\phi = \lambda/r \qquad (6)$$

When the inflow angle is known, the effective angle of attack can be calculated, $\alpha_{eff} = \theta - \phi$. After, the angle of attack is obtained, lift coefficient, drag coefficient and the air velocity acting on blade are known and aerodynamic forces can be calculated for each differential blade section. Air velocity acting on the blade has two components. One of them is the speed due to the rotation of the propeller and is parallel to the rotation plane, the other is the velocity caused by the propeller inducing air and is perpendicular to the rotation plane, i.e. Fig. 2. These speeds can be calculated using the formulas below. Then, these speeds are combined in Eqn. (15) to find the final resultant velocity (Leishman, 2006).

When the inflow angle is known, the effective angle of attack can be calculated, $\alpha_{eff} = \theta - \phi$. After, the angle of attack, lift coefficient, drag coefficient and the air velocity acting on blade are known, aerodynamic forces can be calculated for each differential blade section. Air velocity acting on the blade has two components. One of them is the speed due to the rotation of the propeller and is parallel to the rotation plane, i.e. $V_R = \Omega R$ the other is the velocity caused by the propeller inducing air and is perpendicular to the rotation plane, i.e. $v_i = \lambda V_{tip}$. The resultant velocity is (Leishman, 2006)

$$U = \sqrt{v_i^2 + V_R^2} \tag{7}$$

Aerodynamic forces acting on each blade can be calculated as follows.

$$dL = \frac{1}{2}\rho U^2 c C_l \, dy , \quad dD$$
$$= \frac{1}{2}\rho U^2 c C_D \, dy \tag{8}$$

The thrust and power values of each blade are calculated using aerodynamic forces are

$$dT = N_b(dL \cos \Phi - dD \sin \Phi),$$
$$dQ = N_b(dL \sin \Phi + dD \cos \Phi)y \tag{9}$$

These values calculated for each blade section are integrated along the blade to get the total thrust and power values.

As a result, the power consumed and the thrust value produced by a helicopter with certain rotor characteristics can be calculated with the BEMT code created. In addition, rotor features such as chord length, pitch angle and airfoil type can be added to the code. The ease of modifications to the code will provide convenience in the propeller design phase.

C. Validation of the Code

After completing the modeling of the code for the helicopter rotor, the validation phase was started. For the validation, the results obtained from tests of the BO-105 hingeless rotor system in NASA 40-80 air tunnel were used Peterson (1995). The properties of the rotor system are given in Table 1.

Table 1 Characteristics of BO-105 hingeless rotor (Peterson, 1995)

Number of blades	4	Linear blade twist(deg)	-8
Radius(m)	4.910328	Solidity	0.07
Blade Chord(m)	0.27	Nominal Rotor Speed(rpm)	425
Airfoil section		NACA 23012	

In this study, the XFLR5 program is used to obtain the graph of the lift coefficient with respect to the angle of attack. An approximate average Reynolds number is determined for the propeller and the graphic is drawn using the program. NACA23012 airfoil is used in BO-105 hingeless rotor. The $C_l - \alpha$ and $C_D - \alpha$ graphics of this airfoil were created using XFLR5 program. Created graphs are given as in Fig. 3. Since the average lift and drag values were produced in approximately 75 percent of the blade, the Reynolds number in this section is used in the analysis.

Then, the drawn graphic is digitized using a plot digitizer and transferred to the MATLAB as two arrays. In MATLAB a first-order function is fitted between angle of attack and lift coefficient. The coefficient of the angle of attack in this function is equal to the slope of the $C_l - \alpha$ graph. The same process is also applied for the $C_D - \alpha$ graph. However, when fitting the function, a function higher than first order is fit due to the characteristics of the $C_D - \alpha$ graph.
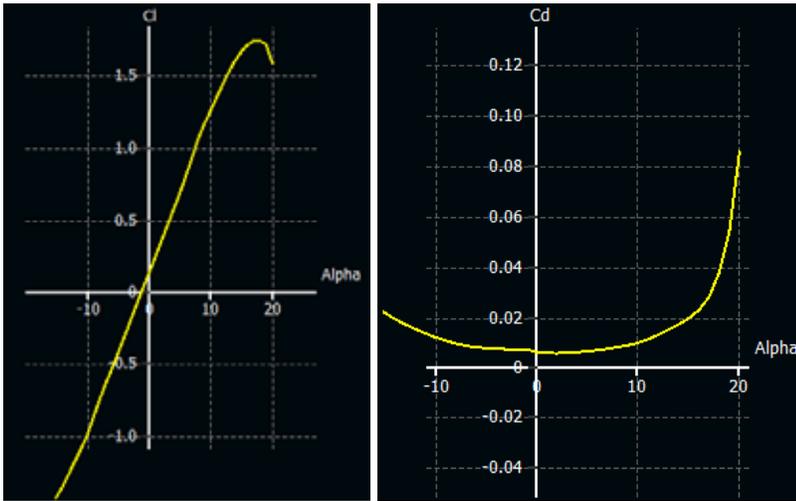
Figure 3 Airfoil Graphs of NACA23012

Figure of Merit (FM), c_T / σ and c_p / σ values were calculated by entering the information of the rotor into the in-house code achieved for helicopter performance calculations. By changing the pitch angle, the variation of the c_T / σ according to c_p / σ and the variation of FM according to c_T / σ has been obtained. The graph drawn from the BEMT code was compared with the graph of the test data. This comparison is presented in the graphic below.

(a)   (b)
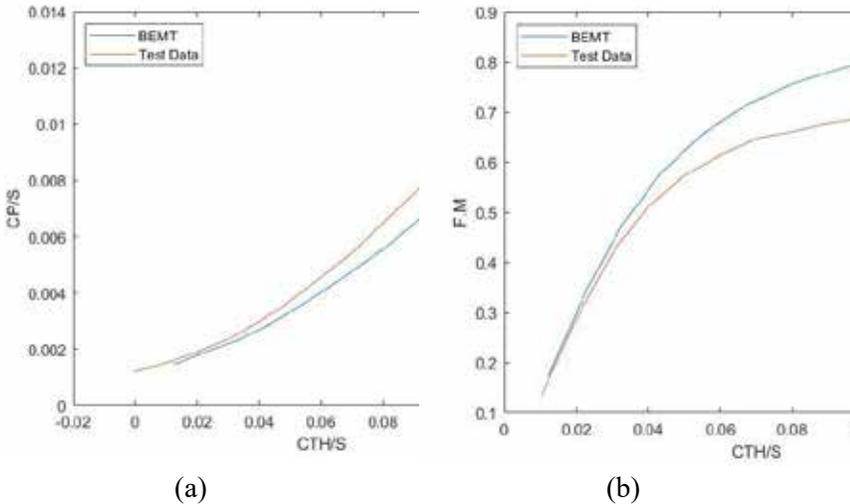
Figure 4 (a) c_T / σ vs c_p / σ (b) c_T / σ vs F.M

In Fig. 4, it is noticed that the code gives results that are compatible with the experimental data. FM variation is progressing slightly above

expectations. This is because not all losses can be modeled and 3D effects are ignored in the Blade Element Momentum Theory formulation.

D. Implementation of the Scale Effect

A correction equation was developed by Snel due to the very high ratio of the chord length to diameter length in the hub parts of the small propellers. This method is developed from boundary layer equations. The *r/R* term in the equation keeps the corrected coefficient realistic at the root (MacNeill and Verstraete, 2017).

$$C_l = C_{l_0} + \frac{r}{R}\tanh\left(3.1\left(\frac{wr}{V}\right)^2\left(\frac{c}{r}\right)^2\right)\left(2\pi - C_{l_0}\right) \tag{10}$$

E. Drone Research

The purpose of the study in this section is to acquire a relationship between blade diameter and weight and to avoid divergence from reality during the design phase. Before starting the blade design, quadcopter multirotor under 2 kg is selected as the target drone group. This type of drone is mostly for entertainment purposes and can take photos and videos. Weights and propeller diameters of quadcopters under 2 kg on the market were investigated.

While searching for the drones in the market, their features were examined in the related sales websites and their weights were taken as data. Propeller properties were obtained from the sale websites of propellers produced and sold externally for selected drones. The weight and propeller diameters of various drones are tabulated as follows and plotted in MATLAB.

3D Robotics Solo	1.99 kg	0.254 m
DJI Phantom 4 Pro	1.388 kg	0.23876 m
DJI MAVIC 2	0.907 kg	0.22098 m
Syma Cheerwing	0.910	0.16307 m
SKEYE NANO	0.014 kg	0.03 m
Hubsan X4 H501S drone	0.410kg	0.185 m
SIMREX X300C Mini Drone	0.2211263 kg	0.045 m
DJI SPARK	0.3 kg	0.1194 m
CSJ S167	0.202 kg	0.145 m
HS720	0.4581283 kg	0.155 m
B20 EUS GPS	0.543 kg	0.182 m
DJI INSPIRE 2	4.250 kg	0.24 m
DJI MAVIC PRO PLATINUM	0.743 kg	0.1 m
CSJ S161 Mini Pro	0.580 kg	0.16 m
Xiaomi FIMI x8 SE 2020	0.765 kg	0.215 m
Go Pro Karma Drone	1.006 kg	0.254 m
X708W	0.726 kg	0.14986 m
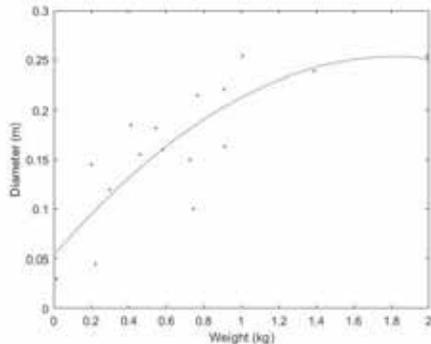
(a)   (b)

Figure 5 (a) Similar Drone Research **(b)** Correlation between weight and blade diameter

Depending on the correlation in Fig.5, the historical equation between drone weight and blade diameter can be expressed as follows.

$$-0{,}0607W^2 + 0{,}2206W + 0{,}0529 \tag{11}$$

F. Airfoil Selection

Since drone blades are very small, even if they rotate at high rpm values, the Reynolds number encountered by the airfoil sections is quite low. When an approximate calculation is made, it is observed that the Reynolds number order is around 100000-150000. A historical study has shown that profiles such as NACA4412, Clark Y, SD7062, Eppler E63, NACA0015 are used in aircrafts with low Reynolds numbers.

These profiles were analyzed in the XFLR5 program for 150000 Reynolds. Airfoil graphics were drawn on top of each other and the profile that is more suitable for the design was chosen to be NACA4412. When looking at these graphs, it was seen that NACA4412 and Clark Y stand out compared to the others. Although the properties of these two airfoils are close to each other, the *cl/cd* ratio of the NACA4412 profile is higher in the possible operating angle of attack range.

G. Optimum Blade Design

According to the results obtained from the BEMT, the inflow for untwisted blade is concentrated toward the propeller tips, Eqn.(12). This result makes the propeller unideal and increases the induced power consumption, Eqn.(13).

$$\lambda(r) = \lambda_{tip} \cdot r^n \tag{12}$$

$$C_T = 4 \int_0^1 \lambda^2 r \, dr = \frac{2\lambda_{tip}^2}{n+1} \rightarrow \lambda_{tip} = \sqrt{n+1}\sqrt{\frac{C_T}{2}} \tag{13a}$$

$$C_{pi} = 4 \int_0^1 \lambda^3 r \, dr = \frac{4\lambda_{tip}^3}{3n+2} \tag{13b}$$

$$C_{pi} = \frac{2(n+1)^{\frac{3}{2}}}{3n+2} * \frac{C_T^{\frac{3}{2}}}{\sqrt{2}} \tag{13c}$$

The situation where *n* equals to zero is the ideal state. When the value of *n* is greater than 1, the value of inflow ratio increases while *r* values changes from 0 to 1. Thus, it behaves similar to the λ value obtained from

the result of the BEMT applied to an untwisted blade. As a result, when the value of n is greater than zero, the induced power coefficient increases and the blade behavior becomes unideal.

It is clearly seen in Eqn.(12) that the distribution of λ depends on the geometric properties of the blade. Therefore, the characteristic of the distribution of λ along spanwise can be changed by changing the blade geometric properties. In this study, this feature was used while trying to design the propeller and it was tried to obtain a high efficiency blade by changing the geometric properties of the blade.

There are two components that are effective in propeller power consumption. One of them is the induced power related to the induced flow through the rotor disk and the other is profile power related to the profile drag on the airfoil. In order to minimize the propeller's total power consumption, both power components must be at minimum levels.

Induced power can be minimized by making the inflow ratio's value independent of r. But at the same time, profile power must be minimized. In order to minimize the profile power, the angle of attack must be at the maximum cl/cd value at each blade section. In this case, Eqn. (2) can be rewritten as follows.

$$dC_T = \frac{\sigma C_{l\alpha}}{2}\left(\theta - \frac{\lambda}{r}\right)r^2\,dr = \frac{\sigma C_{l\alpha}}{2}\alpha_1 r^2\,dr \tag{14}$$

If Eqn. (1) and Eqn. (14) are equalized, the inflow ratio is found as follows.

$$\lambda = \sqrt{\frac{\sigma r C_{l\alpha}\alpha_1}{8}} \tag{15}$$

In this case, the "σr" expression must be constant for making inflow ratio independent of r. Sigma expression is solidity and can be expressed as follows.

$$\sigma = \frac{N_b c}{\pi R} \tag{16}$$

Therefore, for sigma expression to be constant, the distribution of the chord length along the blade should be as follows.

$$c(r) = \frac{C_{tip}}{r} \tag{17}$$

Eqn.(17) gives the change in chord length which is called the optimum taper. However, the taper alone is not sufficient for minimum power consumption. As can be seen in Eqn. (14), the blade must be given such a

twist that the angle of attack must be equal to α_1 in each section. The α_1 value here is the angle of attack at which C_l/C_d ratio is maximum. In this case, the distribution of the twist angle for optimum blade design should be as follows.

$$\theta(r) = \alpha_1 + \frac{\lambda}{r} \qquad (18)$$

Using historical data, the starting point in the design was chosen and the optimum blade design that should produce a certain thrust was made. A propeller with a diameter 20.556 cm was designed to carry a drone weighing 930 grams. The characteristics of the propeller are determined as in Table 2.

Table 2 Optimum Blade Design Parameters

Number of Blades	2
Propeller diameter	20.556 cm
Twist distribution(degree)	$35{,}06r^2 - 66{,}52r + 43.91$
Taper distribution(m)	0.0088/r
Root cutout	3 cm

Although the most efficient propeller structure is as in Table 2, the taper and twist properties of the geometry are linearized for ease of analysis and production. Propeller with linear taper and linear twist are less efficient than the optimum geometry. However, its efficiency is much higher compared to a rectangular and untwisted blade. Taper and twist equations are translated from eq.30 and eq.31 to eq.32 and eq.33 through linearization.

$$C(i) = C_{tip} + (R - y(i)) \cdot C_s, \quad \theta(i) = \theta_{tip} + (R - y(i)) \cdot \theta_s \qquad (19)$$

where C_s is the slope of the taper and θ_s is the slope of the twist.

After linearization the propeller properties are changed from Table 2 to Table 3.

Table 3 - Linearized Blade Design Parameters

Number of Blades	2
Propeller diameter	20.556 cm
Twist distribution(degree)	20.52534 - 153*y
Taper distribution(meter)	0.0303892 - 0.14*y
Root cutout	1.02785 cm

H. 3D Drawing of the Designed Propeller

CATIA V5 program was used as a drawing tool. The drawing is basically made by drawing the airfoils at certain stages. First of all, data was taken from the pitch angle and chord length arrays produced by the code in which the design was made. Eleven NACA4412 airfoils were drawn from the Airfoil Tools website with the pitch angle and chord length properties. These airfoils have been downloaded as an excel file. The x and y points of the airfoils have been transferred to CATIA via the GSD_PointSplineLoftFromExcel file. These airfoils form the framework of the design. A surface was created on the framework with the "MultiSections Surface" command in Generative Shape Design part of CATIA. Then the propeller hub is drawn. A rapidly shrinking airfoil section is used as a root cutout. This root cutout part connects the designed part and the hub. The fact that the root cutout part has an additional airfoil geometry has little effect on the thrust produced. Because this part is subject to low air velocity since it is close to the rotation center due to its location. The geometry drawn is shown in the Fig.6.
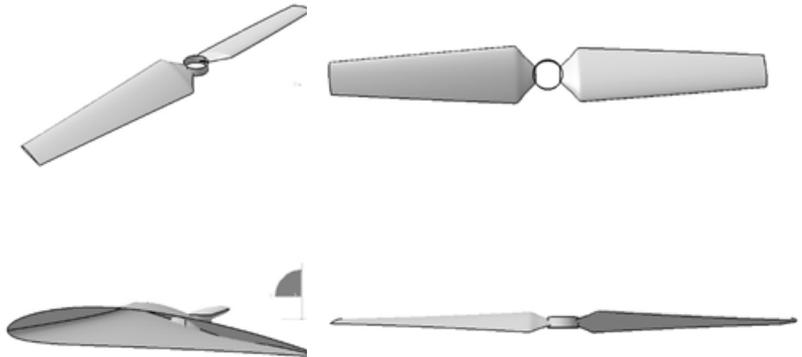
Figure 6 Linearized Blade Geometry

The geometry shown in Fig.6 was saved as *.stp* file extension and transferred to the Design Modeler section of Ansys Fluent. The propeller was drawn as surface in the CATIA program. The reason why it is drawn in this way is that the structural analysis will be done after the CFD analysis. Different thicknesses will be given to the appropriate material selected in the structural analysis and the analysis will be repeated. Therefore, there is a need for the geometry without thickness. The geometry is given a small thickness before inserting it into the CFD

analysis. Since it is not necessary in the CFD analysis, the amount of thickness given was not considered. More attention has been paid to ensure that all surfaces are closed.

I. CFD Analysis of the Designed Propeller

CFD analysis of the propeller designed with respect to the BEMT theory has been done. The main goal here is to compare theory with CFD to see if the archived computer code is accurate enough to start the design process. If the theory gives accurate results to a certain level, it can be used quickly in the first design stage. CFD analysis is much more expensive in terms of time than running a BEMT code. Therefore, if the code gives appropriate results, it will save time and money for the designer.

The geometry designed with BEMT in MATLAB and drawn with CATIA has been transferred to Ansys Design models. Two enclosure has been created here for the geometry. The first enclosure is a small volume that is in the form of a cylinder and covers the geometry. The purpose of this enclosure is to introduce the effect of propeller rotating to the program in this region. Another enclosure is made as a rectangle to define the static region. Fig.7 shows the rotating region and static region created through enclosures. The width of the rectangle was set to 4 times the propeller diameter, while the length was set to about 10 times the diameter. The reason for these high rates is that the flow is not desired to be exposed to the wall effect. In addition to enclosures, a solid body is drawn between static and rotating regions. Through this piece, "body of influence" will be made at the meshing stage. "Body of influence" tool in the ANSYS-Meshing provides arranging the mesh size in a particular volume. User can decrease the mesh size via this tool. The goal here is to prevent sudden changes in mesh element dimensions. CFD analysis results can be affected by sudden size changes of mesh elements.
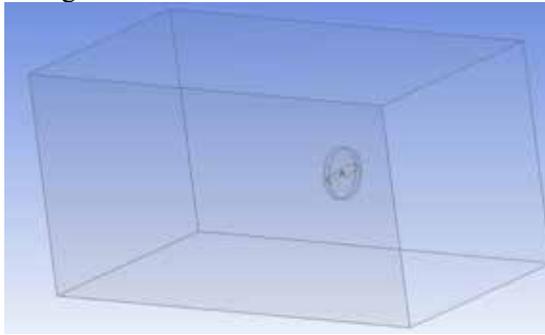
Figure 7 Rotating & static regions used for CFD analysis

After the enclosures were made, the propeller was removed from the rotating region with the boolean operation and the rotating region was removed from the static region. However, while extracting the rotating

region from the static region, the extracted element is preserved. Because, during the meshing, the body sizing will be made and the element size will be decreased in this region. When the subtraction is done, the volume it emits in space is analyzed, not the geometry itself. This process saves time during the meshing phase.

After the enclosures were created, the geometry was transferred to the mesh section. Body sizing was created for the rotating region by means of insert sizing in the mesh section. The purpose of creating body sizing in this region is to better capture the flow physics here. For this reason, while global mesh sizes are around 40-45 mm, mesh sizes around the rotating region are around 6 mm. In addition, the propeller geometry has a very twisted structure. For this reason, while body sizing is done, the capture curvature feature has been turned on and the normal angle value of curvature has been reduced to 5 degrees. Thus, the shapes of the airfoil, root cutout and hub geometries are well captured. In the mesh global settings, adjustments are generally made for the static region, so the mesh sizes are kept large. In addition to body sizing and global mesh adjustments, body of influence was made using solid created in the Design Modeler. Thus, the size of the mesh elements did not change very quickly in the transition from rotating region to static region. After the mesh was created, the geometry section was taken as in the Fig.8 and it was checked whether the physical properties of the geometry were captured.
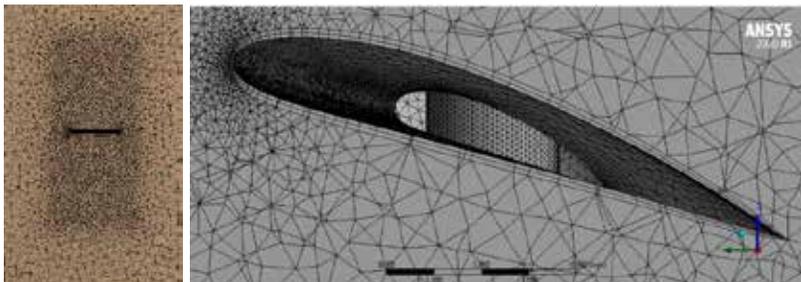
Figure 8 Mesh section

Body sizing and body of influence effects can be clearly seen in the sections. In these parts, it is seen that the mesh sizes decreased in two stages. After adjusting the mesh dimensions, an inflation layer is defined on the propeller surface to capture the flow physics near the wall. The height of the first mesh layer and the number of layers were determined according to the selected turbulence model and boundary layer thickness. The first layer height is determined from the following equation

$$y = \frac{y^+ \mu}{U_\tau \rho} \tag{20}$$

where

$$U_\tau = \sqrt{\frac{\tau_w}{\rho}}, \quad \tau_w = \frac{1}{2}C_f\rho U_\infty^2 \text{ and } C_f = \tag{21}$$
$$0.058(Re_l)^{-0.2}$$

Here, the choice of y+ value is critical. Turbulence models and wall functions operate at different y+ values. Realizable k-e method was used to solve the problem. While using this method, scalable wall function is used as a wall function. In order to capture the flow physics in the scalable wall function, the y+ value must be greater than 11.5 and when using the realizable k-e method, the y+ value is usually chosen above 30. After a few trials, the y+ value was chosen as 50 because the skewness values gave good results. Apart from these calculations, the boundary layer thickness must be determined to determine the number of inflation layers. The boundary layer thickness can be determined from Eqn. (38). Using the boundary layer and first layer thicknesses, the number of layers can be obtained from Eqn. (39).

$$\delta = \frac{0,37x}{Re^{1/5}} \tag{22}$$

$$\delta = y * \frac{(1 - (GR)^{NL})}{1 - GR} \tag{23}$$

The term GR in Eqn. (39) stands for growth rate. 1.2 is selected by default in ANSYS. If a more detailed mesh is desired, 1.1 can be selected to make the mesh grow more slowly up to the boundary layer. This value is kept at 1.2 in order not to decrease the skewness values and increase the mesh number. The term NL in Eqn. (39) means number of layers. The number of layers can be obtained by leaving the NL value alone.

Because the physics of flow is based on rotation, different sections of the propeller are exposed to different velocities. This causes the boundary layer and initial mesh layer thickness to vary in different sections. The first mesh layer thickness in the propeller tip region, where the first mesh layer thickness is the smallest, is based on to capture all initial mesh layer thicknesses. In order to capture the entire boundary layer thickness, the boundary layer thickness of the root cut out region, where the boundary layer is the thickest, is taken as a basis. When this boundary layer thickness and first mesh layer heights are substituted in Eqn. (39), the number of layers is found to be 2. First layer thickness, boundary layer thickness and number of layers used in CFD analysis are given in Table 4.

Table 4 Inflation layer properties of the linearized geometry

First Layer Thickness (m)	0.00021939
Boundary Layer Thickness(m)	0.0016
Number of Layers	2

Fig.8 shows the inflation layer around the airfoil created using the features in Table 4. After the inflation step, the largest mesh sizes that capture the geometry were obtained with a few tires. As a result, the number of mesh elements is 2302327 and the number of nodes is 496765. The maximum skewness value of these elements was measured as 0.89855 and was accepted because it was lower than 0.95.

As the solution method, realizable K-epsilon method was used. This method is a very common turbulence model. The K-epsilon model has many advantages. It gives a very good estimate of the propagation rate of circular and planar jet streams. It gives great results when used in separating and rotating flows. In addition, it is a model that captures the recirculation physics in separation flows well. Hence, it captures the flow over complex geometries well. The main reason for using this model in this project is its superior performance in rotating flows (Shaheed et al., 2019).

After choosing the solution model, movement was given to the mesh from the cell zone conditions section. The 5500 RPM angular velocity is assigned to the mesh elements in the rotating region. Thus, the rotational physics of the propeller was introduced to ANSYS. Since the hover situation was requested to be analyzed, speed regulation was not made in the inlet and outlet conditions. Finally, report definition was created to measure the thrust generated by the propeller. Calculation of the force in the direction of the z axis, which is the rotational axis of the propeller, is described in this section. Then hybrid initialization was done and the solution was started. Fig.9 shows the calculation of the thrust force as a result of iterations and its convergence. The graph is obtained in the Ansys for the linearized geometry.

As can be seen from the convergence of the thrust force, the thrust produced by the designed propeller is in the order of 1.5 N. Therefore, the thrust force of the propeller is calculated as 2.3 N from the BEMT code, while the thrust force from the CFD analysis is 1.5 N. CFD analysis calculates about 35% less thrust. In studies conducted for larger thrust, it has been observed that this difference gradually decreases. For example, for the impulse of 9.3 N calculated by BEMT, the CFD analysis result was found to be about 7 N. Therefore, as the geometry and the amount of thrust grow, the margin of error decreases. For this reason, in order to generate a thrust of 2.3 N in CFD analysis, the force calculated in BEMT must be slightly less than 1.6 times the force to be calculated in CFD. However, a conservative calculation was made and 1.65 times of the required thrust was calculated with BEMT. A second propeller with a thrust of 3.8 N was designed with BEMT. This propeller designed with BEMT is expected to

generate slightly more thrust than 2.3 N as a result of CFD analysis. The physical properties of this propeller are shown in Table 5.
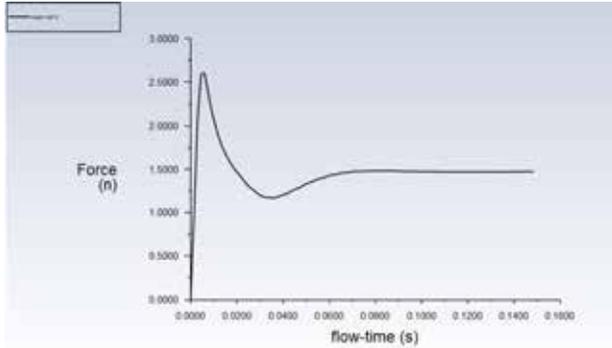
Figure 9 Thrust Calculation for First Design

Table 5 Properties of the second propeller

Number of Blades	2
Propeller diameter	20.556 cm
Twist distribution	24.9865 - 175*y
Taper distribution	0.04453 - 0.19*y
Root cutout	1.02785 cm

The second design made with the BEMT code was likewise drawn through the CATIA program. The new design is shown in Fig.10. This design has a higher twist and taper rate than the first design. Thus, 3.8 N thrust was generated with the BEMT code.
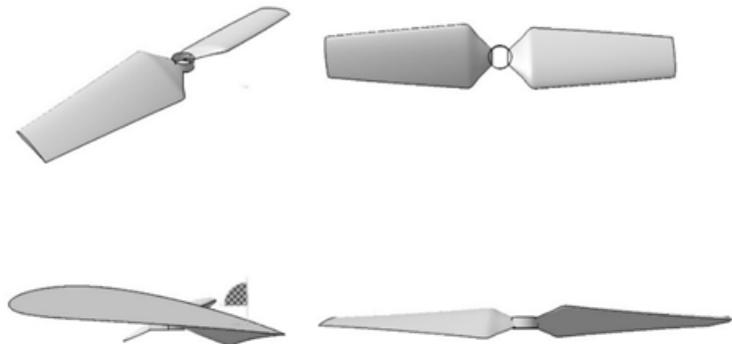
Figure 10 Corrected Design Geometry

After drawing the design on the CATIA, all mesh operations and solution methods are the same as the previous design. However, the boundary layer and initial mesh layer thicknesses calculated in the second design will be slightly different from the initial design. The reason for this is that although the velocity to the sections is the same, the lengths of the airfoil chord vary. Inflation layer properties used in CFD analysis of the second design are given in Table 6.

Table 6 Inflation layer properties of the corrected geometry

First Layer Thickness (m)	0.00021939
Boundary Layer Thickness(m)	0.0016
Number of Layers	2

Since all the steps are the same as the previous design, the graph of the converging thrust value as a result of the Ansys-Fluent analysis is given directly in Fig.11. As predicted, the thrust was achieved to be about 2.36, slightly above 2.3. It is desirable that the calculation be conserved. Because the propeller may not produce the same thrust with the same rotation speed as a result of bad weather conditions. As a result, the designed propeller produces 2.36 N thrust. Since the propeller is designed for a Quadcopter drone, the total thrust generated by the drone will be 9.44 N. In this case, 930 grams, which is the weight determined at the beginning, can be easily transported by the designed propellers.
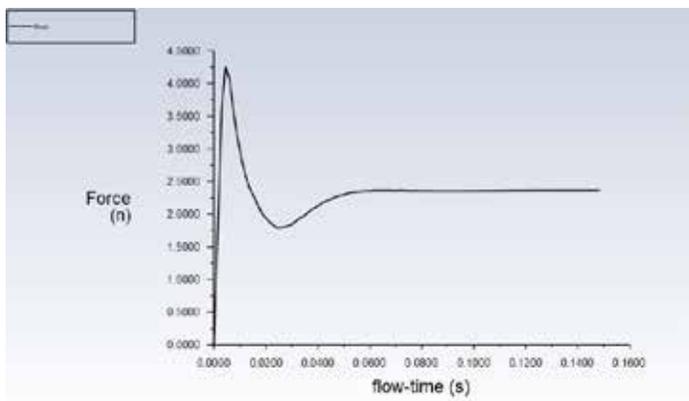
Figure 11 Thrust Calculation of the Corrected Design

After the analysis was completed, the results were examined in the Post Process stage. It has been checked whether there is anything contrary to the physics of the flow. It was decided that the observed results fit the flow physics. In Fig.12 (a), plane is assigned to the center of the propeller along ZY coordinates and streamlines are observed. As expected, the propeller

draws air in from the front part and the air contracts towards the propeller disc. In addition, the air rotates as it passes through the propeller and progress to rotate behind the propeller. This situation is clearly seen in the image taken from behind the propeller in Fig. 12(b). In addition, the speed of the flow passing through the propeller was also controlled. As expected, the flow velocity reaches its maximum towards the ends as it goes to zero towards the hub. This situation is shown in Fig. 13. As a result, it is clearly understood at the post-process stage that the rotational physics of the propeller is perceived by the program and the results are made accordingly.

(a)   (b)
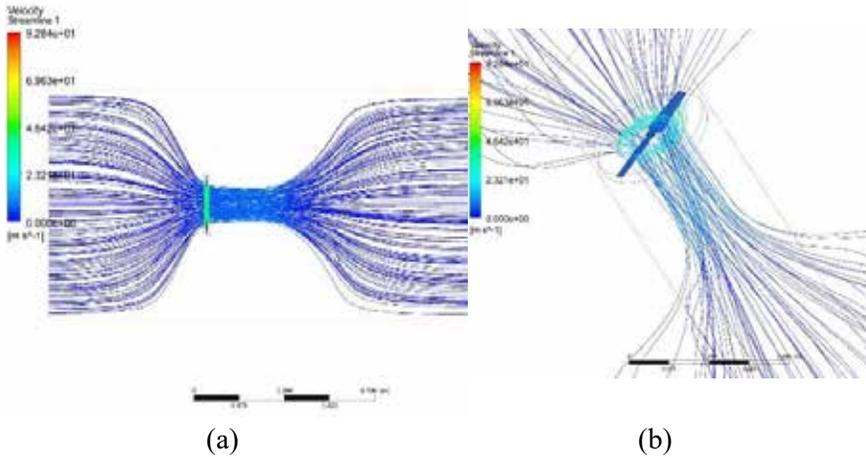
Figure 12 (a) Midplane Streamline **(b)** Flow behind the propeller
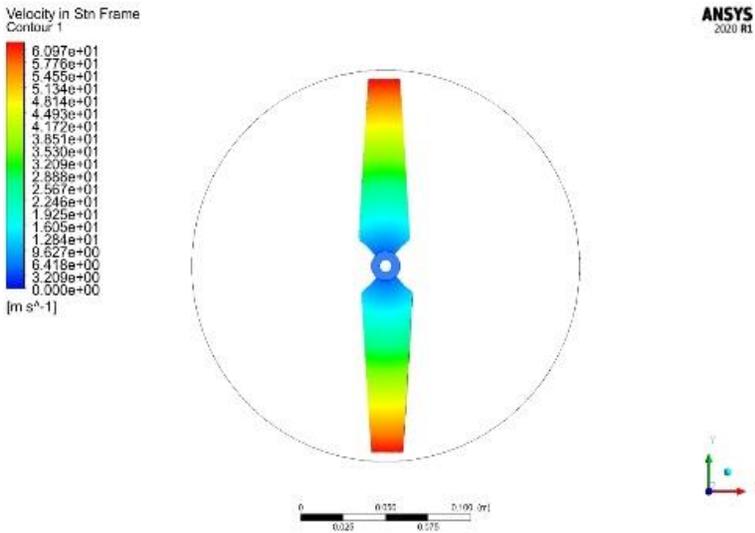
Figure 13 Flow velocity distribution

J. Material Selection Criteria for Drone Propellers

Appropriate material will be selected in this part of the study for the aerodynamically designed propeller. In the first stage of the material selection study, propeller materials used in academic research and companies were investigated. In addition, the criteria considered in the selection of materials from similar sources were investigated. As mentioned in the previous sections, the most important design parameter for a drone is lightness. Even the slightest reduction in weight means flying longer and being able to climb higher. Therefore, although the effect of the choice of propeller material on the weight is in the order of grams, the most important parameter in the selection is lightness. An indirect effect of weight is that it is effective in determining moment of inertia. A lighter design will have a lower moment of inertia. Also, making the design in the form of a shell will reduce the moment of inertia dramatically. Lowering the moment of inertia increases the drone's controllability. As an effect of this, the drone can make speed changes faster. Therefore, besides the performance-enhancing effects of reducing weight, it also has the effects of increasing controllability (Turcanu et al., 2015).

Another important criterion in material selection is that the selected material does not fail as a result of the stresses on it. If the stresses acting on the material exceed the maximum stress limits it can resist, the material may undergo plastic deformation or even fracture.

The type of drone to be used also constitutes a criterion in the selection of propeller material. For instance, the use of aluminum propellers can be efficient in drones used in the agricultural sector without harsh environmental conditions. There is no need for an ultra-strong propeller as there are no harsh conditions. In addition, the aluminum propeller is inexpensive and easy to repair and replace. However, in drones used in more vital areas such as rescuing and searching operations, it is more appropriate to use composite materials both in order to increase performance and to prevent failure in case of a possible accident. In the entertainment industry, composite and plastics are generally used for drone blades. Composite propellers are generally used in drones used to take photos and videos. Because these drones are performance based. In addition, drones that take photos and videos should not be affected by vibration. Light propellers reduce the vibration. Plastic propellers are mostly used for drones that appeal to small age groups. In these drones, cheapness is more important than performance. Also, since plastics are flexible, they are safer for children.

K. Structural Analysis and Material Selection

The aerodynamic design was made for recreational drones. For this reason, composite and plastic materials were assigned to the designed propeller and transferred to structural analysis. In addition, aluminum was also analyzed due to its ease of use and cheapness. These analysis results

were compared and the most suitable material was selected for the aerodynamic design. Analyzes were performed in the static structural module of ANSYS. Although the analysis type is static, the dynamic physics of the problem is introduced to the program by opening the inertia relief function in ANSYS. Before starting the analysis, the geometry used in CFD was prepared for structural analysis. For this purpose, an inward direction thickness about 0.2 mm was given to the surface which produce in CATIA at the SPACECLAIM program. The geometry which has 0.2 mm thickness is shown in Fig.14. "Share topology" tool is used between the hub and the propeller. "Share topology" is an Ansys-Spaceclaim tool that provides connection between different geometry parts. Information flow between the meshes in the hub and the propeller is not interrupted via this tool. After the geometric arrangements, the pressure distribution obtained from the CFD was transferred to the static structural module of ANSYS.
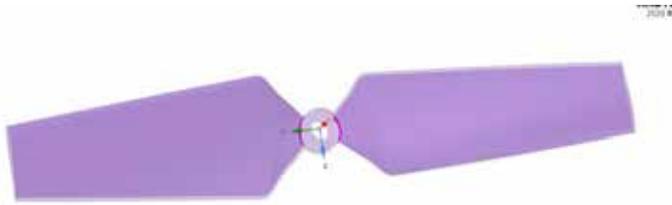
Figure 14 Corrected propeller with 0.2 mm thickness

In the static structural model, a mesh model was first created for the geometry. 2 million meshes have been created as computer capacity allows. The main point of attention when creating the mesh is the transition area between the propeller and the hub. The quality values of the mesh structures here are well kept. Because the maximum load will be experienced in this region. After the mesh model is prepared, the material is assigned to the geometry. Analyzes were repeated for aluminum, plastic, epoxy fiber, glass fiber and carbon fiber materials. After the material is defined, inertia relief feature is turned on in the program and remote displacement is defined. In static analysis, if there is a net force acting on an object and there is no constraint preventing the motion of this object, the model becomes unsolvable. If non-existent constraints are identified and movement is prevented, much more stress will be observed in the parts where the constraint is applied than in the real situation. The inertia relief mechanism basically defines acceleration to balance the net force acting on a structure. It returns the sum of the reaction forces in the constraints to zero. Thus, an additional reaction force due to the constraint does not occur. After defining the inertia relief on the propeller, a very low angle of freedom was defined in the propeller rotation axis by means of the remote constraint. Therefore, in this section, the propeller will have an acceleration

definition with the results from the CFD analysis. As a result, the dynamic behavior of the propeller is modeled in the static structural mode at ANSYS.

Before solving the analysis, von misses stress, directional deformation and safety factor solution files were created. The reason for using directional deformation is that only the deformations in the direction of rotation axis are wanted to be known. Since an angle of freedom of 5 degrees is given to the rotation axis, the deformations in other axes depend on the positional change of the material, not the structural change. In addition, the reason for solving the safety factor is to understand whether the material will fail according to the maximum von misses stress.

After the analysis preparations were completed, the calculations were repeated for the selected materials. Fig.15 and Fig.16 show the analysis results for the aluminum propeller.
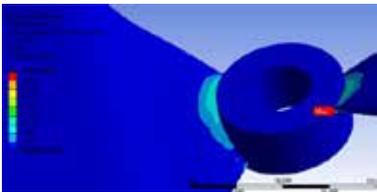
Figure 15 Maximum stress   **Figure 16** Directional deformation
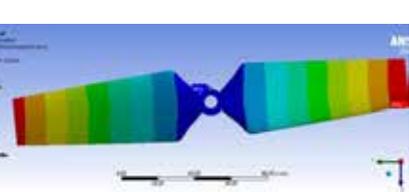
Fig.15 shows the region where the maximum stress occurs on the aluminum propeller. Maximum stress occurs at the part where the propeller is connected to the hub. It is clearly seen that the stresses increase in the root part of the propeller. This result is expected, since the bending moment created by the aerodynamic forces acting on the propeller is maximum in the root region. When the deformation results are examined in Fig.16, the deformation towards the two ends of the propeller is maximum. This result is also compatible with the material structure and the location of the connection point. These analyzes were repeated for all materials. Visual results of the Epoxy/Carbon Fiber analysis are given in the Appendix. Table 7 summarizes the considered parameters of all analysis results.

Table 7 Selected Materials and Properties

Material	Propeller Weight	Max. Stress	Max deformation	Safety Factor	Young Modulus	Shear Modulus	Tensile yield strength
Aluminium Alloy	8,0955 gr	115,55 MPa	0,3200 mm	2,4231	71000 MPa	26692 MPa	280 MPa
Epoxy/Carbon fiber,QI [0, +45,-45,90]	4,7807 gr	115,89 MPa	0,5221 mm	3,9641	43430 MPa	16266 MPa	459,4 MPa
Epoxy/glass fiber,UD prepreh,QI	5,7898 gr	117,34 MPa	1,1384 mm	4,0897	19970 MPa	7642,6 MPa	479,9 MPa
ABS Plastic	3,4894 gr	112,04 MPa	9,3681 mm	0,3695	2390 MPa	854,18 MPa	41,4 MPa
Nylon(PA6)	3,7557 gr	114,65 MPa	21,307 mm	0,3759	1060 MPa	392,59 MPa	43,1 MPa
Nylon 6- glass fiber reinforced(PA6 -GF)	4,3148 gr	114,61 MPa	3,7905 mm	1,0820	5960 MPa	2207,4 MPa	124 MPa

When the results are examined, it is seen that the least deformed material is Aluminum. However, aluminum is much heavier than other composite and plastic materials. The maximum stress values affecting the

materials are close to each other, but since the tensile yield strength properties of the materials are very different, the safety factor values differ. It is obvious that plastic and nylon will fail if they are used alone. When Nylon reinforced with glass fiber is used, the minimum safety factor is 1.08. This means that the material will not fail under normal conditions. But it is not in a safe range. In aviation, the safety factor is usually 1.5. The two best material choices seem to be carbon fiber and glass fiber. The safety factor of fiber glass is larger than carbon fiber, but fiber glass is heavier and undergoes more deformation. Besides being the lightest material remaining in the safe zone, another striking feature of carbon fiber is its low deformation. As a result of the analysis, it is seen that the most suitable material for aerodynamic loadings and problem physics is epoxy carbon fiber.

L. Results and Conclusion

In this study, it has been tried to make an efficient propeller design starting from scratch. BEMT is coded and validated and arranged for small propellers. Using historical data, the starting point in the design was chosen and the optimum blade design that should produce a certain thrust was made. A blade with a diameter 20.556 cm was designed to carry a drone weighing 930 grams. The characteristics of the propeller are determined as in the Table 2. When the optimum blade characteristics are as in the table and the propeller rotates at 5500 rpm, the drone will generate enough thrust to be hovered. Although the losses are tried to be modeled, BEMT has a 2-dimensional basis. Many three-dimensional effects cause the results of this theory to diverge from reality. Therefore, the results must be validated by experiments or CFD analysis before they can be used directly. For this purpose, geometry has been simplified and linearized in the other part of the study. It was then drawn in CATIA and transferred to the Ansys Fluent. As a result of CFD analysis, it was seen that BEMT theory is deviated from reality for low thrust values. As the thrust value increases, the BEMT and CFD results converge. Although drones work with low thrust values, BEMT is a good starting point for design stage. By comparing CFD and BEMT results, the design can be quickly shaped in an iterative way. For example, in this study, it is seen that the thrust force of 2.3 N calculated by BEMT is 1.5 N when calculated in CFD. For this reason, a new design has been made with BEMT that will produce 3.8 N of thrust. When CFD is applied to the new design, it is seen that the obtained thrust is 2.36 N.

In short, the final target of 2.3 N was approached very quickly. The main goal in this study is to enable the designer to quickly design an efficient propeller. However, material selection is also critical for an efficient propeller production. Too heavy materials cause an increase in

moment of inertia and a decrease in controllability. In addition, the selected material should not undergo excessive deformation under aerodynamic loads. This can reduce the thrust produced because it adversely affects the flow physics. Structural analysis was carried out in order to make the best material selection for the aerodynamically designed propeller. As a result of the structural analysis, carbon fiber material, which has the lightest weight, undergoes less deformation and remains in the safe zone, was chosen as the most suitable material for aerodynamic design. In this paper, efficient propeller production is aimed with analyzes made in two different areas. Increasing the efficiency of the drone blades increases the flight time. Nowadays, drone usage is widespread in every field. Especially their activities in life-saving areas stand out. Therefore, drones that will be used to reach people after a disaster can stay in the air for a longer time, and this can have very important consequences. From another point of view, more efficient batteries reduce environmental pollution and contributes to the individual economy of people.

This study is a basic study on direct design. The work can be improved in many ways. For example, by performing performance calculations, the extended flight time compared to a rectangular blade can be calculated. Many different physical effects can be calculated and the model can be brought closer to reality. The results of CFD analysis and BEMT code can be checked by doing real experiments. With vibration analysis, the natural frequency of the structure can be determined and precautions can be taken against resonance. In short, this study is a basic study and can be taken to more advanced levels and branched into many different fields. But in this simple form, it gives important results in the first design phase of the blades and saves time for the designer.

Appendix

Structural Analysis Results of the Epoxy Carbon Fiber
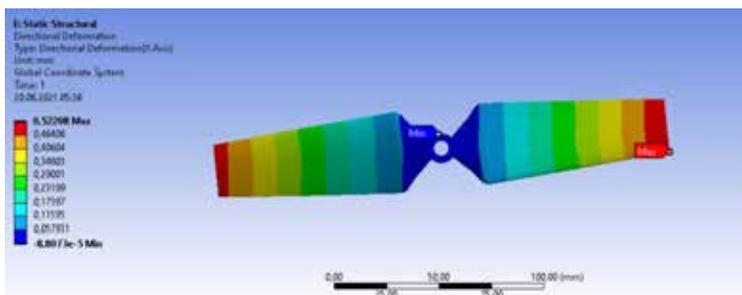
Figure A1 Epoxy Carbon Fiber Directional Deformation
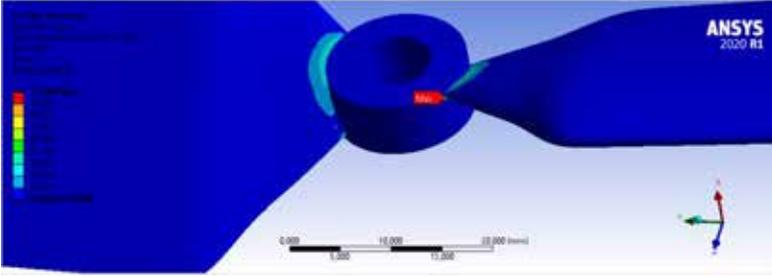
Figure A2 Epoxy Carbon Fiber Equivalent(von-Misses) Stress

Figure A3 Epoxy Carbon Fiber Safety Factor

References

Andria, G., Di Nisio, A., Lanzolla, A., Spadevecchia, M., Pascazio, G., Antonacci, F. & Sorrentino, G. (2018). Design and performance evaluation of drone propellers, *5th IEEE International Workshop on Metrology for AeroSpace*, pp. 407–412.

Leishman, G. J. (2006). *Principles of helicopter aerodynamics*, Cambridge University Press.

MacNeill, R. & Verstraete, D. (2017). Blade element momentum theory extended to model low Reynolds number propeller performance, *The Aeronautical Journal*, **121 (1240),** pp. 835–857.

Peterson, R. L. (1995). *Full-scale hingeless rotor performance and loads., NACA Report*.

Shaheed, R., Mohammadian, A. & Gildeh, H. K. (2019). A comparison of standard k–ε and realizable k–ε turbulence models in curved and confluent channels, *Environmental Fluid Mechanics*, **19(2),** 543-568.

Turcanu, D., Nicola, I., Prisecaru, T., Predoi, C., Todirica, C., & Ciobanu, M. C. (2015) The influence of carbon fiber propeller on the brushless DC motor control, *Materiale Plastice*, **52 (4),** pp. 525–528.

Vergouw, B., Nagel, H., Bondt, G., and Custers, B. (2016). Drone technology: Types, payloads, applications, frequency spectrum issues and future developments. *The future of drone use*, Springer.
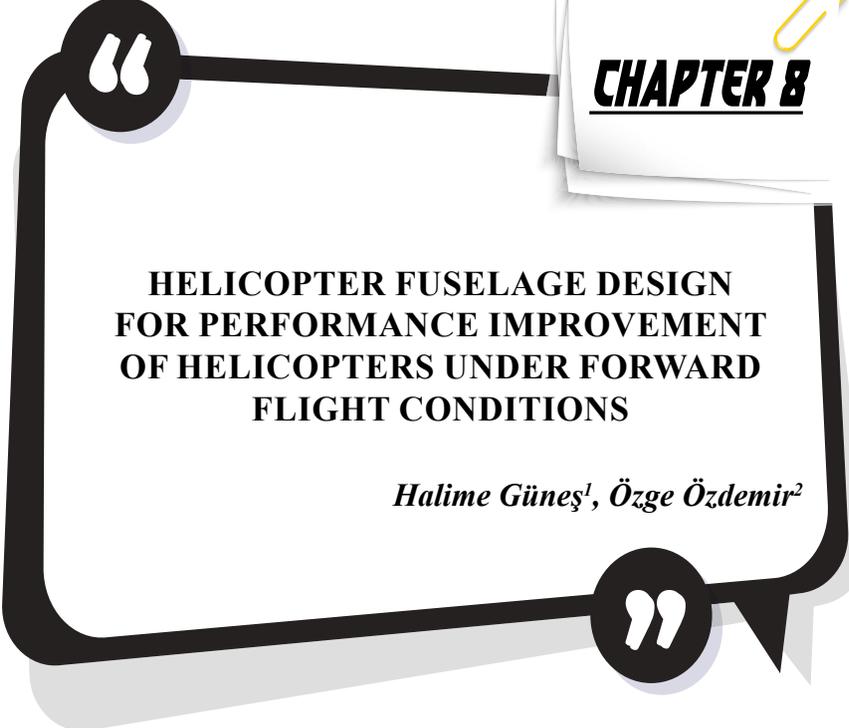
HELICOPTER FUSELAGE DESIGN FOR PERFORMANCE IMPROVEMENT OF HELICOPTERS UNDER FORWARD FLIGHT CONDITIONS

Halime Güneş[1], Özge Özdemir[2]

1 Performance Engineer, TR Motor, Çankaya, Ankara, Türkiye, ORCID: 0000-0002-6057-9304, halime.gunes@trmotor.com.tr
2 Asst. Prof. Dr., Department of Aeronautical Engineering, Istanbul Technical University, Türkiye, ORCID: 0000-0002-4755-2094, ozdemirozg@itu.edu.tr

I. Introduction

Helicopters have been widely used air vehicles for years due to their wide range of motion. There are varieties of helicopters such as conventional, coaxial, tandem, tilt rotor, and compound type. In this study, conventional helicopters were investigated because the use of conventional helicopters is more common than others and it is possible to apply the results to other helicopters. Since the use of helicopters in the military and civilian areas is widespread, it continues to be researched and developed.

Helicopters are used for fast and easy transportation, observation, journey, security, defense, etc. One advantage of helicopters over fixed wing air vehicles is that they have the ability for vertical take-off and landing. The fact that small areas are sufficient for landing and take-off for helicopters provides a great advantage for both military and civilian use. Another advantage is the hovering and wide range of motion capabilities of helicopters. Helicopters can hover in the desired area, and can go left, right, or backward. This allows staying near a targeted point for rescue operations, camera capture, observation, or attack. In military use, the high maneuverability of helicopters provides a great advantage. It allows helicopters to fly over difficult terrains and allows them to be protected from attacks.

In short, helicopters have been the subject of research, due to their wide usage areas and many advantageous aspects. As a result of efforts to increase their performance, helicopters have worked more efficiently and become reliable vehicles day by day. Many parameters express the efficiency of a helicopter. Accordingly, an efficient single parameter does not mean that the entire helicopter is efficient. After examining each parameter separately, it is necessary to look at the total helicopter performance. Within the scope of this study, the helicopter fuselage will be analysed and it is aimed to increase the aerodynamic efficiency of the fuselage. Here, aerodynamic efficiency is primarily related to the drag parameter. Aerodynamic improvement of the helicopter fuselage reduces drag. A decrease in drag is desirable in every aspect. Keys and Wiesner (1975) says that a typical conventional helicopter in cruise flight uses 45% of its power to compensate for its body drag. By looking at this huge effect of fuselage drag, it can be said that less helicopter drag means less power needed to overcome it. Therefore, it means that the power required to be produced by the main rotor is reduced. This leads to a smaller and lighter engine that powers the main rotor and many more effects.

In the first stage of the study, a literature review was conducted. As a result of the research, it has been seen that; the fuselage, hub, and skid generate most of the parasitic drag of a typical twin-engine light-class

helicopter in forward flight, respectively. Here, 38% of the total drag is the fuselage, 23% is the rotating rotor head, and 13% is the skids (Stepanov et al., 2016). As can be seen from here, it is a good option to make improvements on the fuselage shape if it is desired to decrease the helicopter drag. In the studies, it has been seen that the most effective components on drag in the fuselage are the aft fuselage, the nose, and the engine cowling. The nose is the first point of contact with the air in forward flight, the engine cowling is the part that first encounters the air from the main rotor, aft fuselage is the transition part to the tail boom, where separations occur and flow cannot follow the fuselage. In this study, the aerodynamic performance increment by aft fuselage improvement will be examined.

Batrakov et al. (2018) studied the effect of rear fuselage improvement on decrement of drag coefficient, and they found that it had a significant share in total drag. On an 11m long helicopter, the result of the optimization made in this section a 2.1% reduction in drag coefficient was obtained with a maximum change of 16.5 cm at the rear. They have also done improvements on the skid. The overall drag coefficient decrease was 4.6% when taken into account with body and skid modification. The commonly used actuator disc model was used to simulate the main rotor. Zhang et al. (2011) said that the most effective component of drag force is the aft part, and they explained that this effect is because of the flow separations and formation of vortices here. However, mission requirements and design constraints often do not allow modifications in this region. They analyzed an EC135 helicopter in a wind tunnel by modifying only its rear part and compared this geometry with the original geometry. As a result, they achieved a 22% drag reduction. The reason for a high amount of drag reduction is that the base geometry of the EC135 helicopter is quite far from the aerodynamic shape. Shi et al. (2020) have made an optimization by changing the upsweep angle on the aft fuselage and the height of the tail boom. Here, both decreasing the upsweep angle and decreasing the tail boom height change the aft fuselage shape and soften the transition from the front to the tail. Thus, the flow separation in this section is reduced. Lowering the tail boom height alone resulted in a 4.37% reduction in drag coefficient at 0° angle of attack.

Based on the studies, it was decided to make changes to the geometry of the rear fuselage to improve the aerodynamics of the helicopter. New geometries going to be obtained by changing the rear fuselage geometry of an existing helicopter, and the geometry which has the lowest drag coefficient will be selected according to CFD results. In this way, the drag coefficient difference between the new geometry and the base geometry will be expressed. The main rotor will be taken into account in the CFD analysis. This is because the main rotor interaction has a crucial effect on

helicopter drag.

Another study on this region is Seddon's (1982) wind tunnel tests. He plotted the variation of drag force with the upsweep angle at the rear of a helicopter by conducting wind tunnel tests at different angles of attack between -18 and 9 deg. The graphs obtained are shown below.
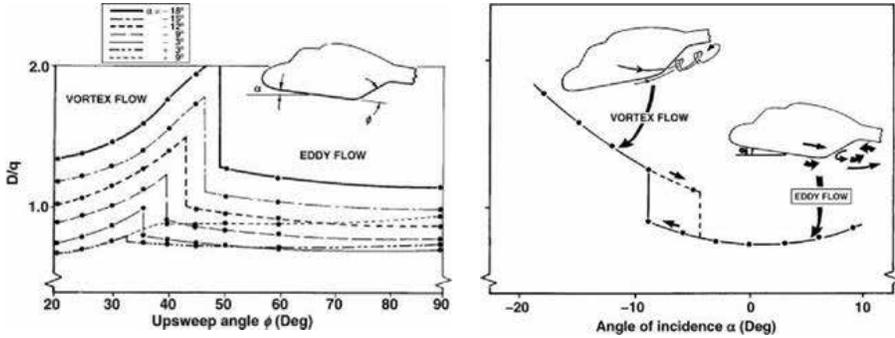
Figure 1 *Seddon's upsweep angle and drag relation plots, Seddon's (1982)*

In this study, a conventional helicopter, the BeeCopter helicopter unmanned airvehicle designed for Technofest competitions in Turkiye, was used. The purpose of this study is to create an example case and to demonstrate the significant effect of changes to the rear part on fuselage parasitic drag. Certainly, the effect of changes on different geometries will be different. But the goal here is to demonstrate and explain what kind of changes are appropriate and meaningful. However, the type of modifications available may vary depending on the helicopter type. The important thing here is to prevent flow separations and soften sharp transitions.

Among the flow analysis types, CFD (Computational Fluid Dynamics) is the most accurate method. High computer power, time and cost are required. But the result is accurate enough to be worth the effort. In this study, CFD will be used as a tool, not a goal. There are some points to be considered to perform CFD analysis. It is very important for this type of analysis that the meshing process should be done with sufficient precision before the analysis. The convergence and accuracy of the analysis are directly related to the mesh elements and the viscous model type. If these criteria are not taken into account, the final work is meaningless. In Ansys Fluent, model types change according to the type of flow and the dominant effects in the flow. According to these models, the required mesh intensities also change. Within the scope of this study, attention was paid to all these criteria and the most suitable modelling was made for the flight condition. CFD programs are programs that solve Navier-Stokes equations with numerical approaches in the background. The solutions of these equations

are made possible by various discretization and finite volume methods. Reynolds-averaged Navier–Stokes equations (RANS) and Large Eddy Simulation (LES) model types are available for turbulence modelling in the Ansys Fluent program to be used within the scope of this study.

RANS-based models are generally suitable for engineering applications. RANS-based models include one-equation, two-equation, and four-equation models. Among these models, the most widely used are Spalart Allmaras, Standard k-ε, Realizable k-ε, Standard k-ω, and SST k-ω. Spalart Allmaras model is a single transport equation model solving directly for a modified turbulent viscosity. It is an economical model that enables the use of large mesh elements. It is suitable for use in areas such as wing profiles, aircraft fuselages, ship hulls etc. However, it is not suitable for flows with heavy separations. In the literature review, it was seen that the Spalart Allmaras model gave sufficient and good results for helicopter fuselage analysis and it was decided to be used in this study.

The effect of the main rotor on the fuselage is very large. Therefore, the main rotor effect will be considered. There are several methods for modelling the main rotor aerodynamics. In this study, the main rotor is modelled as an actuator disk using the Momentum Theory and an in-house code is achieved because the Momentum Theory gives results that are sufficient enough for this study. Renaud, et al. (2004) says that the computational cost of this modelling is significantly lower compared to the Navier Stokes calculation of unsteady flow around the rotating blades.

D. Helicopter Power Components and Parasitic Power

First of all, the types of drag affecting the helicopter and the forces that the main rotor must provide to overcome them should be examined. As mentioned before, the design will be made in forward flight condition. In forward flight, the required total power consists of induced power (P_i), profile power (P_0), parasitic power (P_p) and climb power (P_c), basically.

$$P = P_i + P_0 + P_p + P_c \#(1)$$

- P_i-induced power is the power required to overcome the drag due to generated rotor thrust. It means this is because of the rotation of the main rotor.

- P_0-profile power is the power required to overcome viscous losses at the rotor.

- P_p-parasitic power is the drag created by the whole helicopter that moves in the air. This is because of viscous shear effects and flow separations. This includes the fuselage and additional components. It increases with the cube of airspeed

- P_c-is the climb power required to increase the gravitational potential of the helicopter (Leishman, 2006).

In addition to that, there are miscellaneous power consumers like the tail rotor, hydraulic pumps, gearbox losses, generators, etc.
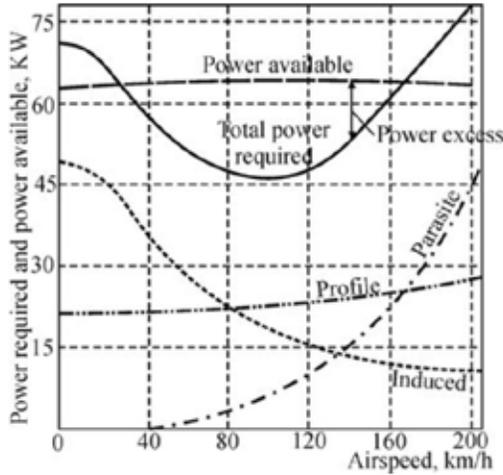
Figure 2 *The variation of power with airspeed, (Rotaru and Todorov, 2017)*

The variation of powers with airspeed and the share of these power types in the total drag is shown in Fig.2.

Parasitic Power

The fuel consumption and cruise speed affect helicopter parasitic drag. For the same gross weight, a helicopter's parasitic drag is significantly higher than a fixed-wing aircraft because, helicopter bodies are not aerodynamic as much as others and the effects of the rotor hub, shaft and blade attachments. The parasitic drag can be defined as;

$$P_p = D.V = \left(\frac{1}{2} \rho V_\infty^2 S_{ref} C_{D_f} \right) V_\infty \quad \#(2)$$

Here ρ is the air density, V_∞ is freestream velocity, S_{ref} is the reference area, C_{D_f} is the drag coefficient belongs to this area. If it is nondimensionalized, the parasitic drag coefficient can be written as;

$$C_{P_p} = \frac{P_p}{\rho A V_{tip}^3} \quad \#(3)$$

$$C_{P_p} = \frac{1}{2}\left(\frac{S_{ref}}{A}\right)\mu^3 \qquad C_{D_f} = \frac{1}{2}\left(\frac{f}{A}\right)\mu^3 \quad \#(4)$$

Here A is the rotor disc area, μ is the advance ratio and f is defined as equivalent flat-plate area or equivalent wetted area. Advance ratio is the ratio of free stream velocity over rotor tip speed.

$$\mu = \frac{V_\infty}{V_{tip}} = \frac{V_\infty}{\Omega R} \quad \#(5)$$

The equivalent flat-plate area defined as

$$f = C_{D_f} S_{ref} \quad \#(6)$$

This parameter depends on the hub, fuselage, landing gear and all external components areas. The drag coefficient can be written as;

$$C_{D_f} = \frac{D_f}{\frac{1}{2}\rho V_\infty^2 S_{ref}} \quad \#(7)$$

If the equivalent flat-plate area is put into Eqn. (7), it becomes

$$f = \frac{D_f}{\frac{1}{2}\rho V_\infty^2} \quad \#(8)$$

The usage of f value prevents any complication because of S_{ref}. The value of f is generally about 0.93 m² for small helicopters, and 4.65 m² for large helicopters.

Forward Flight Force Balance
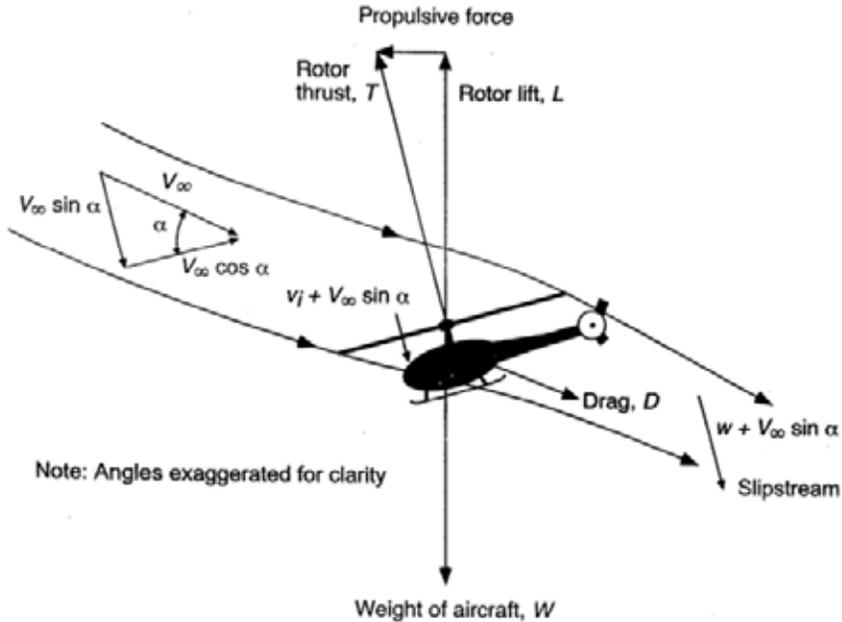
Figure 3 *Forward flight force balance, Seddon (1982)*

Since the analyses will be made in forward flight, the forward flight force balance should be known. In hover, upward thrust is generated from the helicopter rotor. In forward flight, the helicopter inclines nose-down to go forward. Thus, the main rotor thrust has two components, forward and upward. The upward component balances the weight of the helicopter. The forward component compensates for the drag of the helicopter.

II. Applications

The fuselage is the largest component of a helicopter. So, its aerodynamic effect is also major. In this paper, aerodynamic fuselage improvements were made. This improvement is related to the reduction of drag force.

A. Improvements on the Fuselage

As mentioned earlier, parasitic drag is related to the body and other external components. So, parasitic power can be reduced with fuselage modifications.
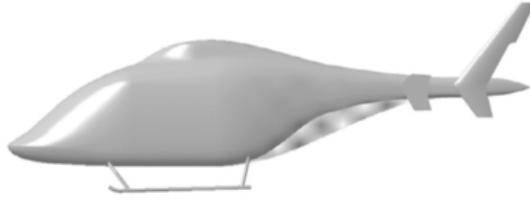
Figure 4 Changing on upsweep angle, Shi et al. (2020)

There is an inclined region located at the passage from the main body to the tail boom. The slope of this part, that is, the narrow angle it makes with the ground, is the upsweep angle. Shi et al. (2020) worked on aft body modifications on helicopter fuselage. They tried to change this upsweep angle and see its effects on drag. And they achieved a lower upsweep angle means lower drag. Here, too much reduction of the upsweep angle increases the helicopter volume and increases the weight. So, there is a limit for the increment of the upsweep angle. Within the scope of this study, a similar study will be carried out and it will be aimed to improve the rear fuselage by changing the upsweep angle.

Figure 5 Changing tail boom height, Shi et al. (2020)

They also studied the effect of the height of the tail boom on parasitic drag. And they found a lower tail boom means lower drag because of prevents the flow separations aft of the fuselage. The second study of this study will be changing the tail boom height. Tail boom height and upsweep angle modifications will be made gradually. Upsweep angle will be reduced at certain intervals; tail boom height will be reduced at certain lengths. It is aimed to acquire lower drag than the base one.

B. Determining Geometry

After deciding on possible modifications that can be made on the fuselage for drag decrement, the first step is to determine the geometry to which these changes will be applied. Searches were made on the internet for the geometry to be used in the study. Real-like helicopter CAD drawings were found on the internet and examined for use. These geometries were mostly in "step" format. Parameters which are determined during drawing, cannot be edited on a step file. So, this does not meet the requirements for this study.

The geometry which will use in this study is selected as ITU BeeCopter Team's helicopter. This helicopter was designed for Teknofest Helicopter Design Competition. This is a light-class utility helicopter. The reasons for using this helicopter are, knowing the design conditions, having full knowledge of the design of this helicopter, the possibility of editing the geometry, and convenience to make changes on the rear. The simplified geometry is shown below.
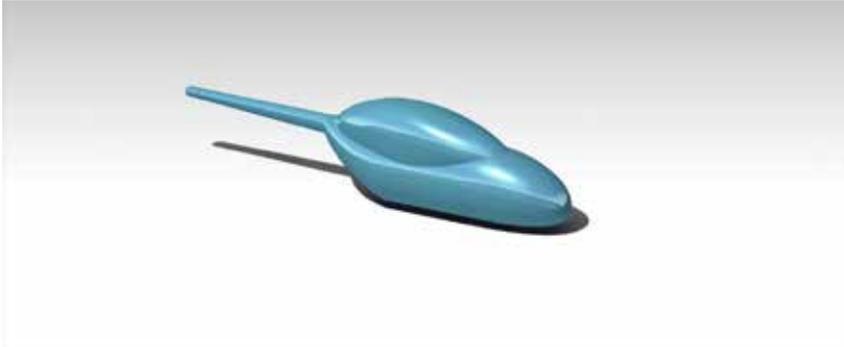
Figure 6 Original geometry

C. Initial Analyses Test Case

1. Preparations

The use of CATIA, Pointwise and Anysy programs was learned for the analyzes to be made within the scope of the study. The purpose of the first test analysis is to experience the use of these programs together, to have more extensive knowledge of the programs, to experience and learn to solve the problems during analysis and to gain the ability to interpret the approximate results. Accordingly, various scenarios have been tried with these three programs and experience has been gained.

BeeCopter's geometry has horizontal tail and landing skids, but in this work, only fuselage shape is considered. The geometry is imported pointwise. In pointwise reference, geometry is called a database. Firstly, meshing is completed by using this database. The program assigns an initial mesh structure with equal size over the entire surface with the dimension value entered by the user. So, this first mesh should be arranged. Since this is a test case, mesh elements were applied as coarse. Generally, large elements were used, but smaller elements were used on sharp edges and high-angle turns. Since separations will occur in these parts, calculations should be made at more points for the accuracy of the analysis. This means that more elements are required in these regions. In addition, during

creating volume mesh inflation layer could not be formed in these regions with large elements. After the arrangements are made, the quality of the elements is checked. If elements with high skewness are not fixed, there is a high probability of wrong calculation results at these points. In addition, these elements will cause problems in the volume mesh and the layered formation will be disrupted. After making appropriate arrangements, the obtained final surface mesh is shown below. This surface mesh has been examined and the max skewness value has been decreased to 0.55. And that is a quite fine value. Finer meshes are applied to the front part of the nose, junction of the engine cowling and main body, rear and front part of the engine cowling, junction of tail cone and main body, and the rear part of the fuselage and trailing part of the tail.

After that, the control volume is created. Generally, the control volume edge length should be 20 times the characteristic length. The element size at the control volume walls should be proportional to the geometry and dimensions of the control volume. To locate the origin of this control volume, a script is used to find the center of the helicopter.

After creating the control volume, a block is created that involves all faces. Volume mesh starts from the geometry and goes to the far field. The first layers on the geometry are sized quite small to analyze the boundary layer. Here, for a better result, the elements are adjusted as triangular prisms with certain heights. Before the volume mesh is created, some parameters should be determined. First layer thickness is the height of the first element of the volume mesh and it is calculated from the $y+$ value. Max layers are the selected number of these layers. The growth rate is the rate of outward growth of these elements. In this case, the maximum number of layers selected as 45, and the growth rate was adjusted to 1.2. To calculate first layer thickness characteristic length and freestream velocity should be known. Things to know about BeeCopter Helicopter and flight conditions for both meshing and next stages are given in the table below.

Table 1: *Flight condition information and characteristics of BeeCopter helicopter*

Forward Speed	62.5 m/s
Altitude	4000 ft
Temperature	300K
Pressure	87511 Pa
Density	1.0154 kg/m^3
Viscosity	$1.846.10^{-5}$
Characteristic Length	8.21 m
Frontal Area	2.448 m^2
Reynolds Number	28.0^6

Freestream velocity is determined as forward flight speed of the helicopter and it is 62.5 m/s. The y+ value is taken as 1. The characteristic length of the helicopter is 8.21 m. The first layer thickness Δs value is found by the following equation series.

$$Re_x = \frac{\rho U_\infty L}{\mu} \quad \#(9)$$

$$C_f = \frac{0.026}{Re_x^{1/7}} \quad \#(10)$$

$$\tau_{wall} = \frac{C_f \rho U_\infty^2}{2} \quad \#(11)$$

$$U_{fric} = \sqrt{\frac{\tau_{wall}}{\rho}} \quad \#(12)$$

$$\Delta s = \frac{y^+ \mu}{U_{fric} \cdot \rho} \quad \#(13)$$

Here Re is the Reynolds number, ρ is the air density, U_∞ is the freestream velocity, τ_{wall} is the shear stress at the wall, μ is the dynamic viscosity of the fluid, y^+ is a dimensionless parameter that represents the distance from the wall measured in viscous lengths. In this case, ρ was taken as 1.0154 kg/m³ at 4000 ft altitude and dynamic viscosity was taken as $1.846.10^{-5}$ kg/m³. With these parameters, the first layer thickness was calculated as 0.0087 mm. Reynolds number calculated as 28247920.4, so the flow is turbulent. With a simple approach, using the boundary layer thickness equation for turbulent flow on a flat plate, it has been checked whether the inflation layer is sufficient or not.

$$\frac{\delta}{x} = \frac{0.16}{Re_x^{1/7}} \quad \#(14)$$

With this equation, it is understood that the boundary layer thickness should be 11.325 cm. In other words, the inflation layer created is sufficient. After setting these parameters volume mesh is created. Boundary conditions were set for analysis. Solver type was selected and mesh data was exported with a "cas" file to use in Ansys Fluent. For the boundary conditions, the given forward flight conditions of the BeeCopter helicopter were used. The helicopter performs its forward flight at 4000 ft altitude at ISA+20°C degrees. This means a temperature of 300 K and a pressure of 87511 Pa. Density and viscosity values calculated from these data are also given in Table 1. Viscous model and method were determined using these data.

One-equation model Spalart Allmaras, one of the RANS models, was chosen as the viscous model. It is solving directly for a modified turbulent viscosity. It allows the use of coarser meshes. It was designed specifically for aerospace applications involving wall-bounded flows on a fine near-wall mesh. In the literature review, it was seen that it gave sufficient results for helicopter fuselage analysis. The number of iterations was determined as 4200. After this number, residual curves continue in the same trend, drag coefficient remains unchanged.

Table 2: *Solver settings*

Solver Type	Pressure Based
Time	Steady
Viscous Model	Spalart Allmaras
Pressure-Velocity Coupling	SIMPLE
Residual Absolute Criteria	10^{-6}
Number of Iterations	4200

2. Test Case Results

For the convergence of the analysis, the momentum equation and the modified turbulent viscosity equation were determined as the first order upwind. After 300 iterations, these two equations were changed to second-order upwind for the accuracy of the analysis. After the necessary settings are made, the analysis is run. The results obtained are as follows.

The velocity reduction at the rear part was seen from the velocity contours. It was clearly seen that the streamlines cannot follow the path behind the fuselage. The high-pressure area at the tip of the nose and the low-pressure areas at the rear of the helicopter was seen. When looking at the residual curves, it was seen that the error rate in the continuity equation was very large. There may be several reasons why the error is so large. Reasons such as the low quality of the mesh elements to display the flow properties, the intensity of the volume meshes, the compatibility of the meshes with the viscous model, and the compatibility of the viscous model to the problem and boundary conditions affect the accuracy and

convergence of the solution.

Another way to check the accuracy of the analysis is to compare the amount of mass flow at the inlet and outlet and to check that mass conservation is achieved at the inlet and outlet. Conservation of mass was achieved in this analysis. Drag coefficient and drag force values obtained from the analysis were not taken into account since they had a very high error rate. For a more accurate interpretation, reanalysis should be run with a more appropriate mesh application and a well-configured setup.

A. Base Geometry Analysis

1. Meshing

For the base geometry analysis, a much denser mesh model was applied compared to the test case. Analyzes were run with several different fine mesh applications with a different number of elements. Since the difference was seen between the results, the elements were minimized until the results did not change. Since the main body and tail junction region have a blunt structure in the base geometry, it was difficult to apply the inflation layer in this section. Since this region is a region where flow separations will occur and should be examined well, it was preferred to apply the elements densely here. However, as the dimensions of the elements decreased, the inflation layer became more difficult to apply and the quality of the elements decreased. The optimum mesh obtained, as a result, the view of this region is given in Figure 7.
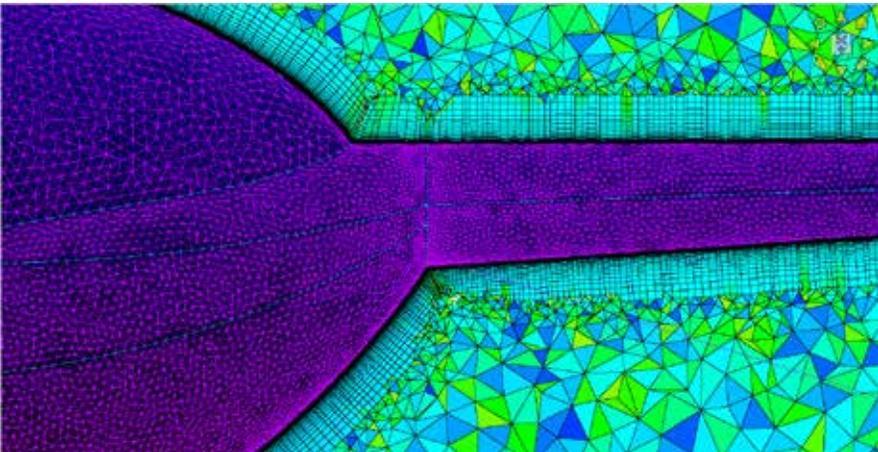
Figure 7 Close look at the inflation layer

In total, the total number of cells is 6,279,262 and the points are 1,884,154. Max Aspect ratio value 16, max equiangle skewness value 0.88, and volume ratio value 13 were applied. These max values are not very

sufficient. But, for the reasons mentioned earlier, the application was able to be done in this way. The important thing here is at how many points these low-quality elements are present. Looking at the average values, it can be said that the quality values are very good. The average skewness equiangle value is 0.30, the aspect ratio value is 1.05 and the volume ratio is 1.52. Since Spalart Allmaras is a sensitive model to the mesh density near the boundary layer, a source was applied around the fuselage. The element size here is set to 4 times the element height in the last inflation layer. The view of the elements here is given in Figure 8.
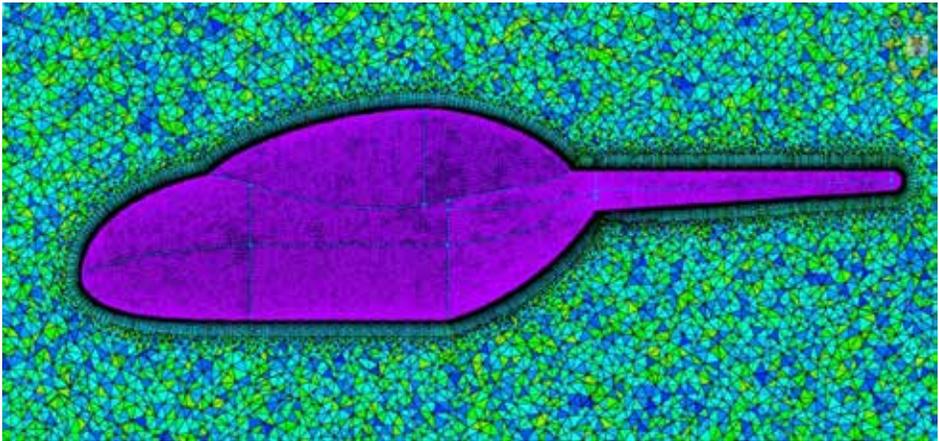
Figure 8 The view of small elements near the fuselage

2. Results

As a result of this analysis, which converged at the end of 4200 iterations and the error rate decreased from 10^0 to 10^{-4}, the drag force was found to be 312.94 N and the drag coefficient was 0.0644. Figure 9 shows the pressure coefficient distribution in the upper and lower halves for the helicopter's mid-section. From here, the points on the body where the pressure increases and decreases can be seen.
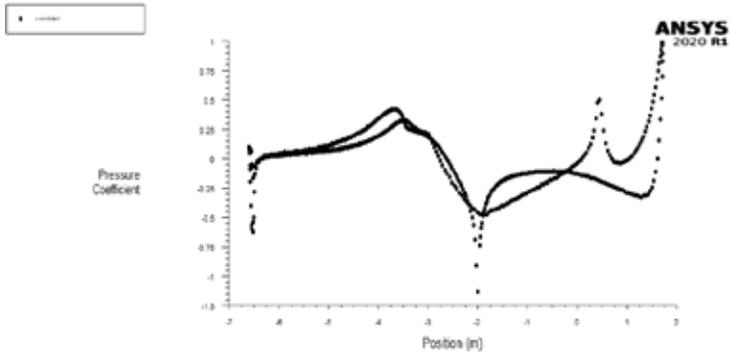
Figure 9 Pressure coefficient distribution over midsection
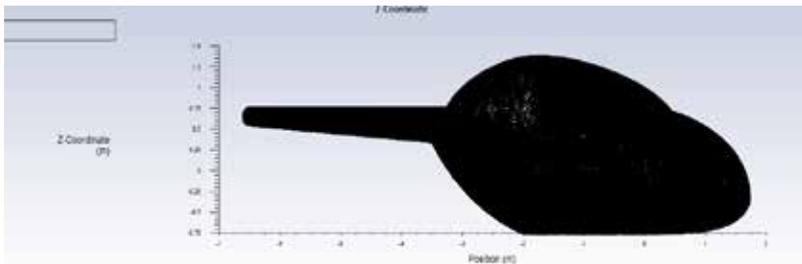
Figure 10 Coordinates on the helicopter

Figure 11 shows the streamlines over the fuselage. As can be seen, streamlines cannot follow the path behind the fuselage. The flow also separated behind the engine cowling, creating a vortex that rotates around the tail with the flow from the rear fuselage. Viewing this distorted flow behind the fuselage has shown that correcting this area is the right way to go.
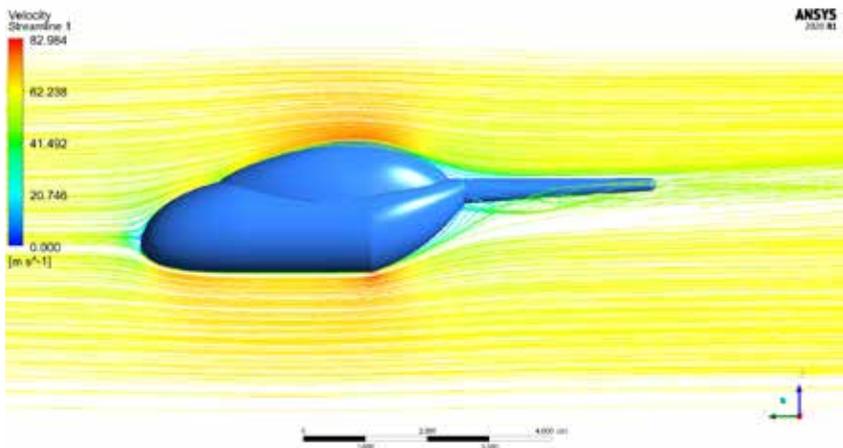
Figure 11 Streamlines over Base geometry
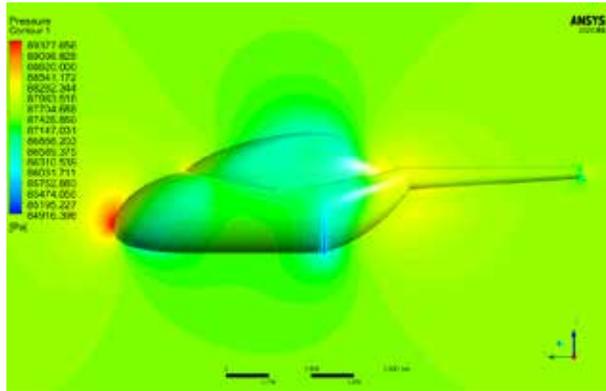
Figure 12 Pressure distribution over Base geometry
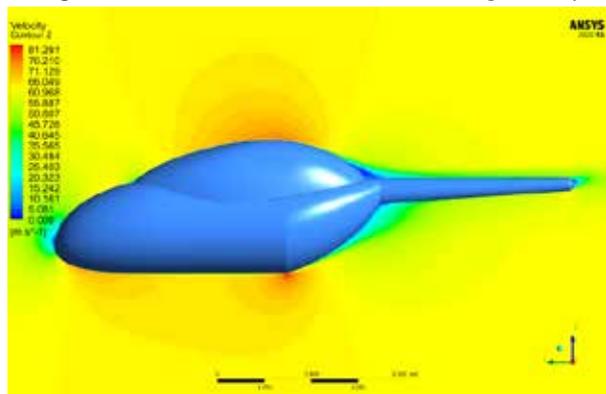
Figure 13 Velocity distribution over Base geometry

The pressure and velocity contours for the base geometry are given in Fig.12 and Fig.13, respectively. It can be seen in Figure 12 where the pressure rises in the nose where the air is forced to stop. Sudden pressure drop is also seen in the part where the main fuselage narrows towards the tail. At the nose tip, behind the engine cowling, at the rear of the fuselage and at the tail end, the low-speed zones are easily seen in Fig.13.
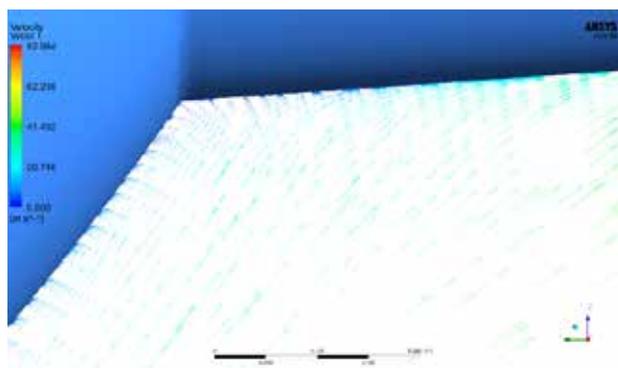
Figure 14 Velocity vectors on the aft fuselage
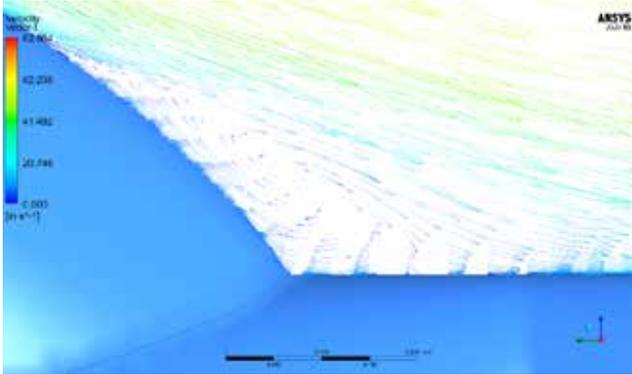
Figure 15 Velocity vectors behind the engine cowling

The vortices behind the rear fuselage and engine cowling were visualized with the help of velocity vectors. Here, paying attention to the direction of the arrows, it can be observed that the flow goes in different directions in these regions. Additionally, it can be seen that the flow coming from under the body is forced to stop here by accumulating in the lower part of the tail.

3. Comparison with literature

In Fig.16, a curve is fitted to the data obtained from the wind tunnel tests of several helicopters and airplanes. Beecopter's fineness ratio is 5.47. The drag coefficient based on the frontal area

$$C_{D_f}$$

corresponding to this value is approximately $= 0.05$ from Fig.16. The equivalent flat plate area is found as 0.1151 from Eqn. (6). Drag force from this value was found as 227 N, by using Eqn. (8).
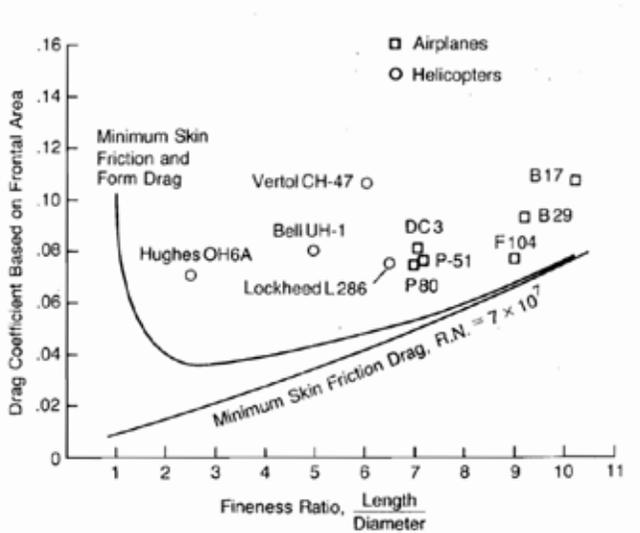
FIGURE 4.17 Fuselage Drag at Zero Lift

Figure 16 Historical trend of fuselage drag coefficient based on the frontal area, Prouty (1995)

As mentioned in Section 5.2, the drag coefficient value of 0.06 is very close to the value of 0.05 taken from the historical trend. The drag force value, which was found as 312.94, is close to the value of 227 N calculated from historical data. In fact, the computation from historical data is only for helping start the computations from the right point during the initial design phase. According to the aerodynamic shape of the fuselage, drag force and coefficient can vary substantially. Therefore, these are approximate values and only give a clue about the accuracy of the method.

B. Obtaining Variants

The original geometry was modified based on studies in the literature to achieve a reduction in drag force. First, a curvature was given to the junction of the main body-tail cone in Variant 2. For each subsequent variant, a certain rate of growth was achieved based on the AA section. It can be seen that the upsweep angle is reduced when a line is drawn between the start and end points of the curve. With these changes, it is aimed to reduce the drag force by preventing flow separations in this region. In Fig. 17, all variants are shown together. The area of each variant in the AA section is increased equally. The names of the variants are written on the figure.
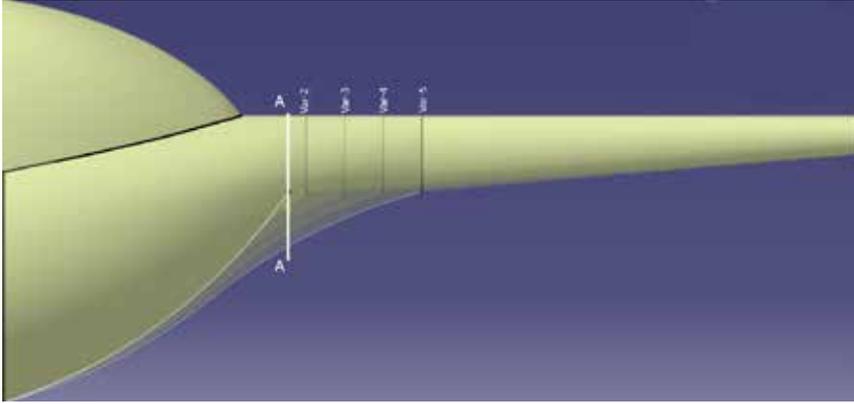
Figure 17 Modifications on the slope of the rear part

Another work was to change the height of the tail boom to prevent flow separations at the rear part with the same hypothesis. Forcing streamlines to follow a long and curved path in this region was causing flow separation. Therefore, reducing this distance can enable the flow to follow the path. Modifications made on Variant-5. The generated variants are shown in Fig.18. Each modification was made by sliding the tail boom 15 cm down the AA section in Fig.17. From left to right, variants are named as Var-5, LT-1, and LT-2, respectively. The height of the tail boom of each new variant is 15 cm less than the previous one.

Figure 18 Modifications on tail boom height

After obtaining geometries, each geometry has meshed one by one. Elements of similar sizes and types were used. The volume mesh and inflation layer are applied similarly for each geometry. Thus, it was aimed to prevent the differences in the analysis results caused by the mesh.

III. Results and Conclusion

After all, analyzes are completed, the drag coefficient and drag force obtained from each are shown in Table 3. For the first modification group, while the drag coefficient was expected to decrease as the transition of the rear part was smoothed, an increase up to Var-3 was observed. "-" sign represents the increase in the

drag coefficient. As the extension increased after var-3, C_D started to decrease. With Var-5, a 3.17% gain in drag coefficient was achieved compared to the initial geometry. The table also shows the decrease in drag coefficient between two consecutive geometries. For Var-4 and Var-5, the modifications caused equal gains from previous geometries.

Table 3 *Results for first modification group*

	Base	Var-2	Var-3	Var-4	Var-5
C_D	0.0645	0.0658	0.0657	0.0639	0.0621
Drag (N)	312.94	319.60	318.98	310.27	301.31
% Reduction		-2.128	-1.929	0.854	3.717
% Reduction compared to previous		-2.13	0.20	2.73	2.89

When the velocity vectors and velocity contours for Var-2 and Var-3 were examined, it was seen that the vortices behind the fuselage could not be prevented. When looking at the streamlines, a large amount of separation and turbulence is still observed around the tail in these geometries. There is no gain from this way, and the surface area is increased additively. The growth of the air-friction surface is a factor that increases drag. Therefore, in these variants, there was no factor that would provide drag reduction, but there are drag-increasing factors. Thus, these modifications did not achieve the goal. For Var-4, a decrease in drag force and the coefficient is observed when compared with the base geometry. For Var-5, this decrease is greater. When the analysis results were examined, it was seen that the modifications in these geometries reduced the separations and vortices experienced at the rear of the fuselage. Thus, the intended gain was achieved, and it was seen that the modifications were successful.

Table 4 *Results for second modification group*

	Var-5	LT-1	LT-2
C_D		0.0621	0.0558	0.0549
Drag (N)	301.31	270.87	266.32
% Reduction		10.103	11.614
% Reduction compared to previous		10.10	1.68
% Total Reduction	3.717	13.445	14.900

In the second modification group, the results obtained by reducing the height of the tail boom are listed in Table 4. A substantial gain in

drag was observed in the LT-1 variant. The gain experienced in the LT-2 variant continues. But its gain is lower than the previous geometry. The reduction of drag coefficient with comparing the Var-5 is 11.614% for LT-2 configuration. If the result is compared to Base, this rate will be 14.9%. When looking at the analysis results for these variants, it is seen that the separations in the rear part are almost completely prevented. In addition, lowering the tail boom height has also affected the geometry behind the engine cowling, softening the sharp shape here. Therefore, the motion of the flow here has also changed. This modification not only prevented the vortices behind the engine cowling but also reduced the secondary vortices caused by the interaction of this disturbed flow with the flow behind the rear fuselage. As a result of all these effects, drag has decreased much more than expected.
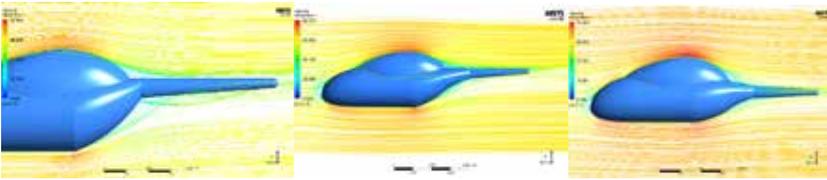
Figure 19 Comparison of streamlines between Base, Var-5 and LT-2 geometries
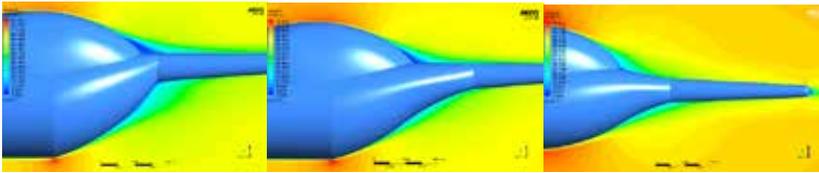
Figure 20 Comparison of velocity contours between Base, Var-5 and LT-2 geometries

As a result, a total reduction in the drag coefficient of 3.7% was achieved by lowering the upsweep angle alone, and an overall reduction in drag coefficient of 11.6% was achieved by reducing the tail boom height in addition to this modification. The predicted results of the research in the literature have been confirmed by performing similar procedures and applying similar solution methods.

As a conclusion, an aerodynamically efficient fuselage was designed for this study. For this, BeeCopter Team's helicopter's fuselage was used and modified. It was decided to modify the rear part of this fuselage and the slope of the junction between the main fuselage and tail boom. It is expected to decrease in upsweep angle will prevent the flow separations at this part. Also, it is decided to change the height of the tail boom. It has

been learned from the literature that, the improvements to these areas will significantly reduce the fuselage drag. Modifications, meshing and CFD analyses were made on CATIA, Pointwise and Ansys Fluent, respectively. It was decided to create a system for modifications, that is making the changes at predetermined intervals. In this way, it will be possible to understand how the analysis result will change when a small change is made. The flight condition for the design is the forward flight, so general helicopter forward flight information is given. The drag forces acting on a helicopter and the power needed to overcome them are explained. Also, it is explained the effect of the fuselage on parasitic power.

For this purpose, a test analysis was carried out. This analysis is to experience the use of programs, learn the connections between them, and examine how to get results from an approximate case. After this analysis, the problems experienced were solved and appropriate modelling was made for base geometry. Base geometry represents the original geometry. In the first step, base geometry has meshed. The elements here were much smaller than in the test case. The analysis was run several times until the appropriate mesh size was found. By making the necessary adjustments, the mesh has been improved and made ready for analysis. At this stage, important parameters for meshing and CFD analysis were explained and decided. Analysis conditions were determined and the mesh was ready to be transferred to Ansys Fluent. Pressure Based model was used because the flow Mach number is low. Based on the information obtained from the literature, Spalart Allmaras was chosen as the viscous model. The number of iterations was determined as 4200, after this number it was observed that the residual curves remained in a certain trend. After completed works, CFD analysis was run and the results were interpreted. The low-speed zone behind the fuselage was visualized and explained. Additionally, streamlines on the mid-section are shown. It was seen that the flow could not follow the fuselage here. In addition, the vortices behind the engine cowling and their interaction with the flow leaving the rear fuselage were explained. Velocity vectors, velocity and pressure contours were visualized. The amount of decrease in error order has been explained. From the results obtained, the C_d value was calculated as 0.0644 and the drag force was calculated as 312.94.

Afterwards, modifications will be started on the main geometry. The meshing process is applied to the obtained geometries in the same way. Analyzes were carried out and the results obtained were listed. Lowering the upsweep angle by a small amount did not cause a drag decrease while lowering it further decreased the drag. The reason is the formation of vortices is not prevented, and the surface area increases at the same time. Afterwards, a total drag decrease was observed by preventing vortices and

separations. Lowering the tail boom height has greatly reduced drag. This is caused by the prevention of both the flow separations in the rear region and the separations behind the engine cowling and their interaction with each other.

At this stage of the study, the main rotor, which has a large share of helicopter fuselage drag, is not taken into account. The main rotor will greatly change the direction, type and character of the flow. It would be a good work to consider the main rotor effects and main rotor-fuselage interaction as a future study.

REFERENCES

Batrakov, A. S., Kusyumov, A. N., Mikhailov, S. A., & Barakos, G. N. (2018). Aerodynamic optimization of helicopter rear fuselage. *Aerospace Science and Technology*. 77(6), 704-712.

Keys, C. N. &Wiesner, R. (1975). Guidelines for reducing helicopter parasite drag. *Journal of the American Helicopter Society*. 20(1), 31–40.

Leishman, G. J. (2006). *Principles of Helicopter Aerodynamics*, 2nd ed., Cambridge University Press.

Prouty, R. W. (1995). *Helicopter performance, stability, and control*.

Renaud, T., O'Brien, D., Smith, M., & Potsdam, M. (2004). Evaluation of isolated fuselage and rotor-fuselage interaction using CFD. Office National D'etudes Et De Recherches Aerospatiales Chatillon (France).

Rotaru, C., & Todorov, M. (2017, December 20). Helicopter flight physics. IntechOpen. Retrieved November 28, 2021, from https://www.intechopen.com/chapters/57483.

Seddon, J. (1982). Aerodynamics of the helicopter rear fuselage upsweep. *Proceedings of the 8th European Rotorcraft Forum (ERF)*.

Shi, W., Li, J., Gao, H., Zhang, H., Yang, Z., & Jiang, Y. (2020). "Numerical investigations on drag reduction of a civil light helicopter fuselage". *Aerospace Science and Technology*. 106.

Stepanov, R., Zherekhov, V., Pakhov, V., Mikhailov, S., Garipov, A., Yakubov, W. & Barakos, G. N. (2016). Experimental study of helicopter fuselage drag. *Journal of Aircraft*, 53(5). pp.1343-1360.

Zhang, Q., Garavello, A., D'Alascio, A. & Schimke, D. (2011). Advanced CFD-based optimization methods applied to the industrial design process of airframe components at airbus helicopters, *37th EuropeanRotorcraft Forum*, Agustawestland, Cascina Costa di Samarte, Italy.
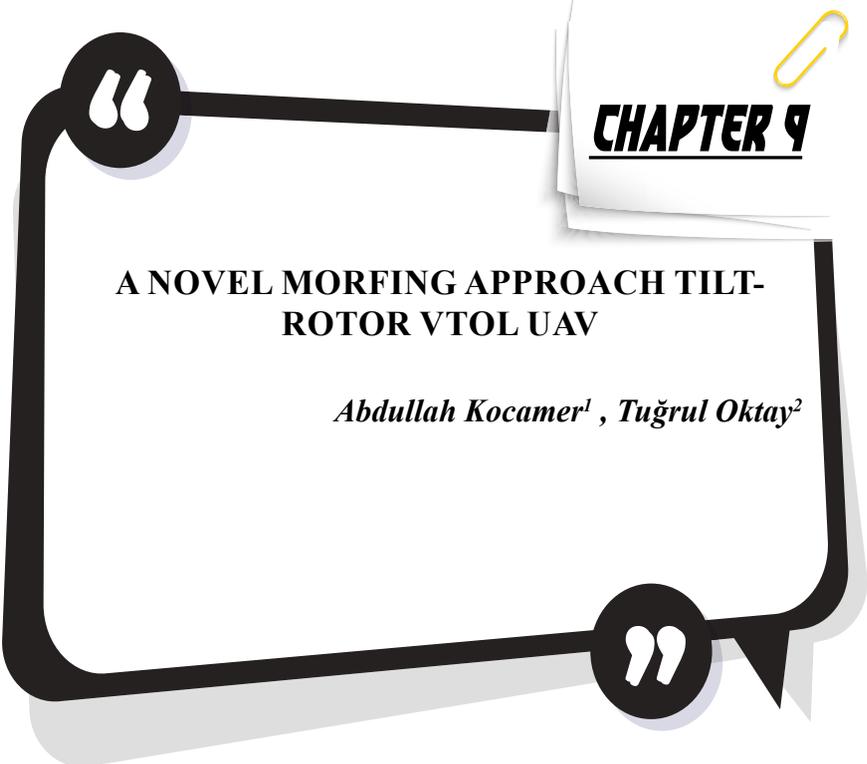
A NOVEL MORFING APPROACH TILT-ROTOR VTOL UAV

Abdullah Kocamer[1] , Tuğrul Oktay[2]

1 Res. Asst., İskenderun Technical University, Department of Airframe and Powerplant Maintenance, Hatay, Turkey, (ORCID: 0000-0001-8948-6390), abdullahkocamer@gmail.com
2 Prof. Dr., Erciyes University, Departmant of Aeronautical Engineering, Kayseri, Turkey, (ORCID: 0000-0003-4860-2230), tugruloktay52@gmail.com

1. INTRODUCTION

Popularity of Vertical landing and take-off aircraft (VTOL), which has an important place among aircraft, is gradually increasing day by day thanks to the advantages they have. The biggest advantage of these VTOL aircraft, which is also produced in unmanned models, is undoubtedly that they do not need a runway for landing and take-off.

VTOL aircraft are produced in many different configurations (Bacchini & Cestino, 2019; Finger et al., 2017). The main ones are tilt-rotor, tilt-wing and fixed-wing aircraft. The tilt-rotor model, which is also the subject of this study, is the model in which only the rotors on the wing tips are rotated, as the name suggests. Tilt-wing is used to describe models in which the rotors are rotated along with all the blades. Fixed wing airborne VTOL aircraft, on the other hand, do not have a rotary system, but the vertical and horizontal flight phases are carried out by activating different engines.

One of the disadvantages of tilt-wing aircraft among these models is the sudden loss of lift during a certain angle while the wing is rotated and the possible sudden loss of altitude due to this. In addition, the necessity of turning the wing completely and having a shaft that must extend along the wing increases the weight of the aircraft. Although the tilt-rotor does not have such a disadvantage, some of the air flow created by the propellers at the wing tips collides with the wing surface after the rotor transitions from the horizontal flight phase to the vertical flight phase in these aircraft (Finger et al., 2017). This situation constitutes the biggest disadvantage of tilt-rotor aircraft.

In order to improve this aerodynamically inefficient situation, there are studies such as tilting curve design (Huang et al., 2020), angle of attack estimation and for the most appropriate problems during landing and take-off in tilt-wing aircraft (Yokota et al., 2021). Again in the literature, there are studies on the improvement of roll, pitch and yaw movements of tilt-wing aircraft (Lindqvist et al., 2015) and a tilt-wing design and characterization study with four engine (Cetinsoy et al., 2012).

In this study, a tilt-rotor unmanned aerial vehicle design, which is a first in the literature, is carried out in which the rotor is rotated together with a part of the wing and the efficiency of the propeller is increased. The part of the wing in contact with the propeller disc area is rotated together with the rotor, preventing some of the air thrown back from hitting the wing surface. Thus, an aircraft design combining the advantages of tilt-rotor and tilt-wing aircraft has been tried to be achieved. The aerodynamic efficiency of the designed aircraft was obtained by numerical analysis.

2. TILT-ROTOR MODELLING

Before designing an aircraft, there are some criteria that must be determined according to the requirements. The first of these is the maximum take-off weight of the aircraft. Then, parameters such as range, flight time or altitude are other data that should be available before design. All these data are obtained based on the mission of the aircraft. Some of the required data of the tilt-rotor unmanned aerial vehicle to be designed in this section are given in the table 2.1.

Table 1: Design Requirements for Tilt-Rotor VTOL Aircraft

Maximum Take-off Weight	10 kg
Payload Capacity	2 kg
Empty Weight (Battery Included)	8 kg
Flight Distance	20 km
Flight Time	2 hrs.
Cruise Speed (Max)	25 m/s

These parameters, which constitute the design criteria, have been determined according to the payload capacity required for the aircraft to perform tasks such as reconnaissance and surveillance.

2.1. DESIGN FOR HOVER

Tilt-rotor aircraft design criteria for vertical flight, namely hover mode, are similar to quadcopters on a large scale. The only design in between is that the aircraft to be realized will perform the flight operation with two engines. Although there are differences in terms of control, this difference is not included in this study.

The lift required to perform the vertical take-off and landing operation must be at least twice the aircraft weight (Hadi et al., 2015). For this reason, the vertical thrust force we need in the aircraft must be 20 kg or more. This thrust will be provided by two engines and two propellers connected to the engines.

2.2. DESIGN FOR CRUISE FLIGHT

In this flight mode, the aircraft will have a profile similar to that of a fixed-wing aircraft. For the thrust value that a fixed-wing aircraft should have, it is assumed that the opposing forces on the aircraft are equal to each other. According to this method, the lift and weight force and drag and thrust force on the aircraft will be considered as equal (Gundlach, 2012; Raymer, 2012) .

The thrust required for a tilt-rotor aircraft to perform vertical flight is greater than that required for cruise. The reason for this is that in the vertical flight phase, the aircraft only performs its flight with the thrust produced by the propellers. However, in the cruise phase, the aircraft's flight depends not only on the thrust created by the indirect propellers, but also on the airflow rate and airfoil of the air passing over the wing, where the lift force is obtained. Since the main purpose of this study is to change the thrust force when the wing is rotated from two different locations, a separate calculation will not be made in this section.

In this aircraft to be designed, the MH 120, which is also used in many tilt-rotor and tilt-wing aircraft, will be used as the wing profile. This airfoil reaches the highest lift coefficient it can have at an angle of 14 degrees, which is predicted to be sufficient for the aircraft whose vertical flight will be achieved by rotating the rotors and wings.

After determining all the necessary parameters for the vertical and horizontal flight phases, a 3D model of the aircraft was created by the computer which has dimensions shown in Figure 1. In this aircraft, which is designed differently from the known tilt-rotors, the rotors rotate not only with the hub part, but also with a part of the wing. The wing and engine position where the aircraft will perform landing and take-off operations are shown in Figure 2. In this position, it is aimed to prevent the contact of the air with the wing by turning the part of the wing as much as the propeller radius. Figure 3 shows the state of the aircraft in the horizontal flight phase, that is, in the fixed-wing flight model. Here, after take-off or before landing, the rotors of the aircraft rotate with the wing at an angle of 90 degrees and change phase.
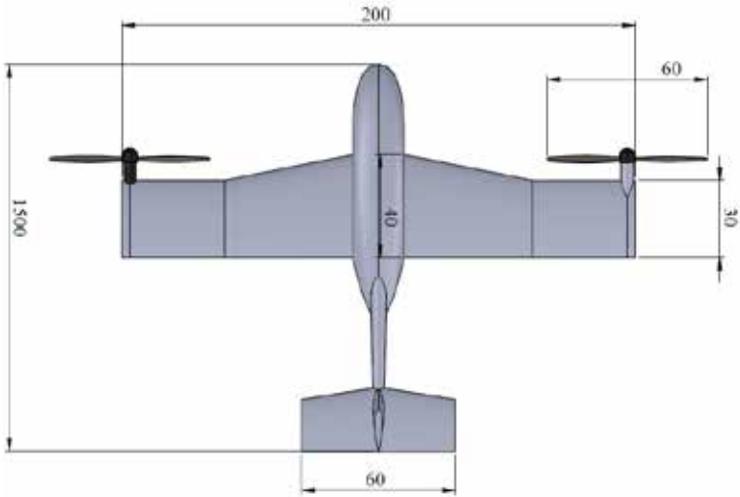
Figure 1: Dimensions of the designed aircraft
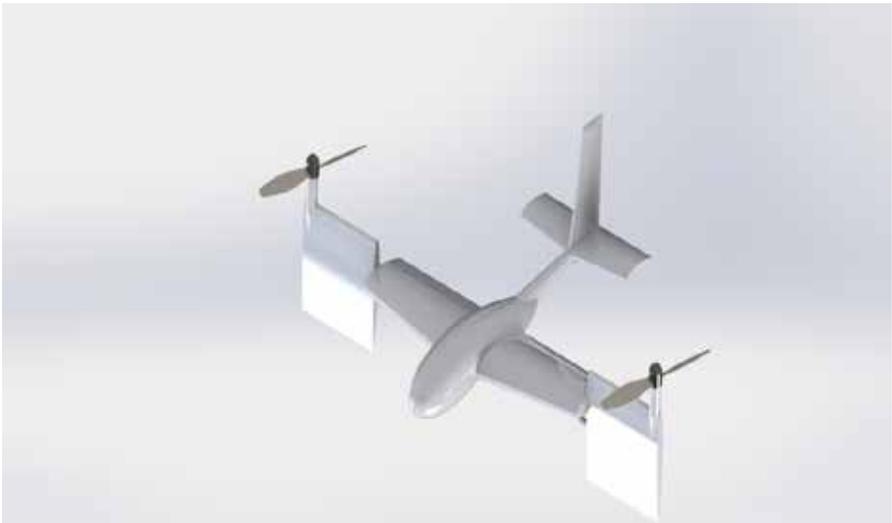
Figure 2: Rotor and wing positions of designed aircraft at hover or vertical flight

Figure 3: Rotor and wing positions of designed aircraft at cruise flight

In order to examine the effect of the air accelerated by the propellers on the wing, a classical tilt-rotor model of the same aircraft with exactly the same dimensions is created and shown in figure 4. While modeling this aircraft shown in Figure 4, care was taken to ensure that the design had a classical tilt-rotor configuration and was especially the same dimensions as the previous model. Thus, it is aimed to obtain more comparable and realistic results in the analyzes to be carried out in the next section.
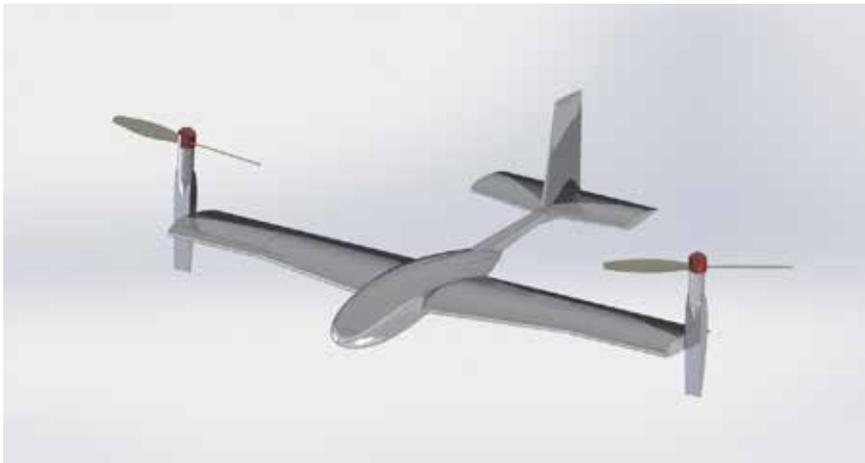
Figure 4: Tilt-rotor model designed in the same dimensions as the intended aircraft

3. PERFORMANCE ANALYSIS

In this section, the flight performance of the aircraft will be tested after the final design, taking into account the design requirements. In this numerical analysis, the ANSYS Fluent module will be used. Since the performance comparison will only depend on the position of the blade, only the rotating part of the blade and the propeller will be analyzed as geometry and the effect of the propeller on the blade will be examined.

In numerical analysis, the appropriateness of the analysis method and environment variable parameters as inputs is very important for the results to be close to reality. The maximum speed of the aircraft to be designed has allowed us to perform pressure-based analysis. By using the Patch-Independent method mesh, very small-scale points that will not affect the result data will be ignored and faster and cleaner results will be obtained. The mesh number of cells was started as 1000000 and increased up to 3000000 controlled meshes. Since no difference was observed in the tests performed after this value, it was considered appropriate as the mesh number and is shown in the figure below.
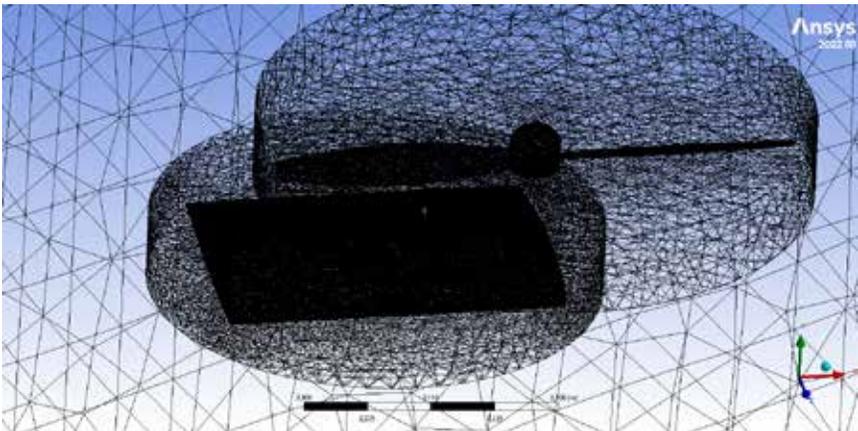
Figure 5: Mesh image of Case 1
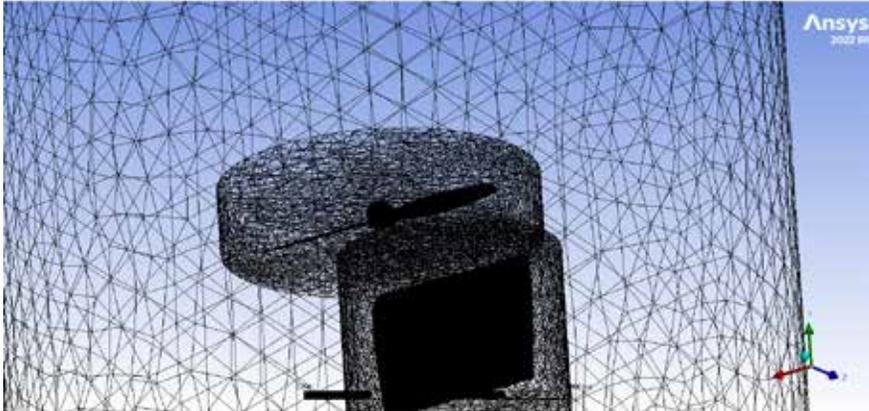
Figure 6: Mesh image of Case 2

4. RESULTS AND DISCUSSION

Case 1 represents the case where the wing surface is perpendicular to the propeller thrust axis, and case 2 represents the case where it is parallel.
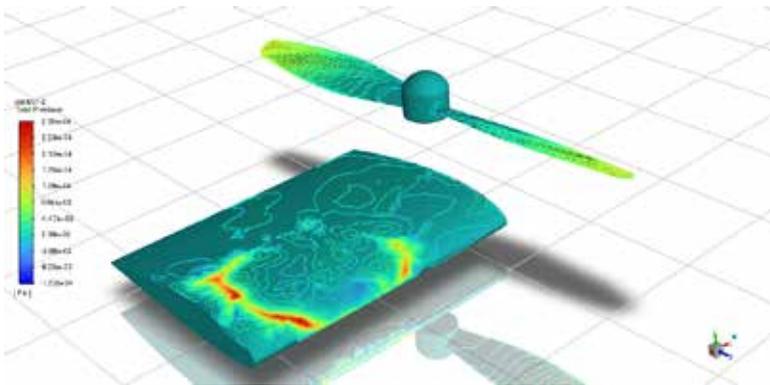
Figure 7: Total pressure in Case 1
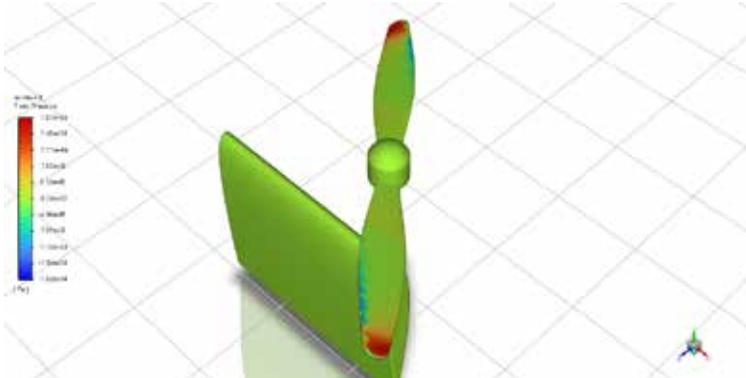
Figure 8: Total pressure in Case 2

As seen in Figures 7 and 8, the total pressure graphs expressing the sum of the static, dynamic and relative pressures created by the thrust created by the propeller on the wing surface are completely different from each other. The main reason for this is that the wing acts as an obstacle when the surface area is perpendicular to the thrust axis and the velocity decreases at this point. The following figures of the flow lines of the air selected as the fluid at the beginning of the analysis will make this situation more understandable.
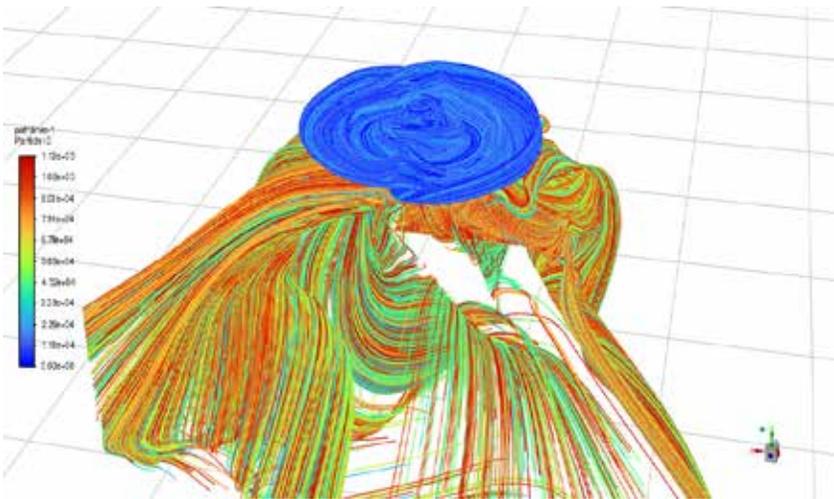
Figure 9: Air path lines over wing surface in Case 1
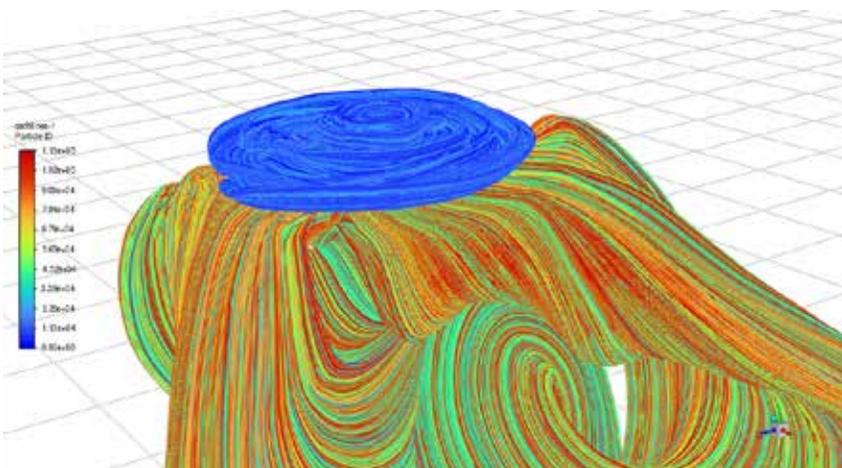
Figure 10: Air path lines over wing surface in Case 1
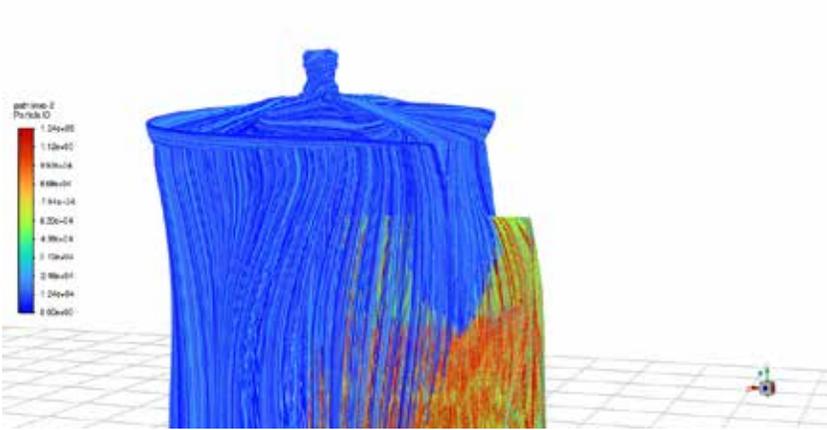
Figure 11: Air path lines over wing surface in Case 2
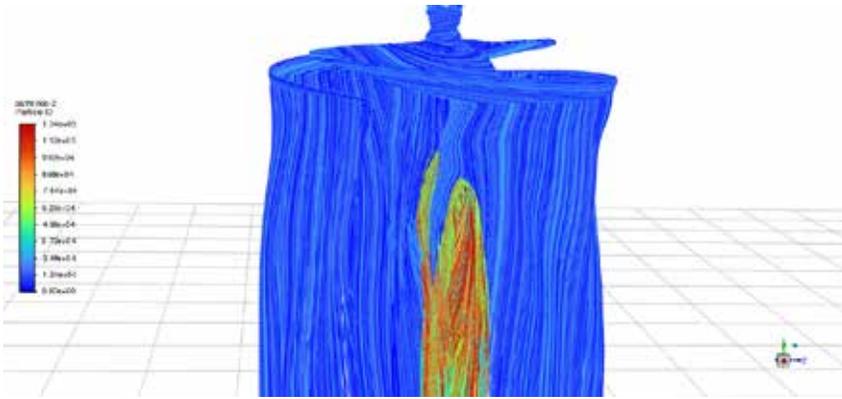
Figure 12: Air path lines over wing surface in Case 2

In figures 9 and 10, the contact of air particles with the wing surface is clearly seen. The air in contact with the wing surface goes down the surface edges, causing local turbulence in the flow. In Figures 11 and 12, the air follows a more linear path after contact with the wing surface, and because the flow contacting cross-sectional area is low, a lower total pressure occurs. The effect of this situation on thrust force was obtained in the force graph of the analysis and shown in figure 13. As a result of the numerical analysis in which the distance between the propeller and the blade is 15 cm and the rotation speed of the propeller is assigned to 5000 rpm, 90 N thrust force was obtained for Case 1, while 112 Newton power was obtained for Case 2. These values were obtained by keeping all environment variables equal in both cases.

4. CONCLUSION

In this study, an aircraft design that combines the advantages of tilt-rotor and tilt-wing VTOL aircraft has been performed. The criteria to be determined before the design were taken as basis and 3D modeling of the design was carried out accordingly. In addition to the innovatively designed aircraft, a normal tilt-rotor aircraft was also modeled, and the interaction region of the blade and propeller of both models was subjected to numerical analysis. As a result of the analysis, it was seen that the rotation of the rotor with a part of the wing during the phase change of the aircraft would be significantly advantageous, such as the 25% thrust gain, and the study was terminated.

REFERENCES

Bacchini, A., & Cestino, E. (2019). Electric VTOL configurations comparison. *Aerospace*, *6(3)*, 26.

Cetinsoy, E., Hancer, C., Oner, K. T., Sirimoglu, E., & Unel, M. (2012). Aerodynamic design and characterization of a quad tilt-wing UAV via wind tunnel tests. *Journal of Aerospace Engineering*, *25(4)*, 574-587.

Finger, D. F., Braun, C., & Bil, C. (2017). A review of configuration design for distributed propulsion transitioning VTOL aircraft. Asia-Pacific International Symposium on Aerospace Technology-APISAT,

Gundlach, J. (2012). *Designing unmanned aircraft systems: a comprehensive approach*. American Institute of Aeronautics and Astronautics.

Hadi, G. S., Kusnaedi, M. R., Dewi, P., Budiyarto, A., & Budiyono, A. (2015). Design of avionics system and control scenario of small hybrid vertical take-off and landing (VTOL) UAV. *Journal of Instrumentation, Automation and Systems*, *2(2)*, 67-71.

Huang, H., Yu, L., He, G., & Wang, X. (2020). Tilting Curve Design of a Novel Tilt-rotor UAV Based on Rotor/Wing Interference Model. 2020 Chinese Automation Congress (CAC),

Lindqvist, A., Fresk, E., & Nikolakopoulos, G. (2015). Optimal design and modeling of a tilt wing aircraft. 2015 23rd Mediterranean Conference on Control and Automation (MED),

Raymer, D. (2012). *Aircraft design: a conceptual approach*. American Institute of Aeronautics and Astronautics, Inc.

Yokota, K., Fujimoto, H., & Kobayashi, H. (2021). Observer-based Angle of Attack Estimation for Tilt-Wing eVTOL Aircraft. 2021 IEEE International Conference on Mechatronics (ICM),
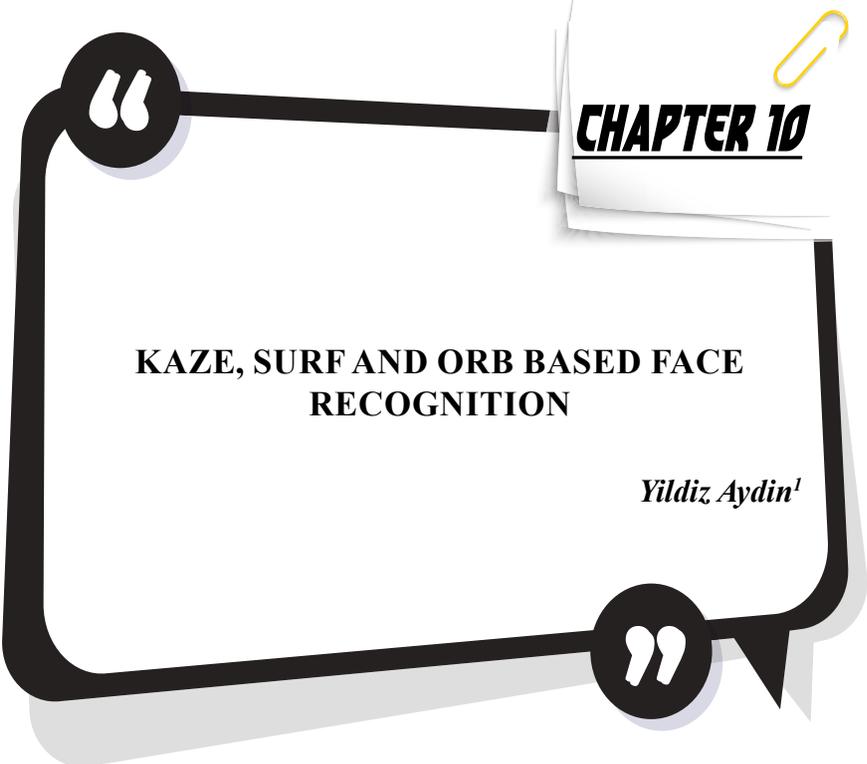
KAZE, SURF AND ORB BASED FACE RECOGNITION

Yildiz Aydin[1]

1 Department of Computer Engineering, Erzincan Binali Yildirim University, Erzincan 24000, Turkey., yciltas@erzincan.edu.tr

1 Introduction

The 2D-Face Recognition System is developing popularity in the area of machine visual. It is often used in real situations for use in areas such as security and surveillance. A procedure that helps identify a face in an image and associates the tagging with the face. A person can easily identify a face element in the real world, despite understanding many of its features. Despite various points of view and differences, he can quickly recognize a person. But a computer must do this by collecting lots of images and tagging them. In this case, he learns using knowledge.

The machine is trained by collecting and preserving numerous properties of the images in memories. This type of properties extracted determines the complete effectiveness of the entity identification system. To create an effective face recognition software, the researchers tested numerous harvesting of features and classification methods. A face recognizing system operates in several stages. First, an instructional series is generated by information extraction from an input image using numerous harvesting of attributes and reducing methodologies. Then the learning set of data is instead categorized in to the different classifications employing image classification methods. A regulated or unattended acquiring knowledge methodology can be used for categorization. In the final process, the information first from information images is compared to the instructional figure's saved data source, and the appropriate label is designated to the item acknowledged. The accuracy of numerous features retrieved from the image collection completely determines the results of this identification system.

As a result, the characteristic extracting approach is particularly important since it enhances the entire effectiveness of a face identification system. Face identification is a difficult task for a computer to perform because it demands more computing work to distinguish the face from the incoming images.

Throughout the comparison analysis, various image description methods are regarded: KAZE, SURF, and ORB. Utilizing those three approaches, an extracted features was created that requires a lot of storage to store. In addition, since the number of features obtained from each image is different and the feature vector given to the classifiers must be of equal size, the bag of words method is used. The collected information vectors is then classified using Support Vector Machines (SVM) and K-Nearest Neighbor (K-NN) classification methods. The researchers ran conducted studies using a publicly available collection, the Face 94 image collection. The collection contains over 3060 images that have been classified into 153 subcategories. Fourth chapter of this paper discusses the actual outcomes.

There are four components to this study. Section 1 provides a brief overview of the situation and the suggested solution. Section 2 contains a review of the research. Section 3 presents the specifics of the suggested systems for face identification as well as the numerous strategies employed in this study. Section 4 examines the actual outcomes in relation to the suggested system. Eventually, section 5 summarizes the suggested work's findings as well as pertinent potential possibilities.

2 Related work

In [1], 5 different datasets, AR, AT&T, LFW, CIE, and Face94, were used. The data sets used were mixed in gray-scale and RGB format. Classification was made by performing a face recognition process with the data. A method is proposed using the graph-based quintet-triple approach. SVM and K-NN were used as machine learning. For AT&T dataset, 100% success was found with SVM method, 97.3% with K-NN, 100% success with Face94 dataset with both methods, 100% success with CIE dataset with both methods, 99.4% with AR SVM, 93.5% with K-NN.

AR and Face94 datasets were used in the study [2]. An attempt was made to classify with a representation-based approach. It is a classification study using various combinations of SRC, LBP+NS, SRC+LBP, TL-SRC+LBP approaches. It has been tried in different ways such as 4:10, 7:7, 10:4 in the process of splitting train and test. The highest results are around 98%.

Barnouti [3] used Principal Component Analysis (PCA) and Back Propagation Neural Network (BPNN) for face recognition. Grimace and Face94 were used as data sets. A total success rate of 100% was found in both data sets.

In this study [4], the Face94 dataset was used and various studies and comparisons were made for a real-time method. A method developed for both recognition and tracking has been demonstrated. A result was obtained with 100% success for face recognition and 93.33% success in real-time work.

Face94 and ORL dataset were used in [5]. The focus is on obtaining a result by performing feature extraction. It was developed with a hybrid method. A success rate of 92% was found in the Face94 dataset with FFNN, and the highest success rate of 94 with SOM.

In this study [6], supervised learning was conducted using the Face94 and FERET datasets. An advanced classification process has been applied to the approaches made. First of all, image files were taken, then pre-processing processes were applied. Then, a feature extraction was done on the images using PCA. Dimension reduction was made and a finalization was made to detect faces.

3   Methodology and experimental design of the proposed system

The research is performed on a Face 94 database using several extraction of features, pattern recognition, and image categorization techniques. Each image is around 180x200 pixels in dimension in Face 94 database. A comparison of these methods is offered based on identification accuracy. Additionally, a 5-fold cross-validation database segmentation is used to increase accurate outcomes depending on several performing assessment metrics. With the use of KAZE and SURF features, very successful results were obtained on the Face 94 dataset. The suggested technology is developed in the steps listed below (see Fig. 1).

- Compiling the image database

- Creating features matrices utilizing the three pattern descriptors KAZE, SURF, and ORB alone and KAZE+SURF.

- Bag of Words

- Using SVM and k-NN for classification.

3.1 Feature extraction techniques

A face identification system's effectiveness is mostly determined by the relevant characteristics derived from the image dataset. The study took into account three feature extracting methodologies: KAZE, SURF, and ORB.
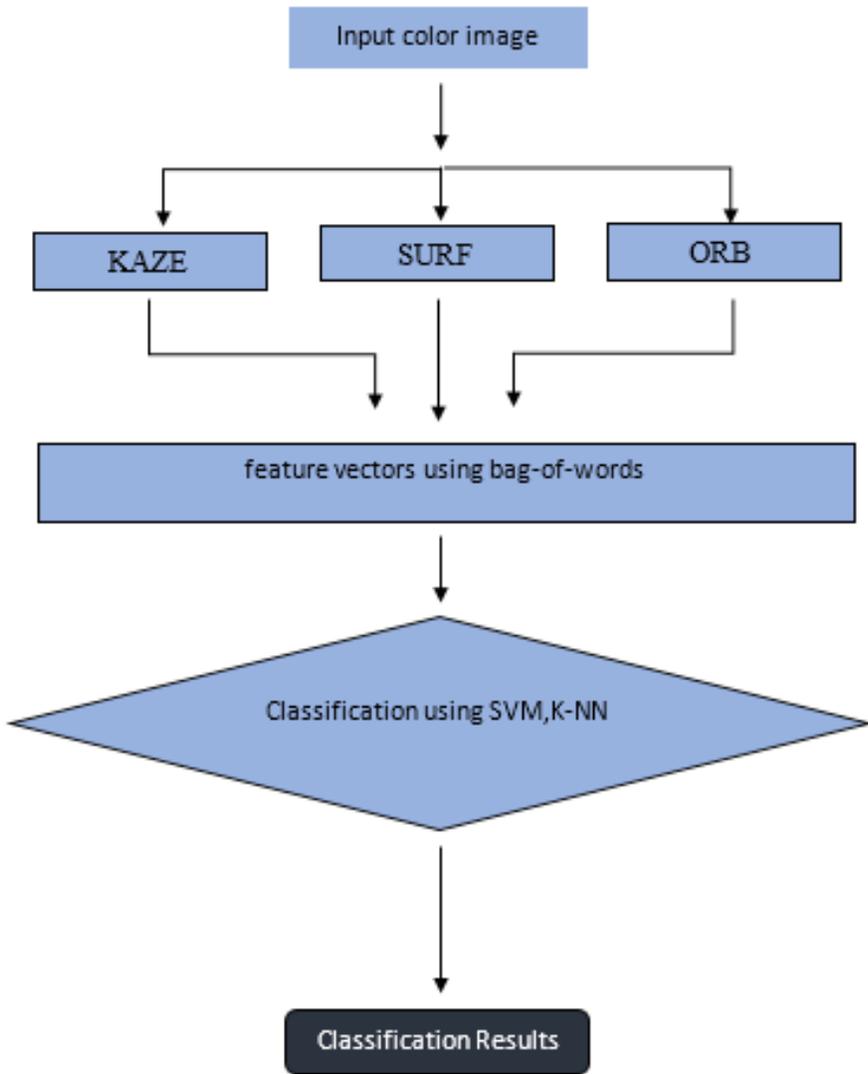
Figure 1. *Block Diagram of the proposed approach for face recognition system*

3.1.1 KAZE

The KAZE feature [7] is an immutable against rotation and scale changes in nonlinear scale spaces. It uses nonlinear diffusion filtering that retains edge and boundary information in the keypoint detection step (Equation 1).

$$\frac{\partial L}{\partial t} = div\{o(x, y, t).\nabla L\}$$

(1)

In equation 1, div is the divergence operator, ∇ is the gradient operator of the original image, t is the scale parameter, and o is the conductivity function.

As a result, nonlinear scale space is determined by using additive operating division techniques and variable conductivity diffusion in the detection of the KAZE feature. By means of this nonlinear scale space, the maxima of the normalized determinant of the Hessian response are determined. In the last step, the main orientation of the detector is calculated and the KAZE feature is obtained.

3.1.2 Speeded up robust feature (SURF)

Bay et al. [8] developed the Speeded Up Robust Feature (SURF). SURF is essentially a crucial point analyzer and description for local keypoints. It generates 64 dimensional descriptions. SURF also works in four stages like Scale Invariant Feature Transform (SIFT) [9], but with some changes. For feature detection, SURF uses Fast - Hessian matrix (Equation 2).

$$H(x,y,\sigma) = \begin{bmatrix} L_{xx}(x,y,\sigma) & L_{xy}(x,y,\sigma) \\ L_{xy}(x,y,\sigma) & L_{yy}(x,y,\sigma) \end{bmatrix} \tag{2}$$

Here, the convolution of the Gaussian quadratic derivative at the point x of the image is shown as $L_{xx}(x,y,\sigma)$. Similarly, $L_{xy}(x,y,\sigma)$, $L_{yy}(x,y,\sigma)$ represents Gaussian quadratic derivative.

Moreover, for feature descriptor, SURF used wavelet responses in vertical and horizontal directions as in Equation (3).

$$V_j = \left[\sum d_x , \sum d_y , \sum |d_x| , \sum |d_y| \right] \tag{3}$$

3.1.3 Oriented Fast and rotated BRIEF (ORB)

Rublee et al. [10] proposed Oriented Fast and Rotated BRIEF (ORB), which was created in the OpenCV lab. ORB is significantly quicker than SURF. It extracts features utilizing the FAST keypoint detector, the Harris corner analyzer, and the BRIEF crucial direction description. To improve efficiency, several more changes are made to the approach. ORB retrieves fewer (32 elements extracted) but more significant image characteristics. It also has a lower processing expense when compared to the SURF

techniques. Furthermore, as contrasted to the proprietary SIFT and SURF technologies, ORB is available to use. But it has more scale invariance than SURF. It also does not operate on fuzzy or damaged images.

3.2 Bag of Words

In the BOW method, which is a learning-based method, all descriptors are divided into a predetermined number of clusters.

Descriptors are assigned to the cluster they are closest to, depending on the distance from the cluster centers. Each cluster central visual word and the set of these visual words are called a dictionary. The histogram to be used in the classification method is created with the number of attributes assigned to each cluster.

3.3 Classification algorithms

3.3.1 K-Nearest Neighbor (K-NN)

The k-NN predictor is the most basic image classification. This predictor basically calculates the similarity between characteristic matrices and selects the category of information items closest to the trial information values. The K-NN technique operates in four stages:

- First, it computes the proximity among every observation item in the trial information and so each datasets point in the trained information.

- The ranges computed in part 1 next are sorted.

- It chooses the k-shortest paths given of the collection of ordered lengths. In this case, K is utilized to choose the quantity of information elements from that a judgment could be formed.

- Finally, it uses plurality vote to provide the category with the highest rating of that experiment dataset.

For instance, if two image classifications are chosen, the k-NN method delivers the classification with the shortest proximity between the information elements of the assessment image and the data sets of the learning image collection. In those various terms, once this technique is performed to assessment information, it allocates the category title that is closest to the pieces of information of assessment information. Some proximity measure or resemblance functional, such as Euclidean proximity or Manhattan blocks separation, is employed to determine the separation in a K-NN classification.

3.3.2 Support Vector Machines

SVM [11] classifies new instances by hyperplane separating training data with maximum margin.

The fixed margin primary optimization problem is solved by the following equation which realizes the maximum edge sub-plane.

$$y_i[\vec{w}, \vec{x_l} + b] > 1, i = 1, \dots, l \tag{4}$$

Here, $E = (\vec{x_1}, y_1) \dots (l, y_i)$ is training sample and $\overrightarrow{(w, b)}$ is hyperplane. In the fixed margin Binary optimization problem, the maximization is handled by the formula shown in equation 5.

$$W(\vec{a}) = \sum_{i=1}^{l} a_i - \frac{1}{2} \sum_{i,j=1}^{n} y_i y_j a_i a_j \vec{x_l} \vec{x_j} \tag{5}$$

Then, using the weight vector $\vec{a}$, the hyperplane with the maximum margin is obtained.

4 Performance Analysis and Experimental Validation

This chapter presents a comparison of several feature extraction techniques using several classifications. The study is evaluated using recognition accuracy. Therefore, recognition accuracy is critical for determining the framework's efficiency. Face 94 dataset [14] comprises 153 image classes. Figure 2 shows some samples from Face 94 dataset.
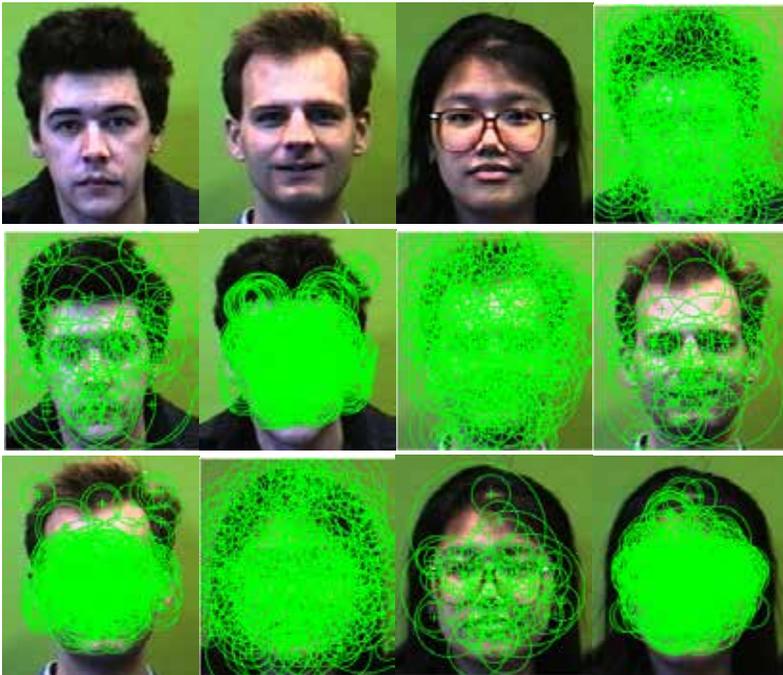
Figure 2. *Images from Face 94: (a) Original image, (b) KAZE Features detected in the image, (c) SURF Features detected in the image, (d) ORB Features detected in the image*

Moreover, the information splitting method outcomes are assessed employing a 5-Fold cross-validation database splitting technique. The techniques are run on an Intel Core i7 CPU running Windows 10 with 16 GB of RAM. Matlab 2022a is utilized for development. Table 1 shows the classifier-specific identification efficiency and empirical results detailing how KAZE features extracting techniques obtained a significant identification success of 99.4 percent when the Support Vector Machines was utilized. Additionally, the researchers used a 5-fold cross-validation datasets segmentation technique to enhance our categorization findings on multiple variables, resulting in an enhancement in identification frequency as shown in Table 1. In this study, it is aimed to be a more successful method by obtaining a hybrid feature by combining the two features with the highest accuracy rate. However, since very high results were obtained with the use of the features separately, the success rate of the application developed with the combination of the features did not change.

Table 1. Recognition accuracy on Face94 database images

Features	Accuracy	
	K-NN	SVM
SURF	0.993	0.993
ORB	0.990	0.991
KAZE+SURF	0.994	0.993
KAZE (Proposed-Method)	**0.994**	**0.994**

4.1 Comparison with other techniques proposed by other authors

This chapter compares some strategies offered by numerous writers on the Face 94 database (Table 2). This contains a comparative predicated on the fusion of traditional feature extractor approaches. For the identical situation, our technique beats the current solutions.

Table 2. Comparative results of proposed method and state-of-the-Art Method

Method	Accuracy
Vinay et al. [12]	0.967
Gupta et al. [13]	0.873
KAZE (Proposed-Method)	**0.994**

5   Conclusion and future directions

The study demonstrates face identification outcomes utilizing KAZE,

SURF, and ORB features descriptions with categorization methods such as k-NN, SVM. Face 94, a publicly available database, was used in the research. The effectiveness of several approaches is assessed in this piece using recognition accuracy rate. The empirical study shows that the KAZE descriptors performs better in all circumstances. Additionally, 5-Fold crossed verification sample segmentation is used to evaluate the efficacy of all features descriptions and classifying approaches discussed in this study. These characteristic descriptions and mixtures of features descriptions can be utilized in further study to enhance the identification outcomes of documentation images, medical images, spectrum images, and so on. It is an experiential research in which the effectiveness of three features descriptions, namely, KAZE, SURF, and ORB, is compared with multiple categorization algorithms in respect of identification efficiency. SVM, K-NN algorithms were utilized in the research study. The investigation demonstrated that the SVM performed on par with the K-NN classifier in terms of accuracy. The major purpose of this research was to demonstrate the usefulness of KAZE, SURF, and ORB pattern analyzers for face detection in the Face 94 accessible dataset.

REFERENCES

[1]   T. Tuncer, S. Dogan, M. Abdar, P. J. M. T. Pławiak, and Applications, "A novel facial image recognition method based on perceptual hash using quintet triple binary pattern," vol. 79, no. 39, pp. 29573-29593, 2020.

[2]   L. Ren and T. Wu, "Classification via two layers sparse representation," in 2012 IEEE International Conference on Computer Science and Automation Engineering (CSAE), 2012, vol. 1, pp. 51-54: IEEE.

[3]   N. H. J. I. J. o. C. A. Barnouti, "Face recognition using PCA-BPNN with DCT implemented on Face94 and grimace databases," vol. 142, no. 6, pp. 8-13, 2016.

[4]   N. H. Barnouti, M. H. N. Al-Mayyahi, and S. S. M. Al-Dabbagh, "Real-Time Face Tracking and Recognition System Using Kanade-Lucas-Tomasi and Two-Dimensional Principal Component Analysis," in 2018 International Conference on Advanced Science and Engineering (ICOASE), 2018, pp. 24-29: IEEE.

[5]   S. N. Kakarwal, R. R. J. I. J. o. A. C. S. Deshmukh, and Applications, "Hybrid feature extraction technique for face recognition," vol. 3, no. 2, 2012.

[6]   S. Kakarwal, R. Deshmukh, and V. J. Patil, "Face Recognition based on Supervised Learning," in Proceedings of the International Conference on Image Processing, Computer Vision, and Pattern Recognition (IPCV), 2012, p. 1: The Steering Committee of The World Congress in Computer Science, Computer

[7]   P. F. Alcantarilla, A. Bartoli, and A. J. Davison, "KAZE features," *Lect. Notes Comput. Sci. (including Subser. Lect. Notes Artif. Intell. Lect. Notes Bioinformatics)*, vol. 7577 LNCS, no. PART 6, pp. 214–227, 2012, doi: 10.1007/978-3-642-33783-3_16.

[8]   H. Bay, T. Tuytelaars, and L. Van Gool, "LNCS 3951 - SURF: Speeded Up Robust Features," *Comput. Vision–ECCV 2006*, pp. 404–417, 2006, [Online]. Available: http://link.springer.com/chapter/10.1007/11744023_32.

[9]   D. G. Lowe, "Object recognition from local scale-invariant features," *Proc. IEEE Int. Conf. Comput. Vis.*, vol. 2, pp. 1150–1157, 1999, doi: 10.1109/iccv.1999.790410.

[10]   E. Rublee, V. Rabaud, K. Konolige, and G. Bradski, "ORB: An efficient alternative to SIFT or SURF," *Proc. IEEE Int. Conf. Comput. Vis.*, pp. 2564–2571, 2011, doi: 10.1109/ICCV.2011.6126544.

[11]   C. CORTES and V. VAPNIK, "Support-Vector Networks," *Mach. Learning,* vol. 20, no. 3, pp. 273–297, 1995, doi: 10.1109/64.163674.

[12]   A. Vinay, D. Hebbar, V. S. Shekhar, K. N. B. Murthy, and S. Natarajan, "Two Novel Detector-Descriptor Based Approaches for Face Recognition Using SIFT and SURF," *Procedia Comput. Sci.*, vol. 70, pp. 185–197, 2015, doi: 10.1016/j.procs.2015.10.070.

[13]   S. Gupta, K. Thakur, and M. Kumar, "2D-human face recognition using SIFT and SURF descriptors of face's feature regions," *Vis. Comput.*, vol. 37, no. 3, pp. 447–456, 2021, doi: 10.1007/s00371-020-01814-8.

[14]   Dr Libor Spacek Computer Vision Science Research Projects,Face94Dataset http://dces.essex.ac.uk /mv/allfaces /faces94.zip
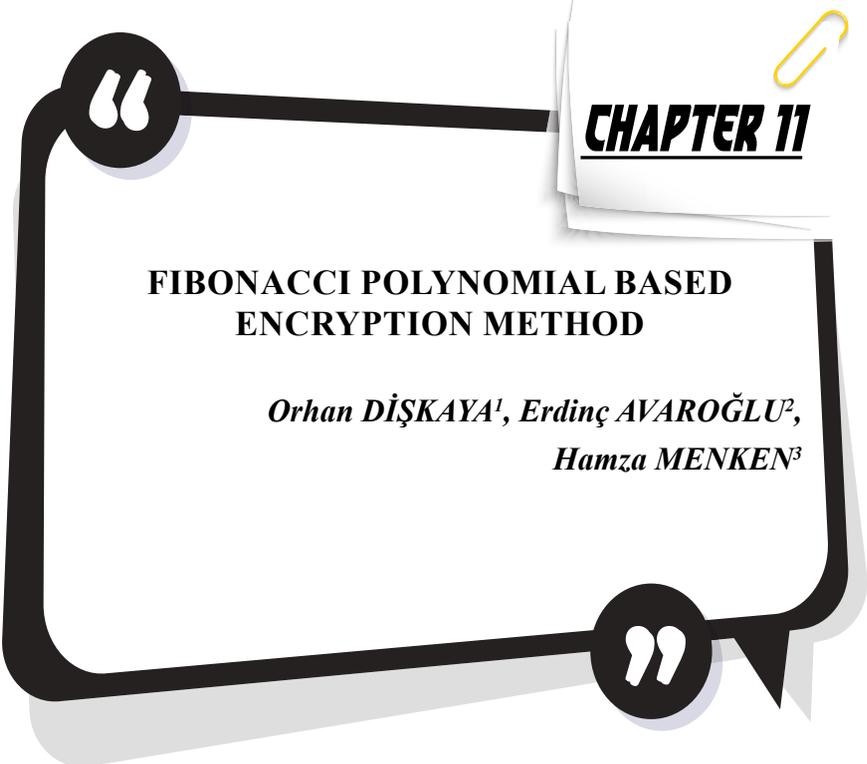
FIBONACCI POLYNOMIAL BASED ENCRYPTION METHOD

Orhan DİŞKAYA[1], Erdinç AVAROĞLU[2],

Hamza MENKEN[3]

1 Ress.Asst.,Mersin University, Faculty of Sciences, Department of Mathematics, Mersin/Turkey, Orcid: 0000-0001-5698-7834

2 Assoc.Prof.Dr., Mersin University, Department of Computer Engineering, Mersin/Turkey, Orcid: 0000-0003-1976-2526

3 Prof.Dr., Mersin University, Faculty of Sciences, Department of Mathematics, Mersin/Turkey, Orcid: 0000-0003-1194-3162

Introduction

Cryptography is a whole of mathematical technical studies related to information security such as authentication, data source verification, data integrity, and privacy issues. Cryptology is encryption science and provides information security. So, the message to be encrypted is called plain text, the message obtained after conversion is encrypted text, the encoding process in the conversion process is called encryption, and the reverse process is called decryption. The same secret key must be used for encryption and decryption.

There are two structures for symmetric key encryption and asymmetric key encryption depending on the state of the key for encryption operations. The distribution of the key used here can be done with a private channel. In asymmetric encryption algorithms, two keys are used, which are private and public. RSA is asymmetric encryption algorithms known as elliptic curve algorithms.

Symmetric encryption algorithm is used only secret (private) key. There are many encryption algorithms currently in use. These algorithms generally try to encrypt the data with different loops. Their main purpose is to ensure that the data can only be obtained by the desired people with the help of the entropy created by the encryption algorithm without using very long keys. DES, the most accepted of these algorithms in the past, has been 3DES with its updated version and AES with the most current version. AES is a symmetric key block encryption with high efficiency in terms of security and speed, known as the standard Rijndael algorithm. In addition, data security, ease of application, and speediness have come to the fore in choosing these algorithms.

In the AES encryption algorithm, AES is a repetitive block password based on the structure of the substitution and permutation network (SPN). AES runs on a 4x4 column byte matrix called state. The polynomial operations are performed on the Galois finite field axioms in operations on matrices, AES supports 128, 192, 256-bit key lengths. The repeat numbers of the rounds are 10, 12 and 14, respectively.

The Fibonacci number sequence was put forward by Fibonacci in 1202 as a result of the calculation of the problem with the breeding of rabbits in the book Liber Abaci. The first numerical value of the array is 0, the second is 1, and each consecutive element is found by summing the value of the previous two elements. The Fibonacci numbers are defined by the recurrence relation $F_{n+2} = F_{n+1} + F_n$ with the initial conditions $F_0 =$

$0, F_1 = 1$. The real roots of the characteristic $x^2 = x + 1$ equation obtained using the difference equations of this number sequence are $x_1 = \frac{1+\sqrt{5}}{2}$ and $x_2 = \frac{1-\sqrt{5}}{2}$. The positive root of this equation gives us the golden ratio, known as the excellent rate in the world of mathematics.

Nowadays, the Fibonacci polynomial matrices are one of the study areas of the Fibonacci numbers, which have hundreds of books and thousands of scientific articles.The Fibonacci polynomials are defined by the recurrence relation $f_{n+2}(x) = xf_{n+1}(x) + f_n(x)$ with the initial conditions $f_0(x) = 1, f_1(x) = x$.

$$Q^n(x) = \begin{pmatrix} f_{n+1}(x) & f_n(x) \\ f_n(x) & f_{n-1}(x) \end{pmatrix}$$

is the Fibonacci matrix obtained by using these polynomial elements (Koshy, 2018; 2019).

In this study, the polynomials used in AES were determined as the Fibonacci polynomials and encryption and deciphering operations of the Fibonacci polynomial matrix are performed.

Galois Finite Field

Definition 1: ([2]) A field F is a set of elements with two binary operations addition and multiplication satisfying the following properties:

1. *F* forms an additive group with the addition operation + and the identity element is 0.
2. All elements of *F* except 0 form a multiplicative group with the multiplication operation × and the identity element is 1.
3. The distributive law holds, i.e., for all *a,b,c* $\in F$:
$$a(b + c) = ab + ac.$$

In extension fields $GF(2^m)$elements are not represented as integers but as polynomials with coefficients in $GF(2)$. In AES-like the finite field contains 2^m elements and is denoted as $GF(2^m)$. In the field, $GF(2^m)$, which is used in AES-like, each element $,A \in GF(2^m)$ is thus represented as:

$$A(x) = a_m x^m + a_{m-1} x^{m-1} + \cdots + a_1 x + a_0$$

$$\{a_i\} \in GF(2) = \{0,1\}$$

Note that there are exactly $16 = 2^4$ such polynomials. The set of these 16 polynomials is the finite field $GF(2^4)$

Definition 2 ([2])   Let $A(x), B(x) \in GF(2^m)$. The sum and the subtraction of $A(x), B(x)$ are computed as

$$A(x) \pm B(x) = (a_m \pm b_m)x^m + (a_{m-1} \pm b_{m-1})x^{m-1} + \cdots \\ + (a_1 \pm b_1)x + (a_0 \pm b_0),$$

$$(a_i \pm b_i) mod 2 \ \ for \ \ i \in \{0,1,\dots,m\}$$

Definition 3 ([2]) Assuma that $A(x), B(x) \in GF(2^m)$ and

$$P(x) = p_m x^m + p_{m-1}x^{m-1} + \cdots + p_1 x + p_0 \ , \qquad p_i \in GF(2^m)$$

İs an irreducible polynomial. Multiplication of the two elements $A(x), B(x)$ is performed as

$$A(x), B(x) \ mod \ P(x).$$

 The irreducible polynomials of $GF(2^4)$ are given as

$x^4 + x + 1, \ x^4 + x^3 + 1, \ x^4 + x^3 + x^2 + x + 1.$

For AES, the irreducible polynomial

$R(x) = x^8 + x^4 + x^3 + x + 1$

is used. It is part of the AES specification. For AES-like, we consider the irreducible polynomial as following

$$P(x) = x^4 + x + 1 \qquad\qquad (1)$$

Definition 4 [(2]) For a given field $GF(2^m)$ and the corresponding irreducible polynomial $P(x)$, the inverse A^{-1} of a nonzero element $A \in GF(2^m)$ is defined by

$$A^{-1}(x)A(x) \ = \ 1 \ mod P(x).$$

 For more information about the Galois field we refer to [8].

The Fibonacci Polynomial Matrix

Definition 5 ([6,7]) The Fibonacci sequence $\{F_n\}_{n \geq 0}$ is defined by

$$F_0 = 0, F_1 = 1 \ \ and \ \ F_{n+2} = F_{n+1} + F_n.$$

Here, F_n is the nth Fibonacci number. The first few members of this sequence are given in Table 1:

Table 1. A few members of the Fibonacci numbers

n	0	1	2	3	4	5	6	7	8	9	10	11	12
F_n	0	1	1	2	3	5	8	13	21	34	55	89	144

Definition 6 ([6,7]) The Fibonacci polynomials sequence $\{f_n(x)\}_{n\geq0}$ is defined by

$$f_0(x) = 0, \qquad f_1(x) = 1 \ and \ f_{n+2}(x) = xf_{n+1}(x) + f_n(x).$$

The first few members of this sequence are given in Table 2:

Table 2. A few members of the Fibonacci polynomials

n	0	1	2	3	4	5	...
$f_n(x)$	0	1	x	x^2+1	x^3+2x	x^4+3x^2+1	...

The polynomials $f_n(x)$ ve $f_n^{-1}(x)$ are obtained as follows using the irreducible polynomial $P(x)$ and mod 2. The $F_n(x)$ Fibonacci polynomial is also obtained using the irreducible polynomial $R(x)$ and mod 2.

Table 3. A few the irreducible polynomials

n	$F_n(x)$	$f_n(x)$	$f_n^{-1}(x)$	Z_2
1	1	1	1	mod 2
2	x	x	$x^3 + 1$	mod 2
3	$x^2 + 1$	$x^2 + 1$	$x^3 + x + 1$	mod 2
4	x^3	x^3	$x^3 + x^2 + x + 1$	mod 2
5	$x^4 + x^2 + 1$	$x^2 + x$	$x^2 + x + 1$	mod 2
6	$x^5 + x$	x^2	$x^3 + x^2 + 1$	mod 2
7	$x^6 + x^4 + 1$	$x^3 + x^2 + x$	$x + 1$	mod 2
8	x^7	$x^3 + x + 1$	$x^2 + 1$	mod 2
9	$x^6 + x^3 + x$	$x^3 + x + 1$	$x^2 + 1$	mod 2
10	$x^4 + x^2$	$x^3 + x^2 + x$	$x + 1$	mod 2
11	$x^6 + x^5 + x$	x^2	$x^3 + x^2 + 1$	mod 2
12	$x^7 + x^6 + x$	$x^2 + x$	$x^2 + x + 1$	mod 2
13	$x^7 + x^5 + x^4 + x^3 + x^2 + 1$	x^3	$x^3 + x^2 + x + 1$	mod 2
14	$x^6 + x^5 + 1$	$x^2 + 1$	$x^3 + x + 1$	mod 2
15	$x^6 + x^5 + x^4 + x^3 + x^2 + x + 1$	x	$x^3 + 1$	mod 2
16	$x^7 + x^4 + x^3 + x^2 + x + 1$	1	1	mod 2

The following identity shows that the Fibonacci polynomials matrix is invertible:

Theorem 1 (Cassini Identity): ([6,7]) If $f_n(x)$ denotes the n th Fibonacci polynomial polynomial, then,

$$f_{n+1}(x)f_{n-1}(x) - f_n^2(x) = (-1)^n, \quad n \geq 1.$$

Theorem 2 (Fibonacci Polynomial Matrix): ([6, 7]) Let,

$$Q(x) = \begin{pmatrix} x & 1 \\ 1 & 0 \end{pmatrix}$$

It then follows by principle of mathematical induction that,

$$Q^n(x) = \begin{pmatrix} f_{n+1}(x) & f_n(x) \\ f_n(x) & f_{n-1}(x) \end{pmatrix} \tag{2}$$

where $n \geq 1$. $Q^n(x)$ is called the Fibonacci polynomials matrix.

Theorem 3 (Inverse of a 2x2 Matrix): The determinant of the Fibonacci polynomials matrix $Q^n(x)$ is

$$|Q^n(x)| = f_{n+1}(x)f_{n-1}(x) - f_n^2(x) = 1.$$

Hence, the inverse of $Q^n(x)$ is given by

$$Q^n(x)^{-1} = \begin{pmatrix} f_{n-1}(x) & f_n(x) \\ f_n(x) & f_{n+1}(x) \end{pmatrix}.$$

For more information see [1].

The F-AES S-box table prepared according to the Fibonacci numbers and prime factor

In this section, a new S-box like in the AES prepared by Kamsia, Fakariah, Suriyani, Nur and Mohd using the Fibonacci numbers and prime factor is given as follows [10].

Table 4. F-AES S-box Based on Fibonacci Numbers and Prime Factor

	00	01	02	03	04	05	06	07	08	09	0A	0B	0C	0D	0E	0F
00	5A	45	4E	42	CB	52	56	FC	09	38	5E	12	C7	EE	92	4F
01	F3	BB	F0	44	C3	60	7E	C9	94	ED	9B	96	A5	9D	4B	F9
02	8E	C4	AA	1F	0F	06	CE	F5	0D	9C	DC	C8	48	E1	08	2C
03	3D	FE	1A	FA	21	AF	3C	A3	3E	2B	B9	DB	D2	1E	8B	4C
04	30	BA	15	23	22	57	63	99	6B	02	EF	8A	10	DA	16	BD
05	6A	E8	39	D4	19	C5	88	62	53	F2	87	00	73	75	61	F6
06	E9	D6	93	C2	7A	74	0A	BC	7C	C0	3B	46	69	05	A6	91
07	68	9A	79	B6	AB	A4	01	CC	85	8F	E3	18	29	C6	CA	EB
08	F4	35	2A	D5	66	AE	7D	2E	FD	9E	47	04	5D	64	20	4A
09	59	B8	76	E5	1B	13	A9	B1	7F	D7	81	2D	E7	67	32	E2
0A	D9	0B	03	33	70	3F	1D	65	FB	EA	95	5B	A8	AC	DD	40
0B	DE	F1	0E	54	B4	EC	77	90	55	6F	CD	D3	5C	43	97	31
0C	83	41	1C	17	25	9F	8D	FF	D1	E4	4D	26	72	84	B2	B3
0D	49	07	8C	5F	71	3A	CF	37	58	0C	6E	80	BF	F8	24	A7
0E	D8	C1	A1	28	50	E0	B7	AD	A2	27	BE	D0	F7	6C	11	E6
0F	B5	98	B0	34	86	DF	7B	51	78	A0	14	36	89	6D	82	2F

Table 5. F-AES Inverse S-box Based on Fibonacci Numbers and Prime Factor

	00	01	02	03	04	05	06	07	08	09	0A	0B	0C	0D	0E	0F
00	5B	76	49	A2	8B	6D	25	D1	2E	08	66	A1	D9	28	B2	24
01	4C	EE	0B	95	FA	42	4E	C3	7B	54	32	94	C2	A6	3D	23
02	8E	34	44	43	DE	C4	CB	E9	E3	7C	82	39	2F	9B	87	FF
03	40	BF	9E	A3	F3	81	FB	D7	09	52	D5	6A	36	30	38	A5
04	AF	C1	03	BD	13	01	6B	8A	2C	D0	8F	1E	3F	CA	02	0F
05	E4	F7	05	58	B3	B8	06	45	D8	90	00	AB	BC	8C	0A	D3
06	15	5E	57	46	8D	A7	84	9D	70	6C	50	48	ED	FD	DA	B9
07	A4	D4	CC	5C	65	5D	92	B6	F8	72	64	F6	68	86	16	98
08	DB	9A	FE	C0	CD	78	F4	5A	56	FC	4B	3E	D2	C6	20	79
09	B7	6F	0E	62	18	AA	1B	BE	F1	47	71	1A	29	1D	89	C5
0A	F9	E2	E8	37	75	1C	6E	DF	AC	96	22	74	AD	E7	85	35
0B	F2	97	CE	CF	B4	F0	73	E6	91	3A	41	11	67	4F	EA	DC
0C	69	E1	63	14	21	55	7D	0C	2B	17	7E	04	77	BA	26	D6
0D	EB	C8	3C	BB	53	83	61	99	E0	A0	4D	3B	2A	AE	B0	F5
0E	E5	2D	9F	7A	C9	93	EF	9C	51	60	A9	7F	B5	19	0D	4A
0F	12	B1	59	10	80	27	5F	EC	DD	1F	33	A8	07	88	31	C7

The Fibonacci Polynomial Encryption Algorithm

In this study, the encryption algorithm is created in 4 stages like AES. So, descriptions of the stages obtained using the Fibonacci polynomials are given following.
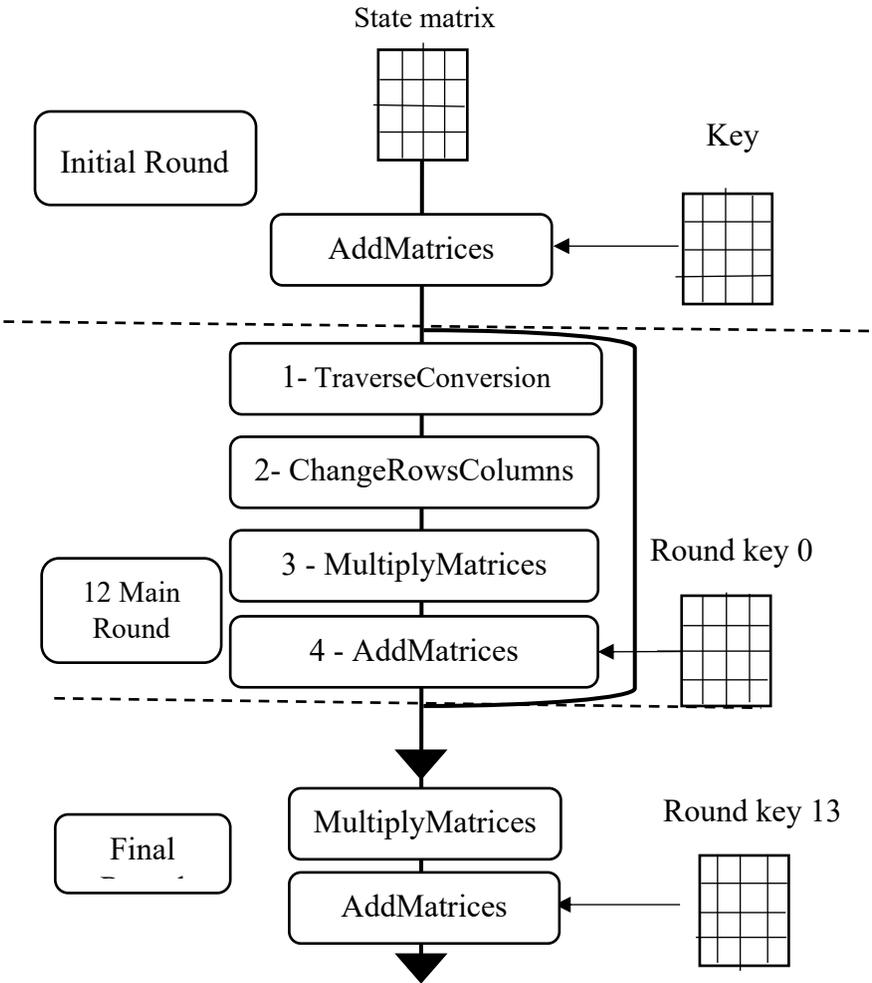
Figure 1. Encryption Process Algorithm

Initial Round:

In the algorithm proposed in Figure 1, the polynomial elements of the state matrix and key matrix are summed in this section as follows.

For $1 \leq i, j \leq 4$, $X_{ij}, Y_{ij}, Z_{ij} \in GF(2^8)$,

$$X_{ij} = a_7^{(ij)}x^7 + a_6^{(ij)}x^6 + \cdots + a_1^{(ij)}x + a_0^{(ij)}, \quad a_k^{(ij)} \in GF(2) = \{0,1\},$$
$$0 \leq k \leq 7$$

$$Y_{ij} = b_7^{(ij)}x^7 + b_6^{(ij)}x^6 + \cdots + b_1^{(ij)}x + b_0^{(ij)}, \quad b_k^{(ij)} \in GF(2) = \{0,1\},$$
$$0 \leq k \leq 7$$

Then

$$Z_{ij} = X_{ij} + Y_{ij}$$
$$= (a_7^{(ij)} + b_7^{(ij)})x^7 + (a_6^{(ij)} + b_6^{(ij)})x^6 + \cdots + (a_1^{(ij)}$$
$$+ b_1^{(ij)})x + a_0^{(ij)} + b_0^{(ij)}$$

Table 6. Addition of the state matrix and key matrix

X_{11}	X_{12}	X_{13}	X_{14}
X_{21}	X_{22}	X_{23}	X_{24}
X_{31}	X_{32}	X_{33}	X_{34}
X_{41}	X_{42}	X_{43}	X_{44}

$+$

Y_{11}	Y_{12}	Y_{13}	Y_{14}
Y_{21}	Y_{22}	Y_{23}	Y_{24}
Y_{31}	Y_{32}	Y_{33}	Y_{34}
Y_{41}	Y_{42}	Y_{43}	Y_{44}

State matrix

$=$

Z_{11}	Z_{12}	Z_{13}	Z_{14}
Z_{21}	Z_{22}	Z_{23}	Z_{24}
Z_{31}	Z_{32}	Z_{33}	Z_{34}
Z_{41}	Z_{42}	Z_{43}	Z_{44}

Key matrix

Main Round:

This section consists of 4 stages as traverse conversion, change rows columns, multiply matrices and add matrices. These stages are described as follows.

Traverse Conversion:

8-bit Z polynomial values according to mode 2 are divided into two 4-bit blocks and 4th order A and B polynomial elements are formed. In other words;

$$Z_{ij} = c_7^{(ij)}x^7 + c_6^{(ij)}x^6 + \cdots + c_1^{(ij)}x + c_0^{(ij)}, \quad c_k^{(ij)} \in GF(2) = \{0,1\},$$
$$0 \leq k \leq 7.$$

For A_{ij}, $B_{ij} \in GF(2^4)$,

$$A_{ij} = c_7^{(ij)}x^3 + c_6^{(ij)}x^2 + c_5^{(ij)}x + c_4^{(ij)}, \quad c_k^{(ij)} \in GF(2) = \{0,1\},$$
$$4 \le k \le 7,$$

$$B_{ij} = c_3^{(ij)}x^3 + c_2^{(ij)}x^2 + c_1^{(ij)}x + c_0^{(ij)}, \quad c_k^{(ij)} \in GF(2) = \{0,1\},$$
$$0 \le k \le 3$$

is taken. Then, the values marked in the state matrix given in Table 7 are multiplied by the Fibonacci polynomial elements. For $1 \le i, j \le 4$, $Z_{ij} \in GF(2^8)$ and A_{ij}, $B_{ij} \in GF(2^4)$.

Table 7. Traverse conversion matrix

Some Fibonacci polynomial elements $f_1(x) = 1$, $f_2(x) = x$, $f_3(x) = x^2 + 1$, $f_4(x) = x^3$, $f_5(x) = x^2 + x$, $f_6(x) = x^2$, $f_7(x) = x^3 + x^2 + x$, $f_8(x) = x^3 + x + 1$ obtained with $mod\ 2$ using the irreducible polynomial $x^4 + x + 1$.

The multiplication of the elements in the state matrix is given in the following recurrence relations (2). The values of a_{ij} and b_{ij} are hexadecimal equivalent values of A_{ij} and B_{ij} polynomials.

$$C_{ij} = A_{ij} \times f_{i+j} \ (mod\ 2) \text{ or } C_{ij} = B_{ij} \times f_{i+j} \ (mod\ 2) \qquad (2)$$

The new matrix resulting from these processes is given in table 8. For decryption,

$$A_{ij} = C_{ij} \times f_{i+j}^{-1}(mod\ 2) \quad \text{or} \quad B_{ij} = C_{ij} \times f_{i+j}^{-1} \ (mod\ 2)$$

Table 8. New traverse conversion matrix

$C_{11}\ B_{11}$	$A_{12}\ C_{12}$	$C_{13}\ B_{13}$	$A_{14}\ C_{14}$
$A_{21}\ C_{21}$	$C_{22}\ B_{22}$	$A_{23}\ C_{23}$	$C_{24}\ B_{24}$
$C_{31}\ B_{31}$	$A_{32}\ C_{32}$	$C_{33}\ B_{33}$	$A_{34}\ C_{34}$
$A_{41}\ C_{41}$	$C_{42}\ B_{42}$	$A_{43}\ C_{43}$	$C_{44}\ B_{44}$

If the A_{ij}, B_{ij} and C_{ij} elements of the matrix in table 8 are converted using hexadecimal base according to the S-box table in table 4, the matrix in table 9 is obtained as follows.

Table 9. Traverse conversion matrix according to S-box

$K_{11} L_{11}$	$K_{12} L_{12}$	$K_{13} L_{13}$	$K_{14} L_{14}$
$K_{21} L_{21}$	$K_{22} L_{22}$	$K_{23} L_{23}$	$K_{24} L_{24}$
$K_{31} L_{31}$	$K_{32} L_{32}$	$K_{33} L_{33}$	$K_{34} L_{34}$
$K_{41} L_{41}$	$K_{42} L_{42}$	$K_{43} L_{43}$	$K_{44} L_{44}$

Change rows and columns :

In this section, the rows of the new traverse conversion matrix are shifted, respectively, by the first four terms of Fibonacci numbers (i.e. 1,1,2,3). Then the similar operations are applied for the columns, respectively

- The first row of the matrix is shifted 1 byte to the left for the first term 1 of the Fibonacci.
- The second row of the matrix is shifted 1 byte to the left for the second term 1 of the Fibonacci.
- The third row of the matrix is shifted 2 bytes to the left for the third term 2 of the Fibonacci.
- The fourth row of the matrix is shifted 3 bytes to the left for the fourth term 3 of the Fibonacci.
  The change row matrix resulting from the row changes is shown in table 10.

Table 10. Change row matrix

$K_{12} C_{12}$	$C_{13} K_{13}$	$K_{14} C_{14}$	$C_{11} K_{11}$
$C_{22} K_{22}$	$K_{23} C_{23}$	$C_{24} K_{24}$	$K_{21} C_{21}$
$C_{33} K_{33}$	$K_{34} C_{34}$	$C_{31} K_{31}$	$K_{32} C_{32}$
$C_{44} K_{44}$	$K_{41} C_{41}$	$C_{42} K_{42}$	$K_{43} C_{43}$

The column change of the matrix formed after the row change is as follows.

- The first column of the matrix is shifted 1 byte to the up for the first term 1 of the Fibonacci.
- The second column of the matrix is shifted 1 byte to the up for the second term 1 of the Fibonacci.

- The third column of the matrix is shifted 2 bytes to the up for the third term 2 of the Fibonacci.
- The fourth column of the matrix is shifted 3 bytes to the up for the fourth term 3 of the Fibonacci.

The Change column matrix resulting from the column changes is shown in table 11.

Table 11. Change column matrix

C_{22} K_{22}	K_{23} C_{23}	C_{31} K_{31}	K_{43} C_{43}
C_{33} K_{33}	K_{34} C_{34}	C_{42} K_{42}	C_{11} K_{11}
C_{44} K_{44}	K_{41} C_{41}	K_{14} C_{14}	K_{21} C_{21}
K_{12} C_{12}	C_{13} K_{13}	C_{24} K_{24}	K_{32} C_{32}

Multiply Matrices :

The matrix in Table 8 is divided into blocks to be multiplied by the 2x2 fibonacci polynomial matrix (2). The resulting new 2x2 matrices are placed in Table 11 using mod 2 and irreducible polynomials (1) , respectively. For $1 \leq i, j \leq 4$, K_{ij}, $L_{ij} \in GF(2^4)$.

$$\begin{bmatrix} K_{22} & L_{22} \\ K_{33} & L_{33} \end{bmatrix} \begin{bmatrix} f_{n+1}(x) & f_n(x) \\ f_n(x) & f_{n-1}(x) \end{bmatrix} = \begin{bmatrix} D_{11} & E_{11} \\ D_{21} & E_{21} \end{bmatrix},$$

$$\begin{bmatrix} K_{23} & L_{23} \\ K_{34} & L_{34} \end{bmatrix} \begin{bmatrix} f_{n+1}(x) & f_n(x) \\ f_n(x) & f_{n-1}(x) \end{bmatrix} = \begin{bmatrix} D_{12} & E_{12} \\ D_{22} & E_{22} \end{bmatrix}, \dots,$$

$$\begin{bmatrix} K_{21} & L_{21} \\ K_{32} & L_{32} \end{bmatrix} \begin{bmatrix} f_{n+1}(x) & f_n(x) \\ f_n(x) & f_{n-1}(x) \end{bmatrix} = \begin{bmatrix} D_{34} & E_{34} \\ D_{44} & E_{44} \end{bmatrix}, \text{ and } \{n = 2 + t : t.tour = t\}.$$

Thus, the D_{ij} and E_{ij} polynomials in Table 12 are formed according to the irreducible polynomial and mod 2.

Table 12. Multiply matrix

$D_{11}E_{11}$	$D_{12}E_{12}$	$D_{13}E_{13}$	$D_{14}E_{14}$
$D_{21}E_{21}$	$D_{22}E_{22}$	$D_{23}E_{23}$	$D_{24}E_{24}$
$D_{31}E_{31}$	$D_{32}E_{32}$	$D_{33}E_{33}$	$D_{34}E_{34}$
$D_{41}E_{41}$	$D_{42}E_{42}$	$D_{43}E_{43}$	$D_{44}E_{44}$

is obtained.

Add Matrices :

The matrix in Table 13 is added with the key matrix obtained in the key formation process. For $1 \leq i,j \leq 4$, $5 \leq k \leq 8$ $Y_{ik} \in GF(2^8)$ and $D_{ij}, E_{ij} \in GF(2^4)$.

Table 13. Multiply matrix and key matrix

$D_{11}E_{11}$	$D_{12}E_{12}$	$D_{13}E_{13}$	$D_{14}E_{14}$		Y_{15}	Y_{16}	Y_{17}	Y_{18}
$D_{21}E_{21}$	$D_{22}E_{22}$	$D_{23}E_{23}$	$D_{24}E_{24}$		Y_{25}	Y_{26}	Y_{27}	Y_{28}
$D_{31}E_{31}$	$D_{32}E_{32}$	$D_{33}E_{33}$	$D_{34}E_{34}$	$+$	Y_{35}	Y_{36}	Y_{37}	Y_{38}
$D_{41}E_{41}$	$D_{42}E_{42}$	$D_{43}E_{43}$	$D_{44}E_{44}$		Y_{45}	Y_{46}	Y_{47}	Y_{48}

So,

Table 14. Add of Multiply matrix and key matrix

$D_{11}E_{11} + Y_{15}$	$D_{12}E_{12} + Y_{16}$	$D_{13}E_{13} + Y_{17}$	$D_{14}E_{14} + Y_{18}$
$D_{21}E_{21} + Y_{25}$	$D_{22}E_{22} + Y_{26}$	$D_{23}E_{23} + Y_{27}$	$D_{24}E_{24} + Y_{28}$
$D_{31}E_{31} + Y_{35}$	$D_{32}E_{32} + Y_{36}$	$D_{33}E_{33} + Y_{37}$	$D_{34}E_{34} + Y_{38}$
$D_{41}E_{41} + Y_{45}$	$D_{42}E_{42} + Y_{46}$	$D_{43}E_{43} + Y_{47}$	$D_{44}E_{44} + Y_{48}$

is obtained.

Key formation :

Rconn :

The Rcon matrix in Table 15 consists of $F_n(x)$ Fibonacci polynomials formed by the irreducible polynomial $R(x)$. It helps to create key matrices.

Table 15. Rcon matrix

$F_1(x)$	$F_2(x)$	$F_3(x)$	$F_4(x)$	$F_5(x)$	$F_6(x)$	$F_7(x)$	$F_8(x)$	$F_9(x)$	$F_{10}(x)$	$F_{11}(x)$	$F_{12}(x)$	$F_{13}(x)$	$F_{14}(x)$
00	00	00	00	00	00	00	00	00	00	00	00	00	00
00	00	00	00	00	00	00	00	00	00	00	00	00	00
00	00	00	00	00	00	00	00	00	00	00	00	00	00

Key generation :

Key generation includes as many rounds as the number of cycles. All keys are obtained by using the keys calculated in the previous round.

Table 16. Round keys

Key matrix					Round 0					
Y_{11}	Y_{12}	Y_{13}	Y_{14}		Y_{15}	Y_{16}	Y_{17}	Y_{18}		. . .
Y_{21}	Y_{22}	Y_{23}	Y_{24}		Y_{25}	Y_{26}	Y_{27}	Y_{28}		. . .
Y_{31}	Y_{32}	Y_{33}	Y_{34}		Y_{35}	Y_{36}	Y_{37}	Y_{38}		. . .
Y_{41}	Y_{42}	Y_{43}	Y_{44}		Y_{45}	Y_{46}	Y_{47}	Y_{48}		. . .

1. **Step.**

The first column of the round 0 matrix is obtained by adding the column matrices obtained in the following steps.

a) The fourth column of the key matrix that is obtained by shifting down one byte.
b) the first column of the key matrix that is obtained by shifting up one byte.
c) The first column matrix of the rcon matrix

$$
\begin{bmatrix} Y_{15} \\ Y_{25} \\ Y_{35} \\ Y_{45} \end{bmatrix} = \begin{bmatrix} Y_{24} \\ Y_{34} \\ Y_{44} \\ Y_{14} \end{bmatrix} + \begin{bmatrix} Y_{41} \\ Y_{11} \\ Y_{21} \\ Y_{31} \end{bmatrix} + \begin{bmatrix} f_1(x) \\ f_2(x) \\ f_f(x) \\ f_g(x) \end{bmatrix}
$$

2. **Step.** The second column of the round 0 matrix is obtained as follows.

$$
\begin{bmatrix} Y_{16} \\ Y_{26} \\ Y_{36} \\ Y_{46} \end{bmatrix} = \begin{bmatrix} Y_{12} \\ Y_{22} \\ Y_{32} \\ Y_{42} \end{bmatrix} + \begin{bmatrix} Y_{15} \\ Y_{25} \\ Y_{35} \\ Y_{45} \end{bmatrix}
$$

3. **Step.** The third column of the round 0 matrix is obtained as follows.

$$
\begin{bmatrix} Y_{17} \\ Y_{27} \\ Y_{37} \\ Y_{47} \end{bmatrix} = \begin{bmatrix} Y_{13} \\ Y_{23} \\ Y_{33} \\ Y_{43} \end{bmatrix} + \begin{bmatrix} Y_{16} \\ Y_{26} \\ Y_{36} \\ Y_{46} \end{bmatrix}
$$

4. **Step.** The fourth column of the round 0 matrix is obtained as follows.

$$
\begin{array}{|c|}
\hline Y_{18} \\ \hline Y_{28} \\ \hline Y_{38} \\ \hline Y_{48} \\ \hline
\end{array}
=
\begin{array}{|c|}
\hline Y_{14} \\ \hline Y_{24} \\ \hline Y_{34} \\ \hline Y_{44} \\ \hline
\end{array}
+
\begin{array}{|c|}
\hline Y_{17} \\ \hline Y_{27} \\ \hline Y_{37} \\ \hline Y_{47} \\ \hline
\end{array}
$$

Other key matrices occur in steps similar to the above process.

Decryption process :

The steps used to decode the encrypted text in the Fibonacci polynomial encryption algorithm is similar to the steps used for encryption. However, it is calculated using reverse processes. The transformations applied to encrypt are reversed and the reverse order of encryption begins.

Conclusion

The AES (Advanced Encryption Standard) is an encryption method whose reliability is accepted. The main rounds steps in the encryption process of the AES encryption algorithm are sub bytes, shift rows, mix columns and add round key. The encryption algorithm in this study aims to create a stronger encryption algorithm by using Fibonacci polynomials to strengthen the steps in AES. The steps traverse conversion, change rows and columns, multiply matrices and add matrices are applied, respectively, instead of sub bytes, shift rows, mix columns and add round key steps in AES. These steps respectively create results as follows.

- When traverse conversion is used instead of sub bytes in the AES, the Fibonacci S-box table is used instead of the S-box table and the cross is multiplied by the fibonacci polynomials to have a stronger structure.
- When change rows and columns are used instead of shift rows in the AES, it is made more complicated by applying row and column shifting according to the first four values of the Fibonacci instead of row shifting in the AES.
- When multiply matrices are used instead of mix columns in the AES, a stronger algorithm is aimed using Fibonacci polynomial matrices.

REFERENCE

[1] Avaroğlu, E., Dişkaya, O., and Menken, Turkish Journal of Engineering, 4(3), 123-128, 2020.

[2] Paar, C., & Pelzl, J. (2009). Understanding cryptography: a textbook for students and practitioners. Springer Science & Business Media.

[3] Kak, A. Lecture 8: AES: The advanced encryption standard, 2016.

[4] Koc, C. K., In Cryptographic engineering (pp. 1-4). Springer, Boston, MA, 2009.

[5] Stinson, D. R., & Paterson, M. Cryptography: theory and practice. CRC press, 2018.

[6] Koshy, T. (2018). "Fibonacci and Lucas Numbers with Applications." Volume 1, John Wiley & Sons, New Jersey.

[7] Koshy, T. (2019). "Fibonacci and Lucas Numbers with Applications." Volume 2, John Wiley & Sons, New Jersey.

[8] Stewart, I. (1990). "Galois theory." Chapman and Hall/CRC.

[9] Uçar, S , Taş, N., and Özgür, N. (2019). "A New Application to Coding Theory via Fibonacci and Lucas Numbers". MSAEN 7: 62-70.

[10] Mohamed, K., Ali, F. H. H. M., Ariffin, S., Zakaria, N. H., & Pauzi, M. N. M. (2018). An Improved AES S-box Based on Fibonacci Numbers and Prime Factor. *IJ Network Security*, *20*(6), 1206-1214.
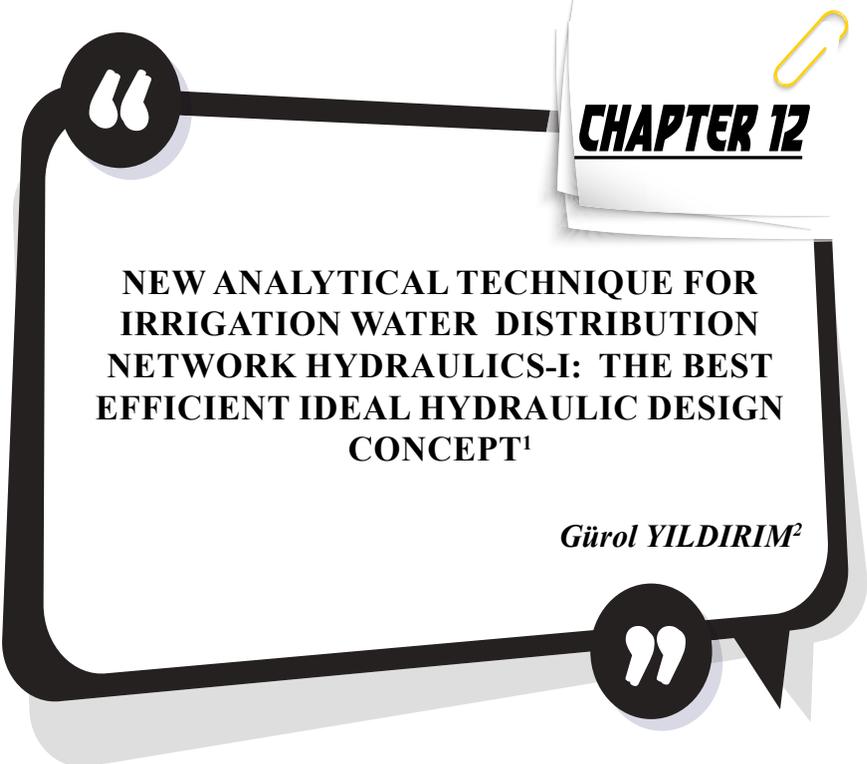
CHAPTER 12

NEW ANALYTICAL TECHNIQUE FOR IRRIGATION WATER DISTRIBUTION NETWORK HYDRAULICS-I: THE BEST EFFICIENT IDEAL HYDRAULIC DESIGN CONCEPT[1]

Gürol YILDIRIM[2]

INTRODUCTION

Determining the actual energy (i.e., pressure head) profiles along the submain lines with a uniform slope is important for proper hydraulic design of water distribution systems. In practice, there are three general pressure head profiles (Type-I, Type-II, and Type-III) along the submain lines depending on different uniform line slope situations. Among all types of pressure profiles, the Type-II profile is considered as the optimal (or ideal) pressure profile which can produce the minimum pressure head difference for a given pipe length. This profile occurs when the total energy loss by friction is just balanced by the total energy gain due to uniform downslope. This paper presents a comprehensive analysis to identify the optimal pressure profile (Type II), to achive the minimal point of the relative maximum pressure variation, Φ_H, which can be defined as the ratio of the maximum allowable pressure head difference (ΔH_{max}) to the total friction drop ($h_{f(L)}$). This minimal point is regarded as "*the most efficient pressure profile*" or "*ideal hydraulic design*" in the literature.

For this purpose, an illustrative figure is developed to compare values of the relative maximum pressure variation versus the dimensionless energy-gradient ratio ($K_S = S_0/S_f$) for all types of pressure profiles. The present ϕ_H curve versus K_S values allows the design engineer to make a decision for the best alternative for selecting the K_S value, where for a given pipe slope (S_0) the K_S value can be selected to meet the minimum pressure variation [$K_S = 1$, (ϕ_H)$_{min}$ = 0.36] or the range of pressure variation as close to the minimum point as possible. The implementation of the procedure based on the energy-gradient ratio (EGR) approach for all types of pressure profiles will be presented covering various design applications.

In water distribution systems, a sub-main line with multiple outlets can be regarded as a typical hydraulic structure, whose design is limited by the operating inlet pressure head (H_{0I}), desired uniformity criterion for water application, total friction drop at the end of line ($h_{f(L)}$), field topography, as well as outlet hydraulic characteristics. Analysis of the hydraulic design of multi-outlet submain lines is important for the proper performance of these systems.

The main objective of this paper is to develop a procedure based an improved Energy Gradient Ratio (EGR) approach which is an improvement on the previous mathematical development (Yıldırım 2008) utilizing analytical approaches (Yıldırım 2006, 2007) and which covers different types of pressure head profiles (Type-I, Type-II.a, Type-II.b, Type- II.c and Type-III) (Gillespie et al. 1979, Wu et al. 1983, Barragan and Wu 2005) under different uniform line slope situations, while determining values of pressure parameters.

The energy-gradient ratio (EGR) approach is useful to identify first which type of pressure profile occurs for a given uniform design slope when other hydraulic variables are initially known, then comprehensively evaluate its hydraulic characteristics along the line. Knowledge of hydraulic properties for any type of pressure profile under consideration enables the design engineer to evaluate pressure parameters through the line sections in a simple way based on the proposed EGR approach. The EGR approach is essentially based on a simple ratio, defined as "the energy-gradient ratio (K_S)" which can be explained as "the ratio of uniform pipe slope (S_0) to the friction slope (S_f) [or the energy-gradient line (EGL) slope] $(K_S = S_0/S_f)$".

The design method, based on the EGR approach, was first presented by Gillespie et al. (1979), Wu and Gitlin (1979), and Wu et al. (1983), considering a single inlet submain line on uniform slopes. Gillespie et al. (1979) derived mathematical equations for pressure profiles resulting from the various possible combinations of friction drop and uniform slope situations. However, in their analysis a direct solution of most of the derived equations for determining the type of pressure profile is difficult. To simplify the implicit nature of their formulation, Barragan and Wu (2005) developed simple nomographs based on a trial-and-error procedure in which pipe (S_0) and friction (S_f) slopes can be estimated for different combinations of pipe diameter (D), total line length (L), and total inlet discharge (Q).

The most important difficulty, when recognizing the type of pressure profile, is the determination of energy-grade line slope (or friction slope) (S_f) which depends on the total inlet discharge (Q) and pipe diameter (D), since Q and D are unknown parameters in most design cases (Yitayew and Warrick 1988; Hathoot et al. 1993). Through the following analysis (Yıldırım and Singh 2013a), an improved EGR approach, based on the recent analytical development (Yıldırım 2006, 2007), encompassing different types of pressure head profiles (***Type-I***, ***Type-II.a***, ***Type-II.b***, ***Type-II.c*** and ***Type-III***) concerning different uniform line slope situations, is presented. In the companion paper (Yıldırım and Singh 2013b), several design examples covering various uniform line slope situations regarding different types of pressure profiles will be presented.

DETERMINATION OF ENERGY-GRADIENT LINE

The energy-gradient line (EGL) in a multi-outlet submain line will not be a straight line but a curve of the exponential type. Fig. 1 sketches a horizontal multi-outlet submain line with a single inlet (single line size system) and shapes of hydraulic (piezometric) (HGL) and energy-gradient (EGL) curves along its length (Yıldırım 2007).

Flow in a submain line is considered to be steady, spatially varied flow with decreasing discharge along the direction of flow (from upstream

inlet to dowmnstream closed end). Flow in a submain line is usually turbulent ($3{,}000 < R < 10^5$; R: Reynolds number). Sometimes fully turbulent flow ($10^5 < R < 10^7$) exists at the upstream end, and flow becomes laminar ($R < 2{,}000$) at the downstream reach where the flow velocity decreases to zero. The transition flow approximately occurs in the interval $2{,}000 < R \leq 3{,}000$, and the flow characteristics are indeterminate for the transition zone (Miller 1990).

The introduction of the Blasius friction factor [$f = a R^{b}$; a and b = empirically determined coefficients, a = 0.316 and b = -0.25 (von Bernuth and Wilson (1989), a = 0.302 and b = -0.25 (Provenzano et al. 2005); and R = Reynolds number] into the Darcy-Weisbach (DW) formula provides an accurate estimate of frictional losses produced by turbulent flow inside uniform pipes with low wall roughness and when Reynolds number changes within the range $3{,}000 < R < 10^5$ (Watters and Keller 1978; von Bernuth and Wilson1989; von Bernuth 1990; Bagarello et al. 1995). In most of the submain lines with plastic material, the flow regime rarely exceeds these flow conditions.

To determine the total amount of actual energy losses along a submain line, head losses through local singularities at the outlet connections must be additionally taken into account. These minor losses, $H_{s(L)}$, are usually calculated as if the pipe length were increased by the so-called equivalent length, l_e, i.e., a length of the same uniform pipe that would have the same head loss (Juana et al. 2002a). The total energy losses along the submain line, $H_{T(L)}$, includes friction ($h_{f(L)}$) and local ($h_{s(L)}$) head losses can be formulated as (Yıldırım 2006):

$$H_{T(L)} = h_{f(L)} + h_{s(L)} = F_S h_{f(L)} = \overline{F} F_S \left(K \frac{Q_I^{m}}{D^{m+3}} L \right) \tag{1a}$$

where

$$F_S = \left(1 + \frac{l_e}{s} \right) \tag{1b}$$

in which $\overline{F} = 1/(m+1) = 1/2.75$: the friction correction factor [m = flow or velocity exponent; for turbulent flow: m = 1.75 for the Darcy-Weisbach (DW) and m = 1.852 for the Hazen-Williams (HW) equations] taking into account continuous and uniform outflow along the submain line [for the $\overline{F}$ formulation based on uniform and discrete outflow from a finite number of operating outlets, see Eqs. (5a) and (5b) in Yıldırım (2006)]; F_S = the amplification or enlargement factor to be applied to the friction losses in the uniform pipe sections, in order to take into account the effect of local losses [note that for the case of neglecting local head losses, F_S is equal to

one (F_S = 1.0)]; l_e = the equivalent length of a minor singularity (m) (Juana et al. 2002b, 2004); s = the distance between successive outlets along the submain line (m); K = constant [$K = a(4/\pi)^{(2+b)}/2g$]; the value of K is equal to 2.458×10^{-2} for the Blasius formula (von Bernuth 1990), and 2.35×10^{-2} from Bagarello et al. (1995); Q_I = the total inflow rate at the pipe inlet (m³s⁻¹); D and L = the pipe internal diameter and length (m), respectively.

The slope of the energy-gradient line (EGL) or the friction slope, S_f, can be written as (for m = 1.75):

$$S_f = \frac{H_{T(L)}}{L} = 8.9 \times 10^{-3} \times F_S \times \frac{Q_I^{1.3}}{D^{4.3}}$$

(2)

The pressure head change from the pipeline inlet to a given length, *l,* is a linear combination of the pressure head change due to friction and uniform slope along the pipeline. Applying the conservation of energy principle between pipe sections, $l = 0$ ($i = 0$) and $l = L$ ($i = 1$), the pressure head profile along the line, H(l), can be determined in terms of the operating inlet pressure head, H_{0I}, from the recent analytical development (Yıldırım 2006):

$$H(l) = H_{0I} + H_V\left[1-(1-i)^2\right] - F_S h_{f(L)}\left[1-(1-i)^{m_\beta+1}\right] - \dot{p}\,\Delta S$$

(3a)

As an alternative derivation, H(l) in terms of the required pressure head, $\overline{H}$, can be written as (for the relationship between Eq. (3b) and Eq. (3a):

$$H(l) = \overline{H} + H_V\left[1-(1-i)^2\right] + h_{f(L)}\left[F_S[\,1-i)^{m_\beta+1}-1] + \frac{m_\beta+1}{m_\beta+2}\right] - p\Delta S\left(i-\frac{1}{2}\right)$$

(3b)

where

$$m_\beta = \beta \times m, \qquad \beta = 1 - 3.322x\log\left[1 + \frac{H_V}{\overline{H}} + \frac{h_{f(L)}}{\overline{H}}\left[\left(\frac{m+3-0.5^{m+1}}{m+2}\right) - F_S\right] + \frac{1}{4\overline{H}}(p\Delta S)\right]$$

(4)

where H(l) = the pressure head at a given section of length l from the pipeline inlet (m); $\overline{H}$ = the required average pressure head for the entire pipeline (m); $i = l/L$: the dimensionless distance as the ratio of length (l) from inlet to the total length (L); H_{VI} = the velocity head at the pipeline inlet (m); β = the nonuniform outflow exponent (Yıldırım 2006); m_β = the improved value of velocity exponent m from Eq. (4); $\Delta S = S_0 \times L$ = the total head loss or gain due to the change in elevation at the closed end of pipeline (m); and S_0 = the line slope assuming to be uniform along the pipeline (m/m). In this procedure, the slope of a downhill pipeline is negative (p = -1), and the slope of an uphill pipeline is positive (p =1).

For determining the energy profile, H(l), Eq. (3b) has a greater

practical importance than Eq. (3a), since Eq. (3a) requires computation of the operating inlet pressure head (H_{0I}) in advance; whereas, Eq. (3b) can be directly used for the required average pressure head, $\overline{H}$, which is initially a known parameter in most usual design cases. In the proposed procedure, the pressure head distribution, H(l), can be determined in terms of H_{0I} or $\overline{H}$ from Eq. (3a) or Eq. (3b), regarding two successive stages. In the first one, EGL can be evaluated from Eq. (3a) or Eq. (3b), assuming that the uniform outflow occurs along the line (m_β =m; β = 1.0); then in the second improved stage, EGL can be exactly determined, based on the nonuniform outflow distribution, by introducing the improved value of the velocity exponent (m_β = m × β, $\beta \neq 1.0$) [Eq. (4)] into Eq. (3a) or Eq. (3b). It should be noted that in most usual design cases, the first initial approximation is sufficiently accurate with a little deviation; however, if a greater precision is required the second improved stage can then be implemented. For simplification of the derived procedure, the localized head loss along the pipe is regarded ($F_S \neq$ 1.0), whereas the change in kinetic head is neglected ($H_V \cong 0$).

TYPES OF PRESSURE HEAD PROFILES FOR UNIFORM LINE SLOPES

When a submain line with multiple outlets is designed using a single inlet system and laid on a uniform slope (S_0), the pressure head profile along the line resulting from the total energy drop by friction, $h_{f(L)}$ [$h_{f(L)} = S_f \times L$; S_f: the slope of energy-gradient line or friction slope] and the total potential energy gain (or loss) due to uniform downslope (or upslope) at the end of the line, ΔS ($\Delta S = S_0 \times L$), can be classified into three general types (Type- I, Type-II and Type-III). The classification can be based on a dimensionless energy gradient ratio, K_S ($K_S = S_0/S_f$).

When the kinetic energy is considered to be small and neglected in a submain line, the shape of profile (pressure variation) will be simply a linear combination of the operating inlet pressure head (H_{0I}), total energy drop due to friction, and total potential energy change (gain or loss) due to uniform line slope, as suggested by Wu and Gitlin (1973,1974), Howell and Hiler (1974), and Gillespie et al. (1979).

A comprehensive description of the energy relations for all types of pressure profiles is synthesized in Table 1, and is also shown in Figs. 2 and 3. From this table, the effect of the dimensionless energy-gradient ratio, K_S = S_0/S_f, on the maximum and minimum pressure values with their positions, can be clearly analyzed. There are five typical pressure head profiles (Type-I, Type-II.a, Type-II.b, Type-II.c and Type-III) under three general types as shown in this figure, and can be expressed (Gillespie et al. 1979, Wu et al. 1983, Barragan and Wu 2005) in what follows:

I. Pressure Profile Type I (Minimum Pressure at the Downstream Closed End:

As shown in Fig. 2(a), the pressure head decreases with respect to the submain length. This type occurs when the submain line is laid on zero or uphill slopes. In this condition, the dimensionless energy-gradient ratio is $K_S = S_0 / S_f \leq 0$. The total energy is lost by both elevation change due to uniform upslope and by friction.

The maximum pressure head, H_{max}, is at the inlet of line and is equal to the operating inlet pressure, H_{0I} ($H_{0I} = H_{max}$); the minimum pressure head, H_{min}, is at the closed end of line, and is equal to the downstream pressure head ($H_d = H_{min}$).

II. Pressure Profile Type II (Minimum Pressure along the Line):

As shown in Fig. 2(b), (c) and 3(d), the pressure head decreases from the upstream end with respect to the pipeline length, reaches a minimum point (i_{min}), and then increases with respect to the submain line. The minimum pressure head is located somewhere along the line ($0 < i_{min} = l_{min}/L < 1$), depending on the large interval of K_S, $0 < K_S = S_0/S_f < 2.75$.

a) Profile II-a: This type of pressure profile (Fig. 2b) occurs under the friction and slope situation, where $0 < K_S = S_0/S_f < 1.0$. In this type, the total energy gain due to uniform downslope at the end of line is smaller than the total energy drop due to friction; so the downstream end pressure head (H_d) is still less than the operating inlet pressure (H_{0I}). The maximum pressure head is at the inlet ($H_{max} = H_{0I}$); and the minimum pressure head is located somewhere along the line.*b) Profile II-b (Optimal Pressure Profile):* This is under the friction slope situation where the dimensionless energy-gradient ratio is $K_S = S_0/S_f = 1.0$. As shown in Fig. 2(c), this profile is similar to Profile II-a, but the profile is such that the downstream closed end pressure head is equal to the operating inlet pressure head ($H_{0I} = H_d$). The maximum pressure is at the inlet ($H_{max} = H_{0I}$) as well as at the closed end of line ($H_{max} = H_d$). The minimum pressure is located somewhere near the middle section of the line.

c) Profile II-c: This is under the friction and slope situation where the dimensionless energy-gradient ratio is $1.0 < K_S < 2.75$ for the Darcy-Weisbach (DW) or $1.0 < K_S < 2.852$ for the Hazen-Williams (HW) equation. This occurs when the line slope is even steeper, so the pressure at the end of line is higher than the operating inlet pressure (Fig. 3.d). In this condition, the maximum pressure is at the downstream closed end of line ($H_{max} = H_d$), and the minimum pressure is located somewhere along the upstream segment of line.

III. Pressure Profile Type III (Minimum Pressure at the Upstream Inlet of Line):

This occurs when the submain line is on a steep downslope where the total energy gain by the uniform downslope is larger than the total energy drop due to friction for all sections along the line. As shown in Fig. 3(e), the pressure head increases with respect to the line length. This is caused by a steep downslope situation where the dimensionless energy-gradient ratio is $K_S \geq 2.75$ for the DW equation, or $K_S \geq 2.852$ for the HW equation. In this condition the maximum pressure is at the downstream closed end of line (($H_{max} = H_d$), and the minimum pressure head is at the pipe inlet and equal to the operating pressure head ($H_{min} = H_{0I}$).

Fig. 1. Shapes of hydraulic (piezometric) gradient line (HGL), and energy-gradient line (EGL) along horizontal submain line with multiple outlets (Yıldırım 2007).

$H_{gf} = H_{max}$

$\overline{H}$

$H_d = H_{min}$

$K_S - S_0 / S_f \leq 0$

$H_{gf} = H_{max} > \overline{H} > H_d = H_{min}$

0

1

(a): Type I (Horizontal or Upslope)

$H_{gf} = H_{max}$

$\overline{H}$

H_{min}

H_d

$0 < K_S = S_0/S_f < 1.0$

$H_{gf} = H_{max} > \overline{H} > H_d > H_{min}$

0

1

(b): Type II-a (Gentle Downslope)

$H_{gf} = H_{max}$

$H_d = H_{max}$

$\overline{H}$

H_{min}

$K_S = S_0/S_f = 1.0$

$H_{gf} = H_d = H_{max} > \overline{H} > H_{min}$

0

1

Dimensionless Distance ($i = l/L$)

Fig. 2. Pressure Head Profiles for (a): Type I, (b): Type II.a and (c): Type II.b
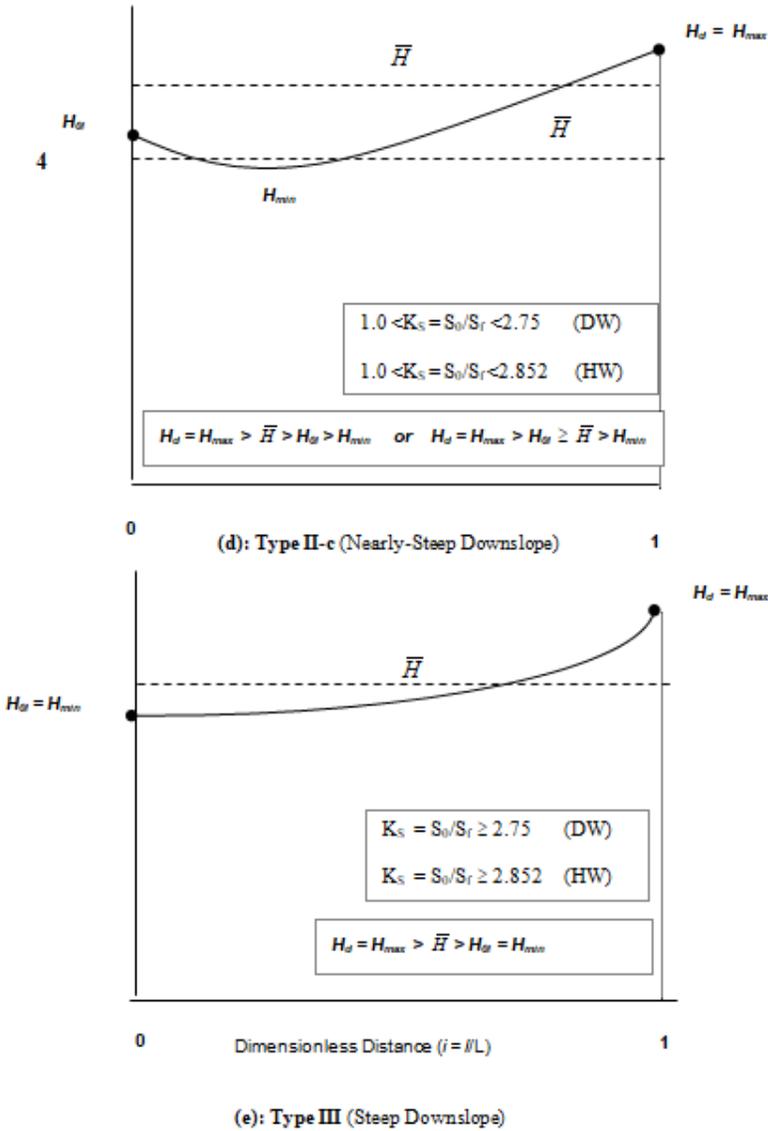
Fig. 3. Pressure Head Profiles in Downslope Situation for (d):Type II.c and (e): Type III

Among all types of pressure profiles, the Type-II profile is considered as the optimal (or ideal) pressure profile which can produce the minimum pressure head difference for a given pipe length as discussed earlier (Wu and Gitlin 1980; Wu et al. 1983). This profile occurs when the total energy loss due to friction is just balanced by the total energy gain due to uniform downslope (Profile II-b) as shown in Fig. 2(b).

PERCENTAGE OF AVERAGE PRESSURE HEAD (δ_H)

and RELATIVE PRESSURE VARIATION (ϕ_H)

The hydraulic design procedure for a submain line with multiple outlets usually establishes that the maximum difference in extreme outlet operating pressure heads along the pipeline is equal to the maximum allowable difference, ΔH_{max}. The uniformity criterion applied for the design of multiple outlet pipelines is that the maximum allowable difference in the outlet operating pressure head along the pipeline, ΔH_{max}, is less than a percentage of the average pressure head, δ_H:

$$\delta_H = \frac{\Delta H_{max}}{\overline{H}} = \frac{(H_{max} - H_{min})}{\overline{H}} \qquad (5)$$

where δ_H = the percentage of the maximum allowable difference in the outlet operating pressure heads to the average outlet pressure head (m/m); ΔH_{max} = the maximum allowable difference in the outlet operating pressure head along the pipeline (m); and H_{max} - H_{min} = the maximum difference in the extreme outlet operating pressure head along the pipeline (m). The usual criterion applied for the design of laterals is that the difference in outlet discharge along a single lateral is less than ± 10%. This corresponds to a maximum difference in the outlet operating pressure head of ± 20% (Cuenca 1989).

Another useful design criterion is defined as the relative maximum pressure variation, ϕ_H, which is the ratio of the maximum allowable pressure head difference to the total head loss due to friction, and is given by the following expression (Barragan and Wu 2005):

$$\phi_H = \frac{\Delta H_{max}}{h_{f(L)}} = \delta_H \times \frac{\overline{H}}{h_{f(L)}} \qquad (6)$$

ϕ_H is an important indicator to practically determine the shape of pressure profile and evaluate the minimum pressure variation along the profile for different slope situations.
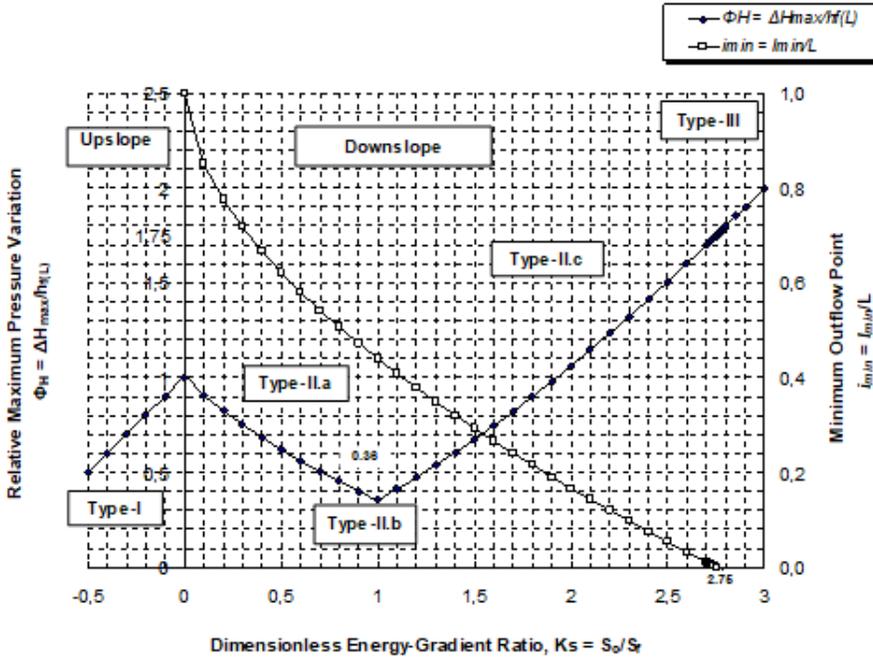
Fig. 4. Variation of Relative Maximum Pressure Variation [ΦH = ΔHmax/hf] and Minimum Outflow Point (imin = lmin/L) Versus Dimensionless Energy-Gradient Ratio, KS = S0/Sf , for Three Types of Pressure Profiles.

In the following section, the extreme pressure heads (H_{max}, H_{min}) will be deduced for all types of pressure profiles to determine the maximum allowable difference in the outlet operating pressure, ΔH_{max}, the percentage of maximum allowable difference (δ_H), and the relative maximum pressure variation, ϕ_H. Table 1 presents a systematic comparison between the relationships for the average and extreme pressures with their locations along the line, and for the relative maximum pressure variation, ϕ_H, with the design case of considering ($F_S \neq 1$), and neglecting ($F_S = 1$) local head losses, for all types of pressure profiles in different slope situations, as discussed in the following section.

COMPARATIVE ANALYSIS OF PRESSURE HEAD PROFILES

Based on the procedure derived above for the design criterion, ϕ_H, a systematic comparison between different types of pressure profiles for different slope patterns will be presented in this section. Note that for simplification, $F_S = 1$ is considered in the related expressions for ϕ_H. For this purpose, the relative maximum pressure variation [$\phi_H = \Delta H_{max} / h_{f(L)}$] [on the

premier axis of y], and the minimum outflow (pressure head) point (i_{min} = l_{min}/L) [on the secondary axis of y] versus the dimensionless energy-gradient ratio ($K_S = S_0/S_f$) [on the x axis] were computed, as shown in Fig. 4.

In the present figure, there are different segments concerning five types of pressure profiles (**Type I, Type II.a, II.b, II.c** and **Type III**), concerning the related intervals of energy-gradient ratio, K_S. Each portion of this curve is individually determined based on the relationships for ϕ_H, derived for each type of pressure profile. As shown in Figure 4, the shape of ϕ_H distribution is linear through the zero/upslope zone ($K_S \leq 0$), whereas it has a curve form through the downslope zone [0<K_S<1, 1<K_S <2.75 and $K_S \geq 2.75$ (for DW)]. This figure also illustrates the minimum outflow point (i_{min}) profile which starts decreasing from the downstream closed end (i_{min} = 1) to the upstream inlet (i_{min} = 0) as the K_S value increases from 0 ($K_S = 0$: **Type I**) to 2.75 ($K_S \geq 2.75$: **Type III**).

In the upslope zone (Type I: K_S <0, i_{min} = 1), the ϕ_H distribution linearly increases and yields values smaller than 1, which means the minimum pressure is at the downstream closed end, and the maximum pressure difference is smaller than the total friction drop [ϕ_H <1; ΔH_{max} <$h_{f(L)}$]. ϕ_H is finally equal to 1 [ϕ_H =1 ; $\Delta H_{max} = h_{f(L)}$], for the value of K_S = 0 (Type I, i_{min} = 1), which means the minimum pressure occurs at the downstream closed end, and the total friction drop is just balanced by the maximum pressure head difference [$\Delta H_{max} = h_{f(L)}$].

In the first portion of the downslope zone (Type II.a: 0<K_S<1), the ϕ_H curve yields smaller values than 1 (0.36< ϕ_H < 1), then reaches a minimum value ($\phi_{H min}$ = 0.36) for K_S = 1 (Type II.b). For this interval (0<K_S<1), i_{min} occurs near the pipe downstream section, 0.44<i_{min}<1, and finally reaches a critical value of 0.44, for **Type II.b** profile (for K_S = 1, i_{min} = 0.44, $\phi_{H min}$ = 0.36). In the second portion of downslope zone (Type II.c: 1<K_S <2.75), the ϕ_H profile increases again for the interval, 0.36< ϕ_H <1.75, with increasing values of K_S; and the i_{min} profile occurs near the upstream section for the interval, 0<i_{min}<0.44.

As a remarkable result from Fig. 4, ϕ_H is equal to 1 (ϕ_H =1) which means that the maximum pressure head difference is just balanced by the total friction drop ($\Delta H_{max} = h_{f(L)}$), for two different values of K_S. The first one is the Type I profile in which when K_S = 0, ϕ_H =1, i_{min} = 1; and the second one is the Type II.c profile in which when $K_{S \cong}$ 1.9, ϕ_H =1, and $i_{min} \cong 0.2$.

This practical consideration may give an idea to the design engineer when selecting the best alternative among these two slope conditions for the submain line design.

In the third portion of downslope zone (Type III: $K_S \geq 2.3$), the ϕ_H profile linearly increases with increasing values of K_S, for the interval $\phi_H \geq 1.3$; and i_{min} just occurs at the upstream inlet point ($i_{min} = 0$), which means the operating inlet pressure is equal to the minimum pressure, and the maximum pressure head difference is much higher than the total friction drop ($\Delta H_{max} \geq 1.3 \times h_{f(L)}$), for the steep downslope case (Type III).

EVALUATION FOR IDEAL (THE BEST EFFICIENT) HYDRAULIC DESIGN

An ideal hydraulic design is to obtain the minimum pressure variation, or a range of pressure variation as close to the minimum point as possible, for a given total friction drop (Barragan and Wu 2005). As illustrated in Fig. 4, among of all five types of pressure profiles, the one (***Type II.b***), which can produce the minimum pressure variation ($\phi_{H\,min} = 0.36$), occurs when the energy-gradient ratio is equal to 1 ($K_S = 1$), and $i_{min} = 0.44$ ($l_{min} = 0.4 \times L$).

In this ideal design case, the ratio of the maximum pressure head difference, ΔH_{max} to the total friction drop, $h_{f(L)}$ is a minimum point which is defined as "*the most efficient pressure profile*", or "*ideal hydraulic design*", however, it may not be feasible because of the restraints in the field. such as slope and layout of the submain unit (Barragan and Wu 2005).

The present ϕ_H curve versus K_S values (Fig. 4) allows the design engineer to make a decision for the best alternative for selecting the K_S value, in which for a given pipe slope (S_0) the K_S value can be selected to meet the minimum pressure variation [$K_S = 1$, (ϕ_H)$_{min} = 0.36$], or the range of pressure variation as close to the minimum point (near $K_S =1$) as possible, then finally the friction slope S_f can be determined, depending on the K_S value, assigned in advance.

CONCLUDING REMARKS

In the present paper, a comprehensive hydraulic analysis for different types of pressure head profiles is carried out, based on the improved energy-gradient ratio (EGR) approach. Practically, five typical pressure head profiles are observed along the submain line for various line slope combinations. When a submain line is designed for a uniform slope, the dimensionless "energy-gradient ratio ($K_S =S_0/S_f$)" can be efficiently used to identify the

type of pressure profile with the corresponding hydraulic characteristics, and determine the proper values of the main pressure parameters through the energy-gradient line.

Considering a single inlet in a submain line on a uniform slope, pressure profiles resulting from the various combinations of friction drop and slope situations are derived. For a given uniform pipe slope, first the type of pressure head profile is primarily assigned, based on the EGR approach; then certain values of the main pressure parameters along the energy-gradient line [operating inlet pressure (H_{0l}), downstream end pressure (H_d), extreme pressures (H_{max}, H_{min}) with their specific positions along the line (i_{max}, i_{min}), total friction drop ($h_{f(L)}$), maximum pressure head difference (ΔH_{max}) and pressure variation (ϕ_H)] are also evaluated. Hence, the operating inlet pressure head is reformulated by incorporating different uniformity patterns, by setting a multiplification factor, α, for the required average outlet pressure head, and β^* for the potential energy head change due to uniform line slope. The procedure is simplified by regarding the localized head loss along the pipe but neglecting the change in kinetic head.

The proposed procedure offers flexibility by directly computing values of the required hydraulic variables along the energy profile incorporating different uniformity patterns and without needing any additional hydraulic variables (pipe diameter, total inlet discharge, required average outflow, downstream end pressure head, total friction drop or outlet characteristics). The procedure performs better than the conventional procedures, and can be efficiently used for different types of pressure profiles in different line slope situations.

Further investigation on the current hydraulic analysis will be presented in a companion book chapter encompassing various design applications, comparative analysis and verification.

Based on the present analysis, the following conclusions can be drawn:

1. Among all types of pressure profiles, there is an "*ideal hydraulic design*" for downslope situation at which the dimensionless energy-gradient ratio is equal to 1 ($K_S = S_0/S_f = 1$), in which the ratio of maximum pressure difference to the total friction drop is a minimum [$(\phi_H)_{min} = \Delta H_{max}/h_{f(L)} = 0.5$], as shown in Fig. 4 (*Type II.b* profile). The present ϕ_H curve versus K_S values (Fig. 4) permits the design engineer to make a decision for the best alternative for selecting the K_S value, in that for a given pipe slope (S_0) the K_S value can be selected to meet the minimum pressure variation, or the range of pressure variation as close to the minimum point (near $K_S = 1$) as possible. Finally, the friction slope S_f can be determined, depending on the K_S value assigned in advance. For *Type-II.b* profile, the minimum outflow

(or pressure head) occurs in the upstream pipe section, $i_{min} = 0.44$ ($l_{min} = 0.44 \times L$).

2. As a remarkable result from Fig. 4, ϕ_H is equal to 1 ($\phi_H = 1$) which means that the maximum pressure head difference is just balanced by the total friction drop ($\Delta H_{max} = h_{f(L)}$), for two different values of K_S. The first one is the ***Type I*** profile in which when $K_S = 0$, $\phi_H = 1$, $i_{min} = 1$; and the second one is the ***Type II.c*** profile in which when $K_S \cong 1.9$, $\phi_H = 1$, and $i_{min} \cong 0.2$. This practical consideration may give an idea to the design engineer to select the best alternative among these two slope conditions for submain line design. For ***Type II.b*** profile, the maximum, minimum and average pressure heads can be functionally expressed by simple relationships, in which when one of the extreme pressures or the average pressure head is required for design, the unknown pressure head can be directly determined, depending on the remaining two pressure heads initially known.

REFERENCES

Anyoji, H. and Wu, I.P. (1987). "Statistical approach for drip lateral design" Transactions of the ASAE, 31(1): 187-232.

Barragan, J. and Wu, I.P. (2005). "Simple pressure parameters for micro-irrigation design" Biosystem Eng. 90(4): 463-475.

Bralts, V. F., Wu, I. P., and Gitlin, H. M. (1981). "Manufacturing variation and drip irrigation uniformity." *Trans. ASAE,* 24(1), 1234-1240.

Bralts, V. F., Edwards, D. M., and Wu, I. P. (1987). "Drip irrigation design and evaluation based on the statistical uniformity concept." *Advances in irrigation*, Vol. 4. Academic, New York, 67-117.

Gillespie, V.A., Phillips, A.L.. and Wu, I.P. (1979). "Drip irrigation design equations. J. Irrig. Drain Division, ASCE, 105(IR3): 247-257.

Hathoot, H. M., Al-Amoud, A. I., and Mohammad, F. S. (1993). "Analysis and design of trickle irrigation laterals." *J. Irrig. and Drain. Eng.,* 119(5), 756-767.

Howell, T.A., Hiler, E.A. (1974). "Trickle irrigation lateral design. Transactions of the ASAE, 17(5), 902-908.

Juana, L., Losada, A.., Rodriguez-Sinobas L., Sanchez, R. (2004). "Analytical relationships for designing rectangular drip irrigation units" J. Irrig. and Drain. Eng., ASCE, 130(1): 47-59.

Kang, Y., and Nishiyama, S. (1996). "Analysis and design of microirrigation laterals." *J. Irrig. and Drain. Eng.,* 122(2), 75-82.

Kang, Y. (2000). "Effect of operating pressures on microirrigation uniformity." *Irrig. Sci*. 20: 23-27.

Keller, J., and Karmelli, D. (1974). "Trickle irrigation design parameters." *Trans. ASAE*, 17(4), 678-684.

Keller, J., and Bliesner, r. D. (1990). *Sprinkler and trickle irrigation*, Van Nostrand Reinhold, New York.

Mahar, P. S., and Singh, R. P. (2003). "Computing inlet pressure head of multioutlet pipeline." *J. Irrig. and Drain. Eng.,* 129(6), 464-467.

Ravikumar, V., Ranganathan, C. R., and Santhana Bosu, S. (2003). "Analytical equation for variation of discharge in drip irrigation laterals." *J. Irrig. and Drain. Eng.,* 129(4), 295-298.

von Bernuth, R. D. (1990). "Simple and accurate friction loss equation for plastic pipe." *J. Irrig. and Drain. Eng.,* 116(2), 294-298.

von Bernuth, R. D., and Wilson, T. (1989). "Friction factors for small diameter plastic pipes." *J. Hydraulic Eng.,* 115(2), 183-192.

Wu, I.P. Sarawatari, C.A. and Gitlin, H.M. (1983). "Design of drip irrigation lateral length on uniform slopes" Irrig. Science, 4, 117-135.

Wu, I. P. (1992). "Energy gradient line approach for direct hydraulic calculation in drip irrigation design." *Irrig. Sci.,* 13, 21-29.

Wu, I. P. (1997). "An assessment of hydraulic design of micro-irrigation systems." *Agric. Water Manage.,* 32, 275-284.

Wu, I.P. and Barragan, J. (2000). "Design criteria for microirrigation systems" Transactions of the ASAE, 43(5),B1145-1154.

Yıldırım, G., and Ağıralioğlu, N. (2004). "Comparative analysis of hydraulic calculation methods in design of micro-irrigation laterals." *J. Irrig. and Drain. Eng.,* 130(3), 201-217.

Yıldırım, G., and Ağıralioğlu, N. (2004a). "Linear solution for hydraulic analysis of tapered microirrigation laterals", *J. Irrig. and Drain. Eng.,* 130(1), 78-87.

Yıldırım, G. (2006). "Hydraulic analysis and direct design of multiple outlets pipelines laid on flat and sloping lands*." J. Irrig. Drain .Engrg., ASCE*, 132(6), 537-552.

Yıldırım, G. (2007a). "An Assessment of Hydraulic Design of Trickle Laterals Considering Effect of Minor Losses." *Irrig. and Drain. (ICID Journal)* 56(4), 399-421.

Yıldırım, G. (2007b). "Analytical Relationships for designing multiple outlets pipelines*." J. Irrig. Drain. Engrg., ASCE*, 133(2), 140-154.

Yıldırım, G. (2008a). "Determining inlet pressure head incorporating uniformity parameters for multioutlet plastic pipelines." *J. Irrig. Drain .Engrg., ASCE*, 134(3), 341-348.

Yıldırım, G. (2009b). "Simplified procedure for hydraulic design of small-diameter plastic pipes." *Irrig. Drain. (ICID J.)* 58(3):209-233.

Yıldırım, G. (2009c). "Total energy loss assessment for trickle lateral lines equipped with integrated in-line and on-line emitters" *Irrig. Science,* 28(4): 341-352.

Yıldırım, G. and Singh, V.P. (2013a). "Operating Pressure Assessment for Multi-outlets Submains: Ideal Hydraulic Design" 6th Congress on "International Perspective on Water Research and Environment" by ASCE & EWRI, İzmir, Turkey.

Yıldırım, G. and Singh, V.P. (2013b). "Operating Pressure Assessment for Multi-outlets Submains: Design Applications" 6th Congress on "International Perspective on Water Research and Environment" by ASCE & EWRI, İzmir, Turkey.

Yitayew, M., and Warrick, A. W. (1988). "Trickle lateral hydraulics. *II*: design and examples." *J. Irrig. and Drain. Eng.,* 114(2), 289-300.

Table 1. Relationships and Design Intervals for Pressure Parameters for Different Types of Pressure Profiles Concerning Various Line Slope Situations

Slope Definition	Type of Pressure Profile	Relationships for Average ($\bar{H}$) and Extreme Pressure Heads (H_{0L}, H_d, H_{max}, H_{min})	Extreme Outflow Points (i_{max}, i_{min}) (also see Table 3)	Energy Gradient Ratio $K_S = S_0/S_f$	Relationships for Relative Maximum Pressure Variation (Φ_H): $\Phi_H = \Delta H^{max}/h_{f(L)}$	
					Considering Local Losses [$F_S = 1.0$]	Neglecting Local Losses [$F_S = 1.0$]
Horizontal & Uphill	Type-I	$H_{0L} - H_{max} > \bar{H} > H_d - H_{min}$	$i_{max} = 0$ (inlet), $i_{min} = 1$ (downstream end)	$K_S \leq 0$ [$S_0 = 0$ and $S_0 > 0$, $S_f < 0$]	$K_S + F_S$ (HW, DW)	$K_S + 1.0$ (HW, DW)
Downhill (Gentle)	Type-II.a	$H_{0L} - H_{max} > \bar{H} > H_d > H_{min}$	$i_{max} = 0$ (inlet), $0.44 < i_{min} < 1$ (downstream segment)	$0 < K_S < 1$ [$S_0 < 0$, $S_0 < S_f$, $S_f < 0$]	$(F_S - K_S) + 0.357 \times F_S^{-0.57} K_S^{1.57}$ (HW), $(F_S - K_S) + 0.368 \times F_S^{-0.54} K_S^{1.54}$ (DW)	$(1.0 - K_S) + 0.357 \times K_S^{1.57}$ (HW), $(1.0 - K_S) + 0.368 \times K_S^{1.54}$ (DW)
Downhill (Efficient)	Type-II.b	$H_{0L} - H_d - H_{max} > \bar{H} > H_{min}$	$i_{max} = 0$ (inlet) and/or $i_{max} = 1$ (downstream end); $i_{min} \cong 0.44$ (HW), $i_{min} \cong 0.43$ (DW)	$K_S = 1.0$ [$S_0 < 0$, $S_0 = S_f$, $S_f < 0$]	$0.357 \times F_S^{-0.57}$ (DW), $0.368 \times F_S^{-0.54}$ (HW)	$0.357 \cong 0.36$ (DW), $0.368 \cong 0.37$ (HW)
Downhill (Nearly-Steep)	Type-II.c	$H_d - H_{max} > \bar{H} > H_{0L} > H_{min}$ and/or $H_d - H_{max} > H_{0L} > \bar{H} > H_{min}$	$i_{max} = 1$ (inlet), $0 < i_{min} < 0.44$ (upstream segment)	$1 < K_S < 2.75$ (DW) [$S_f < S_0 < 2.75 S_f$], $1 < K_S < 2.852$ (HW) [$S_f < S_0 < 2.852 S_f$]	$0.357 \times F_S^{-0.57} K_S^{1.57}$ (DW), $0.368 \times F_S^{-0.54} K_S^{1.54}$ (HW)	$0.357 \times K_S^{1.57}$ (DW), $0.368 \times K_S^{1.54}$ (HW)
Downhill (Steep)	Type-III	$H_d - H_{max} > \bar{H} > H_{0L} - H_{min}$	$i_{max} = 1$ (downstream end), $i_{min} = 0$ (inlet)	$K_S \geq 2.75$ (DW) [$S_0 \geq 2.75 S_f$], $K_S \geq 2.852$ (HW) [$S_0 \geq 2.852 S_f$]	$K_S - F_S$	$K_S - 1.0$ (HW, DW)

Note: HW: Hazen-Williams Equation and DW: Darcy-Weisbach Equation; F_S: Amplification factor to be applied to friction losses to take into account the effect of local losses ($F_S = 1 + l_s/l_f$).

NEW ANALYTICAL TECHNIQUE FOR IRRIGATION WATER DISTRIBUTION NETWORK HYDRAULICS-II: DESIGN APPLICATIONS[1]

Gürol YILDIRIM[2]

INTRODUCTION

This paper presents various design applications for multi-outlets submains based on an Energy-Gradient Ratio (EGR) approach presented in the companion paper (Yıldırım and Singh 2013a), mainly focusing on identifying the types of energy profiles for a given design slope and determining the required hydraulic variables through the energy-grade line. In this procedure, for a given pipe slope (S_0), the type of a pressure head profile is assigned, first; then proper values of the required hydraulic variables for energy profiles-the operating inlet pressure head (H_{0I}), downstream closed end pressure head (H_d), extreme pressure heads (H_{max}, H_{min}) with their positions along the line (i_{max}, i_{min}), and the total energy drop due to friction $h_{f(L)}$-are determined, ensuring the desired water application uniformity as well as the maximum allowable pressure head variation (ΔH_{max}). Hence, the operating inlet pressure head is reformulated by incorporating different uniformity patterns, and setting a multiplification factor, α, and the required average outlet pressure head, and β^*, for the change in potential energy head due to the uniform line slope. The procedure is simplified by regarding the localized head loss along the pipe but neglecting the change in kinetic head. The proposed procedure is simple, direct, and sufficiently accurate for a wide range of water application uniformity, and can be efficiently used for different types of pressure profiles in different line slope situations, without requiring any additional hydraulic variables (pipe diameter, total inlet discharge, required average outflow, downstream end pressure head, total friction drop or outlet characteristics). Analysis of results shows that the proposed procedure performs sufficiently accurately in comparison with the computer-aided step-by-step procedure.

Analysis of the hydraulic design of multi-outlet submain lines is important for the proper performance of water supply systems. Design engineers are often faced with three types of problems in most design cases. In the first problem type (energy profile determination), for the given design values of S_0 and $\overline{H}$, the required hydraulic variables concerning the pressure head profile [the operating inlet pressure head (H_{0I}), downstream closed end pressure head (H_d), extreme pressure heads (H_{max} and H_{min}) with their locations along the line (i_{max}, i_{min}; i: percentage of length, l is a length from the inlet in m, and L is the total length of the submain line in m), and the total energy drop due to friction $h_{f(L)}$], can be determined ensuring the desired level of water application uniformity as well as the allowable pressure head variation along the line (Yıldırım 2007).

In the second problem type (water application uniformity evaluation), when H_{0I} is given as an input parameter together with the required average outlet pressure head ($\overline{H}$) and for a given design slope (S_0), the proper

values of required uniformity parameters (U_C, D_U, CV_q, E_U) can be directly approximated (Yıldırım 2008). In the third problem type (direct sizing procedure), the required parameters are the pipe diameter (D) or length (L) for a given design slope (S_0), the desired level of water application uniformity, and the required average outlet pressure head ($\overline{H}$), with the remaining variables as design variables (Yıldırım 2006).

In this classification of the design problems, determination of the actual pressure head (or outflow) profile along the line is greatest important concern for hydraulic design. The energy-gradient line (EGL) method is traditionally used for the determination of lateral pressure head and outflow profiles (Wu and Gitlin 1973, 1974, 1975). Application of the analytical EGL or Revised Energy-Grade Line (REGL) (Wu 1992, 1997, Wu and Yue 1993) method is very easy; however, it has a limitation of the application region due to the constraints in the outlet flow regime and outflow variation along the line. Recently, an improved EGL method has been presented (Yıldırım 2006, 2007) to solve hydraulic design problems of various types of multi-outlet submain lines in different flow regimes and uniform line slope cases.

In the analytical development, the improved energy-grade line is determined based on the average friction drop approach with a simple exponential function, to express the nonuniform outflow concept. The solution technique of this analytical procedure is simple and direct, and sufficiently accurate in comparison with the numerical stepwise procedures.

The operating inlet pressure head, H_{0I}, is a main hydraulic component for the proper design and evaluation of pressure head distribution along the line. This head can be achieved in a stepwise manner, either starting from the required pressure head at the downstream closed end, H_d, working back to the inlet upstream direction, by computing the friction head loss in each pipe segment between successive outlets (BSP: backward-step procedure) (Kang and Nishiyama 1996; Kang 2000); or starting from the inlet pressure head, H_{0I}, computing forward in the downstream direction (FSP: forward-step procedure) (Hathoot et al. 1993).

In this procedure, H_{0I} is determined by adding a reasonable head increment to the required average outlet pressure head, ensuring initial and boundary conditions to be based on the design algorithm discussed by Yıldırım and Ağıralioğlu (2004) and Yıldırım (2008).

In order to avoid the stepwise computer-aided design procedures (Kang and Nishiyama 1996; Kang 2000; Hathoot et al. 1993), Keller and Karmeli (1974) and Keller and Bliesner (1990) presented a graphical relationship among the required average outlet pressure head, pipe friction loss, and operating inlet pressure head for a sample design example, This procedure is efficient for the design of a multioutlet submain line with single-diameter

and two-diameter, as well as multidiameter pipelines.

In conventional design procedures (Keller and Karmeli 1974; Perold 1977; Keller and Bliesner 1990; Mahar and Singh 2003), H_{0I} is essentially related to the main hydraulic variables of the energy profile, such as uniform pipe slope; S_0, downstream closed end pressure head, H_d; and/or total friction drop, $h_{f(L)}$, and required average outlet pressure head, $\overline{H}$. However, it may be hard to compute H_{0I}, directly, as $\overline{H}$ and S_0 are known a priori, whereas H_d and/or $h_{f(L)}$ cannot be determined in advance, since the pipe diameter, D, is an additional unknown parameter for the required operating inlet pressure head, H_{0I}, in most usual design cases (Yitayew and Warrick 1988; Hathoot et al. 1993).

To overcome the implicity problem, Yıldırım (2008) proposed an alternative computing technique to directly determine H_{0I} which incorporates different uniformity patterns for water application. In this analysis, first, simple mathematical expressions are deduced to relate uniformity parameters; then H_{0I} is simply reformulated by setting a multiplification factor α for the required average outlet pressure head, and β^* for the potential energy head change due to uniform line slope. This procedure is simple, direct, and sufficiently accurate to determine the required hydraulic variables along the pressure head profile.

However, the applicability of this procedure is only limited for the design case of a Type- I pressure profile for horizontal or uphill slope situation.

The main objective of this chapter is to develop a procedure to solve the first and second types of design problems, based on improved Energy Gradient Ratio (EGR) approach which is an improvement on the previous mathematical development (Yıldırım 2008) utilizing analytical approaches (Yıldırım 2006, 2007) and which covers different types of pressure head profiles (Type-I, Type-II.a, Type-II.b, Type- II.c and Type-III) (Gillespie et al. 1979, Wu et al. 1983, Barragan and Wu 2005) under different uniform line slope situations, while determining values of pressure parameters (H_{0I}, H_d, H_{max}, H_{min}, $h_{f(L)}$, ΔH_{max}).

The proposed procedure incorporates simple mathematical formulations encompassing different uniformity patterns for water application, such as Christiansen's uniformity (U_C), lower-quarter distribution uniformity (D_U), coefficient of variation of outflows (CV_q), emission uniformity (E_U), and fraction of the required average pressure head (δ_H).

The procedure is simplified by regarding the localized head loss along the pipe line but neglecting the change in kinetic head. The proposed methodology is found to be simple, sufficiently accurate, and can be used

efficiently for different types of pressure profiles in different line slope situations. It offers considerable flexibility by directly computing values of the required hydraulic variables along the energy profile, incorporating different uniformity patterns and without requiring any additional hydraulic variables, such as pipe diameter, total inlet discharge, required average outflow, downstream end pressure head, total friction drop or outlet characteristics.

LITERATURE REVIEW

The energy-gradient ratio (EGR) approach is useful to identify first which type of pressure profile occurs for a given uniform design slope with other hydraulic variables initially known, then comprehensively evaluate its definite hydraulic characteristics along the line. Knowing the hydraulic properties for any type of pressure profile regarded enables the design engineer to evaluate pressure parameters through the line sections in a simple way based on the proposed EGR approach. The EGR approach is essentially based on a simple ratio, defined as "the energy-gradient ratio (K_S)" which can be explained as "the ratio of uniform pipe slope (S_0) to the friction slope (S_f) [or energy-gradient line (EGL) slope] ($K_S = S_0/S_f$)".

The design method, based on the EGR approach, was first presented by Gillespie et al. (1979), Wu and Gitlin (1979), and Wu et al. (1983), considering a single inlet submain line on uniform slopes. Gillespie et al. (1979) derived mathematical equations for pressure profiles resulting from the various possible combinations of friction drop and uniform slope situations. However, in their analysis, a direct solution of most of the derived equations for determining the type of pressure profile is difficult.

To simplify the implicit nature of their formulations, Barragan and Wu (2005) developed simple nomographs based on a trial-and-error procedure in which pipe (S_0) and friction (S_f) slopes can be estimated for different combinations of pipe diameter (D), total line length (L) and total inlet discharge (Q).

The most important difficulty when recognizing the type of pressure profile is the determination of energy-grade line slope (or friction slope) (S_f), which depends on the total inlet discharge (Q) and pipe diameter (D), since Q and D are unknown parameters in most design cases (Yitayew and Warrick 1988; Hathoot et al. 1993). Through the following analysis, the implementation of the proposed EGR approach (Yıldırım and Singh 2013a), to cover different types of pressure head profiles (***Type-I***, ***Type-II.a***, ***Type-II.b***, ***Type-II.c*** and ***Type-III***) covering various design applications concerning different uniform line slope situations, will be presented.

RELATIONSHIPS BETWEEN UNIFORMITY PATTERNS
(U_C, CV_q, E_U, D_U) for PRESSURE PROFILES

For a submain line system designed for high uniformity, all uniformity expressions can be related to each other. That means the design criterion made for any single uniformity expression can be converted and used for other uniformity expressions (Barragan et al. 2006). The Christiansen uniformity coefficient (U_C) (Christiansen 1942) which evaluates the mean deviation, and a statistical term, the coefficient of variation of discharge (CV_q), which evaluates the standard deviation, and is statistically defined as the standard deviation of discharge divided by the mean value and expressed in percent (Wu 1997), are the two most commonly used uniformity expressions.

Both U_C and CV_q require a number of selected samples for calculation. Other frequently used uniformity measures are the distribution (or lower-quarter distribution) uniformity (D_U) (Merriam and Keller 1978), and emission uniformity (E_U) (Keller and Karmeli 1974), which express a ratio of minimum and mean discharge (Wu and Barragan 2000).

For normal distribution, U_C, is related to CV_q, as given by the following expression (Yitayew and Warrick 1988):

$$U_C = 1 - 0.798 \times CV_q \qquad (1a)$$

U_C and E_U can also be shown as follows (Keller and Bliesner 1990, Wu and Barragan 2000):

$$U_C = 1 - 0.6 \times (1 - E_U) \qquad (1b)$$

For uniform distribution, U_C is related to D_U as follows (Warrick 1983, Warrick and Yitayew 1988):

$$U_C = 0.3 + 0.6 \times D_U \qquad (1c)$$

For evaluating U_C, the following simple formulations incorporating the uniform pipe slope, S_0 and the friction slope, S_f, can be directly used for all types of pressure profiles (in different slope situations) are:

Type I: Zero/Upslope ($p = 0$ and $p = 1$):

$$U_C \cong 1 - 0.2 \frac{L}{\overline{H}}(S_0 + S_f) \qquad (2a)$$

Types II.a: *(Downslope, p = -1):*

$$U_C \cong 1 - 0.3 \frac{\pounds}{H}(S_f - S_0)$$

(2b)

Type II.b ($K_S = 1$, $S_0 = S_f$)***:*** *(Downslope, p = -1):*

$$U_C \cong 1 - 0.6 \frac{\pounds}{H}S_f = 1 - 0.6 \frac{\pounds}{H}S_0 \qquad (2c)$$

Types II.c and Type III: *(Downslope, p = -1):*

$$U_C \cong 1 - 0.3 \frac{\pounds}{H}(S_0 - S_f) \qquad (2d)$$

INTERRELATIONSHIPS BETWEEN UNIFORMITY PATTERNS

USING DIMENSIONLESS PHYSICAL NUMBERS

In this section, mathematical relationships for each type of pressure profile will be deduced to evaluate the uniformity criteria (U_C, CV_q, E_U, D_U). Before starting the analysis, some dimensionless physical numbers for uniformity patterns are deduced as:

$$\lambda_1 = \frac{(1 - U_C)}{x}, \; \lambda_2 = \frac{CV_q}{x}, \; \lambda_3 = \frac{(1 - E_U)}{x}, \qquad \lambda_4 = \frac{(1 - D_U)}{x}, \; \lambda_5 = \frac{\overline{H}}{L} \qquad (3)$$

Type I Profile $(K_S \leq 0)$***:***

From Eq. (2a), one can obtain the following simple transformation for this type of profile:

$$U_C \cong 1 - 0.3 \frac{\pounds}{H}(S_0 + S_f) = 1 - 0.3 \; x\delta_H \qquad (4)$$

The uniformity parameters (CV_q, E_U and D_U) can be written in terms of the dimensionless physical numbers ($\lambda_1, \lambda_2, \lambda_3, \lambda_4, \lambda_5$) as given by the following expression:

$$\delta_H = k_1 \times \lambda_1 = k_2 \times \lambda_2 = k_3 \times \lambda_3 = k_4 \times \lambda_4 \qquad (5)$$

where k_1, k_2, k_3, k_4 = design coefficients and are: $k_1 = 4.357$, $k_2 = 3.477$, $k_3 = 2.745$, and $k_4 = 2.92$.

Type II.a Profile (0<K_S<1):

As indicated in Table 1 (Yıldırım and Singh 2013a), there is no the relationship for δ_H in terms of S_f, since it is not possible to subtract S_f. For convenience, Eq. (2b) should be directly used to relate S_f and U_C.

Type II.b Profile (K_S =1):

Rearranging DW equation for the friction slope, S_f ($F_S = 1$), and substituting into Eq. (2c) for U_C, the following expression can be obtained:

$$U_C \cong 1 - 0.6 \ \frac{Ł}{\overline{H}} S_f = 1 - 0.6 \ \times \frac{Ł}{\overline{H}} \times \left(\frac{1}{0.357} \times \delta_H \times \frac{\overline{H}}{L} \right) = 1 - 1.286 x \delta_H \qquad (6)$$

The uniformity parameters (CV_q, E_U and D_U) can be written in terms of the dimensionless physical numbers ($\lambda_1, \lambda_2, \lambda_3, \lambda_4, \lambda_5$) as given by the following expression:

$$\delta_H = k_1 \times \lambda_1 = k_2 \times \lambda_2 = k_3 \times \lambda_3 = k_4 \times \lambda_4 \qquad (7)$$

where k_1, k_2, k_3, k_4 = design coefficients and are: $k_1 = 0.778$, $k_2 = 0.621$, $k_3 = 0.490$, and $k_4 = 0.521$.

Type II.c Profile (1<K_S<2.75):

Rearranging DW equation for the S_f ($F_S = 1$), and substituting into Eq. (2d) for U_C:

$$U_C \cong 1 - 0.3 \ \frac{Ł}{\overline{H}} (S_0 - S_f) = 1 - 0.3 \ \times \frac{Ł}{\overline{H}} \times \left\{ S_0 - \left[0.164 \times S_0^{2.3} \ \times \left(\delta_H \frac{\overline{H}}{L} \right)^{-1.3} \right] \right\}$$

The above expression is reformulated for δ_H in terms of dimensionless physical numbers ($\lambda_1, \lambda_2, \lambda_3, \lambda_4, \lambda_5$) as:

$$\delta_H = S_0 \times \left(1 - k_1 \times \frac{\lambda_1 \times \lambda_5}{S_0}\right)^{-1/1.3} \times \frac{k_5}{\lambda_5} \tag{8a}$$

$$= S_0 \times \left(1 - k_2 \times \frac{\lambda_2 \times \lambda_5}{S_0}\right)^{-1/1.3} \times \frac{k_5}{\lambda_5} \tag{8b}$$

$$= S_0 \times \left(1 - k_3 \times \frac{\lambda_3 \times \lambda_5}{S_0}\right)^{-1/1.3} \times \frac{k_5}{\lambda_5} \tag{8c}$$

$$= S_0 \times \left(1 - k_4 \times \frac{\lambda_4 \times \lambda_5}{S_0}\right)^{-1/1.3} \times \frac{k_5}{\lambda_5} \tag{8d}$$

where k_1, k_2, k_3, k_4, k_5 = design coefficients and are: k_1 = 4.357, k_2 = 3.477, k_3 = 2.745, k_4 = 2.92, k_5 = 0.356.

Type III Profile ($K_S \geq 2.3$)***:***

Introducing the equation for δ_H (F_S = 1) into Eq. (2d) for U_C, one can obtain the following simple transformation:

$$U_C \cong 1 - 0.3 \frac{L}{H}(S_0 - S_f) = 1 - 0.3 \ x\delta_H \tag{9}$$

The uniformity parameters (CV_q, E_U and D_U) can be written in terms of the dimensionless physical numbers ($\lambda_1, \lambda_2, \lambda_3, \lambda_4, \lambda_5$) as given by the following expression:

$$\delta_H = k_1 \times \lambda_1 = k_2 \times \lambda_2 = k_3 \times \lambda_3 = k_4 \times \lambda_4 \tag{10}$$

where k_1, k_2, k_3, k_4 = design coefficients and are: k_1 = 4.357, k_2 = 3.477, k_3 = 2.745, and k_4 = 2.92.

DETERMINING FRICTION SLOPE (S_f) and
OPERATING INLET PRESSURE HEAD (H_{0I})

To overcome the implicity in the procedure (Keller and Bliesner, 1990), Yıldırım (2008) recently proposed an improved direct computing technique to determine H_{0I} for a single line size system which incorporates different uniformity patterns for water application. In this analysis, first, simple mathematical expressions are deduced to relate uniformity parameters; then H_{0I} is simply reformulated by taking into account a multiplification factor

α, for the required average outlet pressure head, and β^*, for the potential energy head change due to uniform line slope.

However, the applicability of this procedure is only limited for the design case of a Type-I pressure profile for horizontal or uphill slope situation.

Eq. (11) can be transformed for a single line size system (k = 0.75), and suitable for the general slope situations (p = 0 and p = 1 for zero and upslope, p = -1 for downslope) as follows:

$$H_{0I} = \overline{H} + L\left(\frac{3}{4}S_f + \frac{1}{2}(\beta_0)\right)$$ (11)

In this section, the computing technique (Yıldırım 2008) based on the recent analytical development (Yıldırım 2006, 2007) which evaluates the operating inlet pressure head, H_{0I} for a single line size system (k = 0.75), will be improved and extended to encmapss different types of pressure profiles concerning different uniform line slope situations, and various design combinations. In the analysis, first the friction slope (S_f) is formulated in terms of dimensionless physical mumbers (($\lambda_1, \lambda_2, \lambda_3, \lambda_4, \lambda_5$), introduced into Eq. (11), and then H_{0I} can be directly determined as follows.

Type I Profile $(K_S \leq 0)$:

The following expression for H_{0I} can be reformulated in the following general form as:

$$H_{0I} = \alpha \times \overline{H} + \beta^* \times (S_0 \times L)$$ (12)

where k_1, k_2, k_3, k_4 = coefficients and are: k_1 = 4.357, k_2 = 3.477, k_3 = 2.745, and k_4 = 2.92; α = multiplification factor for the required average pressure head, and β^* = multiplification factor for the potential energy head ($S_{0 \times L}$) as:

$$\alpha = 1 + c_1 \times \delta_H = 1 + c_1 \times k_1 \times \lambda_1 = 1 + c_1 \times k_2 \times \lambda_2 = 1 + c_1 \times k_3 \times \lambda_3 = 1 + c_1 \times k_4 \times \lambda_4$$ (13)

$$c_1 = \frac{0.3}{F_S} \qquad [c_1 = 0.75 \text{ for } F_S = 1]$$ (14a)

$$\beta^* = \frac{1}{2} - \frac{0.3}{F_S} \qquad [\beta^* = -0.3 \quad \text{for } F_S = 1]$$ (14b)

Type II.a Profile (0<K_S<1):

Under a similar consideration, the following expression for H_{0I} can be written as follows:

$$\alpha = = 1 + c_1 \times k_1 \times \lambda_1 = 1 + c_1 \times k_2 \times \lambda_2 = 1 + c_1 \times k_3 \times \lambda_3 = 1 + c_1 \times k_4 \times \lambda_4 \quad (15)$$

$$c_1 = \frac{0.5}{F_S} \qquad\qquad [c_1 = 0.75 \text{ for } F_S = 1] \qquad\qquad (16a)$$

$$\beta^* = \frac{0.5}{F_S} - \frac{1}{2} \qquad\qquad [\beta^* = 0.3 \quad \text{for } F_S = 1] \qquad\qquad (16b)$$

Type II.b Profile ($K_S = S_0/S_f = 1$, $S_0 = S_f$):

Under a similar consideration, the following expression for H_{0I} can be deduced:

$$\alpha = 1 + c_1 \times \delta_H = 1 + c_1 \times k_1 \times \lambda_1 = 1 + c_1 \times k_2 \times \lambda_2 = 1 + c_1 \times k_3 \times \lambda_3 = 1 + c_1 \times k_4 \times \lambda_4 \quad (17)$$

$$c_1 = \frac{0.0}{F_S^{-0.5}} \quad [c_1 = 0.70 \text{ for } F_S = 1] \qquad\qquad (18)$$

where k_1, k_2, k_3, k_4 = coefficients and are: $k_1 = 0.778$, $k_2 = 0.621$, $k_3 = 0.490$, and $k_4 = 0.521$. Note that for Type II.b profile, the multiplication factor, β^* for the potential energy change is equal to zero ($\beta^* = 0$), by setting the equality of the friction slope, S_f, to the uniform pipe slope, S_0 ($K_S = 1$, $S_0 = S_f$).

Type II.c ($1 < K_S < 2.75$) and Type III ($K_S \geq 2.5$) Profiles:

Under a similar consideration, the following expression for H_{0I} can be written:

$$\alpha = = 1 + c_1 \times k_1 \times \lambda_1 = 1 + c_1 \times k_2 \times \lambda_2 = 1 + c_1 \times k_3 \times \lambda_3 = 1 + c_1 \times k_4 \times \lambda_4 \quad (19)$$

$$c_1 = -\frac{0.5}{F_S} \qquad\qquad [c_1 = -0.75 \text{ for } F_S = 1] \qquad\qquad (20a)$$

$$\beta^* = \frac{0.5}{F_S} - \frac{1}{2} \qquad\qquad [\beta^* = 0.3 \quad \text{for } F_S = 1] \qquad\qquad (20b)$$

CALCULATION PROCEDURE for IMPROVED ENERGY-GRADIENT

RATIO (EGR) APPROACH

For the sake of comparison between the formulations derived for design parameters [the friction slope, S_f, fraction of the required average pressure head, δ_H, and multiplication factors (α and β^*) for operating pressure], regarding the five types of pressure profiles (*Type I*, *Types II.a, II.b, II.c* and *Type III*), all formulations are sythesized and are shown in Table 1.

Before starting the present algorithm, the following input data for hydraulic variables are assigned in advance to finally evaluate the required pressure parameters along the profile.

Input (initially known) parameters: S_0: pipe slope which is assumed to be uniform along the line (%), L: total length of the submain line (m), $\overline{H}$: required average pressure head (m), (U_C, CV_q, E_U or D_U): uniformity parameters for the desired level of water application uniformity (%), l_e: equivalent length (m) to determine the enlergement factor (F_S) (Yıldırım and Singh 2013a), s and x: outlet spacing (m) and outlet discharge exponent, respectively.

Output (required) parameters: S_f: the friction slope (or the slope of *EGL*) (%), $K_S = S_0/S_f$: the dimensionless energy-gradient ratio, which primarily identifies the type of pressure profiles, $h_{f(L)} = S_f \times L$: the total friction drop at the end of line (m), H_{max}, H_{min}: the extreme pressure heads (m) with their locations (i_{max}, i_{min}), ΔH_{max}: the maximum allowable pressure head difference along the line (m), $\delta_H = \Delta H_{max}/\overline{H}$: the fraction of the required average pressure head (%), $\phi_H = \Delta H_{max}/h_{f(L)}$: the relative maximum pressure variation (%), α and β^*: the multiplification factors to the operating inlet pressure (H_{0I}), H_{0I} and H_d: the operating inlet and downstream end pressure heads (m), respectively, and β: nonuniform outflow exponent (Yıldırım and Singh 2013a) to evaluate the nonumiform outflow distribution along the line.

Based on the present improved EGR approach, the following calculation steps are implemented, respectively, using the related formulations for each type of pressure from Table 1 (Yıldırım and Singh 2013a):

Step (a). For a desired value of the uniformity coefficient (U_C, CV_q, E_U or D_U), and the outlet discharge exponent (x), the related dimensionless physical numbers (λ_1, λ_2, λ_3 or λ_4) are computed; and for a given value of

required average pressure head ($\overline{H}$) and the total length of submain line (L), the dimensionless physical number, λ_5, are computed from the related expression.

Step (b). Select the proper formulation for S_f in accordance with the given design slope (S_0) condition [zero ($p = 0$), upslope ($p = 1$), or downslope ($p = -1$)]. Then S_f is evaluated, depending on dimensionless physical numbers (λ_1, λ_2, λ_3, λ_4 and λ_5) and certain values of design coefficients (k_1, k_2, k_3, k_4 and k_5).

Step (c). Compare the friction slope (S_f) to the uniform pipe slope (S_0) with respect to the design intervals of the energy-gradient ratio ($K_S = S_0/S_f$), and make a decision about the type of pressure profile depending on the K_S value assigned in **Step (b)**.

It should be noted for downslope condition, as an initial computation, the S_f formulation given for the pressure profiles Type II.c and Type III is first used; then if a negative value of S_f is reached, this would indicate that S_f is greater than the pipe slope, S_0; that means the formulation for S_f deduced for Type II.a profile should be used (see, Table 1).

Step (d). For the type of pressure profile assigned in **Step (c)**, select the proper formulation to evaluate the percentage of the required average pressure head (δ_H) from Table 1. Then, compute the total friction drop, $h_{f(L)}$.

Step (e). For the type of pressure profile decided on above, compute multiplication factors (α and β^*) for the operating inlet pressure head (H_{0I}), depending on the dimensionless physical numbers (λ_1, λ_2, λ_3, λ_4 and λ_5) and certain values of design coefficients (c_1, k_1, k_2, k_3, and k_4) from Table 1. Then, evaluate the operating inlet pressure head (H_{0I}) for both the design cases (considering or neglecting local losses).

Step (f). For the above type of pressure profile, determine the extreme pressure heads (H_{max}, H_{min}) with their positions along the line (i_{max}, i_{min}), and evaluate the maximum allowable pressure head difference (ΔH_{max}) to check the value of δ_H computed from **Step (d)**. Then, determine the relative pressure variation ($\phi_H = \Delta H_{max}/h_{f(L)}$) from Table 1.

Step (g). Compute the downstream end pressure head (H_d) from the conservation of energy principle or the related analytical equations derived for each type of profile. Then, set the order of operating inlet (H_{0I}), downstream end (H_d), extreme (H_{max}, H_{min}) and required average ($\overline{H}$) pressure heads to check the identity for the assigned type of pressure profile from **Step (c)**.

Step (h). Introduce the value of S_f previously determined in **Step (c)** to reveal the certain form of the pressure head profile along the line. Then,

check the identitiy of the specific hydraulic characteristics between the certain and assigned pressure profiles, with regard to Table 1. Note that if a higher precision is required, the nonumiform outflow distribution along the line should be taken into consideration.

For this case the nonuniform outflow exponent, β (Yıldırım and Singh 2013a) is evaluated depending on the values, S_0, x, L, $\overline{H}$, F_S, and S_f [determined from **Step (b)**]. Then, **Steps (f)~(h)** are repeated to evaluate the nonuniform outflow distribution.

Step (ı). For water application uniformity evaluation, the proper values of required uniformity parameters (U_C, D_U, CV_q, E_U or δ_H), are computed respectively.

DESIGN APPLICATIONS COVERING DIFFERENT TYPES OF PRESSURE PROFILES AND VARIOUS DESIGN CONFIGURATIONS

In the following design applications, the data (Hathoot et al. 1993) are originally selected herein, without needing further input data for the required hydraulic variables. To present a comprehensive comparative analysis (Table 2), covering various design configurations for a wide range of water application uniformity, U_C, and for a large range of uniform line slope situations regarding three outlet discharge exponents (x = 0.2, 0.5 and 1.0), will be presented inTable 2 (please see "Results and Discussion").

Application-I: Steep Downslope Situation (Type-III Pressure Profile)

In order to demonstrate the applicability of the proposed improved EGR approach to compute the required pressure parameters along the energy-grade line (*EGL*), the original data given by Hathoot et al. (1993), are selected herein. The total length of the submain line is 151 m (L = 151 m), and the required average pressure head is 7.2 m ($\overline{H}$ = 7.2 m), considering the turbulent flow condition through the pipeline (the velocity exponent, m = 1.75 for the DW equation).

The steep-downslope situation, S_0 = 0.05, is considered and the desired level of water application uniformity is evaluated, U_C = 90.5%, based on the nonuniform outflow concept ($m_\beta = \beta \times m$, $\beta \neq 1$), and the change in the kinetic energy head ($H_V \cong 0$) and local head losses ($F_S = 1$) are neglected.

Step a. For U_C = 0.905, $\overline{H}$ =7.2 m, L = 151 m and x = 0.5, dimensionless physical numbers, λ_1 and λ_5 are already computed as follows: $\lambda_1 = 0.9$ and $\lambda_5 = 0.048$.

Steps b. and c. The friction slope, S_f is directly computed from (k_1 = 4.357):

$$S_f \; = \; S_0 - k_1 \times \lambda_1 \times \lambda_5 = 0.6 \; - 4.357 \times 0.9 \; \times 0.048 = 0.0105 \quad , \quad S_f = 1.05\%$$

The dimensionless energy-gradient ratio, $K_S = \dfrac{S_0}{S_f} = \dfrac{0.6}{0.0105} = 4.3$

$K_S = 4.3 \; > 2.3$ (Table 1), therefore ***Type-III*** profile is observed along the line.

Total friction drop, $h_{f(L)} = S_f \times L = 0.0105 \times 151 = 1.586 \cong 1.9$ m.

Total energy gain due to steep-downslope situation, $\Delta S = S_0 \times L = 0.6 \; \times 151 = 7.5$ m.

For the nonuniform outflow distribution along the line, the nonuniform outflow exponent, β is evaluated depending on the values of S_0, x, L, $\overline{H}$, F_S, and S_f, as follows:

$$\beta = 1 - 3.322 x \log\left[1 + \frac{H_r}{\overline{H}} + \frac{h_{f(L)}}{\overline{H}}\left[\left(\frac{m+3-0.5^{m+1}}{m+2} \right) - F_S \right] + \frac{1}{4\overline{H}}(p\Delta S) \right]$$

$$\beta = 1 - 3.322 \times 0.5 \times \log\left[1 + 0 + \frac{1.9}{7.2} \times \left[\left(\frac{4.3 \; - 0.5^{2.3}}{3.3} \right) - 1 \right] + \frac{1}{4 \times 7.2} \times (-1) \times 7.5 \right]$$

$\beta = 1.172$, therefore the improved value of velocity exponent, m_β : $m_\beta = \beta \times m = 1.172 \times 1.3 \; = 2.6$

Step d. For ***Type III*** profile, δ_H can be directly determined from (k_1 = 4.357):

$$\delta_H = k_1 \times \lambda_1 = 4.357 \times 0.9 \; = 0.828, \; \delta_H = 8 \%$$

Step e. For ***Type III*** profile, multiplication factors (α and β^*) are computed from:

$k_1 = 4.357$, $c_1 = -0.75$ for $F_S = 1$]:

$$\alpha = 1 + c_1 \times \delta_H = 1 - 0.3 \; \times 0.828 = 0.379$$

$$\alpha = 1 + c_1 \times k_1 \times \lambda_1 = 1 - 0.3 \ \times 4.357 \times 0.9 \ = 0.379 \text{ , and } \beta^* = 0.3 \quad \text{(for } F_S = 1\text{)}.$$

The operating inlet pressure head (H_{0I}) is directly computed from:

$$H_{0I} = \alpha \times \overline{H} + \beta^* \times (S_0 \times L)$$

$$H_{0I} = 0.379 \times 7.2 + 0.3 \ \times (0.6 \ \times 151) = 4.617 \cong 4.6 \quad \text{m.}$$

Check the value of H_{0I}, for $i = 0$, for $S_f = 0.0105$ and $m_\beta = 2.6$:

$$H_{0I} = H(l = 0, i = 0) = \overline{H} + H_V\,[1 - (1 - i)^2] + h_{f(L)}\left[F_S[\,1 - i)^{m_\beta + 1} - 1] + \frac{m_\beta + 1}{m_\beta + 2}\right] - p\Delta S\left(i - \frac{1}{2}\right)$$

$$= 7.2 + 0 + 1.9 \ \times \left[1 \times [\,1 - 0)^{2.6 \ + 1} - 1] + \frac{2.6 \ + 1}{2.6 \ + 2}\right] - (-1) \times 7.5 \ \times \left(0 - \frac{1}{2}\right) = 4.6 \quad \text{m.}$$

The downstream end pressure head, H_d, can be directly evaluated from the conservation of energy principle:

$$H_d = H_{0I} + L \times (S_0 - S_f) = 4.6 \ + 151 \times (0.6 \ - 0.0105) = 0 \ .585 \cong 0 \ .9 \ \text{m.}$$

Check the value of H_d, for for $i = 1$, for $S_f = 0.0105$ and $m_\beta = 2.6$:

$$H_d = H(l = L, i = 1) = 7.2 + 0 + 1.9 \ \times \left[1 \times [\,1 - 1)^{2.6 \ + 1} - 1] + \frac{2.6 \ + 1}{2.6 \ + 2}\right] - (-1) \times 7.5 \ \times \left(1 - \frac{1}{2}\right) = 0 \ .582 \cong 0 \ .8$$
m.

Steps f., g. and **h.** The location of minimum pressure head (i_{min}) can be evaluated from:

$$i_{min(IV\ )} = \frac{l_{min}}{L} = 1 - 0.561 \times \left(\frac{K_S}{F_S}\right)^{0.5} = 1 - 0.561 \times \left(\frac{4.3}{1}\right)^{0.5} = -0.6 \ ,$$

Minus sign indicates the minimum outflow just occurs at the upstream pipe inlet point ($i_{min} = 0$), therefore the operating pressure head at the pipe inlet is just identical to the minimum pressure head along the line ($H_{0I} = H_{min}$

= 4.62 m), and the maximum pressure head occurs at the downstream closed end ($H_{max} = H_d = 10.58$ m)

The maximum pressure head difference,

$\Delta H_{max} = H_{max} - H_{min} = 10.8 - 4.8 = 5.0$ m.

Check the value of δ_H from: $\delta_H = \dfrac{\Delta H_{max}}{\overline{H}} = \dfrac{5.0}{7.2} = 0.828$, $\quad (\delta_H = 83\%)$

Compute parameter, ϕ_H, to evaluate the pressure variation:

$$\phi_H = \frac{\Delta H_{max}}{h_{f(L)}} = \frac{5.0}{1.9} = 3.3$$

which means the excessive level for the pressure variation along the line for a given steep downslope situation (for $K_S = 4.75 > 2.75$)

Check the pressure orders for **Type- III** profile:

$H_d = H_{max} = 10.6 > \overline{H} = 7.2 > H_{0I} = H_{min} = 4.6$ m.

The distribution of pressure parameters evaluated based on the EGR approach is verified by the **Type- III** profile as demonstrated in Fig. 3 (e).

Step 1. For water application uniformity, or **Type III** profile ($c_1 = -0.75$, $k_1 = 4.357$ and $\beta^* = 0.25$), regarding the design value of operating pressure head, $H_{0I} = 4.62$ m, and $\lambda_5 = \overline{H}/L = 7.2/151 = 0.048$, the uniformity parameters are evaluated as follows:

$$\theta = \frac{H_{0I}}{\overline{H}} - \beta^* \times \frac{S_0}{\lambda_5} - 1 = \frac{4.8}{7.2} - 0.3 \times \frac{0.6}{0.048} - 1 = -0.61875$$

$$\delta_H = \frac{\theta}{c_1} = -\frac{0.61875}{-0.3} = 0.825 \cong 8 \ \% \quad \lambda_1 = \frac{(1-U_C)}{x} = \frac{\theta}{c_1 \times k_1} = \frac{-0.61875}{-0.3 \times 4.357} = 0.1894$$

$$U_C = 1 - \lambda_1 \times x = 1 - 0.1894 \times 0.5 = 0.905 \cong 0.5\%$$

Application-II: Efficient Downslope (Type II.b Profile) for "Ideal Hydraulic Design"

To achieve "*the most efficient*" pressure profile or "*the ideal hydraulic design*" case, using the data in Application-I (L = 151 m, $\overline{H} = 7.2$ m), a

sample solution is presented for the desired value of the water application uniformity, $U_C = 90.5\%$, based on the following calculation steps:

Step a. Dimensionless physical numbers, λ_1 and λ_5 from:

$$\lambda_1 = \frac{(1-U_C)}{x} = \frac{(1-0.905)}{0.5} = 0.9 \quad \text{and} \quad \lambda_5 = \frac{\overline{H}}{L} = \frac{7.2}{151} = 0.048$$

Steps b and c. The friction slope, S_f, which must be equal to the uniform pipe slope (S_0) for "*the most efficient*" design case (***Type II.b*** pressure profile: $K_S = S_0/S_f = 1$), is directly computed from (for ***Type II.b*** profile: $k_1 = 2.178$):

$$S_0 = S_f = k_1 \times \lambda_1 \times \lambda_5 = 2.178 \times 0.9 \times 0.048 = 0.0198 \cong 0.0 \;,\; S_0 = S_f = 2\%$$

Step d. For the desired ***Type II.b*** profile, δ_H can be determined by two alternative ways:

By neglecting local losses ($F_S = 1$):

$$\delta_H = 0.357 \times F_S^{-0.5} \times S_f \times \frac{L}{\overline{H}} \cong 0.5 \times S_f \times \frac{L}{\overline{H}} = 0.5 \times 0.0 \times \frac{151}{7.2} = 0.148 \; (\delta_H \cong 5\%)$$

Alternatively, directy computed from ($k_1 = 0.778$):

$$\delta_H = k_1 \times \lambda_1 = 0.778 \times 0.9 = 0.148 ,\; \delta_H \cong 5\%$$

Total friction drop,

$$h_{f(L)} = S_f \times L = 0.0 \times 151 = 3.0 \;\; \text{m} \; (\Delta S = S_0 \times L = 0.0 \times 151 = 3.0 \;\; \text{m})$$

Step e. For the desired ***Type II.b*** profile, multiplication factors (α and β^*) are computed from[$k_1 = 0.778$, $c_1 = 0.70$ for $F_S = 1$]:

$$\alpha = 1 + c_1 \times \delta_H = 1 + 0.0 \times 0.148 = 1.104$$

$$\alpha = 1 + c_1 \times k_1 \times \lambda_1 = 1 + 0.0 \times 0.778 \times 0.9 = 1.104 \text{ and } \beta^* = 0$$

The operating inlet pressure head (H_{0I}) is directly computed from:

$$H_{0I} = \alpha \times \overline{H} + \beta^* \times (S_0 \times L)$$

$$H_{0I} = 1.104 \times 7.2 + 0 \times (0.0 \times 151) = 7.949 \cong 7.9 \;\; \text{m.}$$

Check the value of H_{0_1} ($H_{0I} = H_d$) for $S_f = 0.0197$ [$\Delta S = h_{f(L)} = 3.02$ m]:

$$H_{max} = H_{0I} = H_{(l=0,i_{max}=0)} = \overline{H} + \left(\frac{m+1}{m+2}\right) \times h_{f(L)} - \frac{\Delta S}{2} = 7.2 + \frac{2.3}{3.3} \times 3.0 \ - \frac{3.0}{2} = 7.905 \cong 7.9$$ m;

$$H_{max} = H_d = H_{(l=L,i_{max}=1)} = \overline{H} + \left(\frac{m+1}{m+2} - F_S\right) \times h_{f(L)} + \frac{\Delta S}{2} = 7.2 + \left(\frac{2.3}{3.3} - 1\right) \times 3.0 \ + \frac{3.0}{2} = 7.905 \cong 7.9$$ m.

Steps f., g. and **h.** The location of minimum pressure head (i_{min}) can be evaluated from:

$$i_{min(IV\ )} = \frac{l_{min}}{L} = 1 - 0.561 \times \left(\frac{K_S}{F_S}\right)^{0.5} = 1 - 0.561 \times \left(\frac{1}{1}\right)^{0.5} \cong 0.4$$

The minimum pressure head (H_{min}) is directly computed for $i = i_{min} = 0.4$:

$$H_{min} = H(i_{min=0.4}\ ) = \overline{H} + H_{V}\ [1 - (1 - i_{min})^2] + h_{f(L)}\left[F_S[\ 1 - i_{min})^{m_\beta+1} - 1] + \frac{m_\beta+1}{m_\beta+2}\right] - p\Delta S\left(i_{min} - \frac{1}{2}\right)$$

$$= 7.2 + 0 + 3.0\ \times\left[1 \times [\ 1 - 0.4\ )^{2.3}\ -1] + \frac{2.3}{3.3}\right] - (-1) \times 3.0\ \times\left(0.4\ - \frac{1}{2}\right) = 6.826 \cong 6.8$$ m.

Alternatively, for the Type-II.b profile, one can use the following simple relationships which evaluates H$_{min}$, in terms of H$_{max}$ and $\overline{H}$:

$$H_{min} = f\left[H_{max}, \overline{H}\right]$$:

$$H_{min} = \frac{1}{2} \times (3 \times \overline{H} - H_{max}) = \frac{1}{2} \times (3 \times 7.2 - 7.9\ ) = 6.825 \cong 6.8$$ m.

Therefore, the maximum pressure head difference,

$$\Delta H_{max} = H_{max} - H_{min} = 7.9\ - 6.8\ = 1.2\ m.$$

Check the value of δ_H from: $\delta_H = \dfrac{\Delta H_{max}}{\overline{H}} = \dfrac{1.2}{7.2} = 0.5\ ,$ ($\delta_H = 15\%$)

Compute parameter, ϕ_H , to evaluate the pressure variation for "*ideal hydraulic design*" case:

$$\phi_H = \frac{\Delta H_{max}}{h_{f(L)}} = \frac{1.2}{2.9} \cong 0.3$$

(acceptable critical level for the minimum pressure variation for ideal hydraulic design)

Check the pressure orders for **Type- II. b** profile:

$$H_{0I} = H_d = H_{max} = 7.95 > \overline{H} = 7.2 > H_{min} = 6.8 \quad \text{m}.$$

The distribution of pressure parameters, assigned based on the EGR approach, is verified by the **Type- II. b** profile, as shown in Fig. 2 (c).

Step 1. For the pressure profile Type II.b ($c_1 = 0.70$, $k_1 = 0.778$ and $\beta^* = 0$), regarding the design value of operating pressure head, $H_{0I} = 7.95$ m, and $\lambda_5 = \overline{H} / L = 7.2/151 = 0.048$, uniformity parameters are evaluated as follows:

$$\alpha_{(K_S=1,\beta^*=0)} = \frac{H_{0I}}{\overline{H}} = \frac{7.95}{7.2} = 1.104$$

Using Eq. (36b) for θ one can yield:

$$\theta_{(K_S=1,\beta^*=0)} = \alpha_{(K_S=1,\beta^*=0)} - 1 = \frac{H_{0I}}{\overline{H}} - 1 = 1.104 - 1 = 0.104$$

$$\delta_H = \frac{\theta}{c_1} = \frac{0.104}{0.70} = 0.149 \cong 15 \ \% \quad \lambda_1 = \frac{(1-U_C)}{x} = \frac{\theta}{c_1 \times k_1} = \frac{0.104}{0.70 \times 0.778} = 0.191$$

$$U_C = 1 - \lambda_1 \times x = 1 - 0.191 \times 0.5 = 0.905 \cong 90.5\%$$

RESULTS and DISCUSSION

For the sake of comparison, the results for the required design variables (S_f, K_S, H_{0I}, H_d, H_{max}, H_{min}, $h_{f(L)}$, ϕ_H) obtained from the proposed EGR approach are compared with those obtained from the previous analytical development (Yıldırım 2007), and the computer-aided step-by-step (SBS) procedure (Hathoot et al. 1993) and are synthesized in Table 2. For the solution of the SBS method, a computer program, *LATCAD* developed in *Visual Basic. 6.0* (Yıldırım and Ağıralioğlu 2004) based on the flowchart presented earlier (Hathoot et al. 1993), was conducted. The computational time was negligible, less than a few minutes for actual calculations, for *LATCAD* implementation.

As a useful reference, regarding three outlet discharge exponents (x = 0.2, 0.5, 1.0), various shapes of pressure head distributions [H(*l*)] versus the dimensionless distance (*i* = *l*/L) are observed for each type of pressure profiles, based on the results from the present EGR approach and the SBS procedure, and shown in Figs. 1, 2 and 3, respectively.

As shown in Fig. 1, three pressure head distributions for **Type-I** profile are demostrated for zero-slope case, S$_0$ = 0 from Fig. (1a), for uniform upslope case with S$_0$ = 2% from Fig. (1b), and for uniform steep-upslope case with S$_0$ = 5% by Fig. (1c), respectively. Fig. 1 reveals that typical hydraulic characteristics of **Type-I** profile are clearly observed in these three figures in which the pressure head exponentially decreases with respect to the line starting from inlet, and reaches a minimum value at the downstream closed end ($H_{0I} = H_{max} > \overline{H} > H_d = H_{min}$).

The maximum pressure head, H$_{max}$, is at the inlet of the line and is equal to the operating inlet pressure, H$_{0I}$ (H$_{0I}$ = H$_{max}$); the minimum pressure head, H$_{min}$, is at the closed end of line, and is equal to the downstream pressure head (H$_d$ = H$_{min}$). The value of the pressure head roughly intersects to the required average pressure head value in the middle section of the line. As shown in Fig. 1, (S$_0$ = 0, 2%, 5%), the pressure head is approximately equal to the average value ($H = \overline{H} = 7.2m$) for the interval of dimensionless distance at about $i = 0.0$ ~ 0.45 through the upstream section.

As shown in Fig. (2a), the pressure distribution for **Type-II.a** profile is demonstrated for gentle-downslope case S$_0$ = 1%. As a typical hydraulic chaacteristic of **Type II.a** profile, the pressure head decreases from the upstream end with respect to the line, reaches a minimum point (i_{min}), and then increases with respect to the line.

However, the downstream end pressure head (H$_d$) is still less than the operating inlet pressure (H$_{0I}$). The maximum pressure head is at the inlet (H$_{max}$ = H$_{0I}$); and the minimum pressure head is located at about i_{min} = 0.70, through the downstream section ($H_{0I} = H_{max} > \overline{H} > H_d > H_{min}$). In this type of pressure profile, the value of the pressure head roughly intersects the required average pressure head value at about $i = 0.3$ through the ustream section.

As shown in Fig. (2b), the pressure distribution for **Type-II.b** profile is demonstrated for efficient-downslope case, S$_0$ = 0.5%. As a typical hydraulic chaacteristic of **Type II.b** profile, the operating inlet pressure head is equal to the downstream closed end pressure head (H$_{0I}$ = H$_d$); the maximum pressure is at the inlet (H$_{max}$ = H$_{0I}$) as well as at the closed end of the line (H$_{max}$ = H$_d$). The pressure head is equal to the average pressure head at two points, $i = 0.5$ along upstream and $i = 0.0$ along downstream section. The

minimum pressure is located near the middle section of the line, $i_{min} = 0.44$, for all performed simulations.

As shown in Fig. (3a), the pressure distribution for **Type-II.c** profile is presented for nearly-steep downslope situation, $S_0 = 2\%$. This type of pressure profile occurs when the line slope is even steeper, so the pressure at the end of line is higher than the operating inlet pressure. In this condition, the maximum pressure is at the downstream closed end of line ($H_{max} = H_d$), which exponentially decreases along the line, and reaches the minimum pressure, located somewhere along the upstream segment of the line, then inceases toward the upstream end ($H_d = H_{max} > \overline{H} > H_{0I} > H_{min}$ or $H_d = H_{max} > H_{0I} \geq \overline{H} > H_{min}$).

In this type of pressure profile, the value of the pressure head roughly intersects the required average pressure head value at two points, $i = 0.6$, near the pipe inlet, and $i = 0.6$ along downstream section for the SBS method, whereas the pressure head is equal to the average pressure head at one point, $i = 0.6$, along downstream segment for the EGR approach. The location of minimum pressure is observed near the upstream end, $i_{min} = 0.2$, for the EGR approach, whereas $i_{min} = 0.3$ for the SBS procedure.

As shown in Fig. (3b), the pressure head distribution for **Type-III** profile is demostrated for steep-downslope case, $S_0 = 5\%$ in which the submain line is on a steep downslope, where the total energy gain due to the uniform downslope is larger than the total energy drop due to friction for all sections along the line. In this case, the pressure head increases with respect to the line length.

In this condition the maximum pressure is at the downstream closed end of the line (($H_{max} = H_d$), and the minimum pressure head is at the pipe inlet and equal to the operating pressure head ($H_{min} = H_{0I}$) [$H_d = H_{max} > \overline{H} > H_{0I} = H_{min}$]. The value of the pressure head roughly intersects the required average pressure head value at the middle section of the line, $i = 0.5$, regarding both procedures.

As concluded from Figs, 1, 2 and 3, among all types of pressure profiles, the **Type-II** profile is considered as the optimal (or ideal) pressure profile which can produce the minimum pressure head difference when the total energy loss due to friction is just balanced by the total energy gain due to uniform downslope (Profile II-b).

CONCLUDING REMARKS

Based on the present EGR approach, the following conclusions can be underlined:

1. Analysis of results obtained from the EGR approach shows that

for given values of the uniform pipe slope, S_0, the required average outlet pressure head, $\overline{H}$, and the outlet discharge exponent, x, as the operating inlet pressure head, H_{0I} increases the fraction of the required average pressure head, δ_H, and the coefficient of variation of outlet discharge, $\mathcal{C}_q$ increase, whereas other uniformity parameters (U_C, D_U and E_U) decrease, for all types of pressure profiles.

2. To evaluate the influence of different uniform pipe slopes on the U_C values, as the upslope increases the U_C values linearly decrease; hence a large decrease in the U_C values is observed for the highest upslope range, S_0 = 0.05 (U_C = 0.70). For a given upslope range, the U_C values rapidly decrease as the x value increases. For instance, for S_0 = 0.05, the smallest value of U_C = 0.70 is observed for the largest value of x = 1.0. For the downhill slope case, the U_C profile has a curve form, even for different *x* values. In this situation, peak points of the U_C profiles approximately occur around the downslope range, S_0 = 1%.

3. To conclude the influence of different uniform pipe slopes on the H_{0I} values; the H_{0I} values increase with increasing upslope whereas decrease with increasing downslope.

4. For all uniform line slope combinations regarded, the water application uniformity gives smaller values with the increase in the outlet discharge exponent, x, generally; for instance for a value of x = 0.2, the uniformity coefficient has highest values, whereas for the laminar flow outlets (x = 1.0), it has smaller values.

5. The pressure head profiles for different uniform line slope situations reveal that the value of the pressure head roughly intersects the required average pressure head value near the middle section of the line. For instance, for ***Type I*** profie (S_0 = 0, 2%, 5%), the pressure head is approximately equal to the average value ($H = \overline{H} = 7.2m$) for the dimensionless distance, $i = 0.40$ ~ 0.45; for ***Type II.a*** profile (S_0 = 1%), $i = 0.42$; for ***Type II. b*** profile ((S_0 = 0.5%), the pressure head is equal to the average pressure head at two upstream and downstream end points, $i = 0.55$ and $i = 0.00$; similarly, for ***Type II.c*** profile (S_0 = 2%), $i = 0.66$ and $i = 0.60$ (for SBS) and $i = 0.5$ (for EGR); for ***Type III*** profile (S_0 = 5%), $i = 0.60$.

6. Examination results shows that for the efficient-downslope case (***Type II.b*** profile), the minimum pressure head nearly occurs at the point, i_{min} = 0.44, through the upstream section, for all performed simulations.

REFERENCES

Anyoji, H., and Wu, I. P. (1987). "Statistical approach for drip lateral design." *Trans. ASAE,* 30(1), 187-192.

Barragan, J. and Wu, I.P. (2005). "Simple pressure parameters for micro-irrigation design" Biosystem Eng. 90(4): 463-475.

Christiansen, J. E. (1942). "*Irrigation by sprinkling.*" California Agricultural Experimental Station Bulletin 670, Univ. of California, Davis, California.

Cuenca, R.H. (1989). "*Irrigation systems design: an engineering approach*". Prentice Hall, New Jersey.

Hathoot, H. M., Al-Amoud, A. I., and Mohammad, F. S. (1993). "Analysis and design of trickle irrigation laterals." *J. Irrig. and Drain. Eng.,* 119(5), 756-767.

Hathoot, H. M., Al-Amoud, A. I., and Mohammad, F. S. (1994). "Analysis and design of sprinkler irrigation laterals." *J. Irrig. and Drain. Eng.,* 120(3), 534-549.

Hathoot, H. M., Al-Amoud, A. I., and Al-Mesned, A. S. (2000). "Design of trickle irrigation laterals considering emitter losses." *ICID Journal,* 49(2): 1-14.

Juana, L., Rodriguez-Sinobas, L., Losada, A. (2002). "Determining minor head losses in drip irrigation laterals. II: experimental study and validation." *J. Irrig. and Drain. Eng.* 128(6): 385-396.

Juana, L., Losada, A., Rodrigoez-Sinobas, L., and Sanchez, R. (2004). "Analytical relationships for designing rectangular drip irrigation units." *J. Irrig. and Drain. Eng.,* 130(1), 47-59.

Kang, Y., and Nishiyama, S. (1996). "Analysis and design of microirrigation laterals." *J. Irrig. and Drain. Eng.,* 122(2), 75-82.

Kang, Y. (2000). "Effect of operating pressures on microirrigation uniformity." *Irrig. Sci*. 20: 23-27.

Keller, J., and Karmelli, D. (1974). "Trickle irrigation design parameters." *Trans. ASAE*, 17(4), 678-684.

Keller, J., and Bliesner, r. D. (1990). *Sprinkler and trickle irrigation*, Van Nostrand Reinhold, New York.

Mahar, P. S., and Singh, R. P. (2003). "Computing inlet pressure head of multioutlet pipeline." *J. Irrig. and Drain. Eng.,* 129(6), 464-467.

Perold, R. P. (1977). "Design of irrigation pipe laterals with multiple outlets." *J. Irrig. and Drain. Eng.,* 103(2): 170-195.

Warrick, A.W. (1983*).* "Interrelationships of irrigation uniformity terms." *J. Irrig. and Drain. Eng.,* 109(3), 317-332.

Warrick, A.W., and Yitayew, M. (1988*).* "Trickle lateral hydraulics. I: analytical solution." *J. Irrig. and Drain. Eng.,* 114(2), 281-288.

Wu, I. P. (1992). "Energy gradient line approach for direct hydraulic calculation in drip irrigation design." *Irrig. Sci.,* 13, 21-29.

Wu, I. P. (1997). "An assessment of hydraulic design of micro-irrigation systems." *Agric. Water Manage.,* 32, 275-284.

Wu , I. P., and Yue, R. (1993). "Drip lateral design using energy gradient line approach." *Trans. ASAE,* 36(2), 389-394.

Valiantzas, J. D. (1998). "Analytical approach for direct drip lateral hydraulic calculation." *J. Irrig. and Drain. Eng.,* 124(6), 300-305.

Wu, I. P., and Gitlin, H. M. (1973). "Hydraulics and uniformity for drip irrigation." *J. Irrig. and Drain. Div.*, *ASCE,* 99(IR2), Proc. Paper 9786, June, pp. 157-168.

Wu, I. P. and Gitlin, H. M. (1974). "Drip irrigation design based on uniformity." *Trans. ASAE*, 17(3), 429-432.

Wu, I. P. and Gitlin, H. M. (1975). "Energy gradient line for drip irrigation laterals." *J. Irrig. and Drain. Eng.,* 101(4), 323-326.

Yıldırım, G., and Ağıralioğlu, N. (2004). "Comparative analysis of hydraulic calculation methods in design of micro-irrigation laterals." *J. Irrig. and Drain. Eng.,* 130(3), 201-217.

Yıldırım, G. (2006). "Hydraulic analysis and direct design of multiple outlets pipelines laid on flat and sloping lands*." J. Irrig. Drain .Engrg., ASCE*, 132(6), 537-552.

Yıldırım, G. (2007a). "An Assessment of Hydraulic Design of Trickle Laterals Considering Effect of Minor Losses." *Irrig. and Drain. (ICID Journal)* 56(4), 399-421.

Yıldırım, G. (2007b). "Analytical Relationships for designing multiple outlets pipelines*." J. Irrig. Drain. Engrg., ASCE*, 133(2), 140-154.

Yıldırım, G. (2008). "Determining inlet pressure head incorporating uniformity parameters for multioutlet plastic pipelines." *J. Irrig. Drain .Engrg., ASCE*, 134(3), 341-348.

Yıldırım, G. (2009). "Simplified procedure for hydraulic design of small-diameter plastic pipes." *Irrig. Drain. (ICID J.)* 58(3):209-233.

Yıldırım, G. (2010). "Total energy loss assessment for trickle lateral lines equipped with integrated in-line and on-line emitters" *Irrig. Science,* 28(4): 341-352.

Yıldırım, G. and Singh, V.P. (2013a). "Operating Pressure Assessment for Multi-outlets Submains: Ideal Hydraulic Design" 6th Congress on "International Perspective on Water Research and Environment" by ASCE & EWRI, İzmir, Turkey.

Yıldırım, G. and Singh, V.P. (2013b). "Operating Pressure Assessment for Multi-outlets Submains: Design Applications" 6th Congress on "International Perspective on Water Research and Environment" by ASCE & EWRI, İzmir,

Turkey.

Yitayew, M., and Warrick, A. W. (1988). "Trickle lateral hydraulics. *II*: design and examples." *J. Irrig. and Drain. Eng.,* 114(2), 289-300.

Table 1. Relationships for the Energy-Grade Line Slope: S_f (%), Fraction of Required Average Pressure Head (H): δ_H (%), Multiplication Factors: α and β', to Determine the Operating Inlet Pressure Head (H_{op}) with Related Design Coefficients (c_i, k_1, k_2, k_3, k_4, k_5) for Five Types of Pressure Profiles [Type-I, Types II a, II b, II c and Type-III]

Type of Pressure Profile(s)	Energy-Grade Line Slope: S_f (%) Design Coefficients (k_1, k_2, k_3, k_4)				Fraction of Required Average Pressure Head: δ_H (%) Design Coefficients (k_1, k_2, k_3, k_4, k_5)				
	k_1	k_2	k_3	k_4	k_1	k_2	k_3	k_4	k_5
Type-I	4.357	3.477	2.745	2.92	4.357	3.477	2.745	2.92	—
Type-IIa	4.357	3.477	2.745	2.92	4.357	3.477	2.745	2.92	0.356
Type-IIb	2.178	1.738	1.372	1.459	0.778	0.621	0.490	0.521	
Type-IIc and Type-III	4.357	3.477	2.745	2.92	4.357	3.477	2.745	2.92	0.356

Type-I:
$$S_f = k_1 \times \lambda_1 \times \lambda_5 - S_0 = k_2 \times \lambda_2 \times \lambda_5 - S_0 = k_3 \times \lambda_3 \times \lambda_5 - S_0 = k_4 \times \lambda_4 \times \lambda_5 - S_0$$

Type-IIa:
$$S_f = S_0 + k_1 \times \lambda_1 \times \lambda_5 = S_0 + k_2 \times \lambda_2 \times \lambda_5 = S_0 + k_3 \times \lambda_3 \times \lambda_5 = S_0 + k_4 \times \lambda_4 \times \lambda_5$$

Type-IIb:
$$S_0 - S_f = k_1 \times \lambda_1 \times \lambda_5 = k_2 \times \lambda_2 \times \lambda_5 = k_3 \times \lambda_3 \times \lambda_5 = k_4 \times \lambda_4 \times \lambda_5$$

Type-IIc and Type-III:
$$S_f = S_0 - k_1 \times \lambda_1 \times \lambda_5 = S_0 - k_2 \times \lambda_2 \times \lambda_5 = S_0 - k_3 \times \lambda_3 \times \lambda_5 = S_0 - k_4 \times \lambda_4 \times \lambda_5$$

Type-I and Type-III (δ_H):
$$\delta_H = k_1 \times \lambda_1 = k_2 \times \lambda_2 = k_3 \times \lambda_3 = k_4 \times \lambda_4$$

Type-IIa (δ_H):
$$\delta_H = k_1 \times \lambda_1 - k_5 \times \lambda_2 = k_3 \times \lambda_3 - k_4 \times \lambda_4$$

Type-IIc (δ_H):
$$\delta_H = S_0 \times \left[1 - k_1 \times \left(\frac{\lambda_1 \times \lambda_5}{S_0}\right)^{-1/1.75} \times \frac{k_5}{\lambda_5}\right] = S_0 \times \left[1 - k_2 \times \left(\frac{\lambda_2 \times \lambda_5}{S_0}\right)^{-1/1.75} \times \frac{k_5}{\lambda_5}\right] = S_0 \times \left[1 - k_3 \times \left(\frac{\lambda_3 \times \lambda_5}{S_0}\right)^{-1/1.75} \times \frac{k_5}{\lambda_5}\right] = S_0 \times \left[1 - k_4 \times \left(\frac{\lambda_4 \times \lambda_5}{S_0}\right)^{-1/1.75} \times \frac{k_5}{\lambda_5}\right]$$

Type of Pressure Profile(s)	Multiplication Factor to the Required Average Pressure Head: α Design Coefficients (k_1, k_2, k_3, c_i)				Multiplication Factor to the Potential Energy Head: β'
	k_1	k_2	k_3	c_i	β'
Type-I	4.357	3.477	2.745	2.92	0.75 ($F_S = 1.0$)	−0.25 ($F_S = 1.0$)
Type-IIa	4.357	3.477	2.745	2.92	0.75 ($F_S = 1.0$)	0.25 ($F_S = 1.0$)
Type-IIb	0.778	0.621	0.490	0.521	0.70 ($F_S = 1.0$)	0
Type-IIc and Type-III	4.357	3.477	2.745	2.92	−0.75 ($F_S = 1.0$)	0.25 ($F_S = 1.0$)

Type-I:
$$\alpha = 1 + c_i \times k_1 \times \lambda_1 = 1 + c_i \times k_2 \times \lambda_2 = 1 + c_i \times k_3 \times \lambda_3 = 1 + c_i \times k_4 \times \lambda_4$$
$$c_i: \frac{0.75}{F_S}\ (F_S \ne 1.0); \qquad \beta': \frac{1}{2} - \frac{0.75}{F_S}\ (F_S \ne 1.0)$$

Type-IIa:
$$\alpha = 1 + c_i \times k_1 \times \lambda_1 = 1 + c_i \times k_2 \times \lambda_2 = 1 + c_i \times k_3 \times \lambda_3 = 1 + c_i \times k_4 \times \lambda_4$$
$$c_i: \frac{0.75}{F_S}\ (F_S \ne 1.0); \qquad \beta': \frac{1}{2} - \frac{0.75}{F_S}\ (F_S \ne 1.0)$$

Type-IIb:
$$\alpha = 1 + c_i \times k_1 \times \lambda_1 = 1 + c_i \times k_2 \times \lambda_2 = 1 + c_i \times k_3 \times \lambda_3 = 1 + c_i \times k_4 \times \lambda_4$$
$$c_i: \frac{0.70}{F_S^{-0.37}}\ (F_S \ne 1.0)$$

Type-IIc and Type-III:
$$\alpha = 1 + c_i \times k_1 \times \lambda_1 = 1 + c_i \times k_2 \times \lambda_2 = 1 + c_i \times k_3 \times \lambda_3 = 1 + c_i \times k_4 \times \lambda_4$$
$$c_i: -\frac{0.75}{F_S}\ (F_S \ne 1.0); \qquad \beta': \frac{0.75}{F_S} - \frac{1}{2}\ (F_S \ne 1.0)$$

Dimensionless Physical Numbers: $\lambda_1 = \dfrac{(1-U_C)}{x}$, $\lambda_2 = \dfrac{CT_g}{x}$, $\lambda_3 = \dfrac{(1-EU)}{x}$, $\lambda_4 = \dfrac{(1-DU)}{x}$, $\lambda_5 = \dfrac{H}{L}$; and F_S = Enlargement factor, to take into account the effect of local losses $[F_S = 1 + (z_e/z_5)]$.

Table 2. Complete Results from the Comparison Test Between the Proposed EGR Approach, Previous Analytical Development (Yıldırım, 2007) and the SBS Procedure (Hathoot et al. 1993), the Required Hydraulic Characteristics (S_f, h_{0L}, H_d, H_{mean}, H_{max}, H_{min}, ΔH_{max}, φ_H) along the Energy-Grade Line (EGL) for Various Uniform Line Uphill and Downhill Slope Situations and three outlet discharge exponents (x = 0.2, 0.5, 1.0), for Five Types of Pressure Head Profiles (*Type-I, Type II.a, Type II.b, Type II.c and Type III*).

Improved Energy-Gradient Ratio (EGR) Approach (Proposed)

x	P,θ	T,y	S_f (%)	K_d	U_c (%)	H_{dl} (m)	H_d (m)	H_{max} (m)	H_{min} (m)	h_{0L} (m)	$φ_H$
0.2	I		1.35	0	98.7	8.73	8.69	8.73	6.69	2.04	1.0
0.5			1.37	0	96.7	8.75	8.68	8.75	6.68	2.07	1.0
1.0			1.43	0	93.1	8.82	8.66	8.82	6.66	2.16	1.0
0.2	II.a		1.32	-1.51	96.8	10.2	10.2	10.2	5.19	2.00	2.5
0.5			1.41	-1.42	91.8	10.3	10.3	10.3	5.16	2.12	2.4
1.0			1.55	-1.29	82.9	10.5	10.5	10.5	5.10	2.34	2.3
0.2	II.b		1.34	-3.74	93.9	12.5	12.5	12.5	2.92	2.02	4.7
0.5			1.52	-3.28	84.3	12.7	12.7	12.7	2.85	2.30	4.3
1.0			1.84	-2.72	67.1	13.1	13.1	13.1	2.73	2.77	3.7
0.2	II.c		0.47	1.07	99.1	7.43	7.43	7.36	7.11	0.71	0.38
0.5			0.46	1.09	97.8	7.44	7.44	7.37	7.11	0.69	0.38
1.0			0.48	1.05	95.4	7.41	7.41	7.36	7.11	0.72	0.38
0.2	II		2.77	0.38	98.3	9.58	9.58	9.58	6.54	4.18	0.73
0.5			2.66	0.38	96.0	9.46	9.46	9.46	6.58	4.02	0.72
1.0			2.62	0.38	92.2	9.41	9.41	9.41	6.59	3.96	0.71
0.2	II		1.07	1.88	99.1	6.90	6.90	8.31	6.74	1.61	0.98
0.5			1.04	1.92	97.7	6.87	6.87	8.32	6.73	1.58	1.01
1.0			1.04	1.92	95.4	6.87	6.87	8.32	6.73	1.58	1.01
0.2	III		1.2	4.32	96.3	4.73	4.73	10.5	4.71	1.75	3.34
0.5			1.1	4.75	90.5	4.62	4.62	10.6	4.59	1.59	3.77
1.0			0.9	5.39	80.4	4.48	4.48	10.6	4.45	1.40	4.40

Previous Analytical Development (Yıldırım, 2007)

S_f (%)	K_d	U_c (%)	H_{dl} (m)	H_d (m)	H_{mean} (m)	H_{max} (m)	H_{min} (m)	h_{0L} (m)	$φ_H$
1.36	0	98.7	8.70	8.66	8.70	8.72	8.79	6.66	2.05	1.0
1.38	0	96.7	8.72	8.65	8.72	8.72	8.72	6.65	2.09	1.0
1.43	0	93.1	8.79	8.62	8.79	8.79	8.79	6.62	2.16	1.0
1.36	-1.44	96.8	10.2	10.2	10.2	5.16	5.16	2.09	2.4
1.45	-1.38	91.8	10.3	10.3	10.3	5.12	5.12	2.19	2.4
1.57	-1.27	82.9	10.4	10.4	10.4	5.06	5.06	2.37	2.2
1.42	-3.53	93.9	12.5	12.5	12.5	2.89	2.89	2.14	4.5
1.54	-3.24	84.3	12.7	12.7	12.7	2.81	2.81	2.33	4.2
1.81	-2.76	67.1	13.0	13.0	13.0	2.69	2.69	2.74	3.8
0.44	1.14	99.1	7.34	7.39	7.39	7.11	7.11	0.66	0.42
0.49	1.02	97.8	7.33	7.40	7.40	7.11	7.11	0.74	0.39
0.47	1.06	95.4	7.35	7.38	7.38	7.11	7.11	0.71	0.38
2.87	0.35	98.3	9.51	9.51	9.51	6.84	6.54	4.33	0.69
2.77	0.36	96.0	9.39	9.39	9.39	6.88	6.58	4.18	0.67
2.68	0.37	92.2	9.35	9.35	9.35	6.90	6.59	4.05	0.68
1.34	1.50	99.1	8.87	8.26	8.26	6.74	6.74	2.02	0.76
1.32	1.52	97.7	8.85	8.29	8.29	6.73	6.73	1.99	0.78
1.29	1.54	95.4	8.85	8.29	8.29	6.73	6.73	1.96	0.79
1.29	3.87	96.3	4.71	10.5	10.5	4.71	4.71	1.95	2.97
1.22	4.08	90.5	4.59	10.6	10.6	4.59	4.59	1.85	3.25
1.12	4.47	80.4	4.45	10.6	10.6	4.45	4.45	1.69	3.64

Computer-Aided Step-by-Step (SBS) Procedure (Hathoot et al. 1993)

U_c (%)	H_{dl} (m)	H_d (m)	H_{max} (m)	H_{mean} (m)	H_{min} (m)	h_{0L} (m)	$φ_H$
98.8	8.66	8.91	8.86	8.70	6.91	7.16	0.72	0.36
96.9	8.70	8.78	8.70	8.70	6.78	7.09	0.69	0.39
93.4	8.57	8.69	8.57	8.57	6.69	7.16	0.70	0.36
96.8	10.4	5.56	10.4	10.4	5.56	1.90	2.5
92.0	10.2	5.39	10.2	10.2	5.39	1.83	2.6
83.2	10.6	5.33	10.6	10.6	5.33	2.31	2.3
93.7	12.9	3.44	12.9	12.9	3.44	1.97	4.8
84.3	12.5	3.36	12.5	12.5	3.36	1.66	5.5
67.4	13.0	3.06	13.0	13.0	3.06	2.38	4.2
99.3	7.37	7.42	7.42	7.16	0.72	0.36
97.5	7.25	7.36	7.36	7.09	0.69	0.39
95.1	7.41	7.33	7.41	7.16	0.70	0.36
98.0	9.57	9.57	9.57	6.71	4.25	0.67
96.2	9.53	9.53	9.53	6.79	3.96	0.69
92.1	9.18	9.18	9.18	6.63	4.22	0.60
99.0	7.14	8.12	8.12	6.75	2.04	0.67
97.6	7.26	8.10	8.10	6.93	2.17	0.54
95.7	7.24	8.04	8.04	6.87	2.22	0.53
96.4	5.17	10.7	10.7	5.17	2.03	2.72
90.3	5.11	10.4	10.4	5.11	2.25	2.35
80.6	5.02	10.5	10.5	5.02	1.99	2.75